AD NUMBER: AD0910453

LIMITATION CHANGES

TO:

Approved for public release; distribution is unlimited.

FROM:

Distribution authorized to U.S. Government agencies only; Administrative/Operational Use; 1 Apr 1973. Other requests shall be referred to

AUTHORITY

SAMSO ltr dtd 17 Jun 1977

SAMSO TR 73-65, Vol III

Final Report

SYSTEM 621B USER EQUIPMENT DEFINITION AND EXPERIMENTS PROGRAM

TASK VI – PHASE II

Volume III – Test Data And Analyses
Part 1

Grumman Aerospace Corporation

Technical Report SAMSO TR 73-65, Vol. III
April 1973

Space and Missile Systems Organization
Air Force Systems Command
Los Angeles, California 90045

ERRATA

for Technical Report SAMSO TR 73-65 Volume III, Part I

1. Page 2-4, Residuals matrix, last three terms now read;
"ΔX"
"ΔY"
"ΔZ"
Should read; "$\Delta \dot{X}$"
"$\Delta \dot{Y}$"
"$\Delta \dot{Z}$"

2. Page 3-7, first bullet item, fourth line now reads; "...expected, but is has..."
Should read; "...expected, but it has...".

3. Page 3-8, para. 3.2, second paragraph third line now reads; "...bias is a constant.".
Should read; "...bias is a line of constant slope.".

4. Page 3-15, Figure 3-7, output of third box now reads; "...(FILTER COORDINATE CORRECTIONS".
Should read; "(FILTER COORDINATE CORRECTIONS)".

5. Page 3-16, sentence following Equation 16 now reads; "...matrix $\bar{\delta}^*$ is not square and $(\bar{\delta}^*)^{-1}$ does not exist.".
Should read; "...matrix $\bar{\gamma}^*$ is not square and $(\bar{\gamma}^*)$ does not exist.".

6. Page 3-17, Equation 22, term to left of = sign now reads; $I\delta\dot{R}$".
Should read; "$I\delta\dot{B}$".

6A. Page 4-4, tabulation in middle of page, right column heading change "r" to "r".

7. Page 4-7, first paragraph, fifth line now reads; "...The same phenomena occurs in...".
Should read; "...The same phenomenon occurs in...".

8. Page 4-8, Figure 4-3, lower set of curves ($\sigma^2_{\dot{R}}$ vs Input Power Level); upper curve should be labeled "HC" and lower curve "MRL".

9. Page 4-9, explanation of terms under second equation, third term now reads;
$\frac{\Delta f}{f}$ = oscillator accuracy".
Should read: $\frac{\Delta f}{f}$ = oscillator accuracy, Δf is the frequency difference between the airborne and ground station oscillators.".

10. Page 4-9, "Scintillation" paragraph, fifth line now reads; "...low elevation angles and is estimated...".
Should read; "low elevation angles and are estimated..."

11. Page 4-26, "Study State Position Error Coupling Into Velocity" paragraph, second line now reads; "...and the transmitters creates a non-negligible position-velocity..".
Should read; "...and the transmitters creates a position-velocity...".

12. Page 4-34, heading for first listing now reads; "Cesium Test Measurement, Nanosec".
Should read; "Cesium Test Measurement, Nanosec (Also see Appendix C)".

13. Page 4-34, last paragraph fifth and sixth lines, delete expression beginning, "In addition, flight 23, which antennas", and ending, "error in channel 4.".

14. Page 4-36, first equation, now reads; $\hat{\phi}_i = \phi_i + ..$".
Should read; $\hat{\phi}_i = \phi_1 + ...$".

15. Page 4-37, third equation now reads; $\hat{D} = \beta - \bar{\hat{\phi}}_i$".
Should read; $\hat{D} = \beta - \hat{\phi}_i$

16. Page 4-37, delete line beginning, "$\hat{\phi}_i$ is the averaged value etc.".

17. Page 4-39, "Coarse Range" paragraph, fourth line now reads; "See Figure 4-16.".
Should read; "See Figure 4-13.".

18. Page 4-40, 17th line now reads; "-14.2 nanosec on the error envelope (see Section 9.8.1).".
Should read; "-14.2 nanosec on the error envelope.".

19. Page 4-52, third paragraph fourth line now reads; "...WSMR BET ($z = z - z_{BET}$).".
Should read; "...WSMR BET ($\delta z = z - z_{BET}$).".

20. Page 4-52, fourth paragraph third line now reads; "...in the antenna time is unknown.".
Should read; "...in the antenna with time is unknown.".

21. Page 4-66, first paragraph, 11th line now reads; "... $\Delta R = 16\,\epsilon_{code}$ and $\Delta \dot{R} = 0.1\,\epsilon_{carrier}$ where ϵ_{code} and $\epsilon_{carrier}$ are the phase...".
Should read; "...$\Delta R = 16\,\dot{\phi}\,\epsilon_{code}$ and $\Delta \dot{R} = 0.1\,\dot{\phi}\,\epsilon_{carrier}$ where $\dot{\phi}\,\epsilon_{code}$ and $\dot{\phi}\,\epsilon_{carrier}$ are the phase...".

22. Page 4-67, Figure 4-41 title now reads; "Hazeltine Carrier Loop Phase Error Response @ 123 dBm".
Should read; "Hazeltine Carrier Loop Phase Error Response @ -123 dBm".

23. Page 4-68, Figure 4-42 title now reads; "Predictable Effects of SC-50".
Should read; "Predictable Effects of SC-50 Multipath and Tropospheric Contributions to Velocity Errors".

24. Page 4-70, Figure 4-43 title now reads; "Predictable Effects of SC-50".
Should read; "Predictable Effects of SC-50 Multipath and Tropospheric Contributions to Velocity Errors".

25. Page 4-71, Figure 4-44 explanation of solid square symbol now reads; "TRANS S/N 4 DC".
Should read; "TRANS S/N 4 DC POWERED".
Also, add; "NOTE: Receiver 1 was used in the aircraft".

26. Page 4-72, Figure 4-47 add; "NOTE: Receiver 2 was used in the MCS."

27. Page 4-74, fourth paragraph, third line now reads; "...,for example, channel 1 4 nanosec and channel 3 −11 nanosec, are...".
Should read; "...,for example, channel 1-4 ≈4 nanosec and channel 3-4 ≈-11 nanosec, are...".

28. Page 4-89/90, Figure 4-60 title now reads; "Flight 2 Oscillator Records".
Should read; "Flight 20 Oscillator Records".
Also, add; "NOTE: Vertical scale factor is 2.5 fps/major division
Horizontal scale factor is 100 sec/major division".

29. Page 4-97/98, Figure 4-64, left margin of figure delete; "Fig. 6.4.5 Cal Pseudo-Dopplers etc."

30. Page 5-17, top of page, second line now reads; "...and draw some conslusions.".
Should read; "...and draw some conclusions.".

31. Page 5-18, Table 5-1, "Observed Error" column

now reads;	should read;
-14K Feet South-	-14K Feet South-
2 ft	2 ft
-4	-40
16	160
-Mid Range-	-Mid Range-
11	11
15	15
11	110
-14K Feet North-	-14K Feet North-
1	16
4	40
112	112

32. Page 6-5, top of page, fourth line now reads; "...end of the flight path.".
Should read; "...end of the flight path (Figure 6-2).".

33. Page 6-5, second paragraph, sixth line now reads; "...is the effect of the linear tranfsormation of the...".
Should read; "...is the effect of the linear transformation of the ...".

34. Page 6-7, Figure 6-4, explanation of scales now reads; "ERROR VECTOR = 10FT/BOX".
Should read; "ERROR VECTOR = 100 FT/BOX".

35. Page 6-9/10, Figure 6-5B, ordinate of curves now reads; "σ_{R1}, FPS and σ_{R3}, FPS".
Should read; "$\sigma_{\dot{R}1}$, FPS and $\sigma_{\dot{R}3}$, FPS".

36. Page 6-13/14, Figure 6-6B, title now reads; "B. PSEUDO-DOPPLER NOISE...".
Should read; "B. PSEUDO-RANGE NOISE...".

37. Page 6-16, para. 6.1.4, third paragraph, fourth line now reads; "At t-20, the aircraft...".
Should read; "At t=20, the aircraft...".

38. Page 6-27, para. 6-2, third paragraph, third line now reads; "Figure 6-27 and 6-28 show...".
Should read; "Figures 6-27, 6-28 and 6-29 show...".

39. Page 6-36, Figure 6-26, in all three plots delete; "$\frac{HAZ}{2}$"

40. Page 6-37, Figure 6-27, number under "Legend" should be "18".

41. Page 6-38, Figure 6-28, number under "Legend" should be "18".

42. Page 6-40, Figure 6-29, number under "Legend" should be; "18".

43. Page 6-42, Figure 6-31, number under "Legend" should be; "18".

44. Page 6-43, Figure 6-32, number under "Legend" should be; "18".

45. Page 6-44, Figure 6-33, number under "Legend" should be; "18".

46. Page 6-46, Figure 6-35, add; "NOTE: $\mu\delta$ R3-1 showed no measurable error as a function of received power (P_r) and is therefore not presented.".

47. Page 6-53/54, Figure 6-41, upper left plot delete; "SC-50 CHAN 4".

48. Page 6-61, Case 3, third line now reads; "...steady-state errors.".
Should read; "...steady-state errors by comparison with the WSMR BET.".

49. Page 6-62, Figure 6-47, add; "N = 1800 for each case.".

50. Page 6-63, Figure 6-48, add; "N = 1800 for each case".

SAMSO TR 73-65, Vol III

Final Report

SYSTEM 621B USER EQUIPMENT DEFINITION AND EXPERIMENTS PROGRAM

TASK VI – PHASE II

Volume III – Test Data And Analyses

Part 1

Prepared by

Grumman Aerospace Corporation
Bethpage, New York 11714

For

Space and Missile Systems Organization
Air Force Systems Command
Los Angeles, California 90045

April 1973

FOREWORD

This report dated 11 April 1973, contains the findings of a program titled "System 621B User Equipment Definition and Experiments Program, Phase II Field Test". The work was accomplished by Grumman Aerospace Corporation (GAC), Grumman Data Systems Corp. (GDSC), both of Bethpage, N.Y. and the Hazeltine Corporation (HC) at Greenlawn, N.Y. and complies with all the requirements of Contract Number F04701-71-C-0176. In addition to the receivers which were designed and built under this contract, the Air Force provided an additional receiver designed and built by the Magnavox Research Laboratory (MRL) of Torrance, California which was also flight tested.

System 621B is a concept for a global satellite - based precision navigation system designed to meet the requirements of land, sea and air military forces in an advantageous cost effective manner. One of the most important elements in this system is the user receiver. This report summarizes a series of flight and ground tests conducted at the White Sands Missile Range to evaluate the performance of a four-channel receiver in typical flight and field environments in order to solidify confidence in the predicted performance of System 621B receivers.

The report is published in three (3) volumes and bears the Air Force report number SAMSO-TR 73-65. Volume I is an Executive Summary, presenting in concise form a description of the program, the ground and flight equipment and an overview of the test results. Volume II contains the detailed program history, equipment description and data processing approach. Volume III contains a detailed presentation of the data taken during the program and a discussion of the results and conclusions to be drawn therefrom.

Grumman wishes to acknowledge the assistance of Lt. Col. V.L. Denninger, Program Manager, and Capt. D. Wilson, of the Air Force Space and Missile System Organization and of Messrs. W. Melton, F. Butterfield, T. Connor, A. Gillogly, W. Feess, Dr. J. Clifford, and Dr. L. Hagerman, of the Aerospace Corporation.

This report was prepared by Messrs. J. Courtney, R. Laho, I. Kadar, P. Richards, M. Moore, M. Neglia, I. Shulman, E. Graber, L. Pangburn, R. Latham, E. Burke of Grumman, R. Regis of Hazeltine, and B. Glazer of Magnavox.

John J. Courtney, Jr.
621B Director

Edward Z. Gray, Director
Special Projects

Publication approval of this technical report does not constitute Air Force approval of the report's findings or conclusions. It is published only for exchange and stimulation of ideas.

Valentine L. Denninger, Lt. Col., USAF
Program Manager
System 621B

ABSTRACT

System 621B is a concept for a global satellite-based precision navigation system designed to meet the requirements of land, sea and air military forces in an advantageous cost effective manner. One of the most important elements in this system is the user receiver. This report summarizes a series of flight and ground tests conducted at the White Sands Missile Range to evaluate the performance of a four-channel receiver in typical flight and field environments in order to solidify confidence in the predicted performance of System 621B receivers.

TABLE OF CONTENTS

For Volume III Part 1

TABLE OF CONTENTS

For Volume III, Part 2

TABLE OF CONTENTS (CONT)

For Volume III, Part 2

APPENDICES

LIST OF ILLUSTRATIONS

For Volume III, Part 1

LIST OF ILLUSTRATIONS (CONT)

For Volume III, Part 2

LIST OF ILLUSTRATIONS (CONT)

For Volume III, Part 2

LIST OF ILLUSTRATIONS (CONT)

For Volume III, Part 2

LIST OF ILLUSTRATIONS (CONT)

For Volume III, Part 2

LIST OF ILLUSTRATIONS (Cont)
For Volume III, Part 2

LIST OF ILLUSTRATIONS (CONT)
For Volume III, Part 2

LIST OF ILLUSTRATIONS (CONT)

For Volume III, Part 2

LIST OF TABLES

For Volume III, Part 1

LIST OF TABLES

For Volume III, Part 2

SECTION I

DATA PRESENTATION APPROACH

The field tests conducted at the White Sands Missile Range (WSMR) consisted of Area Navigation tests to determine navigation system performance, Instrument Landing System (ILS) type approaches and landings, and Ground User Multipath tests. The field operation took place during January to December 1972 and included 23 area navigation flights, eight ILS flights and multipath effects testing at four different locations.

The test data results in this volume are presented in three major groupings. After summarizing the overall results of the field tests, the first major section presents the test results generically according to error source. Error sources considered are random, steady state and systematic periodic components. The error sources are related to the test system configuration and their impact on the system performance is evaluated.

The second group of sections presents the flight test chronologically in accordance with the various test objectives and system configurations of the test program. It is instructive to present the data within the broad chronology since there is a definite relationship between the quality of the test data and the decisions to change system configuration and testing techniques at various stages of the test program.

Lastly, the results of the multipath testing are treated. The multipath data are presented by considering each test environment and the resulting measurements separately according to the characteristics of the reflected signals. The receiver test performance relationship to theoretical expectations is shown as well.

Additional material is presented which supports the test results and clarifies the system operation. The mathematical aspects of the experiment program implementation are examined prior to the detailed discussions of the error sources. This provides a foundation upon which the significance of errors can be established and clarifies the rationale for the test system configuration.

Equipment reliability for the field test is reviewed. The performance is shown to be adequate for the test program.

Some measure of the quality of the WSMR reference data is also presented in order to help interpret the performance of the test system. The generation of the WSMR data and of our navigation solution is quite different as are the types of errors which are typical of each system. This fact, together with observations made by WSMR personnel, are joined in a discussion of the basic trajectory data sets in order to place the primary topic of the test system accuracy on a firm foundation.

The test results are generally presented from two different viewpoints. One set of conclusions can be drawn by observing the behavior of the residuals obtained from a comparison of WSMR reference trajectory with the test sytsem navigation solution.

The other major set of conclusions is drawn from examining the behavior of the test system data alone.

This volume is intended to be used with Volume II. Only where the test results must be related to specific configurations or procedures is a detailed discussion of these aspects of the test program presented in Volume III. Generally, the system hardware descriptions, measurement techniques, test procedures, and data handling procedures are described in Volume II and should be referred to as required.

SECTION II

TEST SUMMARY

The field test program consisted of 31 flights at White Sands Missile Range (WSMR) and four ground user multipath tests. Useable test data were collected on 21 of the flights and on all of the multipath tests. WSMR has provided matching reference trajectories for the 21 flights. The test program goals and objectives are summarized in the following paragraphs and are related to the test results. General conclusions about the experimental navigation system performance are presented at the end of this section.

2.1 TEST PROGRAM OBJECTIVES AND RESULTS

The principal objective of the test program was to evaluate the performance of a four-channel receiver in typical flight and field environments. From this objective, a set of specific test objectives were derived. These test objectives were:

Flight Test Objectives

- Establish the range and range-rate accuracy of a four-channel receiver in an airborne environment
- Determine the effects of the aircraft flight environment on the receiver and airborne antenna performance
- Determine the effects of various aircraft-to-transmitter geometries on system performance including acquisition
- Evaluate the effects of different signal power levels on system performance
- Evaluate the system vertical positioning and sink rate accuracy during landing flare out
- Evaluate system capabilities to provide runway heading information during landing roll-out
- Evaluate the general system performance for landing navigation using a "typical" operational system configuration.

Ground User Multipath Test Objectives

- Evaluate the sensitivity of receiver accuracy to multipath signals
- Establish the receiver accuracy while operating in typical multipath environments
- Verify the theoretical understanding of multipath effects on the receiver by qualitative comparison of test results with predicted performance.

To accomplish the flight test objectives, an area navigation and an aircraft final approach and landing test program evolved. The area navigation portion of the test program was accomplished on flights 1 to 23, and the Instrument Landing System (ILS) portion on flights 24-31.

To accomplish the ground user multipath test objectives, a test program using selected ground sites at WSMR representative of various typical user environments, was devised.

The flight and ground test program designed to realize these test objectives was synthesized by defining each test condition and test procedure in great detail. A planning device called a test point, was used to establish the detailed procedures. A test point may be thought of as the totality of necessary equipment configurations and operational instructions required to evaluate a single specific aspect of test system behavior. For example, the requirement to evaluate the navigation receiver range rate accuracy when the received power level is -123dbm, the aircraft is at 34,000 feet MSL traveling at 700 fps, and the system geometry is similar to a Y satellite configuration centered over CONUS might define a test point. Test points similar to this were established for area navigation, ILS, and ground multipath testing. A tabular summary of these are contained in Ref. 20.

2.2 BRIEF HISTORY OF FIELD TESTS

A brief history of the field test program from flight 1 to flight 31 is presented herein as an aid in the readers understanding of the test data grouping in the later sections. A more detailed program history is provided in Volume II.

Flights 1 and 2 were checkout and shake-down flights, while flight 3 produced the first good navigation solution, which was the first major test program milestone. Comparison of the navigation solution with WSMR radar trajectories showed the system was working well enough to proceed with the tests. At this point very little was known about the real quality of the test system data or of the WSMR radar data. Within a month of flight 3, enough was learned to state that the test system ranging errors were less than 50 ft. This was considered the second test program milestone. As the testing continued, progress was made in determining the causes for steady-state biases in the observed ranging errors and in systematically removing them. At the same time testing was accomplished to broaden the data base along guidelines originally laid out in the test plan.

Flights 4-15 provided the data necessary to attempt the third program milestone, ranging errors of 10-15 ft. The error source investigation results from these flights indicated the bulk of the steady-state errors derived from the calibration procedures by which the calibration receiver data recorded at the Mobile Calibration Station (MCS) was referenced to the uplink transmitting antennas. The reasons for this were threefold:

1. The time delay in some of the cabling in the signal path had several nanoseconds of variability.

2. The ground rf link (monitor link) from transmitter sites to the MCS also had several nanoseconds of variability.

3. The internal delay in the transmitters between the uplink and monitor link outputs did not appear well controlled. One transmitter indicated a change of 40 nanosec during this period.

A change in the ground system configuration was made after flight 16 which removed most of these three error sources.

The data gathered during flights 4 - 15 also satisfied the program objectives of investigating the test system response to variables such as signal level, different aircraft flight environments, and aircraft to transmitter geometries.

Flights 17-23 provided data with the new ground system configuration. The expected ranging accuracies of 10-15 ft were realized. At this point the objective was to conduct further fine grain analyses of the remaining errors to determine if greater accuracy could be achieved. We recognized that our capability to determine these errors was becoming limited by the quality of the test equipment and the WSMR reference data. However, further work was accomplished, resulting in the uncovering of systematic errors associated with the uplink antennas, clarification of the rf path length measurements from transmitters to the calibration receiver, and further investigation of rf cable length variability.

The area navigation test phase was completed by flight 23. The ground system was then moved to Northrop Strip and configured for the aircraft approach and landing navigation test phase. The ILS type testing was accomplished during flights 24-31.

Flight 24 provided basic information on the ILS test system configuration "airworthiness" as had flights 1 and 2 for area navigation. Several adjustments were made in the configuration as a consequence of the flight results.

Flights 25-27 provided data on the approach phase of landing. Low approaches were performed, but no actual landings were attempted. The test system performance generally resulted in ranging errors of less than 10 ft.

Flights 28-31 provided data on the landing phase. Aircraft touchdown and rollout was accomplished on each run of these flights after a normal approach pattern. Additional WSMR instrumentation was installed to measure the aircraft position at touchdown for comparison with the navigation solution at this point. Program objectives of evaluating the effects of signal power level, aircraft-to-transmitter geometry and landing navigation configuration were satisfied.

Range rate measurement performance was determined during all of the flight testing. There was little emphasis placed on this aspect of the test system since the performance was very good and did not exhibit any of the problems encountered in the measurement of range. Errors are less than 1 fps and may be less than 0.5 fps depending upon the absolute accuracy of the WSMR reference.

2.3 TEST PROGRAM RESULTS

The test program results are presented for the Area Navigation, ILS and Ground User Multipath Tests. For each test, the results shown are related to the primary objectives of the test. For area navigation, the primary objective was navigation system accuracy; for ILS the primary objective was vertical navigation accuracy and

general system performance, and for ground user multipath the primary objective was qualitative receiver performance in typical multipath environments.

2.3.1 Area Navigation

Navigation system accuracy was determined from the test data collected on area navigation flights 17-23, where the test system was configured in its final form. Flight 1-16 served the purpose of surfacing the major test system design problems and lead to the changes in test system configuration used during flights 17-23. The data from the earlier flights support the general conclusions regarding system accuracy in a qualitative way insofar as the flight test data accuracy improved by predictable amounts as improvements were made in the test system configuration.

The test system provided navigation data in the form of position, velocity, and time of day in a coordinate system of the users choice. For this test program, we have chosen a rectilinear coordinate system with the origin located close to ground level at the center of the transmitter grid. The range of magnitudes of the user data for area navigation is:

Coordinate	Magnitude
X (East - West)	+60,000 to -60,000 ft
$\dot{X}$	+700 fps to -700 fps
Y (North - South)	+60,000 to -60,000 ft
$\dot{Y}$	+700 fps to -700 fps
Z (Vertical AGL)	+3,000 ft to 32,000 ft
$\dot{Z}$	-60 to +60 fps

The accuracy and precision of the data is to some extent a function of the specific implementation of the user equipment. For example, the data sampling rate, user platform dynamics, user computer sophistication (both word size and extent of system error modelling), and additional measurement aiding (user platform mounted accelerometers, rate gyros, or inertial navigators) all affect the quality of the user's navigation quantities. We have used only the test system data (no external aiding) and chosen a sampling rate of 5 samples/sec. (The extent of system error modelling was minimal with emphasis placed on the performance of the receivers as designed.) The data therefore reflect the capability of a user navigating with the 621B system but without using external aiding.

The navigation system accuracy is summarized in Table 2-1. The table shows the statistical characteristics (mean value, standard deviation or rms about the mean, and the rms value) of the residuals from comparison of the test system navigation solution with WSMR reference trajectory. The residuals are formed by:

Residuals		Nav Solution		WSMR Reference
$\begin{bmatrix} \Delta X \\ \Delta Y \\ \Delta Z \\ \Delta \dot{X} \\ \Delta \dot{Y} \\ \Delta \dot{Z} \end{bmatrix}$	=	$\begin{bmatrix} X \\ Y \\ Z \\ \dot{X} \\ \dot{Y} \\ \dot{Z} \end{bmatrix}$	-	$\begin{bmatrix} X \\ Y \\ Z \\ \dot{X} \\ \dot{Y} \\ \dot{Z} \end{bmatrix}$

Table 2-1 Navigation System Accuracy Summary

	CASE 1			CASE 2			CASE 3		
	MEAN	1σ	RMS	MEAN	1σ	RMS	MEAN	1σ	RMS
X, FT									
HC	3.4	6.8	7.6	6.5	5.7	8.5	-1.0	5.8	5.9
MRL	2.4	7.2	7.6	5.1	5.7	7.7	-2.3	6.1	6.5
Y, FT									
HC	18.4	11.6	21.8	4.3	15.3	15.9	0.4	10.3	10.3
MRL	11.2	15.2	18.9	4.3	13.6	14.2	1.3	8.2	8.3
Z, FT									
HC	-28.6	19.3	34.5	-23.1	15.7	27.9	-4.1	12.0	12.7
MRL	-14.7	25.3	29.2	-18.9	12.1	22.5	1.6	8.5	8.6
$\dot{X}$, FPS									
HC	0.1	0.6	0.6	0.1	0.6	0.6	0.1	0.6	0.6
MRL	-0.1	0.6	0.6	0.1	0.5	0.5	0.1	0.5	0.5
$\dot{Y}$, FPS									
HC	-0.1	0.7	0.7	-0.2	0.9	0.9	-0.1	0.6	0.7
MRL	0.2	0.8	0.8	0.2	1.0	1.0	0.2	0.7	0.7
$\dot{Z}$, FPS									
HC	0.3	0.9	1.0	0.7	0.6	0.9	0.3	0.6	0.7
MRL	-1.0	1.3	1.6	-0.3	0.9	1.0	-0.5	0.9	1.0

The navigation solution and the WSMR reference trajectory (BET) are aligned using a common time base (IRIG B which is recorded along with the data during the test) and the residuals are computed at the 5 sample/sec data rate for all portions of the flight path which correspond to aircraft-to-transmitter geometries representative of an operational satellite system. Thus Table 2-1 summarizes approximately 10,000 solution points collected during flights 17-23, which cover the full range of realistic aircraft-to-transmitter geometries, received power levels at the user between -110dbm and -140dbm, and range rate dynamics (see Section 4).

Three different versions of these data are presented; cases 1, 2, and 3. Case 1 represents the navigation solution which was computed during the test period. Case 2 represents the data quality achieved as a result of identifying two sources of error present during the flight 17-23 test period and recomputing the navigation solution after removing these errors. Case 3 represents the data quality achievable by minimizing the residual between the navigation solution and the WSMR reference, a navigation quality which may be achievable by a user in a future operational situation. A discussion of the particulars of each case and the rationale for presenting the data in this manner follows.

To compute the navigation solution for the WSMR field test configuration, some important measurements must be made on ground system components and the data then used along with the pertinent system range and range rate data collected in the aircraft during the test. These measurements are required to reference the transmitted signal phase as recorded at the ground calibration receiver site to the transmitter uplink antennas. The measurements consist of rf cable time delay and propagation time delays from the transmitter sites to the calibration receiver site. The navigation solution for Case 1 utilizes values for these delays based on a measurement history accumulated from flight 7 up to flight 23. The values selected from this history were judged, at the time of these tests, to accurately describe the signal path length. The resulting navigation solutions contained steady state errors of similar magnitude for both HC

and MRL derived trajectories (see Table 2-1), leading to the conclusion that there were unaccounted error sources associated with the ground system (the major common element in both Hazeltine Corp. (HC) and Magnavox Research Lab (MRL) navigation solutions).

Analysis of the test results from flights 17-23 indicated that there were two error sources associated with the ground system contributing to most of the observed navigation solution error. These were erroneous values of the ground propagation signal path length and a previously unrecognized signal delay effect produced by the uplink antenna. Additional measurements of the ground propagation path length and of the four uplink antennas provided data required to correct for these effects (see Section 6 for the details of these measurements). Case 2 shows the navigation solution after these two errors have been removed.

It is important to recognize that these errors are associated with the ground components of the test system. This portion of the test system is unique to the WSMR field test configuration and will not be present in an operational satellite system. The errors associated with these components of the test program tend to mask the true performance of the flight hardware which could be expected in an operational system. Case 2, therefore, represents the navigation accuracy of the flight system after the major identified error sources peculiar to the WSMR configuration have been removed.

Observations of the general behavior of the test equipments throughout this program lead us to present the navigation solution from a third viewpoint. This side-by-side comparison of navigation performance from the HC and MRL experimental equipments has proved to be one of the most important results of this program. There is remarkable similarity in the quality of the navigation solution produced by these two receivers, as shown by Table 2-1, considering the different design approaches implemented by the two companies. At the same time, both receivers have shown shortcomings peculiar to each. For example, the HC receiver shows an error in ranging accuracy as a function of received signal level, while the MRL receiver is largely insensitive to this effect. Conversely, the MRL receiver produces data with statistical serial correlation, an undesirable characteristic for most conventional data filters, while the HC data show predominantly white noise characteristics. Equipment improvements in these and other areas in future designs will improve the navigation solution performance. Even so, there may still remain small steady state systematic errors in the position and velocity solutions. In the event these bias errors can be calibrated, their effect could be removed from the navigation solution. Case 3 is an application of this concept to the test system data.

The average steady state error of both HC and MRL navigations solutions from Case 2 results are used to generate Case 3 solutions. As in the previous cases, the navigation solution errors are determined by comparison of the test system trajectory with the reference trajectory supplied by WSMR. A single average value for both receivers is determined from the comparison residuals. This value is converted to an equivalent range error and used as a correction term to the measured ranges when the navigation solution is recomputed. The equivalent range errors used for the Case 3 computation are: $R_1 = 0.0$ ft, $R_2 = 8.9$ ft, $R_3 = 0.6$ ft, and $R_4 = 5.8$ ft (see Appendix C).

This is considered a realistic application of the Case 3 philosophy insofar as the single correction term set represents a compromise of the optimum values which could be selected for either the HC or the MRL receiver alone. A similar situation

is likely to apply to an operational system where the correction terms may be derived from a few specially instrumented users and the results applied to a large class of user equipments.

A representative data run has been selected from the flight 17-23 group to show the time series of the residuals derived from comparison of the navigation solution trajectory processed through a two-state filter (to be discussed later in this section) with the WSMR reference, and to illustrate the impact of the three different cases considered on the data quality. The data shown in Figures 2-1 through 2-6 applies to Flight 19, Run 5, a flight path on which the aircraft is at 34,000 MSL heading due south at a speed of 660 fps. The flight path passes directly over the center of the ground transmitter grid and simulates flying over the equator while using a rotating 30°Y satellite cluster centered over the equator. The average received power level for this run was approximately -130dbm.

The HC and MRL X-coordinate position residuals are shown in Figure 2-1. The plot spans a 40 sec time period where the aircraft is over the center of the transmitter grid (Salt Site) at t = 20 sec. The data are presented at the system sampling rate of 5 sample/sec. A positive residual indicates that the navigation solution is numerically greater than the WSMR reference. Thus for the coordinate system used the following conventions apply

Sign	Sense of Error
X Coordinate Residuals	
+	Nav Solution is to the east of WSMR BET
-	Nav Solution is to the west of WSMR BET
Y Coordinate Residuals	
+	Nav Solution is to the north of WSMR BET
-	Nav Solution is the south of WSMR BET
Z Coordinate Residuals	
+	Nav Solution is above WSMR BET
-	Nav Solution is below WSMR BET

The X coordinate data is minimally affected by the changes used to generate Case 2. This is expected because these changes primarily affect channel 1 and 4 ranging data which strongly influence the Y and Z coordinate data in the WSMR test geometry, but weakly influence the X coordinate (this subject is comprehensively treated in the solution sensitivity analysis in Section 4). Case 3 data shows improvement in the solutions, as expected, since the average equivalent range correction is applied.

The Y and Z coordinate position residuals are shown in Figures 2-2 and 2-3 respectively. While Case 2 improves the Y coordinate solution accuracy by approximately 10 ft, there is also a change in slope of the residual. This slope is peculiar to the WSMR tests and is related to the scaled down dimensions of the test system. The small scale geometry (a flight of 10 n mi approximates the geometry change a user would experience flying across the entire U.S.) magnifies the navigation solution errors. The slope of the residual in Figure 2-2, Case 2 is caused primarily by

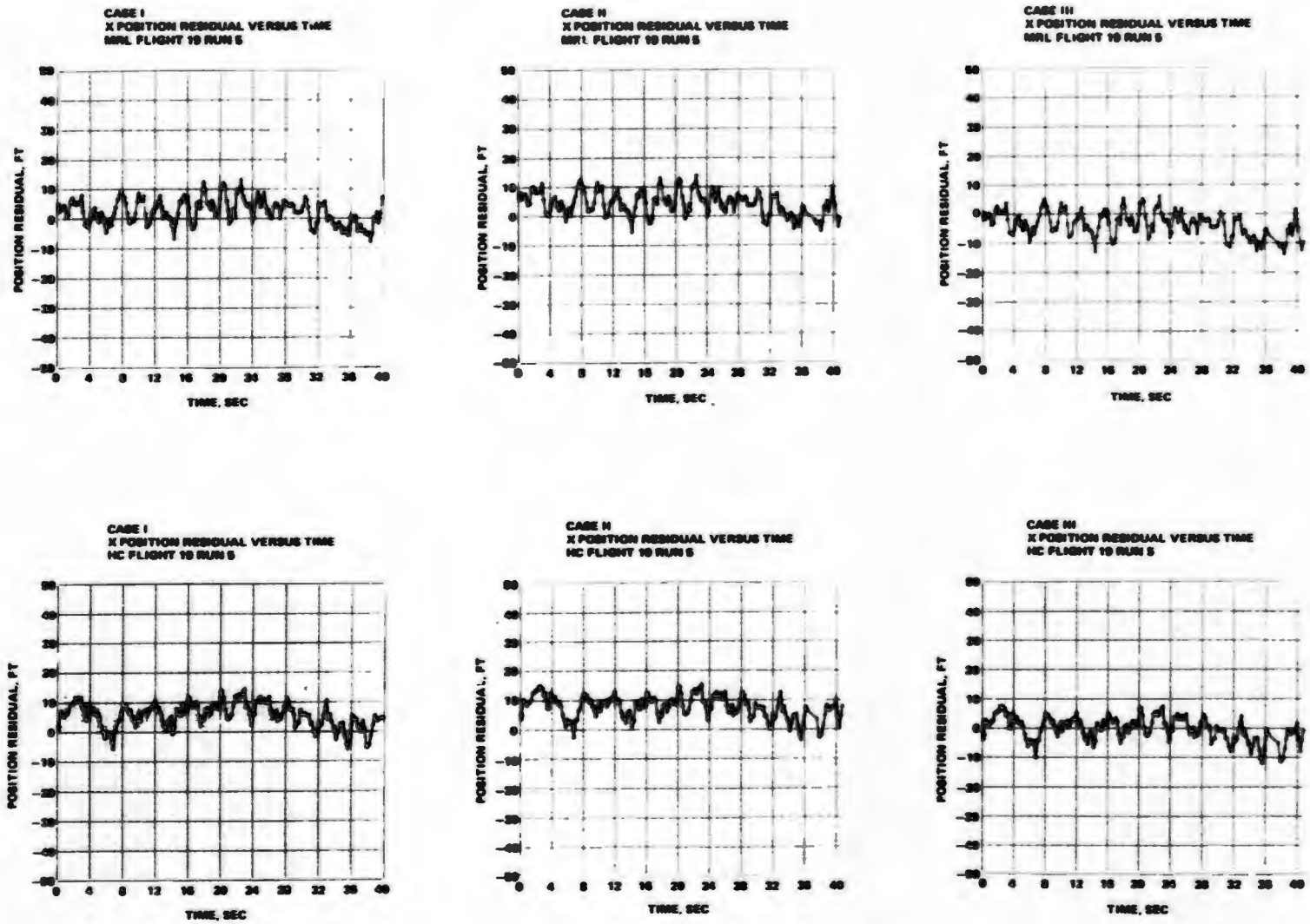

Figure 2-1 MERGE Program Outputs–X Position Residuals

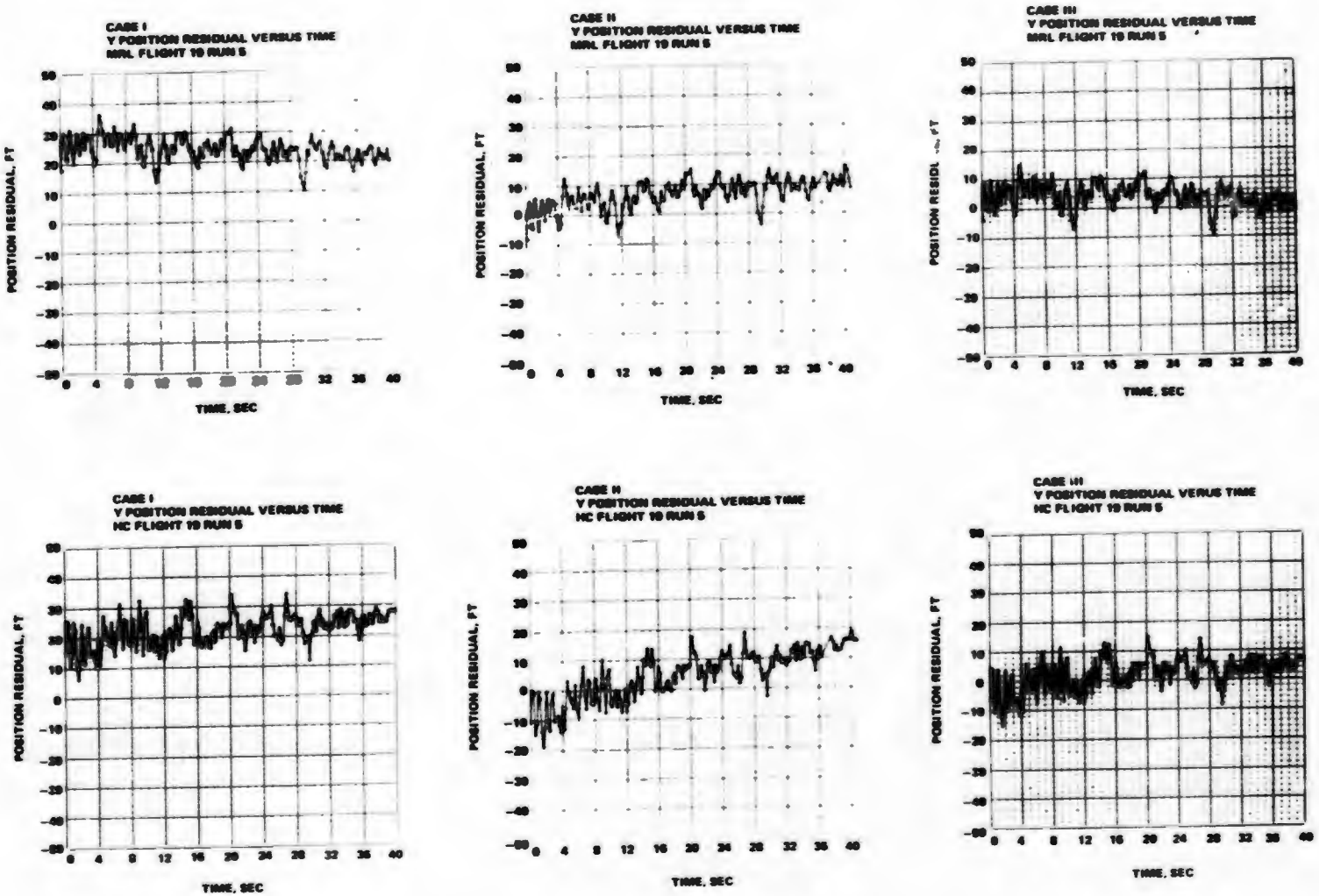

Figure 2-2 MERGE Program Outputs–Y Position Residuals

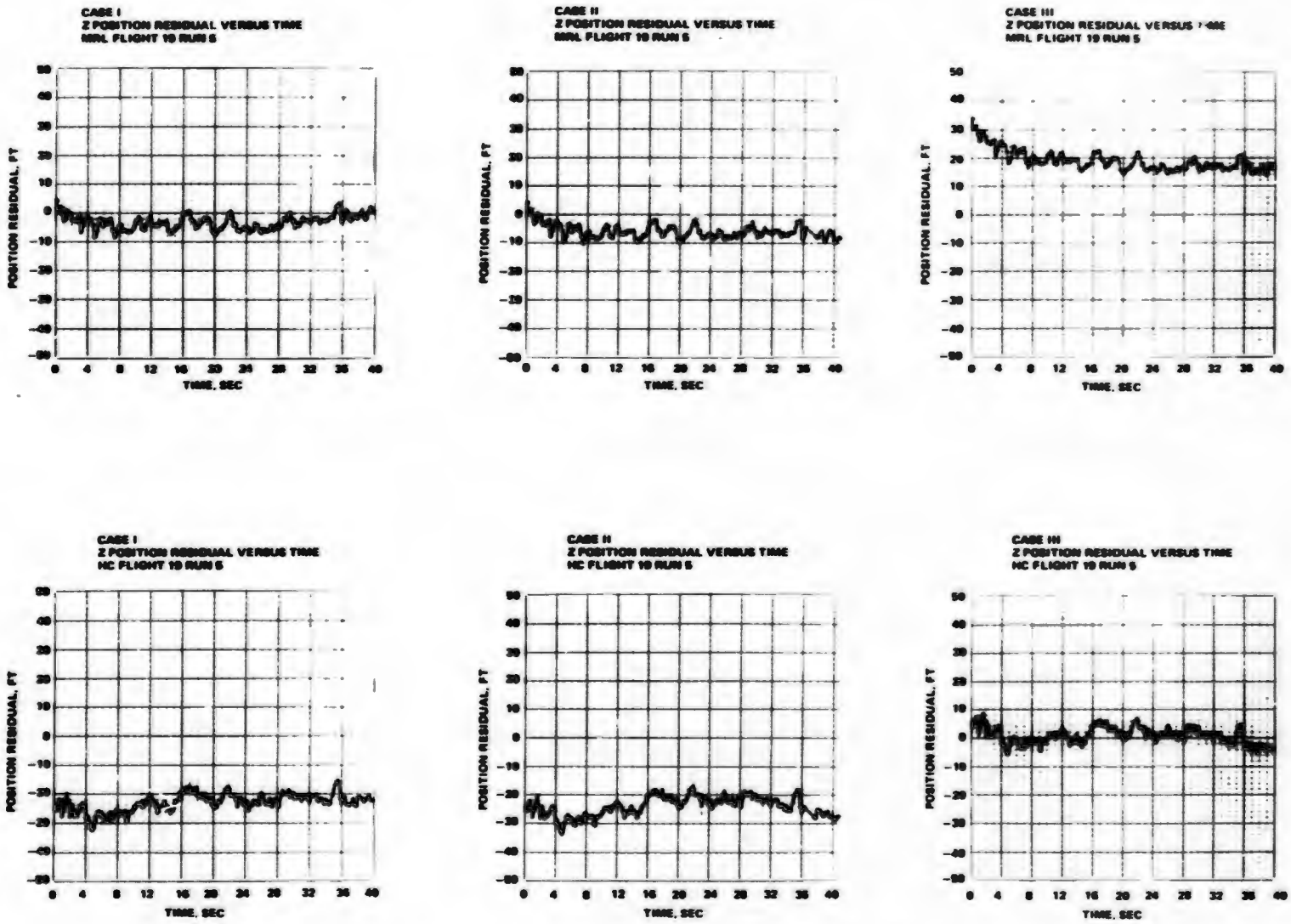

Figure 2-3 MERGE Program Outputs-Z Position Residuals

a steady state error of approximately 5 ft somewhere in the system on channel 1. This error is not lumped in one component but, rather, is distributed among a number of system components (error sources and magnitudes are discussed in Section 4). Although the error is basically steady-state, it contains some slowly varying components which change the navigation accuracy slightly as a function of time. Therefore Case 3 data on Figure 2-2 still shows some slope (remaining steady-state ranging errors) even though average values of these errors have been removed (in Case 3). One could find data runs where this slope is negligible, which represent runs where the bias errors happen to match the average value of the calculated error. For example, the MRL Y position error shown in Figure 2-2 for Case 3 has negligible slope. For this particular set of data, the average value of Case 3 was a good approximation of the real errors affecting Y coordinate. Referring to Figure 2-3 Case 3, we see that the Z position error for MRL does show some slope indicating the channels influencing the Z coordinate at this location (but at the same time weakly influencing the Y coordinate as seen in Figure 2-2) contain a small amount of steady state error.

The statistical summary in Table 2-1 for the navigation accuracy provides a good measure of the variability of the test data since the table covers all of flights 17-23. Further analysis of these effects is presented in Section 6 which discusses flights 17-23 in detail.

The remaining residual plots, Figures 2-4 through 2-6, show the system velocity comparisons to the WSMR reference The velocity accuracy is affected by the 3 case presentation indirectly through a position/velocity coupling matrix. Velocity data in user coordinates is derived by resolving measured range rate information onto user coordinate frame axes through the unit vectors which relate the user's position to the position of the system transmitters. Thus any errors in the user position causes erroneous unit vectors, which in turn degrade the accuracy of converting range rate into coordinate velocities. The effects of this position/velocity coupling is minor as shown on Figures 2-4 through 2-6.

The rather large velocity error excursions, (for example, on Figure 2-4 the X error goes from -0.4 fps to +1.2 fps around t=20 sec) are caused by the WSMR reference and not the test system. The test system and WSMR reference velocity accuracies are very similar, making analysis of this data somewhat difficult. However, since these error excursions are not too frequent, the velocity accuracy summary presented in Table 2-1 is considered valid.

2.3.2 ILS

After completing the area navigation tests, the test system was evaluated for suitability as a landing navigation aid. The aircraft landing navigation testing was accomplished by relocating the ground equipment at a dry salt lake bed and conducting both low approaches and actual touchdowns with the aircraft. The primary area of interest was the accuracy of aircraft vertical position and velocity information provided by the navigation system. To improve the test geometry relative to vertical position accuracy, the center transmitter was suspended in a balloon at about 5000 ft altitude.

The vertical axis (Z) system accuracy is summarized in Table 2-2. The system accuracy is determined by the same techniques used for area navigation. This consists of comparing the test system navigation trajectory with a reference trajectory supplied by WSMR. Table 2-2 presents a statistical characterization

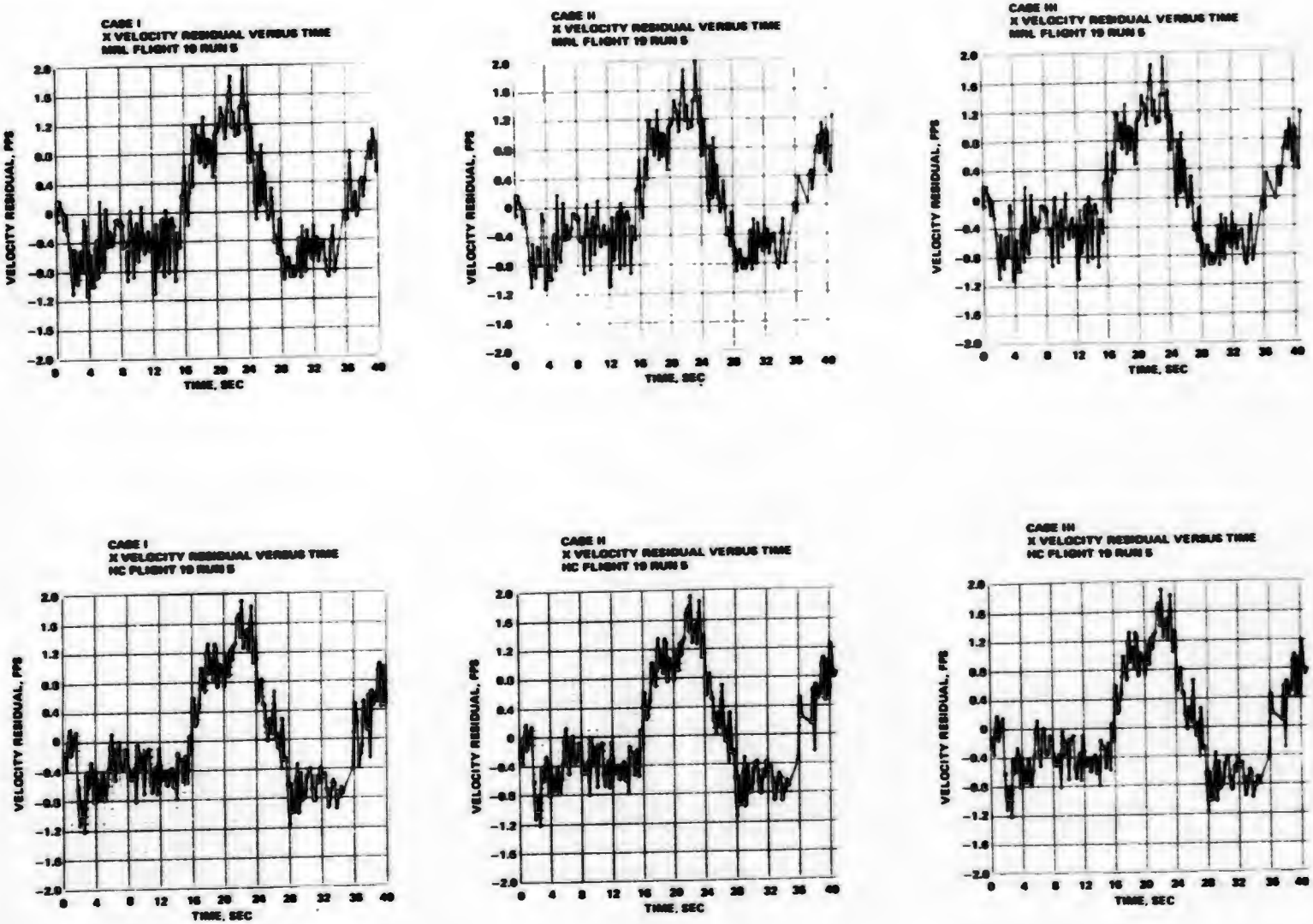

Figure 2-4 MERGE Program Outputs-X Velocity Residuals

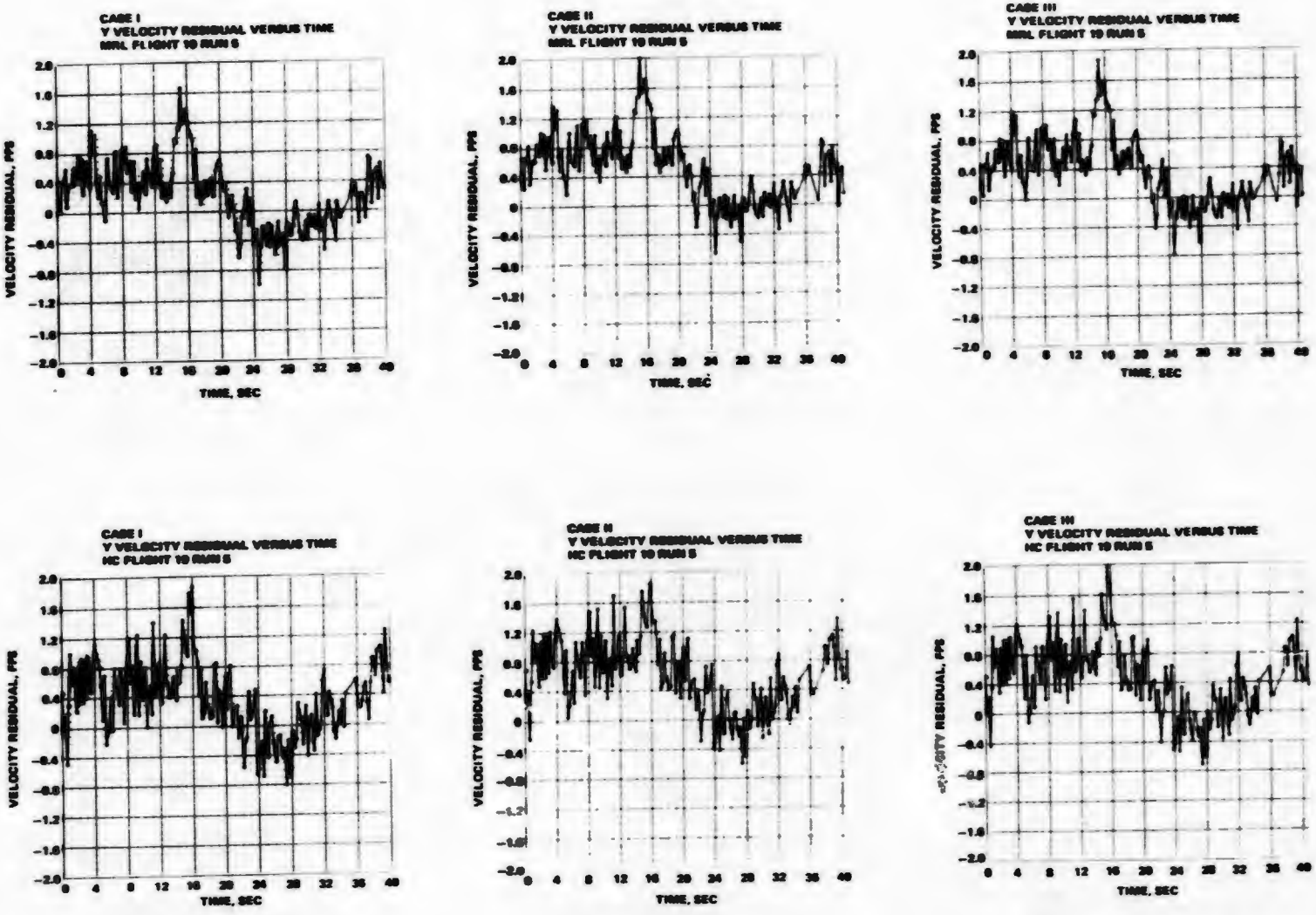

Figure 2-5 MERGE Program Outputs-Y Velocity Residuals

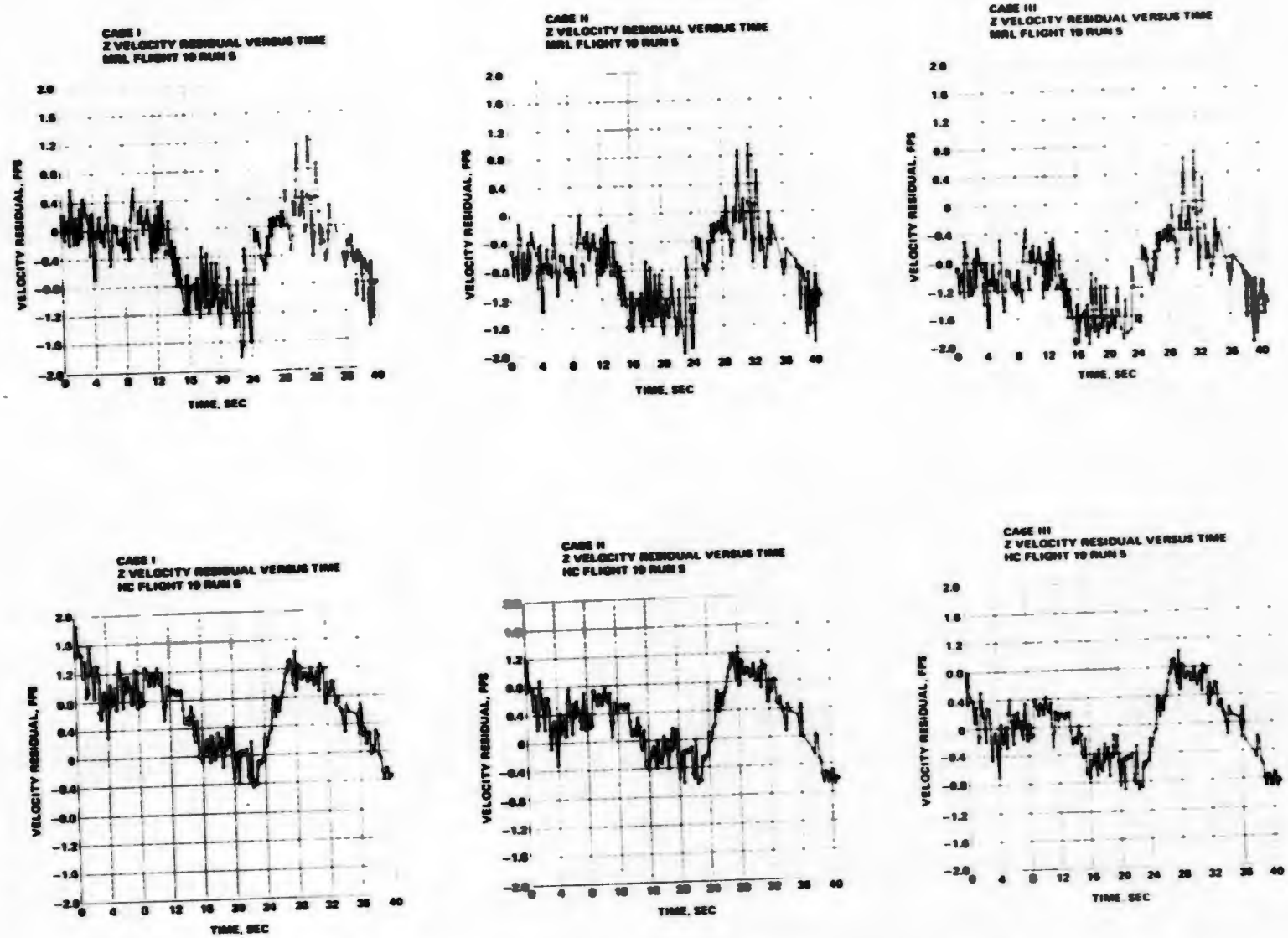

Figure 2-6 MERGE Program Outputs-Z Velocity Residuals

Table 2-2 ILS Vertical Navigation Accuracy

	MEAN	1σ		MEAN	1σ
X, FT			X, FPS		
HC	0.3	3.3	HC	0.2	1.1
MRL	-1.1	7.3	MRL	0.2	1 4
Y, FT			Y, FPS		
HC	-2.7	11.4	HC	-0.5	1.7
MRL	2.2	12.3	MRL	-0.2	2.2
Z, FT			Z, FPS		
HC	-1.3	13.3	HC	-0.2	2.3
MRL	-1.3	8.3	MRL	-0.4	2.0

(mean value, standard deviation or rms about the mean, and rms) of the residuals obtained from the trajectory comparisons. The table summarizes approximately 2000 navigation solution points obtained from five test flights. The data are obtained from a region on the aircraft flight path from approximately 8000 ft before the nominal aircraft flare point to approximately 7000 ft beyond the runway threshold at the approach end. This region requires the most accurate vertical navigation information and corresponds to a position on the approach path where the aircraft is approximately 300 ft above ground to a position where the aircraft is braking on the runway.

The distribution of the Z coordinate errors is presented in Figure 2-7. Histograms of both HC and MRL navigation solutions errors in position and velocity are shown. The velocity performance of both solutions is similar. The velocity accuracy may be superior to that shown since, in the ILS case as in area navigation, the WSMR reference velocity accuracy is similar to the accuracy of the test system (see Section 10 for a discussion of this topic).

The Z coordinate position error distribution is not the same for both HC and MRL solutions. This is a peculiarity of the ILS test data and does not appear in any of the other data collected during this test program. The HC data show a considerable spreading of the error distribution (rms =13.4 ft) compared to the relatively narrow error distribution (rms =8.4 ft) of the MRL data. This is a consequence of the different equipment designs implemented by HC and MRL. The ILS system configuration utilized in this test program shares a shortcoming with most ILS system implementations, namely a signal environment which is characterized by large signal level variations, inherent multipath, and large range dynamics ($\dot{R}, \ddot{R}, \dddot{R}$). However, the 621B navigation concept is theoretically insensitive to these types of signal phenomena and should show virtually no degradation in performance in an ILS environment. The ILS test data collected during this program supports this theory and at the same time clarifies the system operation. The spread of HC Z-position errors shown in Figure 2-7 is the direct result of the receiver sensitivity to a multipath error signal present in the channel whose transmitter is suspended 5000 ft above the runway. The HC receiver design permits the tracking loop bandwidth to widen to approximately 100Hz, which then allows the multipath signal (fade frequency $\approx$ 24Hz) to pass unattenuated into the tracking circuits. The MRL receiver design on the other hand, maintains a tracking loop bandwidth of approximately 10Hz thereby excluding the multipath signal from the tracking circuits. This maintains a narrow Z axis position error distribution in the MRL case. Thus, the test that has been performed demonstrates that there is an undesirable multipath environment present during the ILS approach, but that equipment can be designed within the 621B navigation concept which is insensitive to this signal phenomena during ILS navigation phases.

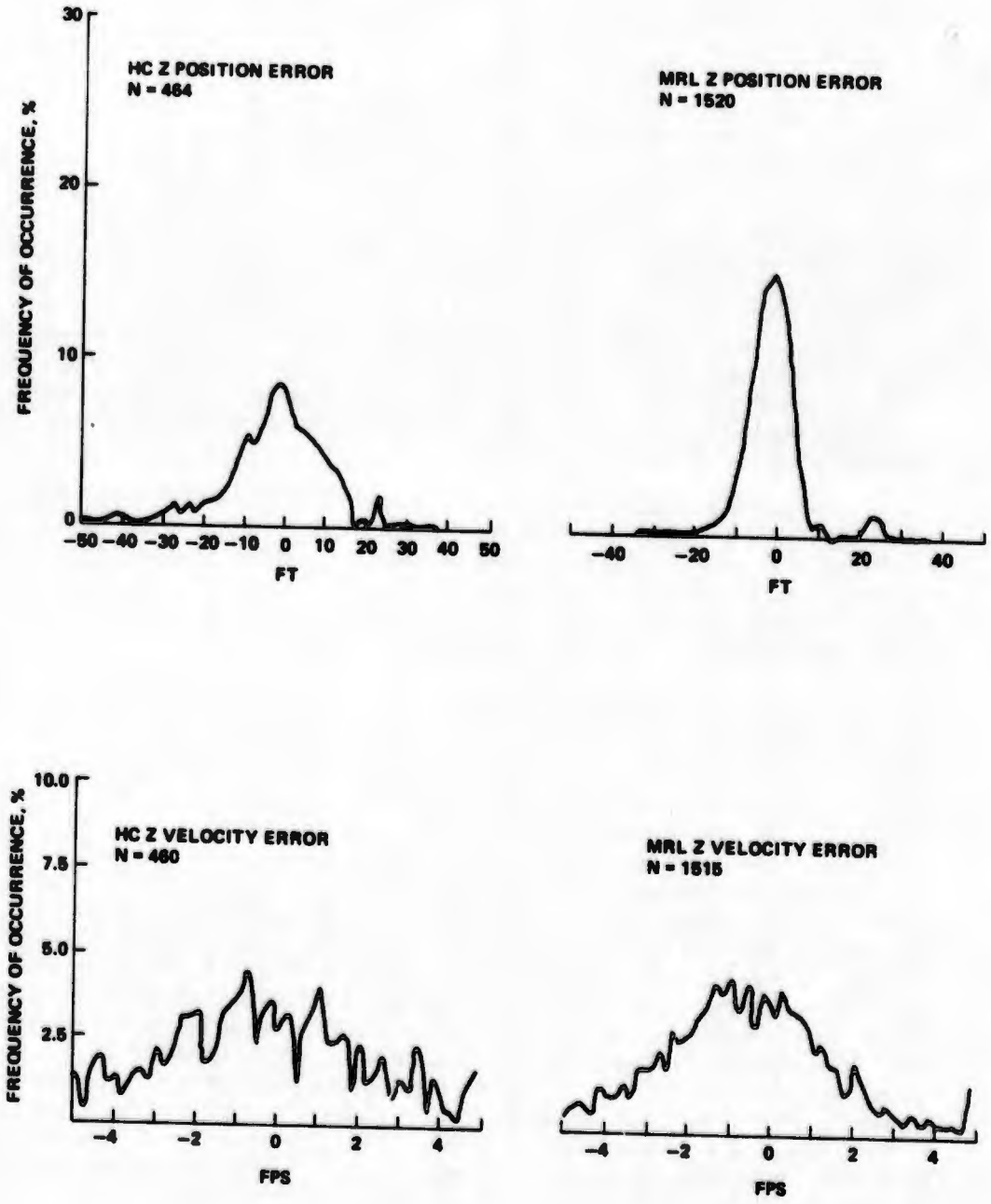

Figure 2-7 ILS Z Axis Navigation Error Histograms

The overall test system performance during ILS testing indicates that the system is suitable for landing guidance. The navigation errors in the horizontal plane are generally small and the cross runway component is sufficiently accurate for runway centerline guidance. Cross runway position accuracy measured was: mean = 1.1 ft, standard deviation = 7.3 ft. The horizontal position errors are summarized in Figure 2-8 which depicts the error component at trajectory intervals of 2 sec (every tenth solution point) for flights 25-31. An illustration of the clustering of the horizontal position errors is shown in Figure 2-9. An error density surface was derived from the entire set of 2000 solution points available from ILS tests. The information shown in this figure is similar to the horizontal error summary in Figure 2-8 but illustrates that the errors are generally less than 10 ft.

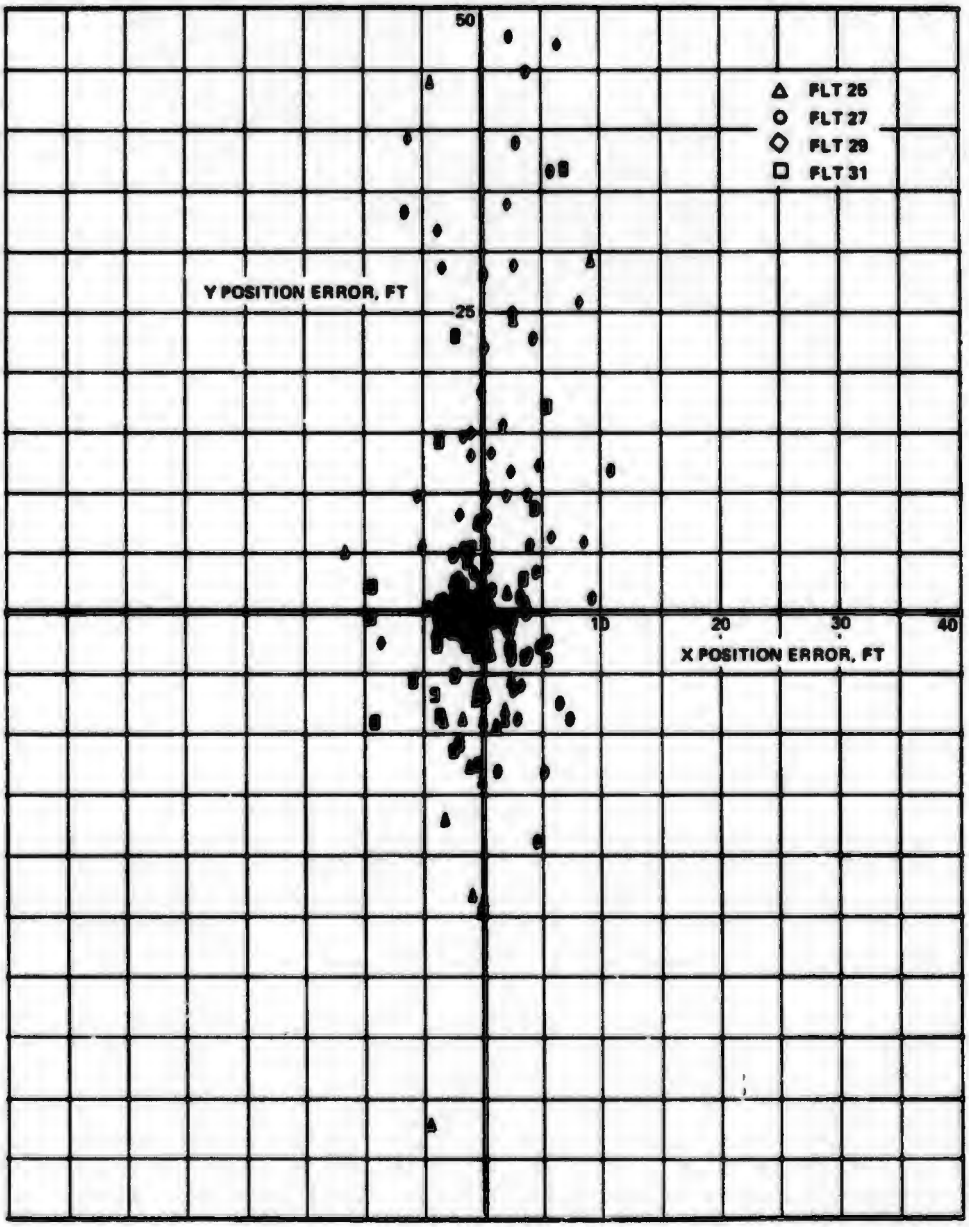

Figure 2-8 MRL Horizontal Position Error During ILS

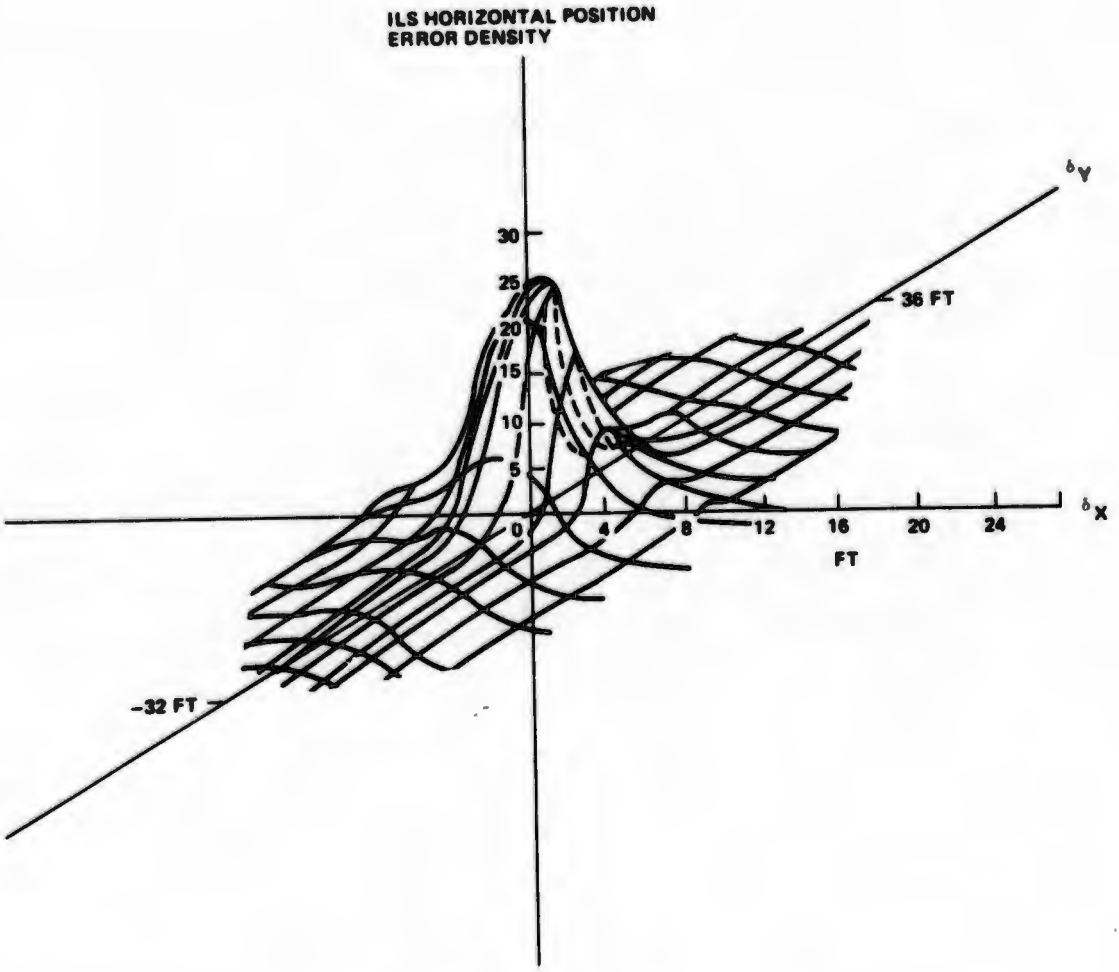

Figure 2-9 Hazeltine Static Solution for ILS

2.3.3 Ground User Multipath

The overall objective of the ground user multipath test was to establish the qualitative receiver performance in typical multipath environments. Multipath signals degrade the ranging accuracy of the receiver by creating a distortion of the modulation envelope of the total received signal. This develops an error in the receiver code tracking loop which affects the range accuracy.

The multipath tests conducted at WSMR consisted of a series of measurements using various transmitter-to-receiver antenna geometries at four separate multipath environments. These environments are characterized in Table 2-3. The overall results of these tests indicate that the theoretical understanding of multipath effects on range accuracy is verified by the experimental results. The theoretical envelope of range tracking error as a function of multipath expressed as the differential delay between the desired and interfering signals is shown in Figure 2-10.

Table 2-3 Ground User Multipath Test Environments

Test Locations	Multipath Characteristics	Multipath Geometries Used
Tule Peak	Specular reflections off a slightly rough surface containing desert sand, bushes, and rocks up to 3 feet in diameter.	• Low grazing angles: 8.5°, 12° • Short differential delay
Dead Man Canyon	Diffracted signals across a gravel pile and construction equipment. The test site was located in a gravel quarry area where excavations were in progress.	• Low grazing angles: < 3° • Short differentia. delay
Northrop Strip	Diffuse, partly diffuse, and specular reflections from the flat surface of a dry alkalai salt flat.	• Grazing angles ranging from high, approximately 60° to low, approximately 10° • Long and short differential delay
White Sands Area	Diffuse and partly diffuse from the gypsum sand dunes in the White Sands National Monument.	• Grazing angles of 30°, 40° and 60° • Long differential delays

Receiver ranging errors can take on any value within this envelope depending upon the exact signal differential delay (see Section 9). The test data follow this prediction as shown in Figure 2-11. This figure shows all the data collected at the Northrop Strip location and is typical of the receiver performance at the other test sites. The theoretical envelope superimposed on this figure contains virtually all of the test data. The few points which fall outside of the envelope are a result of uncertainty in the true transmitter position and therefore, uncertainty in the value of differential delay determined from the transmitter-to-receiver geometry. This means the measured tracking errors (ordinate) cannot be properly located on the plot of Figure 2-11. The transmitter position cannot be precisely measured since, for these tests, the transmitter was carried 2000 ft above ground by a tethered balloon which drifted slightly in the wind.

The test program has confirmed that multipath effects on receiver performance are understood and are therefore predictable. A ground user on the average will experience ± 25 ft of multipath error depending of course on the exact system geometry. However, the differential delay sensitivity of the satellite-to-ground user geometry is only a function of the user antenna height above ground. This allows the ground user to determine the presence of multipath by changing his antenna height. Since the power level variation is correlated with multipath error, the user, by observing the power variation, can locate himself in low multipath error environments. In general the antenna height variation need only be in the order of a wavelength (approximately 0.6 ft).

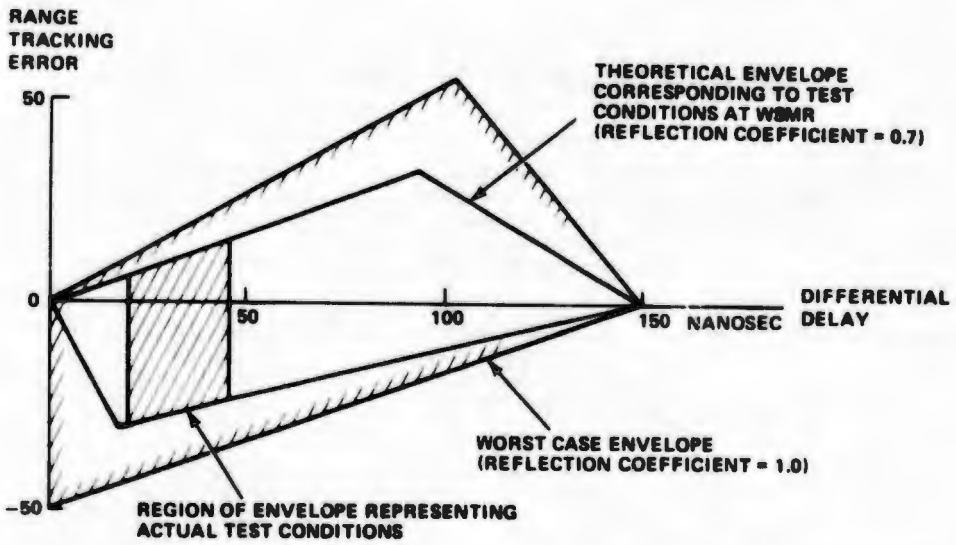

Figure 2-10 Theoretical Envelope of Range Tracking Error Caused by Signal Multipath

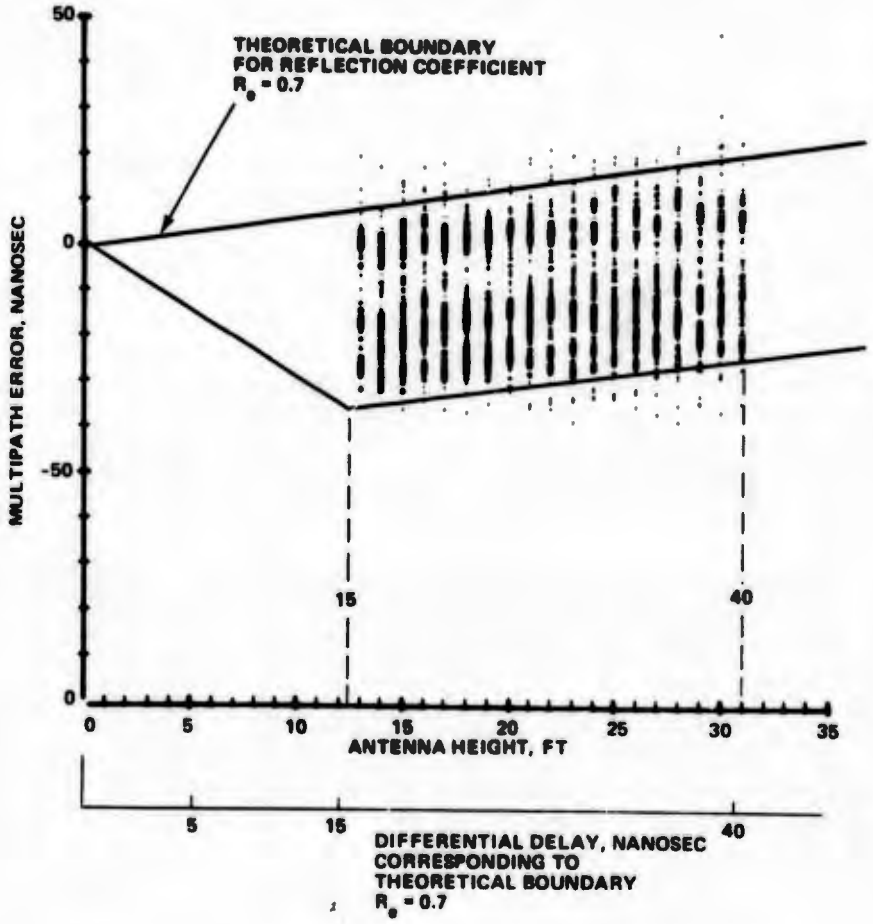

Figure 2-11 Multipath Test Data From Northrop Strip

2.4 GENERAL CONCLUSIONS

The test program successfully met the principal objective of evaluating a four channel receiver in typical flight and field environments. The specific test objectives and the related test results are given in Table 2-4. Confidence in the 621B concept was solidified through the actual test system performance. Analysis of the error components indicate that an unexplained range error exists, which is approximately 2 ft (see Section 6). The range rate errors were difficult to accurately assess with available instrumentation but are generally less than 1.0 fps.

Several observations were made about the system behavior. Perhaps the most important among these is that ranging bias errors are extremely difficult to control. Although many of the error mechanisms have been determined through analysis of the data, some small steady state error remains unexplained. In addition, the known error mechanisms point up the extreme care that must be used during design and manufacturing to control signal delay variability to less than one nanosecond, throughout the system.

The ILS testing conclusively demonstrated the suitability of 621B navigation in the aircraft landing environment. The system performance of each receiver is given in Table 2-2. An overall performance for vertical navigation has been determined by summing the data populations (weighted according to sample size) from the two receivers resulting in overall position accuracies of $\mu = -1.6$ft, $\sigma = 8.9$ft and velocity accuracies of $\mu = -0.4$ fps, $\sigma = 2.1$ fps. These test results indicate that the signal environment during this phase of aircraft operation will not degrade the navigation accuracy.

The performance of the receiver in the presence of multipath, typical of ground user operation, matches the theoretical predictions of the system behavior. A condition was found in which the receiver can develop a false lock with large associated range errors. However, the condition is unstable and will disappear with small motion of the ground user antenna (see Section 9.) A ground user will probably require a multipath presence detector built into the equipment for repeatable accuracy, but this is not seen as a problem since only small user antenna movements (less than 8 in.) will generally place the ground users in region of negligibly small error.

The navigation system accuracy achieved with the test system configuration at WSMR is given in Figure 2-12. These data are derived from the area navigation flight test and represent user error after the error sources unique to the special WSMR aspects of the test system required to simulate an operational system (those not representative of an operational system - see Case 2 criteria in Section 2.1) have been removed. The data in Figure 2-12 show the percentage of navigation solution points having less than a specified total error. Thus a user could expect to achieve a total spherical probable error (SPE) of less than 35 ft in position and less than 1.7 fps in velocity for 80% of the solution data.

Table 2-4 Test Program Objectives and Results

Test Objectives	Test Results
• Establish the range and range rate accuracy of a four channel receiver in an airborne environment.	• $\sigma_\rho \simeq 3.0$ ft, $\sigma_{\dot\rho} \simeq 0.25$ fps $\mu_\rho \simeq 2.0$ ft, $\mu_{\dot\rho} < 1.0$ fps
• Determine the effects of the aircraft flight environment on the receiver and airborne antenna performance.	• The NC-135 aircraft has a well controlled thermal and vibration environment. Measurements were not affected by this environment.
• Determine the effects of various aircraft-to-transmitter geometries on system performance including acquisition.	• The small scale geometry magnified steady state errors making analysis possible without requiring high quality position references. • The uplink antennas exhibited a delay error as a function of antenna look angle; the error caused 10 ft errors in computed Z position. • Multipath from SC-50 (Ch. 4) was significant when at low elevation angles; multipath was also observed overhead of Salt (Ch. 1) and SC-50. • Signal acquisition achieved when nominal signal level was a −123 dbm. HC normally acquired x 12 nm from the transmitters. MRL acquired x 9 nm from the transmitters.
• Evaluate the effects of different signal power levels on system performance.	• HC data showed sensitivity of range accuracy to signal level on some channels. Range errors could change from 3 to 12 ft as power went from −110 dbm to −140 dbm. MRL data showed no effects.
• Evaluate the system vertical positioning and sink rate accuracy during landing flare out.	• Vertical position accuracy is $\mu = -1.6$ ft, $\sigma = 8.9$ ft. Vertical sink rate accuracy is $\mu = -0.4$ fps, $\sigma = 2.1$ fps.
• Evaluate system capabilities to provide runway heading information during landing roll out.	• Cross runway position accuracy is $\mu = 1.0$ ft, $\sigma = 7.3$ ft.
• Evaluate the general system performance for landing navigation using a "typical" operational system configuration.	• System can be designed to operate in ILS signal environment as evidence by comparison of HC & MRL performance and respective receiver designs.
• Evaluate the sensitivity of receiver accuracy to multipath signals for ground users.	• Receiver behaves as predicted by theory. Receiver tracking errors can change as much as 50 ft for user antenna vertical movements of 1 wavelength.
• Establish the receiver accuracy while operating in typical multipath environments for ground users.	• Wide variety of multipath environments and associated receiver performance make it proper to consider each class of environment separately. However, with this understanding a broad statement can be made. Receiver will generally have errors of ± 25 feet if no attempt is made to locate user antenna in regions of small signal distortion.
• Verify the theoretical understanding of multipath effects in the receiver by qualitative comparison of test results with predicted performance.	• The measured receiver data falls within the theoretical error envelope for the test situations. Agreement of data with theory is very good.

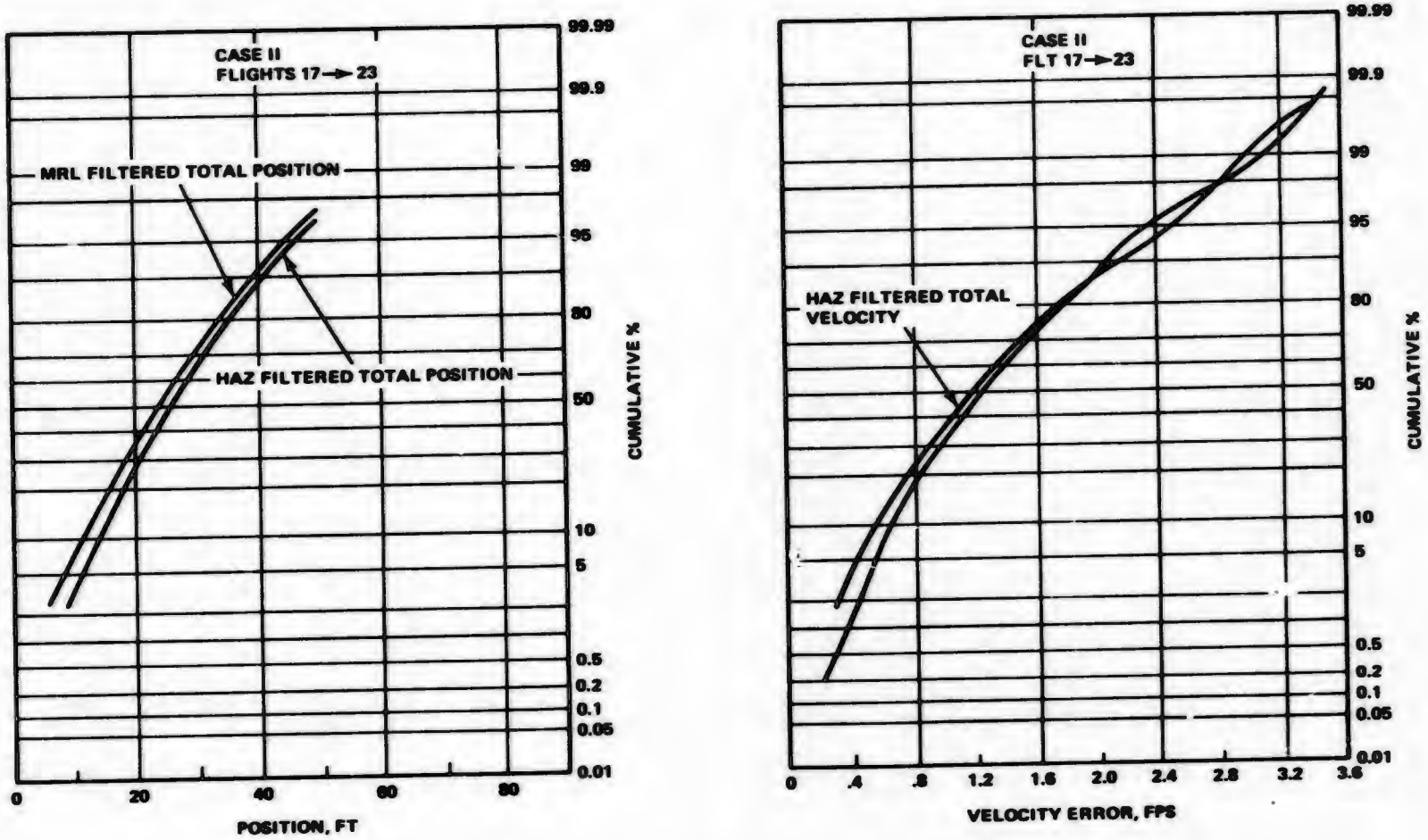

Figure 2-12 Cumulative Distribution of Total Position and Velocity Errors for Case II

SECTION III

TEST DATA GENERATION AND FILTERING

Before beginning a detailed discussion of the test results, some background is required to indicate how the test data is generated. In this section we will present a brief review of the general test approach and a discussion of the techniques used in the WSMR test to synchronize the transmitters via the ground system and associated software, to calculate the raw user navigation solution from range measurements and to subsequently smoothe the solution parameters.

3.1 EXPERIMENT PROGRAM IMPLEMENTATION

The principal elements of the Field Test Navigation System are the ground transmitters/calibration receiver segment and the airborne receiver (user) segment. Both the ground and airborne segments utilize four-channel correlation receivers to extract apparent time of arrival and doppler history of the incoming signals. Each ground transmitter generates a navigation signal consisting of a pseudo-random noise (PRN) code modulated on an L-band rf carrier.

In an operational satellite system the signals emanating from each transmitter would be approximately synchronized in both code phase (time) and frequency to a reference oscillator in a master ground station. Synchronization errors with respect to the reference oscillator would be measured and made available to the system user, so that the user would be, in effect, viewing "perfectly" synchronized transmitters.

In the field test program at WSMR, this same general concept was implemented, but, of course, mechanized quite differently than in a satellite system. Since there was no requirement to compute the navigation solution by the user in real time, and we wanted to keep the test equipment designs as simple as possible, a signal synchronization scheme using post flight data reduction software was implemented. The scheme basically consists of measuring the code phase and oscillator frequency of each transmitter with respect to a reference oscillator at a Mobile Calibration Station (MCS). Since the four transmitters are not even approximately synchronized to a reference oscillator (unlike the satellite case) the user requires not just a synchronization error term for each signal as in the operational case, but the entire value of the code phase and frequency offsets from the reference oscillator must be provided. The offset information is recorded at the MCS and made available to the post-flight data reduction process, in conjunction with the signal history of pseudo-range and pseudo-range rate recorded in flight.

The transmitter code phase and carrier frequency history recorded at the MCS has to be referenced to the center of the uplink antenna by the software synchronization process, since this is the location from which the airborne user receives the signal. To accomplish this, the total signal delay from uplink antenna to MCS receiver must be known. The recorded signal is in effect backed out of the MCS, backed over the monitor link and down the pole to the transmitter, backed through the transmitter, then out the transmitter uplink port up the pole to the uplink antenna.

A typical ground link configuration used in WSMR flight tests is shown in Figure 3-1. The transmitter provided two outputs, one for the uplink to the aircraft and the other for the monitor link to the MCS (calibration receiver). In order

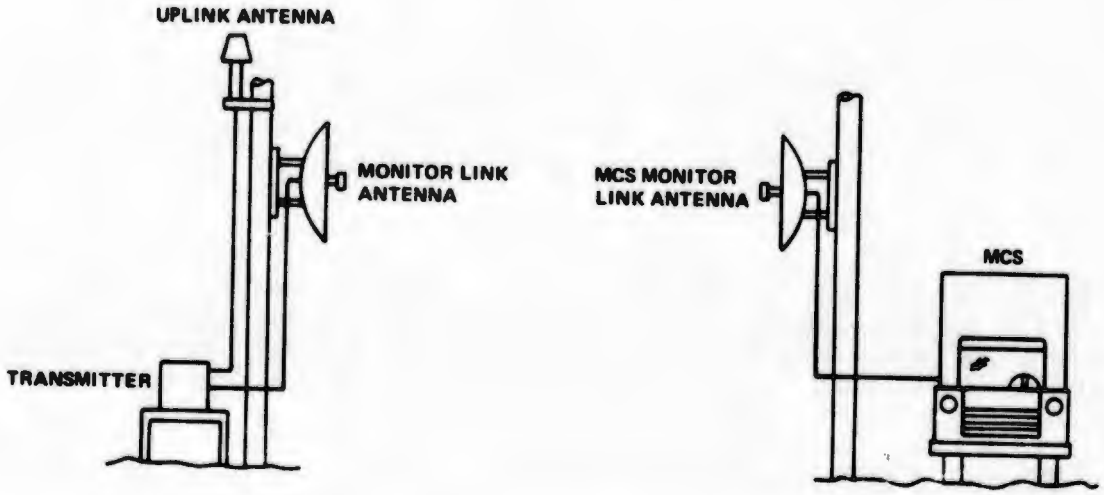

Figure 3-1 Typical Ground System Configuration for Flights 1-15

to avoid possible confusion at the MCS over which signal was being received, the transmitter sent out the monitor link signal 200 nanosec ahead of the uplink signal, and at a higher power level. Thus, the MCS was able to "see" the high power signal first and lock onto it with ambiguity.

A timing diagram showing the code phase at various points in the ground system is given in Figure 3-2. Referring to the ground configuration in Figure 3-1, the timing diagram indicates the code sequence seen at the two output ports of the transmitter, the code received at the MCS four-channel receiver, and the code observed at the phase center of the uplink antenna. The code phase and frequency offsets from the reference oscillator located in the ground receiver are recorded at the MCS. The data processing software is mechanized to determine the code phase (time) at the transmission point (center of the uplink antenna) from the received code phase at the MCS (the code phase can be thought of as a numerical value of time) and from stored constants which are functions of the fixed signal path delays.

The code phase received at the MCS in the timing diagram is labeled t_o. To determine the code phase at the uplink antenna (t_c), the code phase is backed out of the MCS and over the link to the transmitter monitor link port, a distance (time) D_l. This distance consists of the rf cables, monitor link antennas, and link propagation paths. The signal is then backed through the transmitter from the monitor link port to the uplink port, a time delay (code phase change) nominally equal to 200 nanosec.

From the transmitter uplink port the code phase is moved to the uplink antenna. This distance consists of rf cabling and antenna delays, and is approximately 50 nanosec. Each of these time delays must be carefully measured since an error in these quantities is equivalent to a system range error. The error sources associated with each of these distance are analyzed in Section 4.

The field test synchronization scheme is illustrated in Figure 3-3. The code phase and frequency offsets with respect to the reference oscillator (PR_{Mcs_l} PD_{Mcs_l}) are recorded at the MCS. The recorded data are referred to the center of the uplink

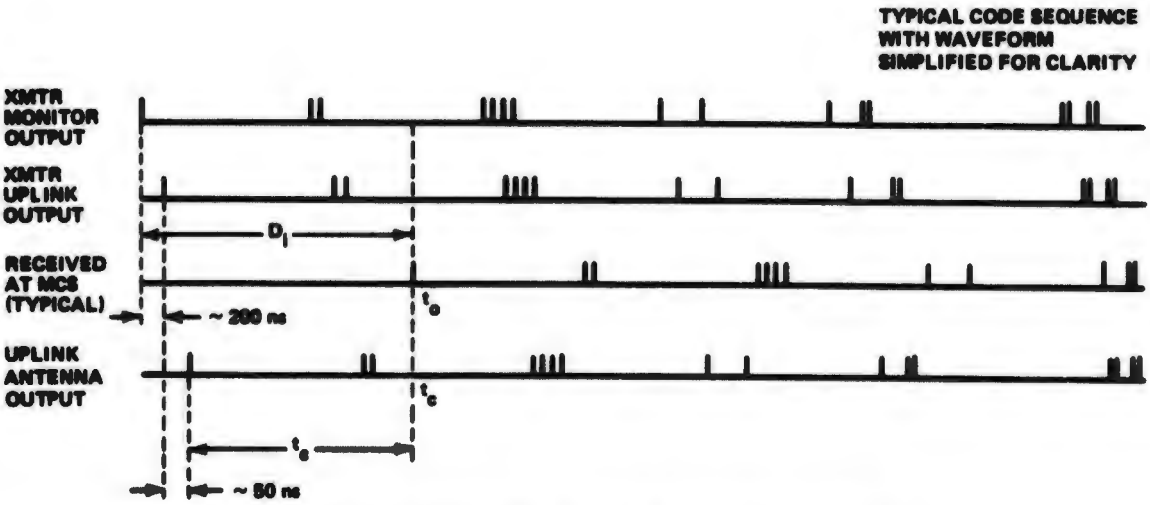

Figure 3-2 50-Mile Area Ground Site Timing

antenna by:

$$PRK_i = l_i + c(PR_{Mcs_i} + \Delta PR_i) \qquad i = 1, \ldots 4$$

$$PDK_i = \dot{l}_i - c(PD_{Mcs_i})$$

where PRK_i, PDK_i are the offsets referred to the uplink antenna (equivalent to t_c in the timing diagram); $PRMcs_i$, $PDMcs_i$ are the offset measurements performed at MCS (equivalent to t_o in the timing diagram); c is the speed of light converting the measurements of time and frequency to feet and feet per second; l_i, $\dot{l}_i$ are the distances and range rates (zero expect for balloon channel in ILS tests) between the MCS and the center of the uplink antenna; ΔPR_i is a correction term to account for different internal delays within the receiver channels.

The distance between the MCS and center of the uplink antennas is given by:

$$l_i = D_i - t_{internal} - C_{3_i}$$

where D_i is the distance from the MCS receiver to the transmitter monitor link port consisting of rf cables at the MCS and transmitter site (C_1 and C_2), and the antennas and propagation path, L_{1i}. That is $D_i = C_{1_i} + C_{2_i} + L_{1_i}$. $t_{internal}$ is the transmitter internal time delay between uplink and monitor link outputs which is approximately 200 nanosec, C_{3i} is the rf cable between the transmitter uplink port and the center of the uplink antenna which is approximately 50 nanosec.

The code phase offset is then adjusted to the time of sample of the user data by

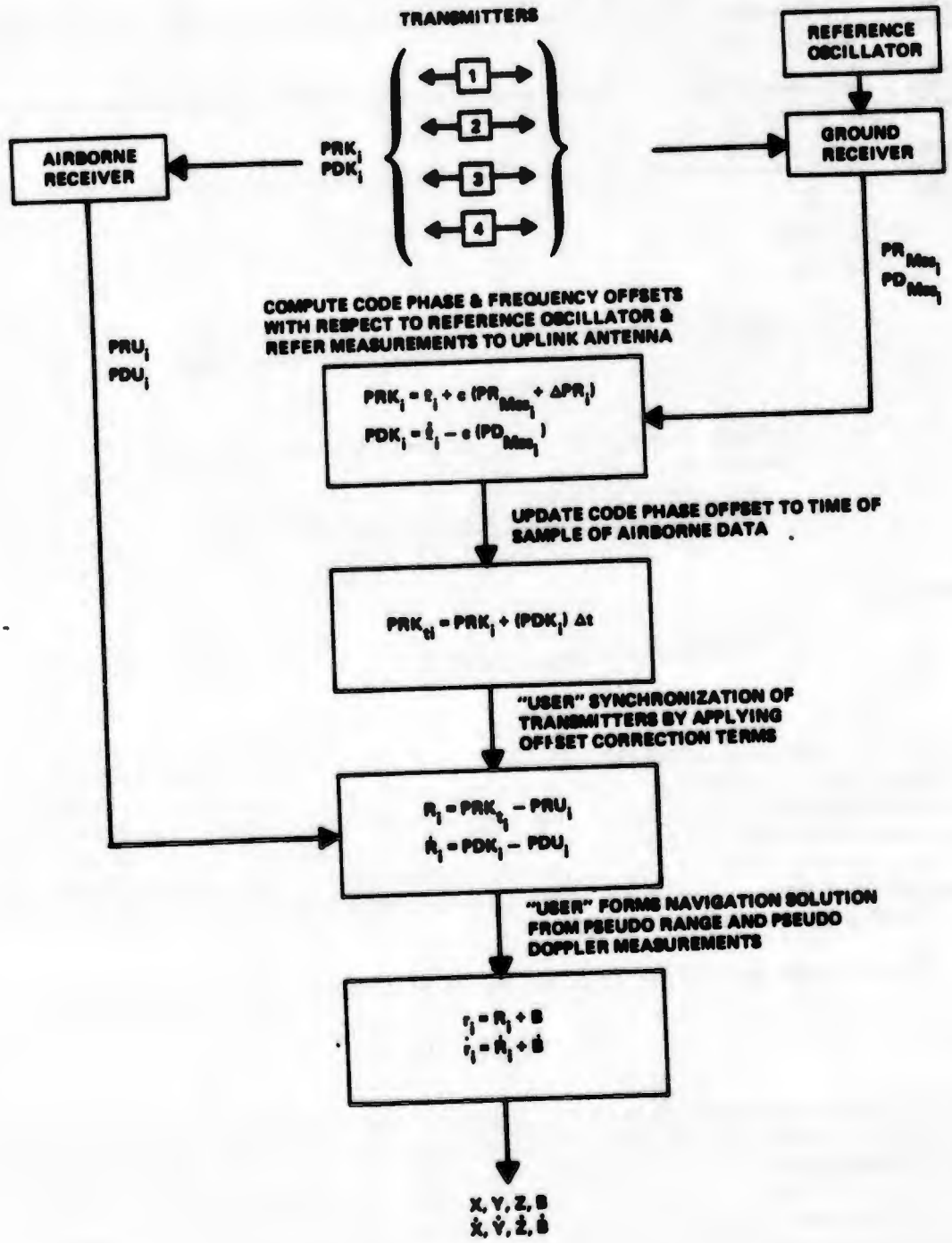

Figure 3-3 Simplified Information Flow of Transmitter Synchronization Process

advancing the code phase at the measured code phase drift rate, (frequency offset)

$$PRKt_i = PRK_i + (PDK_i)\Delta t$$

where $PRKt_i$ is the adjusted code phase offset at the user sample time and Δt is the time difference between the ground receiver measurement of code phase offset and the user code phase measurement.

The information is now in the correct form to enable the user to synchronize the four transmitters to the common reference oscillator at the MCS. The user code phase and carrier frequency measured during the test flight (PRU_i, PDU_i) is synchronized by the ground recorded data ($PRKt_i$, PDK_i) to form the system (total) pseudo-range and pseudo-doppler measurements.

$$R_i = PRKt_i - PRU_i$$

$$\dot{R}_i = PDK_i - PDU_i \quad .$$

The navigation solution is obtained from the system pseudo-range and pseudo-doppler by

$$r_i = R_i + B$$

$$\dot{r}_i = \dot{R}_i + \dot{B}$$

where r_i, $\dot{r}_i$ are the computed true range and range rates between the aircraft and the transmitter locations (phase center of the uplink antennas); B, $\dot{B}$ are the differences in code phase and frequency between the user's oscillator and the ground based reference oscillator.

The computational details involved in the solution of the true range and range rate equations are located in Appendix D. The form of the solution was outlined in Volume II, Section 1.2 for an earth-centered coordinate system. To differentiate the field test coordinate system solution from the earth centered coordinate system, the notation has been changed in accordance with the definitions in Figure 3-4. This notation was used throught the test program and is adhered to in this volume.

The field test transmitter synchronization scheme, although conceptually adequate, produced a number of practical problems that had to be dealt with. The ground system was initially configured as shown in Figure 3-1. Data were collected using this configuration for the first 16 flights of the test program. Flight test results indicated navigation solution inaccuracies of roughly the same magnitude for both Hazeltine Corp. (HC) and Magnavox Research Lab. (MRL) data. Investigations of various components of the system indicated that there were instabilities in the ground system equipments that make up the ℓ_i term. Thus the stored constants in the software for ℓ_i were in fact time varying quantities and errors were introduced in the calculation of the measured code phase and frequency affects when referencing the data to the uplink antennas.

The errors were primarily associated with two aspects of the ground system; the transmitter internal delay (t internal) and portions of the rf cabling (C_1, C_2, C_3).

When accounting for the effective delay through the transmitter, the built-in

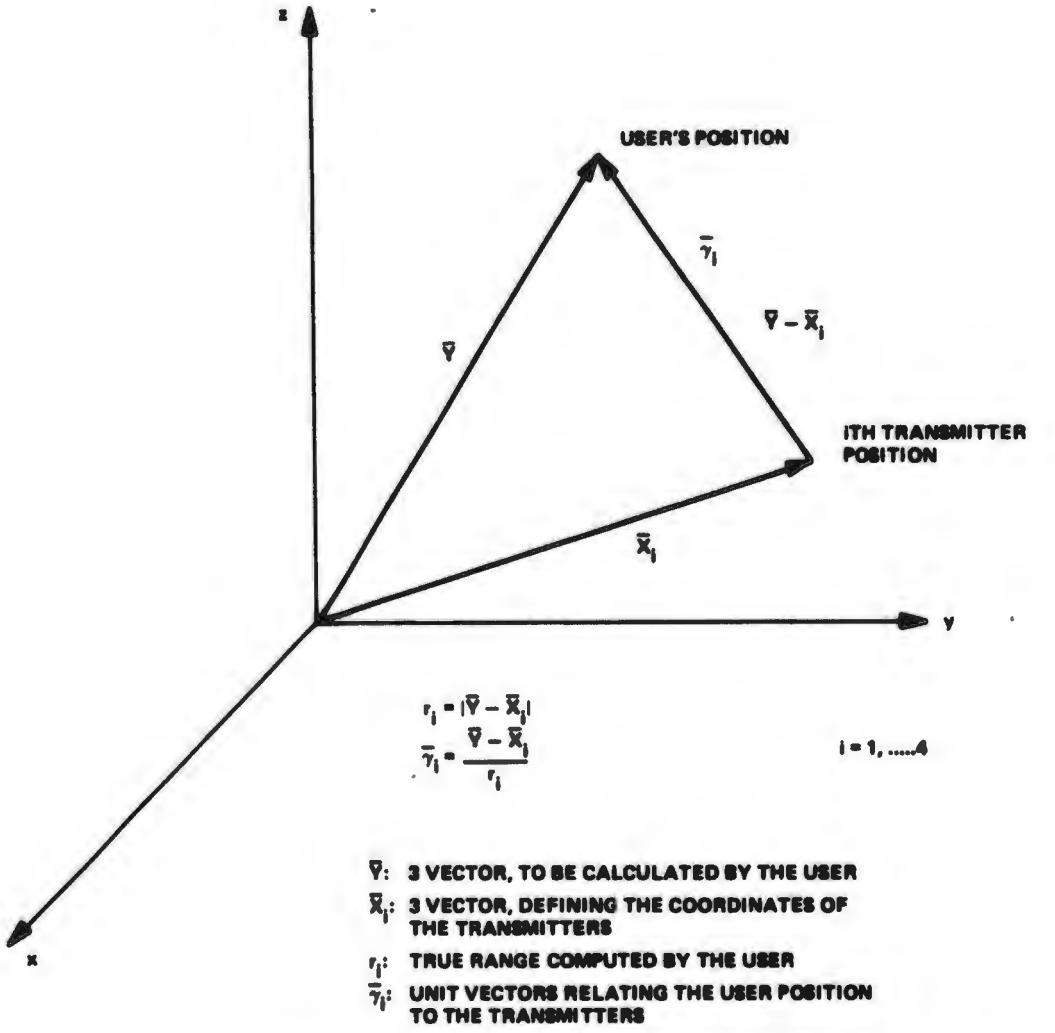

Figure 3-4 Field Test System Coordinates

200 nanosec delay must be accurately known. Therein lies a major problem. It does not suffice to make a measurement of the internal transmitter delay by standard techniques such as observing the relationship of appropriate code clock pulses on an oscilloscope. The significant measurement is the delay difference between the transmitter uplink and monitor link outputs. The receiver measurement is sensitive to factors such as signal spectrum shape, and stray rf leakage. We tried a number of different measurement techniques using the receiver as the basic measurement tool. The conclusion was that for whatever reasons, we could not determine the transmitter internal delay to sufficient accuracy. (See Section 4 for details of this problem).

A similar problem was occurring in some of the cables in the signal path. The cabling was basically of two types:

- RG-214/U - a flexible coaxial cable with the center conductor supported by a solid polyethylene sheath. The outer conductor is a braid around the polyethylene sheath - this cable is easy to work with and was used in locations where frequent equipment movements were expected, but is has a comparatively high loss of 0.13db/ft.

- Prodelin Spiroline - a semi-rigid coaxial cable consisting of an extruded aluminum casting (outer conductor) and a solid copper inner conductor supported by 6 coaxial polyethylene tubes. This line has low loss (0.04db/ft) and was used in permanent installations having long runs.

The Spiroline cabling delay measurements indicated an instability of 5-10 nanosec on some lines. Inspection of these lines revealed that moisture was entering the cable and causing changes to the dielectric properties resulting in variable signal propagation characteristics. This problem only occurred on the Spiroline cable because this cable is essentially hollow. (See Section 4 for details on this topic.)

Both the majority of the Spiroline cable and the transmitter internal delay were eliminated by reconfiguring the ground system as shown in Figure 3-5. One may question why the original configuration was used since the new configuration is much simpler and would seem to be the obvious choice. A major goal in the satellite simulation was to provide a constant signal level along the aircraft path within a few db. This required the uplink antennas to have a highly directional radiation pattern. The long distances from the transmitter sites to the MCS (~20,000 ft), the require-

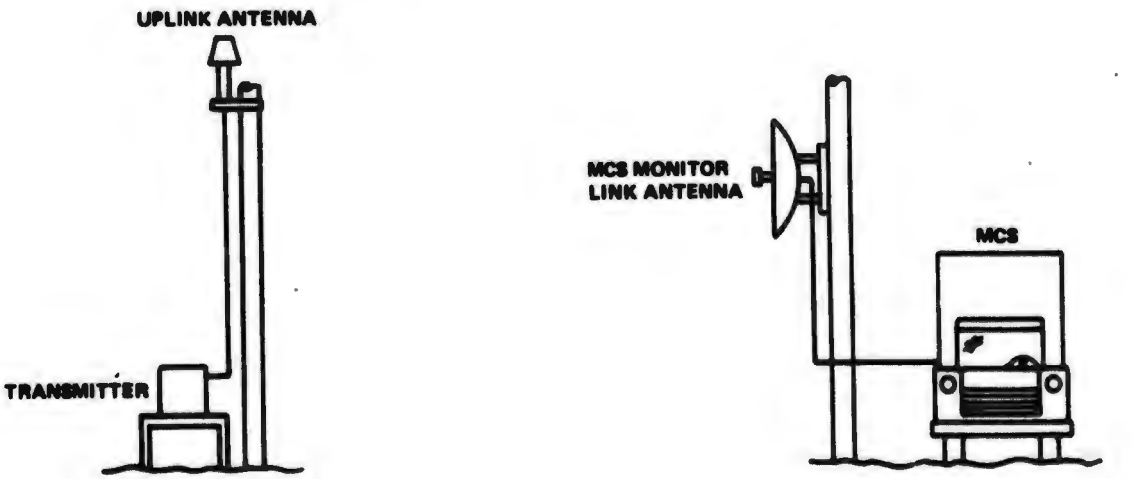

Figure 3-5 Typical Ground System Configuration for Flights 17-23

ment to have sufficient power at the MCS to acquire the signal and the directional pattern of the uplink antenna all pointed to the need for a separate, controllable signal path from transmitters to the MCS; thus the monitor links.

After identifying the monitor links as a major error source, and discovering that the MCS could lock-on to the signals from the uplink antennas, we decided to eliminate the monitor links and accept a slight loss in our ability to separately control the signal level along the aircraft flight path (this occurs primarily at WC-50, channel 2, because the long path from transmitter to MCS means the transmitter must be run at a higher than desired power to supply enough signal level at the MCS for acquisition). The power increase at the aircraft from the channel 2 transmitter is slight (a few db) and does not affect the overall results.

New measurements were made of the ground system resulting in a set of constants for the MCS-to-uplink antenna distance (ℓ_i) to be stored in the post flight data processing software. The data obtained on flights 17-23 reflect an improved accuracy over earlier flights as a result of this change (see Section 6).

3.2 THE TWO-STATE FILTER

The method of passive-user, four-coordinate radio navigation used in the experimental test program employs the pseudo-range formulation. The pseudo-ranging equations contain information about the clock bias* between the user reference oscillator and the overall system time reference. This term, usually expressed in feet, is called the pseudo-range bias and it relates the measured pseudo-range quantities to the user's true range from each of the 621B transmitters:

$$r_i = R_i - B \tag{1}$$

where r_i are the true ranges, R_i the (measured) pseudo-ranges and B is the pseudo-range bias.

The pseudo-range bias is, ideally, a function of user and ground timing only, and is therefore well behaved. In fact, with no oscillator drift, the pseudo-range bias is a constant.

When the pseudo-ranging concept is applied to the measured doppler signals, a similar bias term evolves. This bias, usually expressed in feet per second, relates the frequency of the user and ground oscillators and is called the pseudo-doppler bias. The true and pseudo-range rates are related by the pseudo-doppler bias:

$$\dot{r}_i = \dot{R}_i - \Delta \tag{2}$$

where $\dot{r}_i$ and $\dot{R}_i$ are the true and pseudo measurements respectively and Δ is the pseudo-doppler bias.

Further, it has been shown (Ref. 1) that to first order

$$\Delta = \dot{B} = \frac{dB}{dt} \tag{3}$$

---

*i.e. The "fourth coordinate"

Since both biases are well behaved and are strongly related to each other, they are especially adapted for filtering. By rendering the errors in these bias quantities insignificant, we may realize four true measurements from the four available pseudo measurements and thus reduce the random errors in the user trajectory.

Clock bias estimation also allows degraded three-measurement navigation under loss of lock conditions.

The two-state clock bias filter takes advantage of the predictable behavior of clock bias and clock bias rate to provide smoothing of these quantities. If the two-state filter could provide exact estimates of the states, the position solution algorithm would become a four true range least squares solution. However, the two-state filter can only provide best and not exact estimates of clock bias and bias rate. Therefore, the solution can only approach the four true range least squares solution. A measure of performance of the two-state filter can be defined in terms of the filter "Improvement Factor", a ratio of the filtered errors to the static errors. It follows from the definition of the Improvement Factor (and from the mechanization of the two-state filter) that the performance of the two-state filter is a strong function of the relative geometry of the user with respect to the transmitters.

3.2.1 Clock Bias Filter Concept

The bias filter concept, Ref. 1, uses a Kalman filter to eliminate the random error introduced to the calculated biases by pseudo-ranging noise. The filter states are bias and bias rate:

$$\bar{X} = \begin{bmatrix} B \\ \dot{B} \end{bmatrix}$$

and the state covariance is derived from the sensitivity analysis of the pseudo-ranging equations:

$$(\bar{Y}_c - \bar{X}_i) \cdot (\bar{Y}_c - \bar{X}_i) = (R_i - B_c)^2 \tag{4}$$

$$\frac{(\bar{X}_c - \bar{X}_i)}{R_i - B_c} \cdot (\bar{V}_c - \dot{\bar{X}}_i) = \dot{R}_i - \dot{B}_c \tag{5}$$

where $\bar{Y}_C$, B_C, $\bar{V}_C$ and $\dot{B}_C$ are the deterministic position and velocity navigation solution, and $\bar{X}_i$ and $\dot{\bar{X}}_i$ are the location and velocities of the four transmitters. The sensitivity analysis gives state covariance from predicted pseudo measurement errors. The state transition matrix uses the first order approximation of (3)

$$\phi = \begin{bmatrix} 1 & \Delta_t \\ 0 & 1 \end{bmatrix}$$

where Δt is the elapsed time between samples. The plant noise matrix models clock bias acceleration (oscillator drift rate) as a zero mean normal random variable with variance $\sigma^2_{\dot{B}}$. The filter is initialized by the deterministic navigation solution and subsequently accepts inputs of: (1) the predicted pseudo-range and pseudo-doppler measurement errors; (2) the predicted bias acceleration variance and (3) the measured static biases B_C and $\dot{B}_C$.

Once the filtered values of the biases are available, this added information is applied to the coordinate trajectory. This is accomplished by forming four true ranges and range rates:

$$r_{fi} = R_i - B_f$$

$$\dot{r}_{fi} = \dot{R}_i - \dot{B}_f \qquad (6)$$

where the f subscript indicates the filtered value. These four true measurements are used in a least squares solution for the coordinate position and velocity. The least squa·es solution is realized by the pseudo-inverse technique. The resulting decrease in random errors in the user trajectory is characterized by the "total filter gain factor", defined:

$$fgf = \sqrt{\frac{\sigma_x^2 + \sigma_y^2 + \sigma_z^2}{\sigma_{xf}^2 + \sigma_{yf}^2 + \sigma_{zf}^2}}$$

where the f subscript indicates the filtered error predictions. For the area navigation field tests typical gain factor values are

fgf $\approx$ 1 at the beginning of the run,
fgf $\approx$ 3 over the center transmitter
fgf $\approx$ 2.5 at the end of the run

This filter scheme tends to change the shape of the random error distribution from highly elongated in Z to approximately spherical.

Prior to presenting an analysis of the two-state filter performance, the concept of static (unfiltered navigation solution) Geometric Dilution of Precision (GDOP) is reviewed since the prime function of the filter is to produce a solution which can, in part, be characterized by an improvement factor leading to a dynamic GDOP.

3.2.2 Static GDOP's

The apparent time-of-arrival and apparent doppler measurements are corrupted by errors caused both by the propagation medium and by the receiver error sources which are a strong function of the signal design.

Starting with noisy measurements, the solution algorithms for position and velocity in three dimensions (based upon pseudo range and pseudo doppler) will result in noisy position and velocity solutions. The position and velocity solutions in three dimensions obtained directly by linear transformations of pseudo-range and pseudo-range rate measurements respectively are called the "static" position and velocity solutions (Ref. 2).

The sensitivity of the position solution to unity measurements errors as a function of the linear transformation (a function of the relative position of the user with respect to the satellites) is a measure of the reduction (or dilution) of the system precision. The covariance of the transformation to unity measurement error variances is called the Geometric Dilution of Precision (GDOP), which is a measure of the degree to which measurement errors are amplified by system geometry effects to produce position errors.

The purpose of filtering the static solution is to obtain the best linear estimate in some sense (i.e., least squares) of the noisy position and velocity solution by taking advantage of the relationships among independent measurements (observables), the physics of the measurement process, and the dynamics of motion. The Kalman filter provides a recursive procedure for providing a linear, statistically optimum estimate of the parameters involved.

The sensitivity equations for position follow from Eq. (7) the pseudo-range equation (see Figure 3-4) with $\delta \bar{X}_i = 0$ as:

$$\bar{\gamma}_i(\bar{Y} - \bar{X}_i) = R_i - B = r_i \tag{7}$$

where

$$\bar{\gamma}_i \cdot \delta\bar{Y} + \delta B = \delta R_i \qquad i = 1, 2, 3, 4 \tag{8}$$

$$M\begin{bmatrix}\delta\bar{Y} \\ \delta B\end{bmatrix} = \delta R_i \tag{9}$$

$$M = \begin{bmatrix} \gamma_{11} & \gamma_{12} & \gamma_{13} & 1 \\ \gamma_{21} & \gamma_{22} & \gamma_{23} & 1 \\ \gamma_{31} & \gamma_{32} & \gamma_{33} & 1 \\ \gamma_{41} & \gamma_{42} & \gamma_{43} & 1 \end{bmatrix}$$

Define $W = \text{col}[\delta\bar{Y},\ \delta B]$

$$W = M^{-1}\delta R_i \tag{10}$$

Taking expected values of both sides of Eq. (20);

$$E\{WW^T\} = M^{-1}E\{\delta\bar{R}_i\delta\bar{R}_i^T\}(M^{-1})^T \tag{11}$$

If $E\left\{\delta\bar{R}_i\ \delta\bar{R}_i^T\right\}$ = (Identity Matrix), the static GDOP's are given by:

$$\text{GDOP}\begin{bmatrix} X \\ Y \\ Z \\ B \end{bmatrix} = \{\text{DIAGONAL}[M^{-1}(M^{-1})^T]\}^{1/2} \tag{12}$$

An example of the static GDOP quantities applicable to the area navigation test geometry is shown in Figure 3-6. This figure shows the GDOP contours in the X-Y plane at 30,000 ft above ground level (AGL). The region displayed covers X = ± 35,930 ft and Y = ± 60,000 ft within which the four transmitter sites are identified by the circled numbers. The numerical values of GDOP are coded with letter symbols according to the legend given in the illustration. The GDOP quantities are continuous throughout this region; however, for clarity in presenting the contour

shape small gaps exemplified by the lack of a letter code are inserted. The GDOP in these gaps has a value between the two adjacent letter codes.

For example, 3 ft of range measurement noise translates into an X coordinate position noise, when the aircraft is 30,000 ft AGL and just south of transmitter 4 (Y is approximately -25,000 ft), of

$$\sigma_X = \text{GDOP}\sigma_R$$

$$\sigma_X = [\text{Between C and D}]\,(3)$$

$$\sigma_X = (1.5 \text{ to } 2)(3)$$

$$\sigma_X = 4.5 \text{ to } 6 \text{ feet}$$

3.2.3 621B Best Estimate Trajectory Errors

The errors in the trajectory are now derived for the two-state bias filter. The errors in pseudo range, position and velocity are computed by the appropriate linear transformation of the system geometry. The cross correlation between pseudo range and pseudo range bias, and between pseudo-range-rate and pseudo-range-rate-bias is assumed zero which leads to a worst case analysis. The coupling between position and velocity peculiar to the area navigation geometry is accounted for in the analysis.

3.2.3.1 Computational Flow:

The block diagram flow of the computational algorithm is shown in Figure 3-7.

The static position and velocity biases are filtered and subsequently used to generate a four true range least squares solution. The sensitivity of position and velocity to bias and ranging errors is computed by linear pertubational analysis of the least squares solution. A linear transformation of the sensitivity equations relates the filtered position and velocity errors to smooth pseudo range and pseudo range rate errors. The error variances of pseudo range and pseudo range rate are obtained by covariance analyses.

3.2.3.2 Position Errors:

The field test system geometry is given in Figure 3-4. The true range of the user, using the notation established in Figure 3-4 is:

$$(\bar{Y} - \bar{X}_i) \cdot (\bar{Y} - \bar{X}_i) = r_i^2 = (R_i - B)^2 \qquad (13)$$

Taking differentials of Eq. (13):

$$(\delta\bar{Y} - \delta\bar{X}_i) \cdot (\bar{Y} - \bar{X}_i) = (R_i - B)\,(\delta R_i - \delta B) \qquad (14)$$

ERROR CONTOUR CODE

A (0.0 to 0.3) B (0.5 to 0.8) C (1.0 to 1.5) D (2.0 to 2.5) E (3.0 to 4.0)
F (5.0 to 6.5) G (8.0 to 10.) H (12. to 15.) I (18. to 21.) J (25. to 30.)

STATIC GDOPS

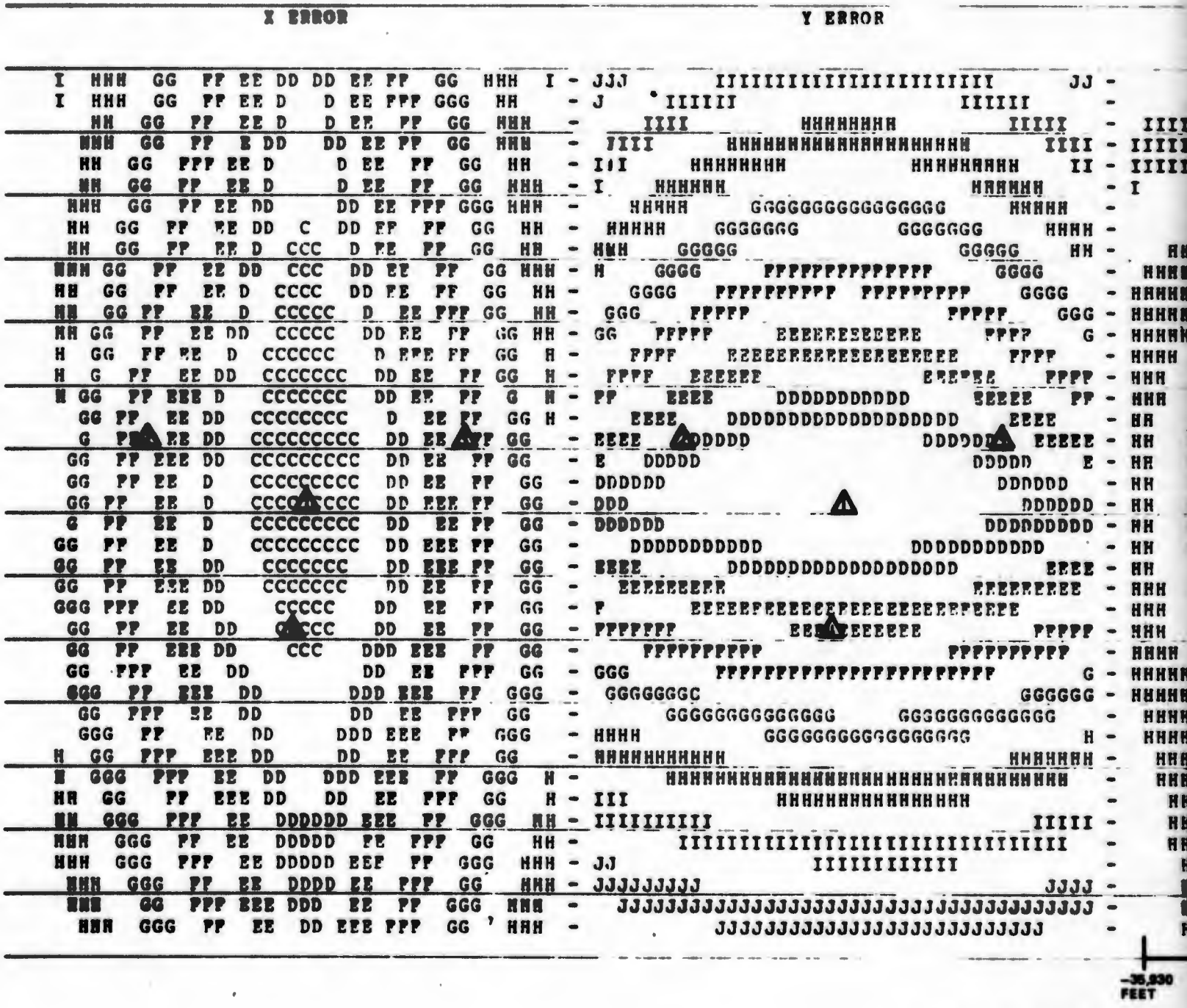

Figure 3-6 Static (Static Solu
Navigation Test G
Above Ground Lev

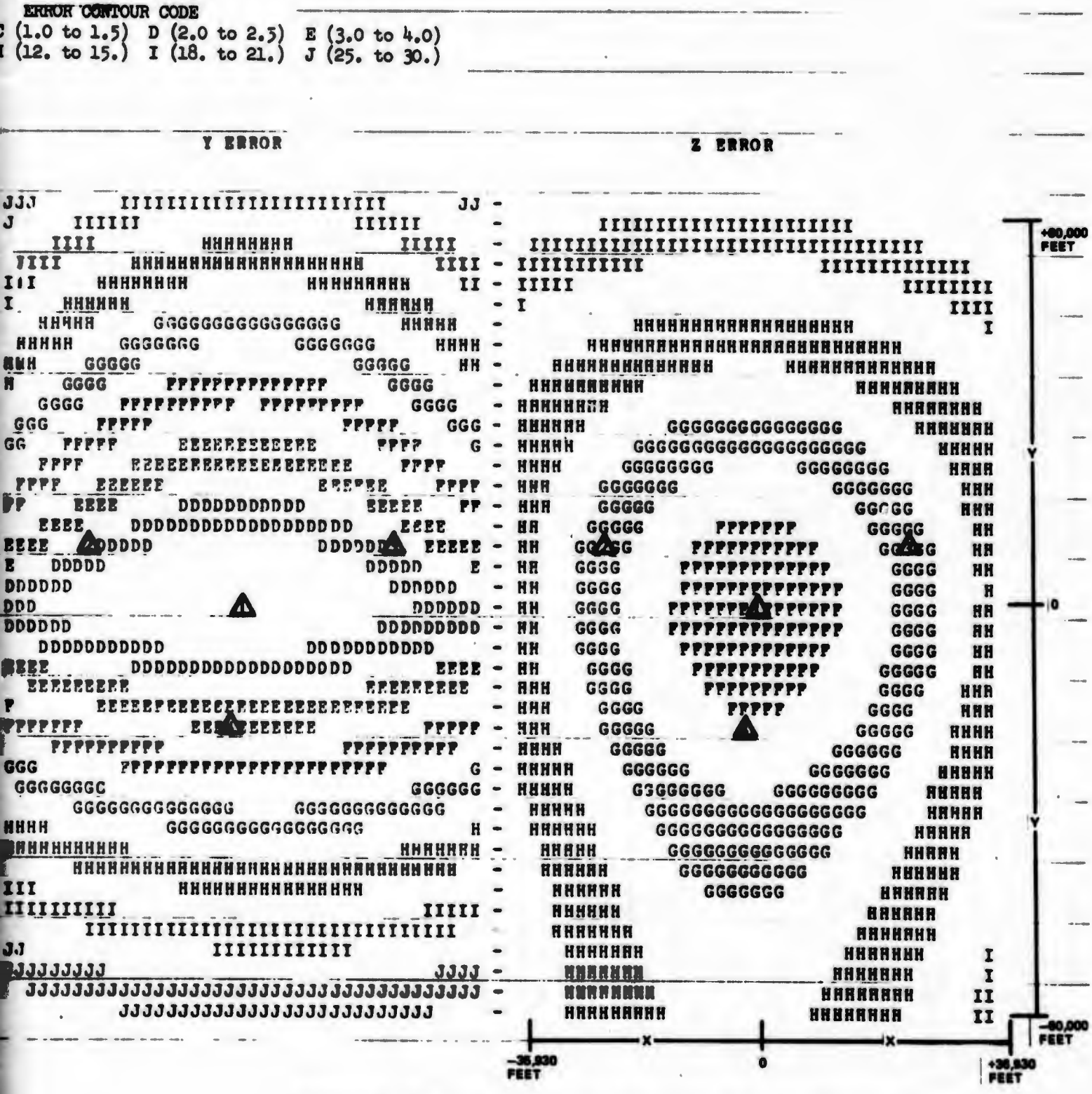

Figure 3-6 Static (Static Solution) Geometric Dilution of Precision Contours for Area Navigation Test Geometry. Contours Shown in X-Y Plane at 30,000 Feet Above Ground Level

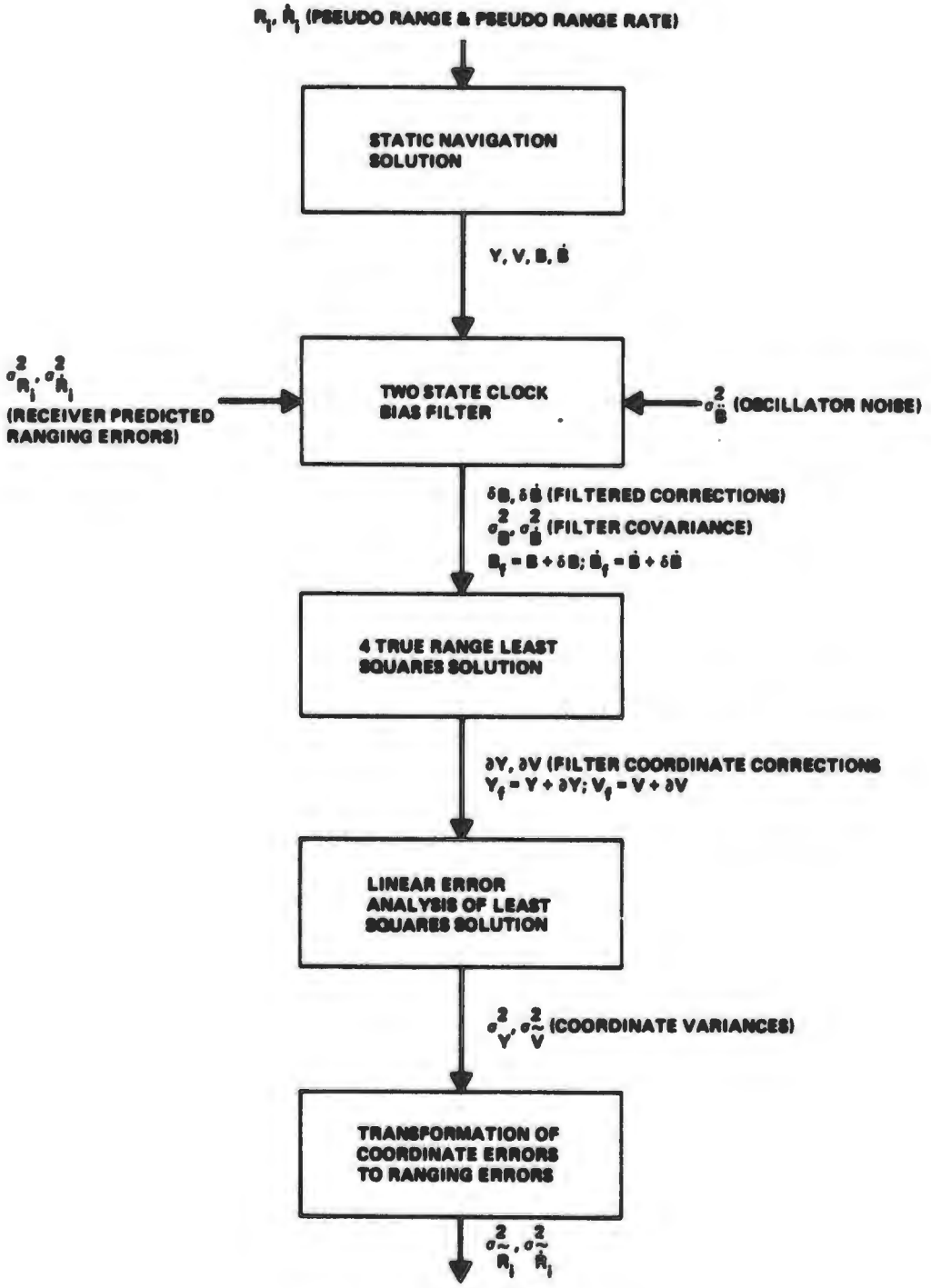

Figure 3-7 Computational Algorithm Functional Flow

Define:

$$\gamma_{ij}^{*} = \frac{Y_j - X_{ij}}{r_i} \quad , \quad \delta\overline{X}_i = \overline{0} \; .$$

Rewriting Eq. (14) in terms of $\overline{\gamma}^{*}$

$$\overline{\gamma}^{*} \cdot \delta\overline{Y} = \delta R_i - \delta B \tag{15}$$

where

$$\overline{\gamma}^{*} = \begin{bmatrix} \gamma_{11} & \gamma_{12} & \gamma_{13} \\ \gamma_{21} & \gamma_{22} & \gamma_{23} \\ \gamma_{31} & \gamma_{32} & \gamma_{33} \\ \gamma_{41} & \gamma_{42} & \gamma_{43} \end{bmatrix}$$

In Eq. (15) the matrix $\overline{\gamma}^{*}$ is not square and $(\overline{\gamma}^{*})^{-1}$ does not exist. In this case a least squares solution exists for $\delta\overline{Y}$ and is given by:

$$d\overline{Y} = (\overline{\gamma}^{*T}\overline{\gamma}^{*})^{-1}\overline{\gamma}^{*T}(\delta R_i - \delta B) \tag{16}$$

Where

$(\overline{\gamma}^{*T}\overline{\gamma}^{*})^{-1}\overline{\gamma}^{*T}$ is the pseudo inverse.

Squaring Eq. (16) and taking expected values of both sides of the resultant expression yields:

$$\sigma_{\tilde{Y}}^{2} = (\overline{\gamma}^{*T}\overline{\gamma}^{*})^{-1}\overline{\gamma}^{*T}[\sigma_{R_i}^{2} + \sigma_{\tilde{B}}^{2}]\,[(\overline{\gamma}^{*T}\overline{\gamma}^{*})^{-1}\overline{\gamma}^{*T}]^{T} \tag{17}$$

where, $E\{\delta R \delta R^{T}\} = 0$, and the superscript $\sim$ denotes filtered quantities.

If $\sigma_{\tilde{B}}^{2} \ll \sigma_{R_i}^{2}$ and $\sigma_{R_i}^{2} = I$ (i.e., $E\{\delta R_i \delta R_i^{T}\} = I$)

then Eq. (17) becomes

$$\sigma_{\tilde{Y}}^{2} = (\overline{\gamma}^{*T}\overline{\gamma}^{*})^{-1} \tag{18}$$

The diagonal elements of Eq. (18) represent the "Dynamic GDOP's,

$$GDOP_D = [\text{Diag}\,[\overline{\gamma}^{*T}\overline{\gamma}^{*}]^{-1}]^{1/2} \tag{19}$$

Note that the pseudo range and bias are uncorrelated since the ranging errors are predominantly caused by receiver thermal noise while the bias error is a function of oscillator statistics.

It can be shown that the following relationship between the filtered position errors and pseudo range errors can be derived from equation (15):

$$\sigma^2_{\bar{R}} = \bar{\gamma}^* \sigma^2_{\bar{Y}} \bar{\gamma}^{*T} + \sigma^2_{\bar{B}} \tag{20}$$

The transformation matrix $\bar{\gamma}^*$ is not recomputed for the filtered solution since the difference between the static and filtered solutions is small compared to the true range.

An example of the dynamic GDOP quantities resulting from Eq. (19) applicable to the area navigation test geometry is shown in Figure 3-8. The regions shown in this figure are identical to those shown in Figure 3-6 for the static GDOP's. The interpretation of the contours is also the same for the two figures. Comparing the dynamic GDOP's in Figure 3-8 with the static GDOP's in Figure 3-6, we see that the contours become almost spherical as a result of the two-state filter. The X and Y GDOP gradients become much smaller in the dynamic case, and the Z GDOP improves by a factor of five from the static to the dynamic case.

3.2.3.3 Velocity Errors:

Differentiating Eq. (13) one obtains:

$$\bar{\gamma}^* \cdot (\dot{\bar{Y}} - \dot{\bar{X}}_i) = \dot{R}_i - \dot{B} = \dot{r}_i \tag{21}$$

Taking differentials, it is readily shown (Ref. 2) that:

$$\underbrace{\begin{bmatrix} \Gamma_{11} & \Gamma_{12} & \Gamma_{13} \\ \Gamma_{21} & \Gamma_{22} & \Gamma_{23} \\ \Gamma_{31} & \Gamma_{32} & \Gamma_{33} \\ \Gamma_{41} & \Gamma_{42} & \Gamma_{43} \end{bmatrix}}_{\bar{\Gamma}^*_{ij}} \underbrace{\begin{bmatrix} \delta Y_1 \\ \delta Y_2 \\ \delta Y_3 \end{bmatrix}}_{\delta \bar{Y}} + \underbrace{\begin{bmatrix} \gamma_{11} & \gamma_{12} & \gamma_{13} \\ \gamma_{21} & \gamma_{22} & \gamma_{23} \\ \gamma_{31} & \gamma_{32} & \gamma_{33} \\ \gamma_{41} & \gamma_{42} & \gamma_{43} \end{bmatrix}}_{\bar{\gamma}^*} \underbrace{\begin{bmatrix} \delta V_1 \\ \delta V_2 \\ \delta V_3 \end{bmatrix}}_{\delta \bar{V}} + I\delta\dot{R} = \underbrace{\begin{bmatrix} \delta \dot{R}_1 \\ \delta \dot{R}_2 \\ \delta \dot{R}_3 \\ \delta \dot{R}_4 \end{bmatrix}}_{\delta \dot{\bar{R}}} \tag{22}$$

where

$$\Gamma^*_{ij} = [1/r_i]\,[(V_j - \dot{X}_{ij}) - \gamma_{ij}\dot{r}_i]$$

is the position – velocity coupling matrix.

Solving Eq. (22) for $\delta\bar{V}$, squaring both sides of the expression and taking expected values,

$$\sigma^2_{\bar{V}} = (\bar{\gamma}^{*T}\bar{\gamma}^*)^{-1}\bar{\gamma}^{*T}[\sigma^2_{\dot{R}} + \sigma^2_{\dot{B}} + \bar{\Gamma}^* \sigma^2_{\dot{Y}} \bar{\Gamma}^{*T}]\,[(\bar{\gamma}^{*T}\bar{\gamma}^T)^{-1}\bar{\gamma}^{*T}]^{-1} \tag{23}$$

where,

$$E[\delta\bar{Y}\delta B^T] = E[\delta\bar{Y}\delta\dot{\bar{R}}^T] = E[\delta\dot{\bar{R}}\delta B^T] = \bar{0}.$$

The filtered velocity errors are related to pseudo range rate errors by Eq. (22), yielding

$$\sigma^2_{\dot{R}_i} = \bar{\gamma}^* \sigma^2_{\bar{V}} \bar{\gamma}^{*T} + \bar{\Gamma}^* \sigma^2_{\dot{Y}} \bar{\Gamma}^{*T} + \sigma^2_{\dot{B}} \tag{24}$$

Filter Improvement Factor:

A Kalman filter "Improvement Factor" may be defined as the ratio of the input and output pseudo range and pseudo range rate variances given by:

$$G_i = \sigma^2_{R_i}/\sigma^2_{R_i} \quad \text{and} \quad G_i' = \sigma^2_{\dot{R}_i}/\sigma^2_{\dot{R}_i} \tag{25}$$

If $\sigma^2_B \ll \sigma^2_{R_i}$ for all i, then

$$G_i = \bar{\gamma}^*[(\bar{\gamma}^{*T}\bar{\gamma}^*)^{-1}\bar{\gamma}^{*T}]\,[(\bar{\gamma}^{*T}\bar{\gamma}^*)^{-1}\bar{\gamma}^{*T}]^T\bar{\gamma}^{*T} + \sigma^2_B/\sigma^2_{R_i} \tag{26}$$

Employing matrix identities, i.e., $(AB)^T = B^TA^T$, Eq. (12) may be expressed in a more convenient form:

$$G_i = \bar{\gamma}^{*T}[(\bar{\gamma}^{*T}\bar{\gamma}^*)^{-1}\bar{\gamma}^{*T}] + \sigma^2_B/\sigma^2_{R_i} \tag{27}$$

where $[(\bar{\gamma}^{*t}\bar{\gamma}^*)^{-1}\bar{\gamma}^{*t}]$ is the pseudo inverse satisfying the least squares solution. Consider,

$$\bar{\gamma}^*[(\bar{\gamma}^{*T}\bar{\gamma}^*)^{-1}\bar{\gamma}^{*T}]\bar{\gamma}^* = \bar{\gamma}^* \tag{28}$$

which follows from the definition of the pseudo inverse.
Let

$$M = (\bar{\gamma}^{*T}\bar{\gamma}^*)^{-1}\bar{\gamma}^{*T} \quad \text{and} \quad L = \bar{\gamma}^* .$$

$$LM = L(L^TL)^{-1}L^T,$$

which may be partitioned into:

$$LM = \begin{bmatrix} A \\ C \end{bmatrix}\left[[A^T \mid C]\begin{bmatrix} A \\ C \end{bmatrix}\right]^T[A^T \mid C^T] = \begin{bmatrix} A \\ C \end{bmatrix}\left[A^TA + C^TC\right]^{-1}[A^T \mid C^T] \tag{29}$$

A matrix L (μ xn) of rank ρ, may be written as

$$L = \begin{bmatrix} A_{\rho x \rho} & B_{\rho x V_C} \\ C_{V_R x \rho} & D_{V_R x V_C} \end{bmatrix} \tag{30}$$

where V_R and V_C are the row-column-nullities. It follows from Eqs. (29) and (30) that the Filter "Improvement Factor", G_i, may not always be less than unity, and it is a function of the geometry under consideration. This may be expected since the two-state filter models B and $\dot{B}$ and does not include equations of motion (i.e. system dynamic states).

3.2.3.4 Clock Bias Filter Models

The two state clock bias filter requires three externally derived parameters:

- The predicted variance of clock bias acceleration is estimated from system oscillator statistics and refined through examination of flight data. It is used in Q matrix computation, and is equal to

$$\sigma^2_{\ddot{B}} = 0.0005 \ (\text{ft/sec}^2)^2$$

- The predicted variances of pseudo-range and pseudo-doppler errors are used

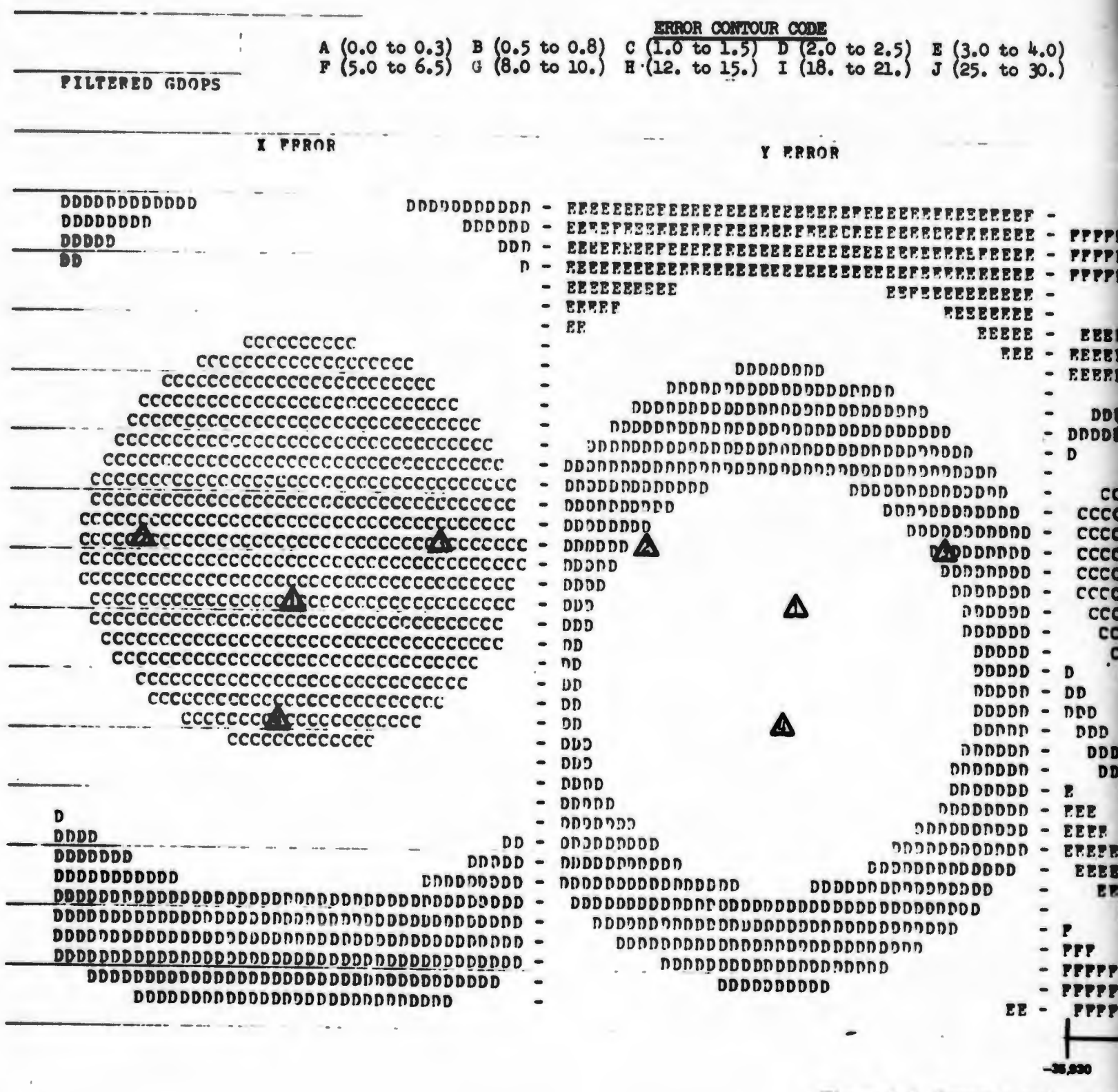

Figure 3-8 Dynamic (Filtered S
Area Navigation Tes
Feet Above Ground

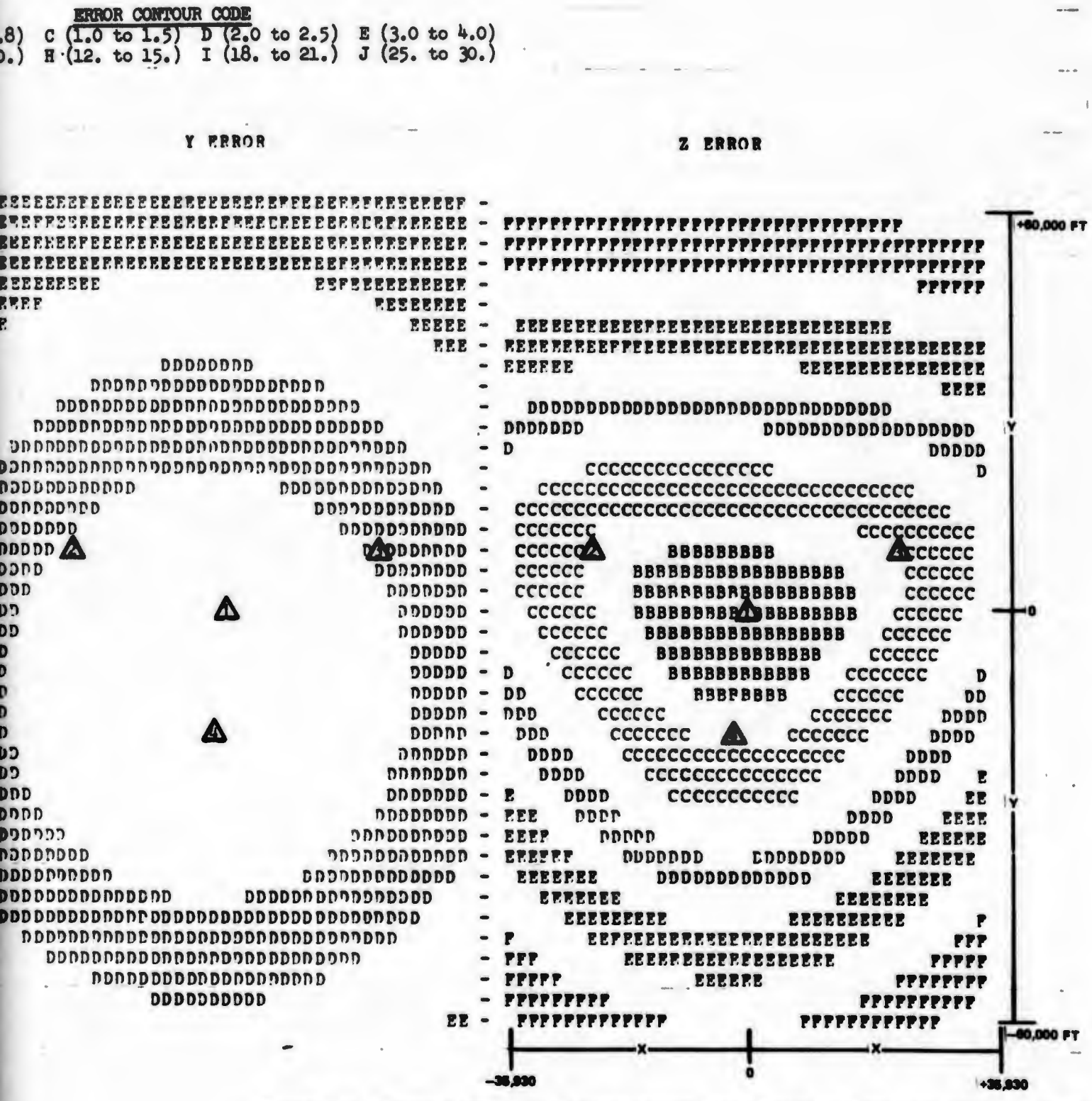

Figure 3-8 Dynamic (Filtered Solution) Geometric Dilution of Precision Contours for the Area Navigation Test Geometry. Contours Shown in X-Y Plane at 30,000 Feet Above Ground Level

to obtain the predicted state covariances. These errors are predominantly multipath and thermal noise, and are modelled as shown by the random error discussion in Section 4.

3.3 11-STATE FILTER

An 11-state Kalman filter was also implemented to smooth the trajectory data. The state vector for this filter consists of position, velocity, acceleration and clock states x, y, z, $\dot{x}$, $\dot{y}$, $\dot{z}$, $\ddot{x}$, $\ddot{y}$, $\ddot{z}$, B, $\dot{B}$. The filter is mechanized along classical Kalman filter guidlines (Ref. 36). A block diagram of the computational flow is given in Figure 3-9, and a flow chart of the program is given in Appendix F.

The initial value of the filter states is obtained from the static solution. Since we also have a measure of the error in the static solution at this point (obtained from the *a priori* knowledge of the measurement variance and the geometric transformation of this error into the static solution) the initial value of the state covariance is chosen as the computer error in the static solution rather than using a fixed constant. This has the advantage of rapid settling of the filter after initialization in those cases where the filter is started in regions having geometry providing good initial values of the states.

Similarly, the noisiness of the pseudo-range and pseudo-range rate measurements used in the filter to update the state estimates is determined dynamically by taking into account the received signal level and the receiver tracking loop bandwidth. Thus, as the received signal level decreases and the measurements become more uncertain, the measurement covariance is adjusted to account for these changes. (See Vol. II, Section 4.) This technique is also used in the two-state filter.

The effect of filtering the data is shown in Figure 3-10. This figure contains a data run from Flight 19 which has been processed by the 2 and 11-state filters and also contains an unfiltered version for comparison. The plots show the residual between the various filtered versions of test system trajectory and the WSMR reference. The upper row of plots show the X-coordinate residual. There is practically no difference between the unfiltered data and that processed through a two-state filter for both the X and the Y-coordinate data for the region of the flight path considered here. The 11-state filter, however, reduces the X and Y data noise by approximately an order of magnitude. The Y-coordinate data is not shown here since it is very similar to the X data.

The Z-coordinate data, on the other hand, has a large reduction, about an order of magnitude, in noise content resulting from the two-state filter as shown by the bottom row of plots in Figure 3-10. The 11-state filter improves the two-state Z data by approximately a factor of 3.

The improvement of the 11-state filter data over the two-state bias filter is a result of modeling the additional velocity and acceleration states, and is also influenced by our selection of Q values, a measure of uncertainty in the estimates of the state dynamics. The state dynamics are known to be relatively small during the field tests. The area navigation flights were essentially straight and level runs which follow closely the mathematical model of rectilinear motion with constant velocity.

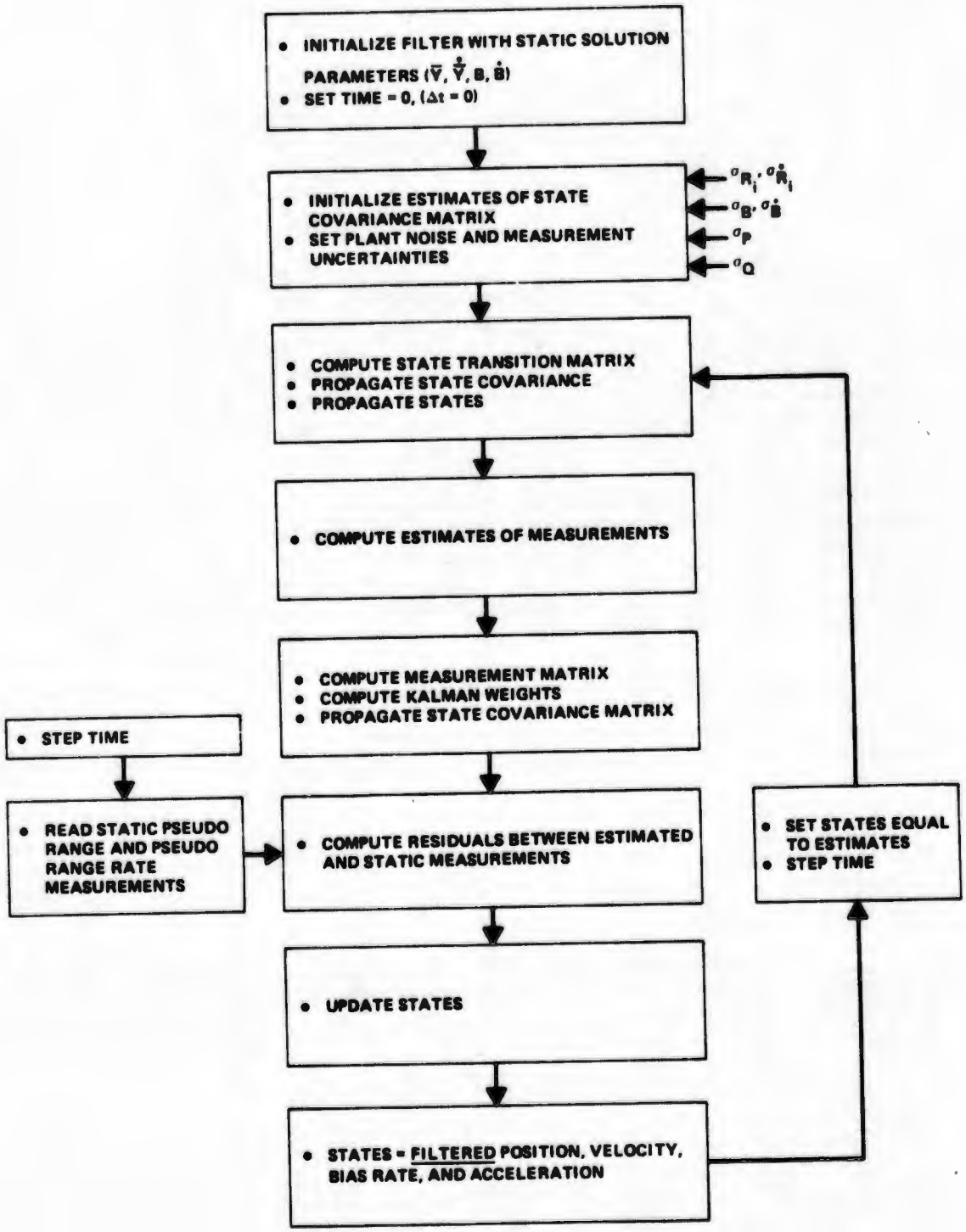

Figure 3-9 Computational Algorithm Flow for 11-State Filter

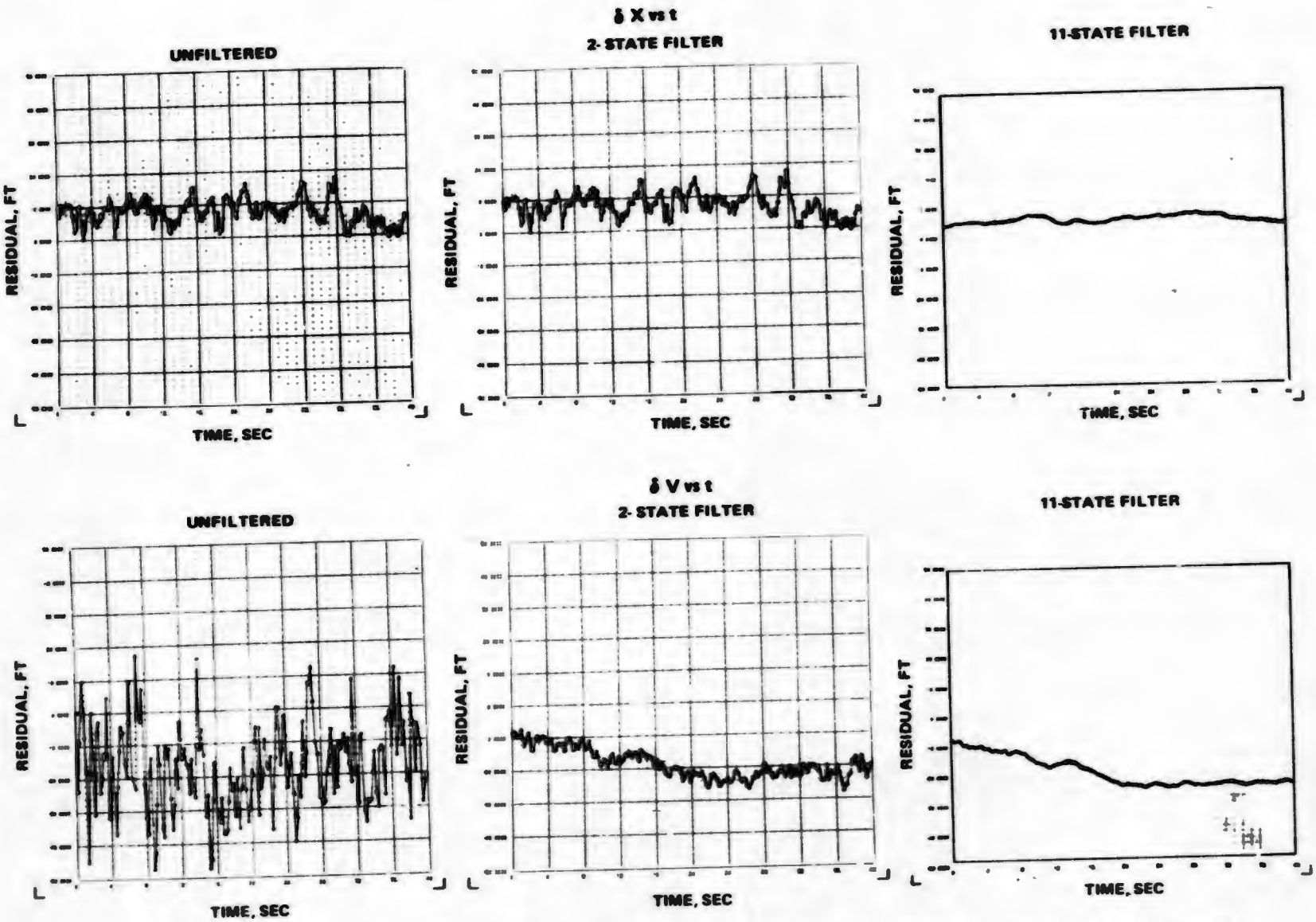

Figure 3-10 Comparison of Unfiltered, Two-State Filtered, and 11-State Filtered Data - Flight 19 Run 6.

The trajectory dynamics during the ILS flights were similar to those experienced during area navigation. The following values of Q were utilized as a result of these considerations:

Diagonal Elements of Q Matrix:

$$\sigma_x^2 = 0, \quad \sigma_y^2 = 0, \quad \sigma_z^2 = 0, \quad \sigma_B^2 = 0$$

$$\sigma_{\dot{x}}^2 = 0, \quad \sigma_{\dot{y}}^2 = 0, \quad \sigma_{\dot{z}}^2 = 0, \quad \sigma_{\dot{B}}^2 = (0.02)^2$$

$$\sigma_{\ddot{x}}^2 = (0.05)^2, \quad \sigma_{\ddot{y}}^2 = (0.05)^2, \quad \sigma_{\ddot{z}}^2 = (0.05)^2.$$

In choosing such small values of Q, the filter is allowed to weight its internal estimates of the dynamic states more heavily than the actual measurements of pseudo-range and pseudo-range rate. Weighting of the measurements is therefore largely controlled by the geometry of the problem. Good geometry regions (small values of GDOP) cause the filter to weight the measurements more than in poor geometry regions. However, in all cases, once a good set of state estimates has been obtained, i.e., the filter has settled and the state covariance values are small, the filter depends much more heavily on its own estimate of state dynamics than upon the measurements. The result of this is the relatively smooth trajectory data shown in Figure 3-10 for the 11-state filter. The conclusion is that the majority of the data noise comes from the system and not from the aircraft motion.

A quantitative measure of the effectiveness of these two filters is provided in Figure 3-11. This figure presents the trajectory noise (standard deviation) in each coordinate for an area navigation flight paths as a function of the degree of filtering. The lines connecting the sigmas for each filter type are shown for clarity in determining the improvement trends and should not be used to imply the performance of potential in-between (e.g., six-state filters). As can be seen in this figure, the Z-coordinate data responds very well to both the 2 and 11-state filters whereas the X and Y-coordinate data require an 11-state filter for any substantial noise reduction. This is, of course, a function of the system geometry. However, the geometry utilized in the field test is representative of that proposed for an operational system, therefore, making the filter performance comparisons in Figure 3-11 reasonable for the user equipment aspects of the 621B system.

The improvement in the 11-state filtered ILS trajectories over other versions is substantial since the ILS system configuration has good geometries only for a small region centered around the flare point on the flight path. In this case the 11-state filter is necessary to effectively remove the trajectory data noise.

3.3.1 Modes of Filter Operation

Under normal conditions the filter program operates in either the two-state or 11-state filter modes. Two degraded modes are available: (1) the secondary three-measurement mode, and (2) the tertiary extrapolate (or dead reckon) mode.

The three-measurement mode is employed when one channel produces bad measurements and at least one previous acceptable navigation point is available for bias extrapolation. In the 11-state filter implementation this is not necessary, since loss of lock or bad data in any one of the channels can be handled by increasing the measurement noise covariance matrix entries for that channel. The filter in this case will de-weight the measurements and operate on its estimates of the dynamic states.

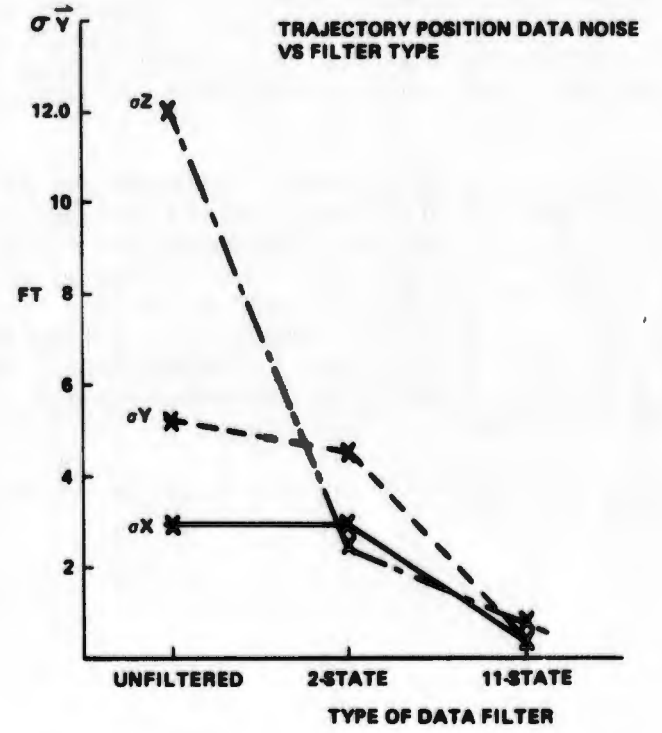

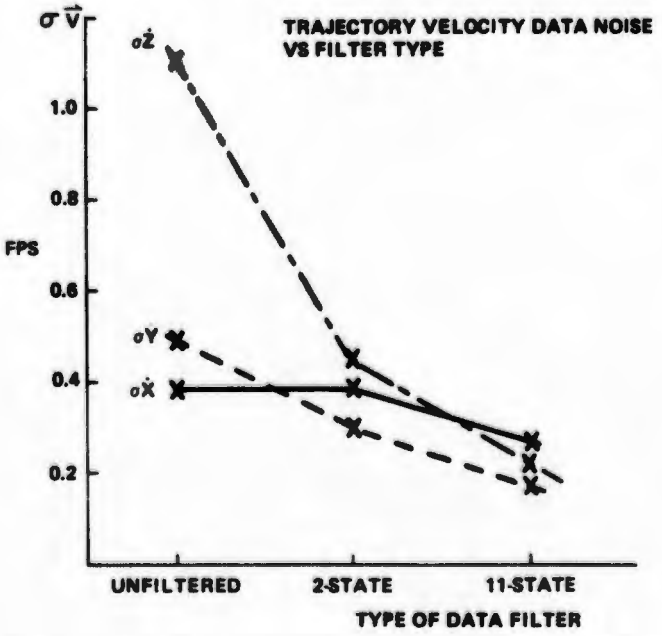

Figure 3-11 Improvement in Trajectory Data Smoothing Resulting From Two and 11-State Filters

When there is no deterministic navigation solution available and/or the primary and secondary modes have failed, the full extrapolation mode is used in an attempt to fill the gap in the data. This highly degraded mode is not used for more than ten consecutive seconds and requires at least five seconds of previous data to operate. The extrapolation is performed on the trajectory coordinates independently by least-squared residual polynomial fits. A linear curve is fitted to the velocity data and is subsequently integrated for position extrapolation. The constant of integration is determined by fitting the integrated velocity curve to the position data by least-squared residuals.

The filter program selects its operating mode in accordance with the logic shown in Figure 3-12. The channel-locked discretes from the user and ground calibration station are checked first. If all four channels show good locks, the deterministic navigation solution is then checked for feasibility. In the present program configuration this feasibility check is based on deterministic geometry, error predictions and a comparison of the raw pseudo-range and pseudo-doppler data. If a bad static navigation solution is indicated, it may be due to a single bad measurement. This one-bad-channel possibility is checked by comparing the first difference of the four pseudo-dopplers to the second difference of the four pseudo-ranges.

When all three program modes fail to produce a meaningful trajectory, the lost data results in time jumps in the output.

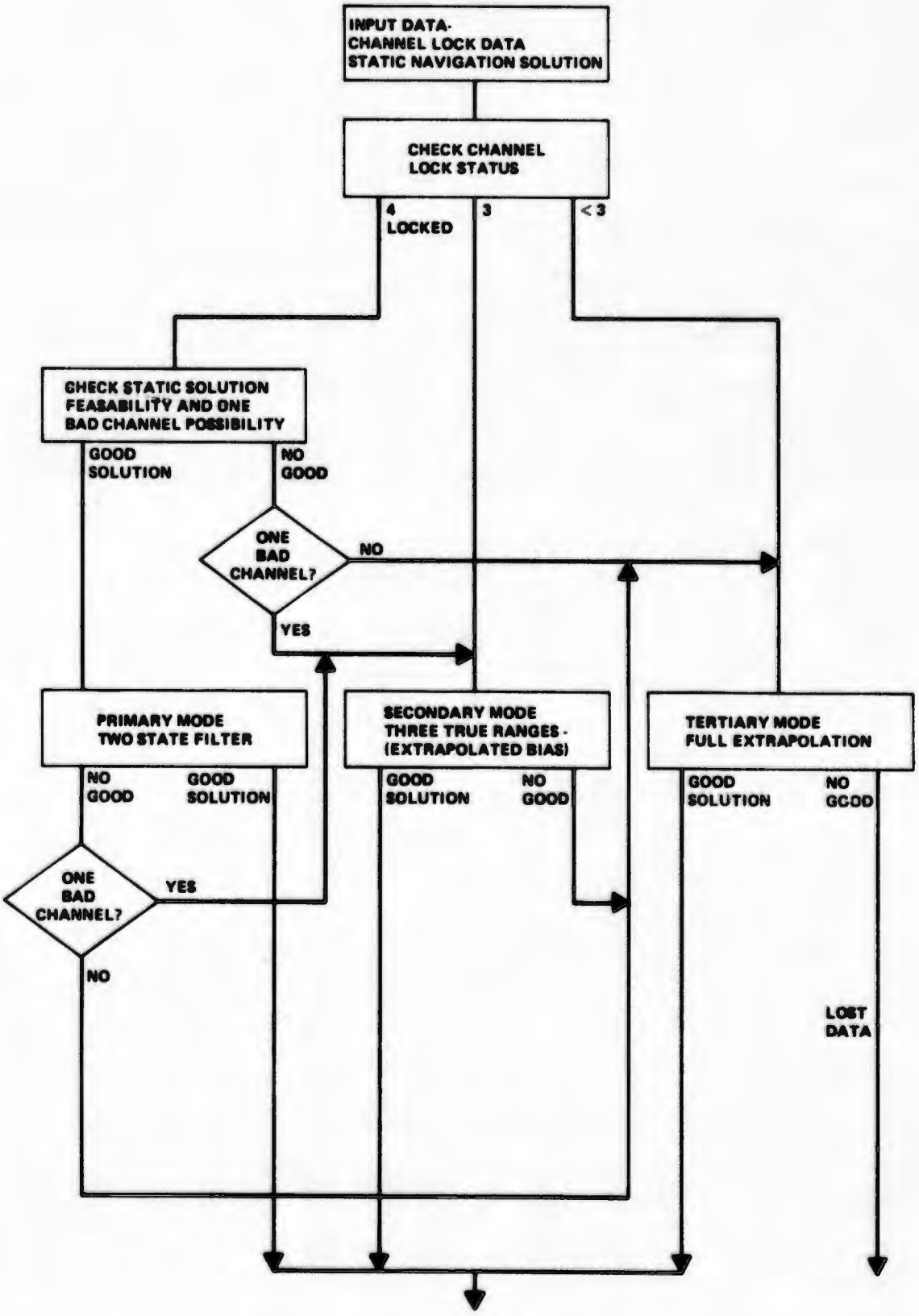

Figure 3-12 Filter Mode Selection

SECTION IV

ERROR ANALYSIS

In order to present a meaningful discussion of the results of the field test program, we must first define the errors whose evaluation will provide the measure of system performance. In the terminology of this report, the set of user's vector position and velocity data, which is the desired system output, is referred to as the "solution domain". Any deviation of the output from an "ideal reference" vector position and velocity represent the navigation errors. However, an ideal (i.e., perfect) reference is a physical impossibility. Therefore, we can only produce an estimate of the navigational error. The precision of the error estimate is a function of the precision of the reference trajectory.

The disturbances creating the navigational errors are assumed to be present at the input of the system. These disturbances are created by the imperfect measurement process or measurement errors. The set of measurements is referred to as the "measurement domain". The two domains can be related to each other by a linear geometric transformation, which is an implicit function of time due to user's motion with respect to the transmitters. This transformation also applies to the errors in the data sets of the two domains and allows identification and modelling of errors in whichever domain it is most appropriate or useful to do so.

In addition to errors caused by receiver noise and bias, there exist additional errors in the measurement domain caused by:

- Unidentified physical phenomena
- Unmodelled physical phenomena
- Imperfect modelling of complex physical processes
- Inherent distortion introduced by the measuring process and device characteristics.

Besides measurement errors, additional errors in the solution domain are caused by:

- Inaccuracy of the linear transformation from measurement to solution domains caused by neglecting higher order terms
- Imperfect modelling of dynamic states in the Kalman filter
- Imperfect modelling of the measurement noise covariance matrix in the Kalman filter.

The degree to which the errors in the measurement domain affect the errors in the solution domain is a function of the geometry of the system (see Section 4.2) and the type of estimation/prediction technique used to smooth the static solution. The analysis of the errors, once identified, is performed in the filtered and static solution domains as well as in the measurement domain. A block diagram highlighting the error analysis flow by identifying the major steps in the analysis is given in Figure 4-1.

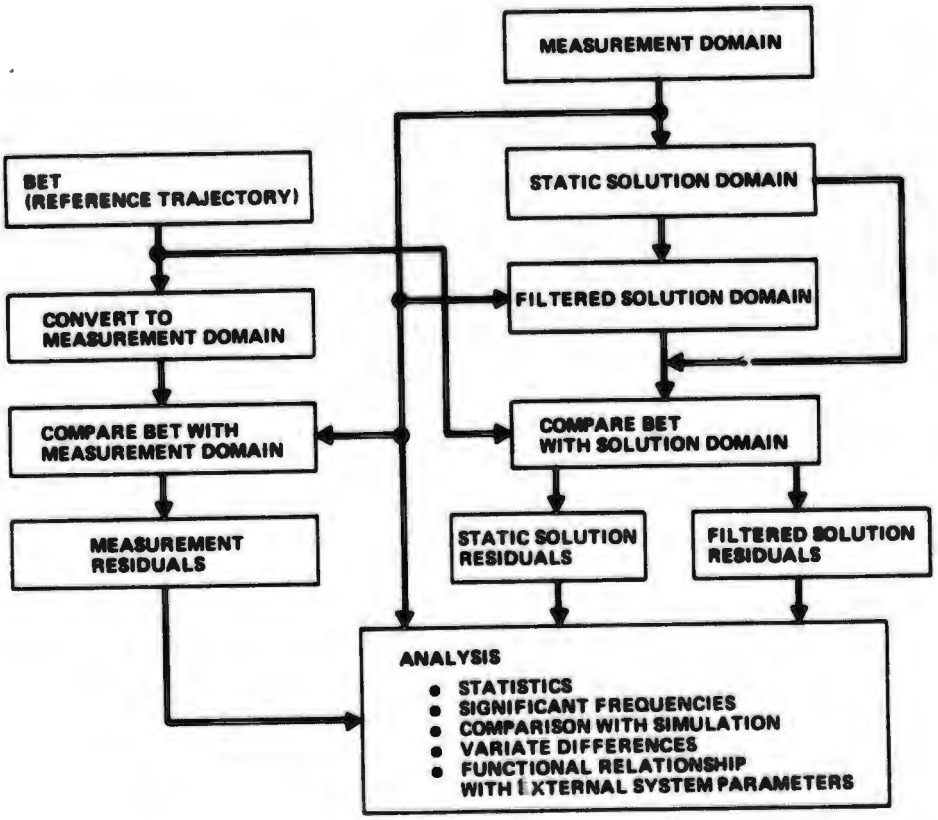

Figure 4-1 Error Analysis Approach

Figure 4-2 represents a system functional flow diagram indicating the source and type of errors associated with the test system. The error sources shown in Figure 4-2 have been classified into three broad categories: random, steady state (bias), and periodic errors.

Some of the error sources are well known, as for example, receiver thermal noise and atmospheric refraction correction residuals. There are other error sources which became evident during the data analysis, such as sensitivity of the receivers to the transmitter spectrum shape and apparent signal delay in some of the antennas. The error producing mechanisms and the contribution of each error source on the navigation solution accuracy are presented herein. A discussion of some aspects of the test system clocks is also included.

4.1 RANDOM ERROR

The analysis of the random components of the test system data is performed in three steps:

1. A quantitative evaluation of system measurement variances.

2. The detection of dependencies between measurement variances and external parameters, and the correlation of these with the a priori error models.

3. The transformation of the observed variances into user navigation coordinates (solution domain) of the demonstration system.

4.1.1 Measurement Variance Estimation

Standard estimation techniques were used to quantify measurement variances. The sample variances, σ^2, (that is, the second central moment) of the differences (residuals) between the navigation data and the WSMR BET were taken in both the measurement domain and the navigation solution domain. These statistics were taken over ten second time intervals for both the static and the (two state) filtered trajectories. Each ten-second time interval contained 50 data points from what has been determined to be a statistically stationary set.

Two separate analyses were performed to determine the solution domain and measurement domain residual variances.

In performing the transformation from measurement coordinates to navigation coordinates, the clock bias in the pseudo-range measurements was eliminated by referencing all delay measurements to a single channel and using these "range differences" in the analysis of position errors. This technique eliminates any covariance terms in the measurement errors and thus measurement residual variances are not directly recoverable from the trajectory residuals.

A separate analysis was performed on selected data (flights 08, 10, 14, 18 and 19) to determine measurement error variances. The method of variate differences (Ref. 26), was applied to the raw pseudo-range and pseudo range-rate data taken over ten second time intervals. This method yields estimates of total channel variances by assuming that the data consists of a smooth trend component (i.e. the true value of pseudo range) plus an additive noise component. The smooth component is eliminated by differencing and the variance estimate based on what remains. For the test data, the variate difference techniques yields σ estimates which are good to about $\pm 10\%$ at 95% confidence.

To obtain an estimate of the interchannel covariance, the variance estimates of the individual channel measurements were used along with a variance estimate of the inter-channel data and the covariance found by solving

$$\sigma^2 R_{i-j} = \sigma^2 R_i + \sigma^2 R_j - 2\mathrm{cov}(R_i, R_j)$$

The mechanisms affecting the covariance terms are common to all four channels:

- Noise in non-coherent portion of the user receiver
- Noise in non-coherent portion of the calibration receiver
- Noise in the calibration reference clock
- Noise in the user reference clock.

Consequently, an overall estimate of covariance can be formed using the average of the observed quantities:

$$\overline{\mathrm{cov}} = \frac{1}{6} \sum_{i<j=2}^{4} \mathrm{cov}(R_i, R_j)$$

When we consider all of the 621B data which showed good results (that is, no known failures occurred), the average value of the random noise is extremely small. Typical values are:

	r	r
Hazeltine	3.0 ft	0.25 ft/sec
Magnavox	2.5 ft	0.25 ft/sec

Further, although some data slices exhibit some form of interchannel noise correlation, the overall covariance term has an approximately zero mean distribution for MRL and is only slightly biased for the Hazeltine data (about 1 ft^2 and 0.01 $(ft/sec)^2$ for range and doppler, respectively).

4.1.2 Functional Relationships for the Measurement Variances

There are many contributing error sources to the total pseudo range and pseudo range-rate noise quantities. Those of particular importance are described in the following paragraphs.

Thermal Noise Range Error

The range error due to thermal noise using phase coherent correlation is given by:

$$\sigma_R \simeq \frac{cT_c}{\sqrt{2[P_R/2B_L N_o]}} \text{ , ft}$$

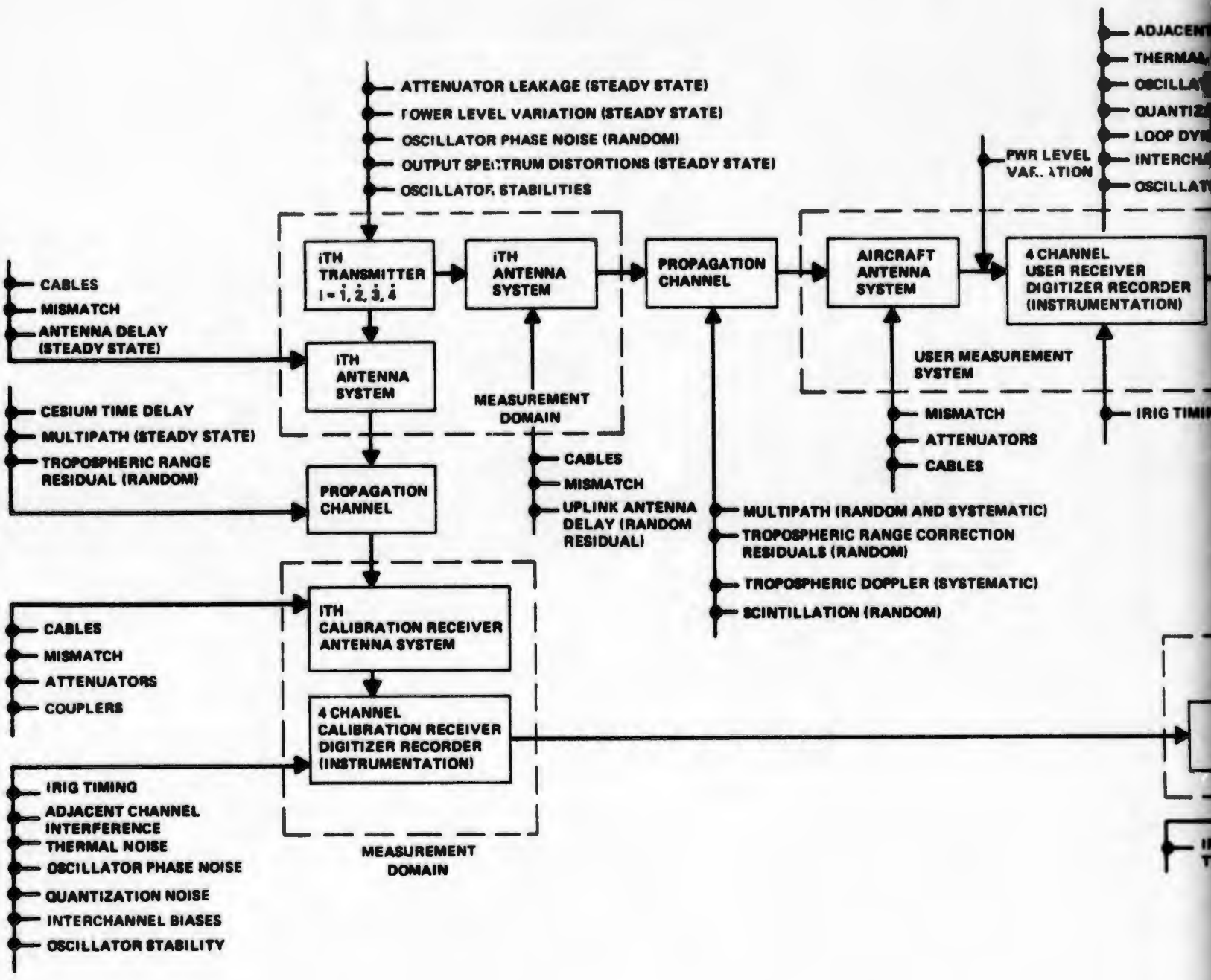
ATTENUATOR LEAKAGE (STEADY STATE)
POWER LEVEL VARIATION (STEADY STATE)
OSCILLATOR PHASE NOISE (RANDOM)
OUTPUT SPECTRUM DISTORTIONS (STEADY STATE)
OSCILLATOR STABILITIES
ADJACENT
THERMAL
OSCILLA
QUANTIZ
LOOP DY
INTERCH
OSCILLAT
PWR LEVEL VAR. ATION
iTH TRANSMITTER i = 1, 2, 3, 4
iTH ANTENNA SYSTEM
PROPAGATION CHANNEL
AIRCRAFT ANTENNA SYSTEM
4 CHANNEL USER RECEIVER DIGITIZER RECORDER (INSTRUMENTATION)
CABLES
MISMATCH
ANTENNA DELAY (STEADY STATE)
iTH ANTENNA SYSTEM
MEASUREMENT DOMAIN
USER MEASUREMENT SYSTEM
MISMATCH
ATTENUATORS
CABLES
IRIG TIMI
CESIUM TIME DELAY
MULTIPATH (STEADY STATE)
TROPOSPHERIC RANGE RESIDUAL (RANDOM)
PROPAGATION CHANNEL
CABLES
MISMATCH
UPLINK ANTENNA DELAY (RANDOM RESIDUAL)
MULTIPATH (RANDOM AND SYSTEMATIC)
TROPOSPHERIC RANGE CORRECTION RESIDUALS (RANDOM)
TROPOSPHERIC DOPPLER (SYSTEMATIC)
SCINTILLATION (RANDOM)
CABLES
MISMATCH
ATTENUATORS
COUPLERS
iTH CALIBRATION RECEIVER ANTENNA SYSTEM
4 CHANNEL CALIBRATION RECEIVER DIGITIZER RECORDER (INSTRUMENTATION)
IRIG TIMING
ADJACENT CHANNEL INTERFERENCE
THERMAL NOISE
OSCILLATOR PHASE NOISE
QUANTIZATION NOISE
INTERCHANNEL BIASES
OSCILLATOR STABILITY
MEASUREMENT DOMAIN

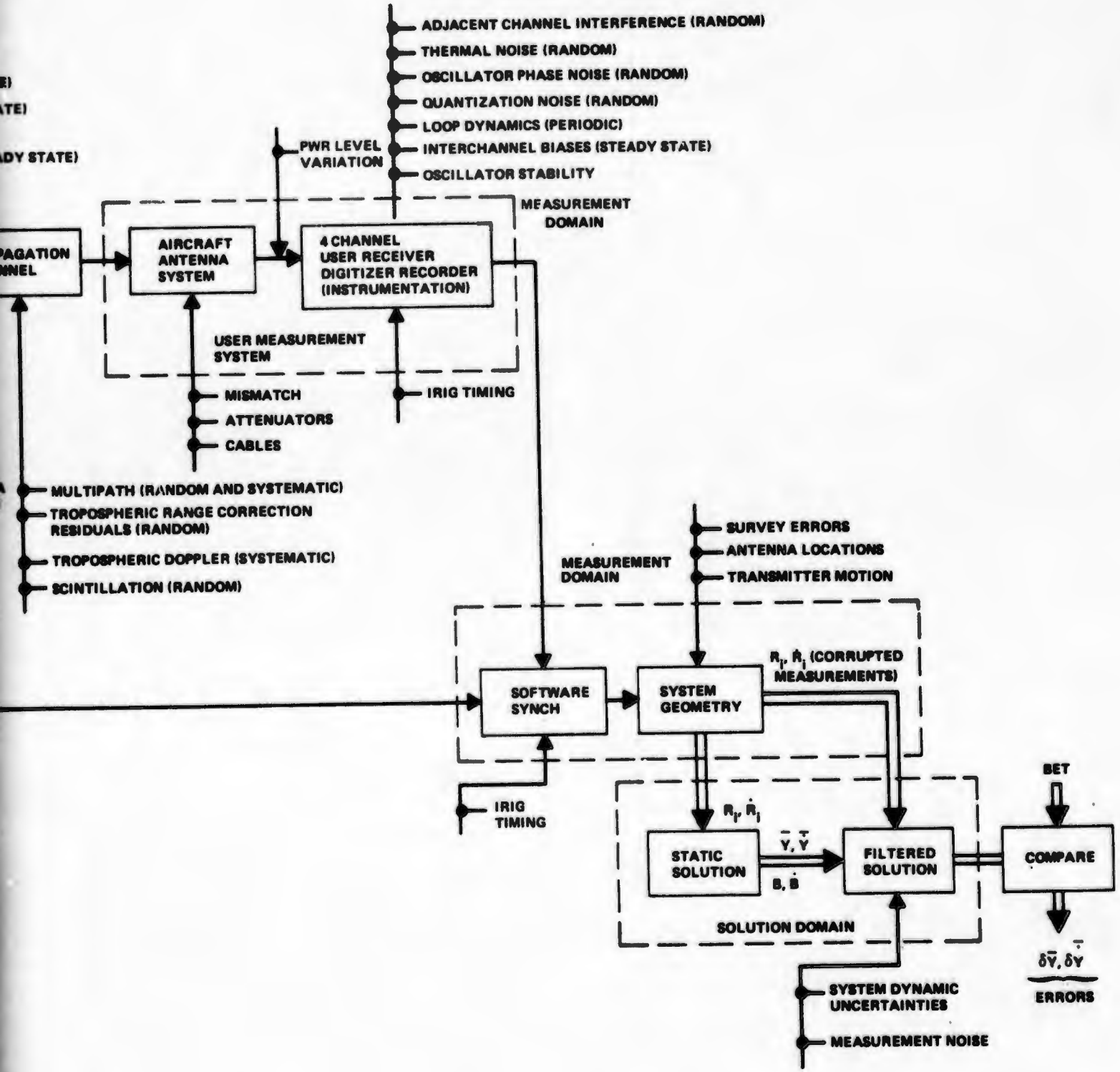

Figure 4-2 Representative Error Sources in Field Test

where c = speed of light, fps

T_c = chip length, nanosec

P_R = total received power, watts

N_o = noise spectral density, watts/Hz

$2B_L$ = two sided loop noise bandwidth of the code tracking loop

For the MRL receiver, the values of σ_R due to thermal effects vary from 0.15 ft at high signal level (-110 dbm), to 2.8 ft at -135 dbm and increase to 4.7 ft at low signal level (-140 dbm) as shown in Figure 4-3. In the same illustration, the HC receiver thermal noise error curve shows an increase over MRL due to the widening of the loop noise bandwidth with increased signal power. The same phenomena occurs in the thermal noise range rate error.

Thermal Noise Range Rate Error

The range rate error due to thermal noise is:

$$\sigma_{\dot{R}} = \frac{c}{2\pi f_o T \sqrt{2 \frac{P_R}{2B_L' N_o}}} \quad , \text{ fps}$$

where f_o = carrier frequency (1.575 GHz)

T_1 = doppler counting time

$2B_L'$ = two sided loop noise bandwidth of the carrier tracking loop

These errors are plotted in Figure 4-3 for both the HC and MRL receivers.

Quantization

The quantization error without bit ambiguity* σ_Q enters into the data as uncertainty in the measurements as follows:

$$\sigma_Q = \frac{cT_c}{2^b \sqrt{12}}$$

where b = number of bits used for quantizing. For 0.5 ft quantization, the resultant standard deviation is 0.145 ft.

If bit ambiguity occurs, the quantization error becomes:

$$\sigma_{QA} = \frac{\sqrt{3}}{2} q$$

where q is the quantization level (0.5 ft). In this case σ_{QA} = 0.43 ft.

---

*Bit ambiguity refers to an uncertainty in measuring the correct code chip (see Ref. 1)

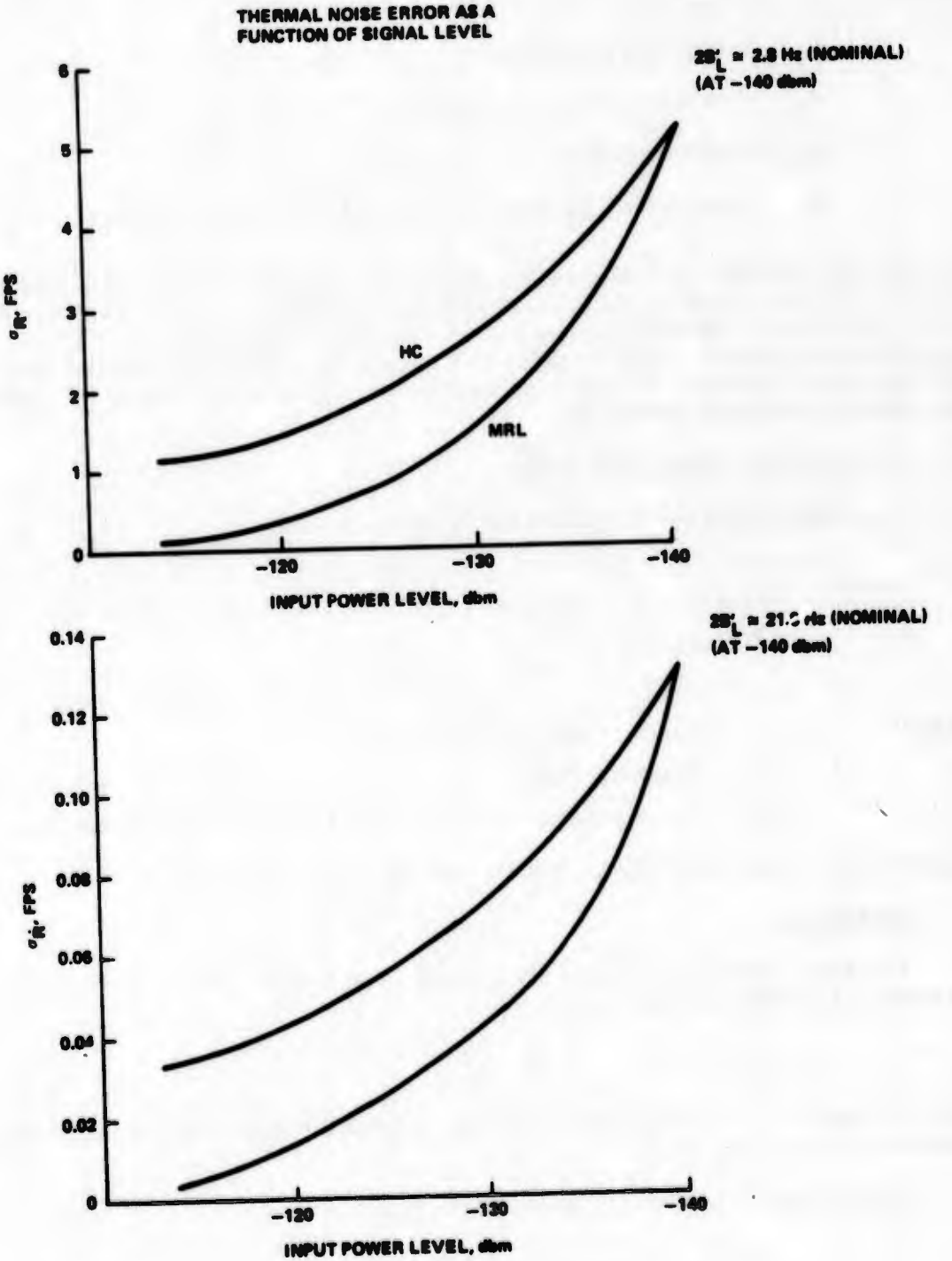

Figure 4-3 Predicted Measurement Error Due to Thermal Noise Showing Effects of HC Variable Bandwidth

Range and Range Rate Errors Due to Oscillator Phase Noise

These random errors are a function of the crystal oscillator design, system vibration levels, code and carrier loop implementations and are defined by the following equation:

$$\sigma_{osc} = K_1 \sqrt{\frac{K_2 A}{(2B_L)^2}} \text{ , ft.}$$

where K_1, K_2 are a function of the system implementation and A is a function of the oscillator spectral purity. The complete analysis of oscillator phase noise is quite complex (see Ref. 1). Our initial estimates of σ_{osc} are 0.02 ft and 0.03 fps for the range and range rate errors, respectively.

Range and Range Rate Errors Due to Clock Errors in the System Implementation

Error in the clock frequency, i.e. $(\Delta f/f)$, introduces the following error in the system:

$$\Delta R_i = |l_i - r_i| \left(\frac{\Delta f}{f}\right) + c\Delta t \left(\frac{\Delta f}{f}\right)$$

where l_i = range from transmitter i to calibration station

r_i = slant range from transmitter i to aircraft

$\frac{\Delta f}{f}$ = oscillator accuracy

Δt = sample misalignment between calibration and airborne data, seconds

This error represents a measurement uncertainty of approximately 0.1 ft.

The range rate error due to the oscillator enters into doppler measurements as an uncertainty in the transmitter frequency. This error is of second order importance in the system and engenders a range rate measurement error of approximately 10^{-4} fps.

Scintillation

There are three types of scintillations of signals passing through the atmosphere: amplitude, phase, and angle of arrival. The scintillation of electromagnetic signals is due primarily to scattering by the irregularities of the refractive index of the atmosphere. Scintillations cause random errors in the measurement domain particularly at low elevation angles and is estimated not to exceed 0.2 ft for the flight test profiles.

Diffuse Multipath Errors

The measurement error due to the presence of a multipath signal can be random (diffuse) or bias-like or oscillatory (specular) depending on system user geometry.

The errors due to diffuse ground multipath occur when the look angles from the user to the transmitters are large (e.g., directly over the transmitter constellation). A complete analysis of these errors was performed by computer simulation during the Phase I effort (Ref. 1) and indicate variances on the order of

$$\sigma_m \approx 3.5 \text{ ft in range}$$

$$\sigma_{\dot{m}} \approx 0.1 \text{ fps in range rate}$$

for the field test configuration (A flight path, antenna height about 40 ft).

Multipath errors can also develop from reflected signals on the calibration links and from aircraft structure reflections. While both of these errors are specular phenomena, the aircraft self induced multipath appears as a "random" error in the data due to the rapidly changing geometry. This error, also discussed in Ref. 1, is predicted to introduce about 0.7 ft of white noise to the range measurements and about 0.07 fps to the doppler measurements.

Adjacent Channel Interference

Some adjacent channel interference is permissible in the design of multichannel correlation receivers. It is caused by the finite cross correlation between adjacent channel codes.

The signal-to-adjacent channel interference ratio in the equivalent noise bandwidth of the loops may be expressed as (Ref. 37):

$$SIR \simeq \frac{3}{8} \frac{B_{IF}}{2B_L'} \frac{P_R}{P_I}$$

where B_{IF} is the prediction bandwidth (IF bandwidth), $2B_L$ is the double-sided loop noise bandwidth, P_R is the desired channel power and P_I is the interference channel power. The SIR sets an upper bound on the range and range rate error performance of the receiver. The thermal noise range rate error, Eq. (4) for example, in the presence of interference may be expressed as (Ref. 37):

$$\sigma_{\dot{R}} = \frac{c}{2\pi f_o T \sqrt{SNR_{eff}}}$$

where

$$SNR_{eff} = \frac{SNR_{Th} SIR}{1 + SIR + SNR_{Th}}$$

and

$$SNR_{Th} = \frac{P_R}{N_o B_L'}$$

The effect of adjacent channel interference becomes noticeable when the $\frac{P_R}{P_I}$ ratio goes well below unity. $\frac{P_R}{P_I}$ becomes approximately 0.1 during some portion of the ILS flights. This causes approximately a 3% increase in the receiver thermal noise.

4.1.3 Summary of Random Errors

Table 4-1 gives a summary of the observed and the theoretically predicted random errors. Of the sources of random errors, the effects of thermal noise, ground multipath and (in the doppler measurement) oscillator phase noise and tropospheric doppler are most prevalent. To summarize, we would expect the following random errors at high signal levels (-120 dbm)

σ_R = (ground diffuse multipath) $\simeq$ 3.5 ft

$\sigma_{\dot{R}}$ = (ground diffuse multipath) + (transmitter oscillator) + (tropospheric doppler) $\simeq$ 0.17 fps

and, at low signal levels (-140 dbm)

σ_R = (ground diffuse multipath) + (thermal noise) $\simeq$ 5.8 ft

$\sigma_{\dot{R}}$ = (ground diffuse multipath) + (transmitter oscillator) + (tropospheric doppler) + (thermal noise) $\simeq$ 0.22 fps.

The observed data (Table 4-1) shows our predictions to be quite reasonable for data summarized over all test conditions (Table 4-1). However, Figures 4-4 and 4-5 do not support the predicted dependence with signal level. We think this is due primarily to the presence of specular ground and aircraft multipath, which, in our analysis, was treated as a random error, but which, in actuality, is nearly periodic and at a high enough frequency to look like a random error to the data processing system. This hypothesis is also supported by the smaller variances of the MRL data. The generally narrower loop bandwidths (i.e. independent of power variation) of the Magnavox receiver tend to lessen the effects of multipath and so reduce σ_R and $\sigma_{\dot{R}}$.

In accordance with this hypothesis, analysis of the variations of measurement noise with user-transmitter geometry should show multipath effects. The variance of random errors in the data was computed by variate differences (as discussed in the previous section) for flights 8, 10, 14, 19 and 20, yielding a total of 390 independent estimates for the HC data and 298 estimates for MRL. The variance estimates were then averaged within groups selected by channel signal level and user Y (north-south) and Z (vertical) position for "A" and "C" flight paths (that is, aircraft flew along the Y axis). Each group of data contains at least 4 (typically 9) independent variance estimates which are accurate to approximately $\pm$ 10% at 95% confidence. Further, a 3-sigma edit eliminated points which contain gross system malfunctions and the data were checked for whiteness before the application of the variate difference estimation technique. Thus, each point represents a statistically significant sample.

The plots of Figure 4-6 and 4-7 show these observed variations of σ_R^2 and $\sigma_{\dot{R}}^2$ with user Y position, as well as the results of the measurement whiteness tests as a function of user Y position. The whiteness plots show the percentage of the 10 sec time slices which displayed oscillatory phenomena in the range-doppler differences, defined by:

$$[R\text{-}D] = (PR_t - PR_{t-1}) - (-PD_t \cdot \Delta t)$$

Table 4-1 System Random Error Summary

	Hazeltine		MRL		Remarks
	σ_R	$\sigma_{\dot{R}}$	σ_R	$\sigma_{\dot{R}}$	
A. Aircraft Receiver					
1. Thermal Noise	1.6	0.05	0.6	0.02	● −123 dbm
2. Oscillator Noise	0.02	0.03	0.02	0.03	Low Vibration
3. Quantization	0.43	0.008	0.145	0.008	
4. Time Delay Mismatch	0.61	0	0.2	0	
5. Dynamics					
(a) Clock Loop	1.3□	N.A.	1.3	N.A.	□ILS Only
(b) Doppler Meas	N.A.	0	N.A.	0	
6. Adjacent Channel Interference	0.05	0	0.02	0	ILS
B. Up-Link					
1. Multipath					
(a) Ground	3.5	0.1	2.5	0.1	Avg All Flts
(b) Aircraft	0.7	0.07	0.7	0.07	
2. Troposphere	1	0.1	1	0.1	Maximum
3. Scintillation	0.2	0.05	0.2	0.05	
C. Transmitter Oscillator	0.4	0.1*	0.4	0.1*	*Maximum
D. Cal Receiver					
1. Thermal Noise	1.5	0.04	1.5	0.04	● −120 dbm
2. Oscillator Noise	0.001	0.003	0.001	0.003	
3. Quantization	0.43	0.008	0.43	0.008	
4. Time Delay Mismatch	0.61	0	0.61	0	
5. Adjacent Channel Inter	0	0	0	0	
E. Cal Link Propagation					
1. Fading Stability	0.06	0	0.06	0	
2. Refraction	0.005	0	0.005	0	
3. Scintillation	0.2	0	0.2	0	
Total (RSS)	4.7	0.2	3.2	0.17	

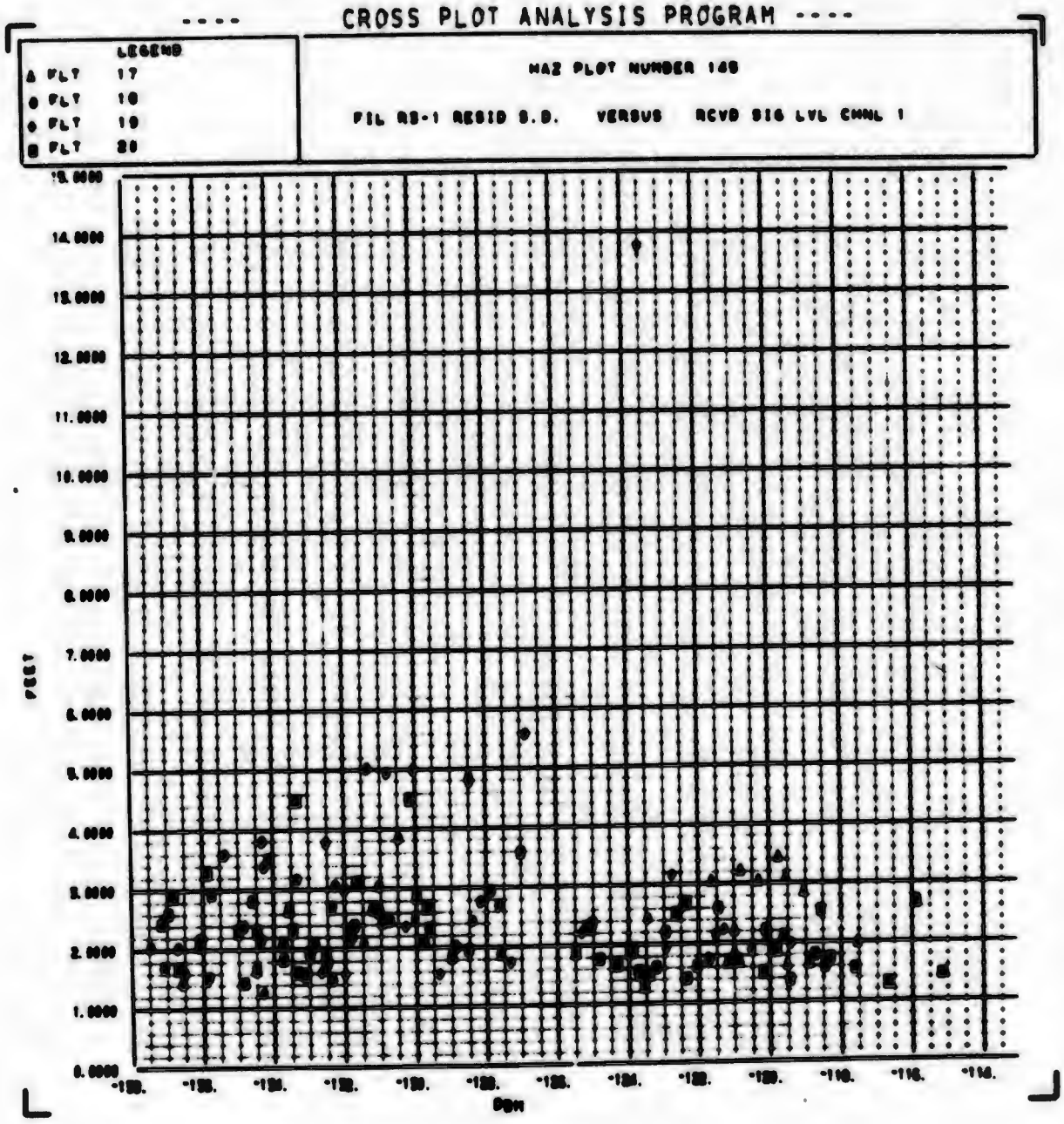

Figure 4-4 Typical Plot of Observed σ Showing No Dependency With Signal Level (HC)

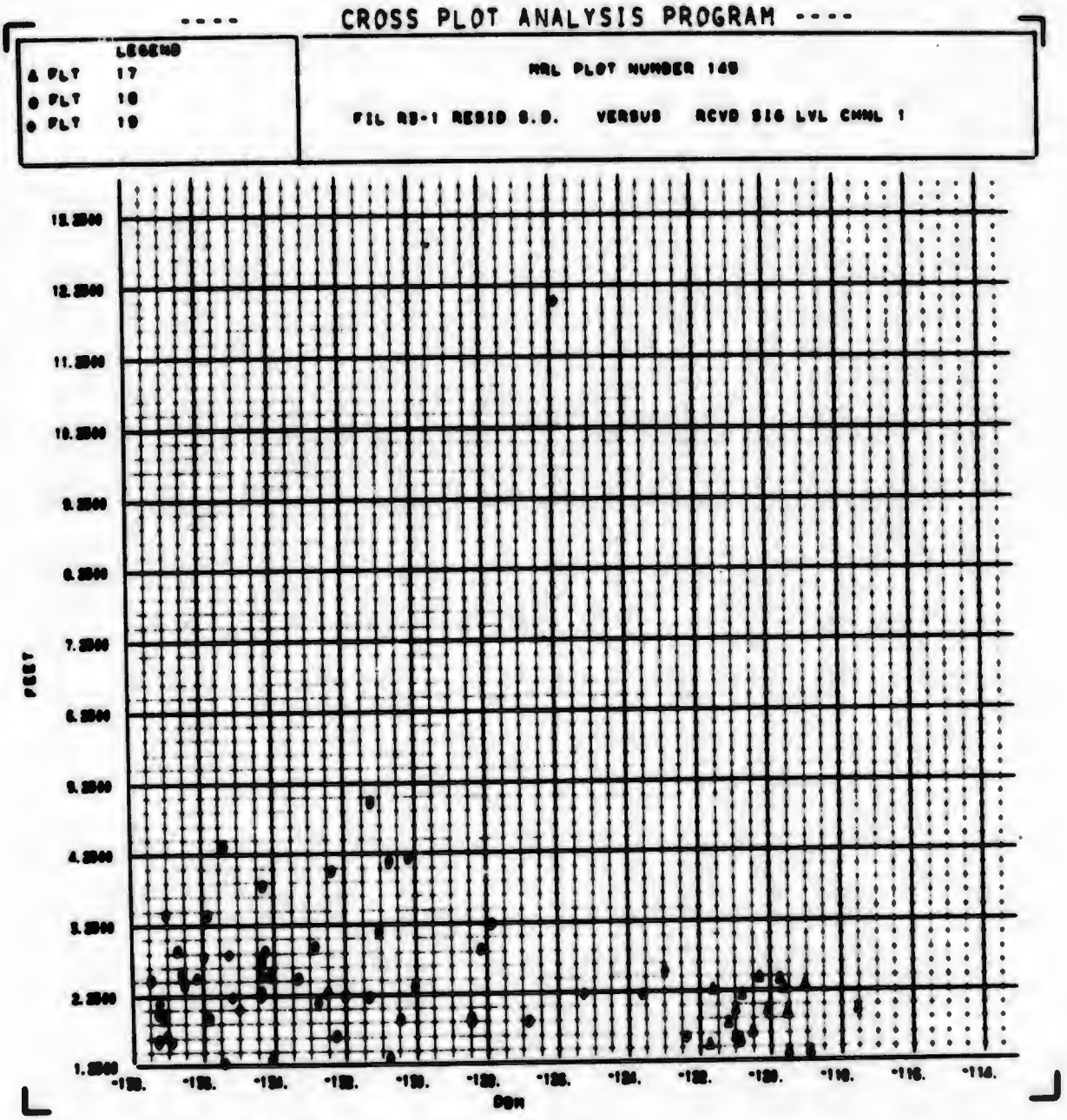

TYPICAL PLOT OF OBSERVED σ SHOWING NO DEPENDENCY WITH SIGNAL LEVEL (MAGNAVOX)

Figure 4-5 Typical Plot of Observed σ Showing No Dependency With Signal Level (MRL)

PSEUDO-RANGE, PSEUDO-DOPPLER VARIANCES AND CHANNEL OSCILLATORY
(MAGNAVOX) AS A FUNCTION OF USER-TRANSMITTER GEOMETRY
(OBSERVED DURING 621B FLIGHT TESTS)

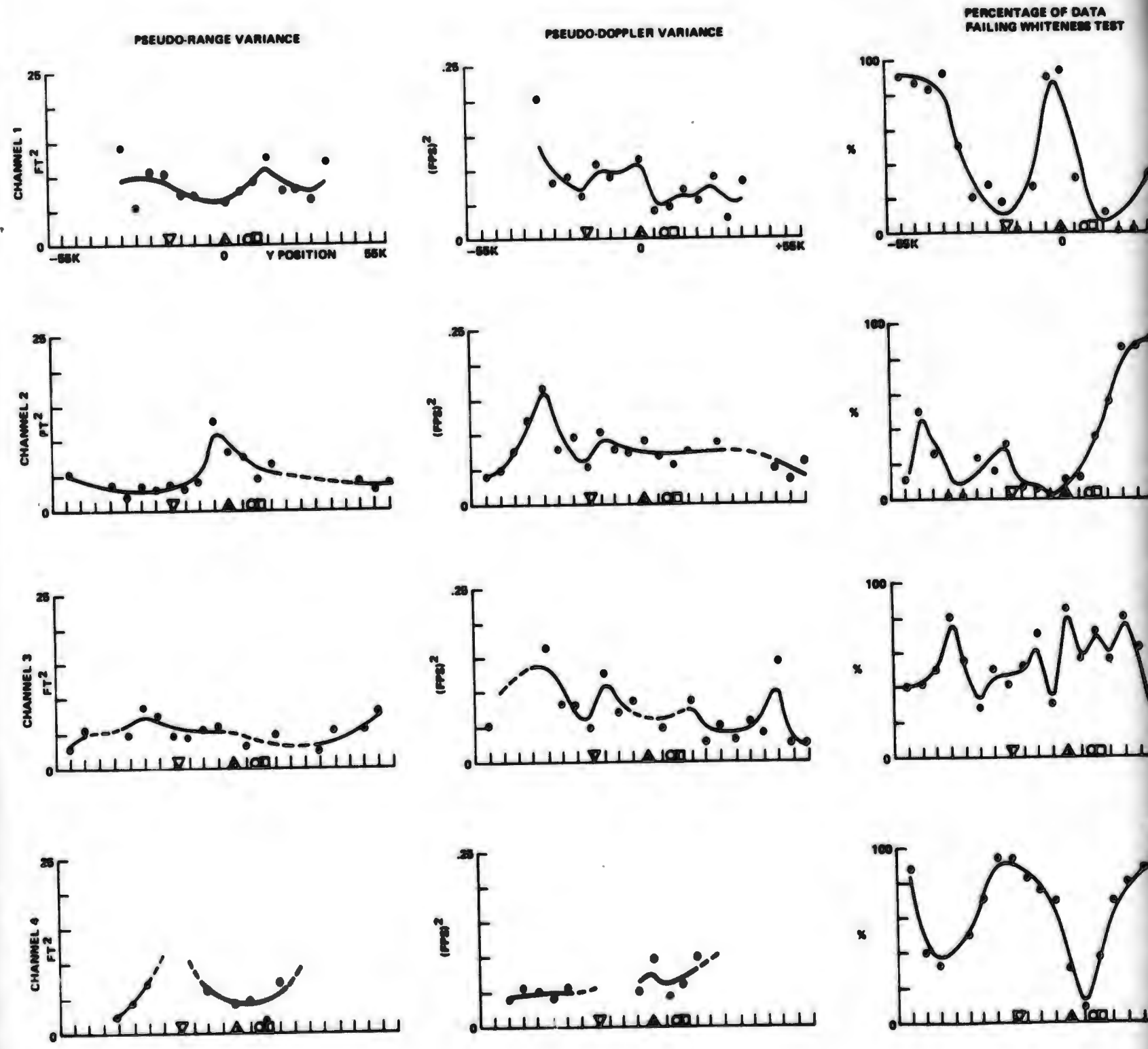

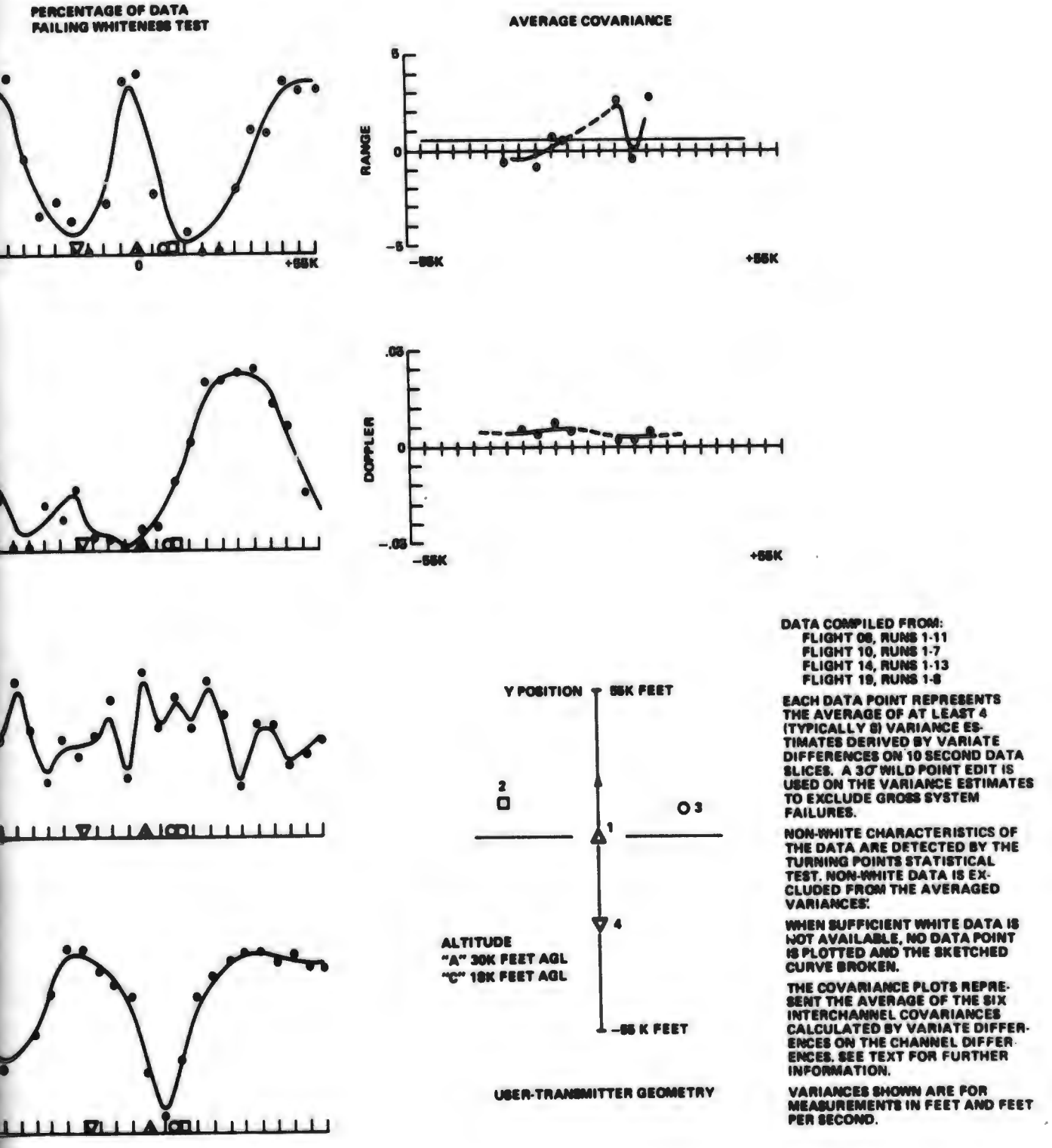

Figure 4-6 Observed Channel Variances and Periodic Content for the MRL Airborne Receiver as a Function of User Y Position for "A" and "C" Flight Paths

PSEUDO-RANGE, PSEUDO-DOPPLER VARIANCES AND CHANNEL OSCILLATORY
(HC) AS A FUNCTION OF USER-TRANSMITTER GEOMETRY
(OBSERVED DURING 621B FLIGHT TESTS)

PSEUDO-RANGE VARIANCE

PSEUDO-DOPPLER VARIANCE

PERCENTAGE OF DATA
FAILING WHITENESS TEST

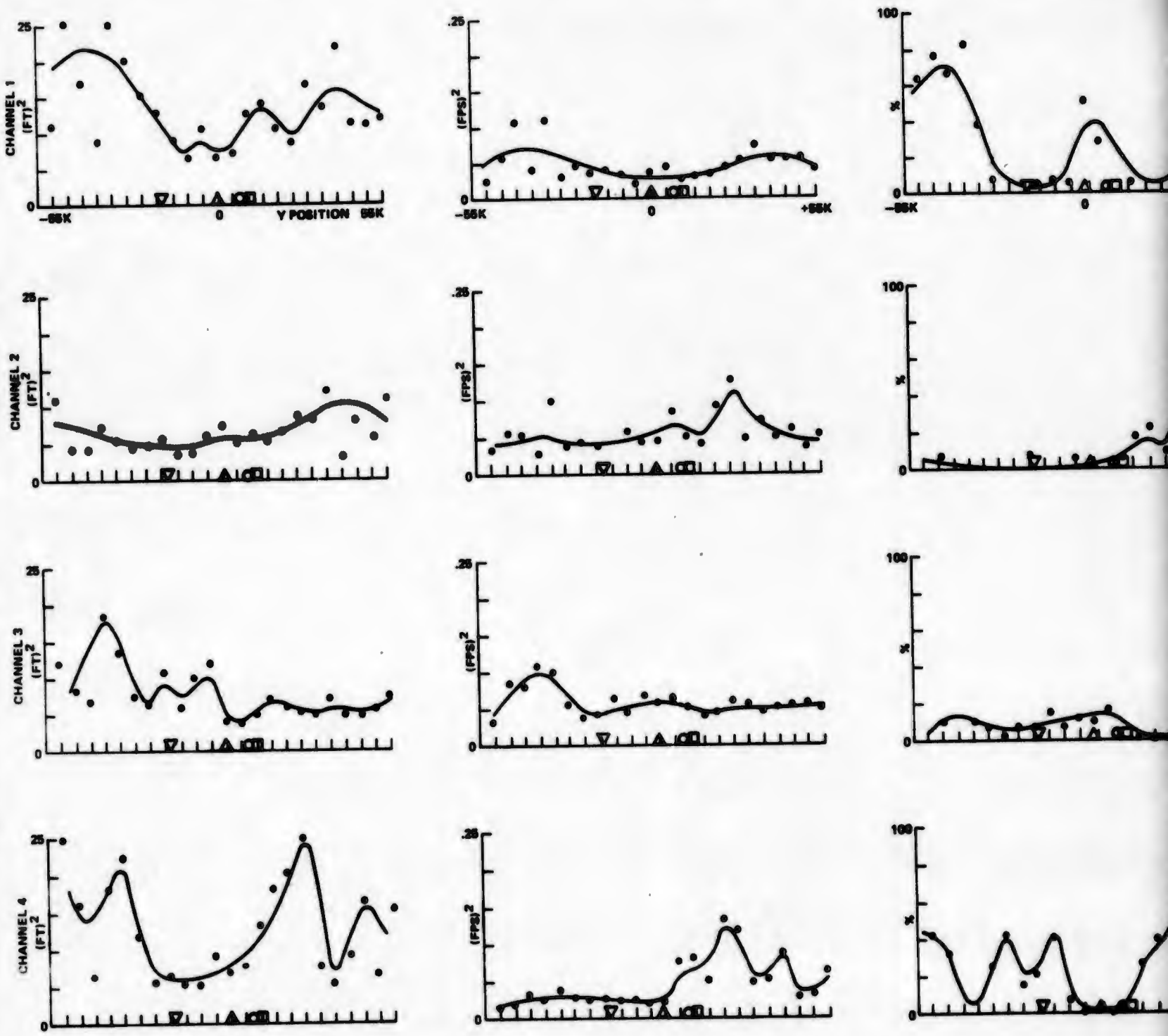

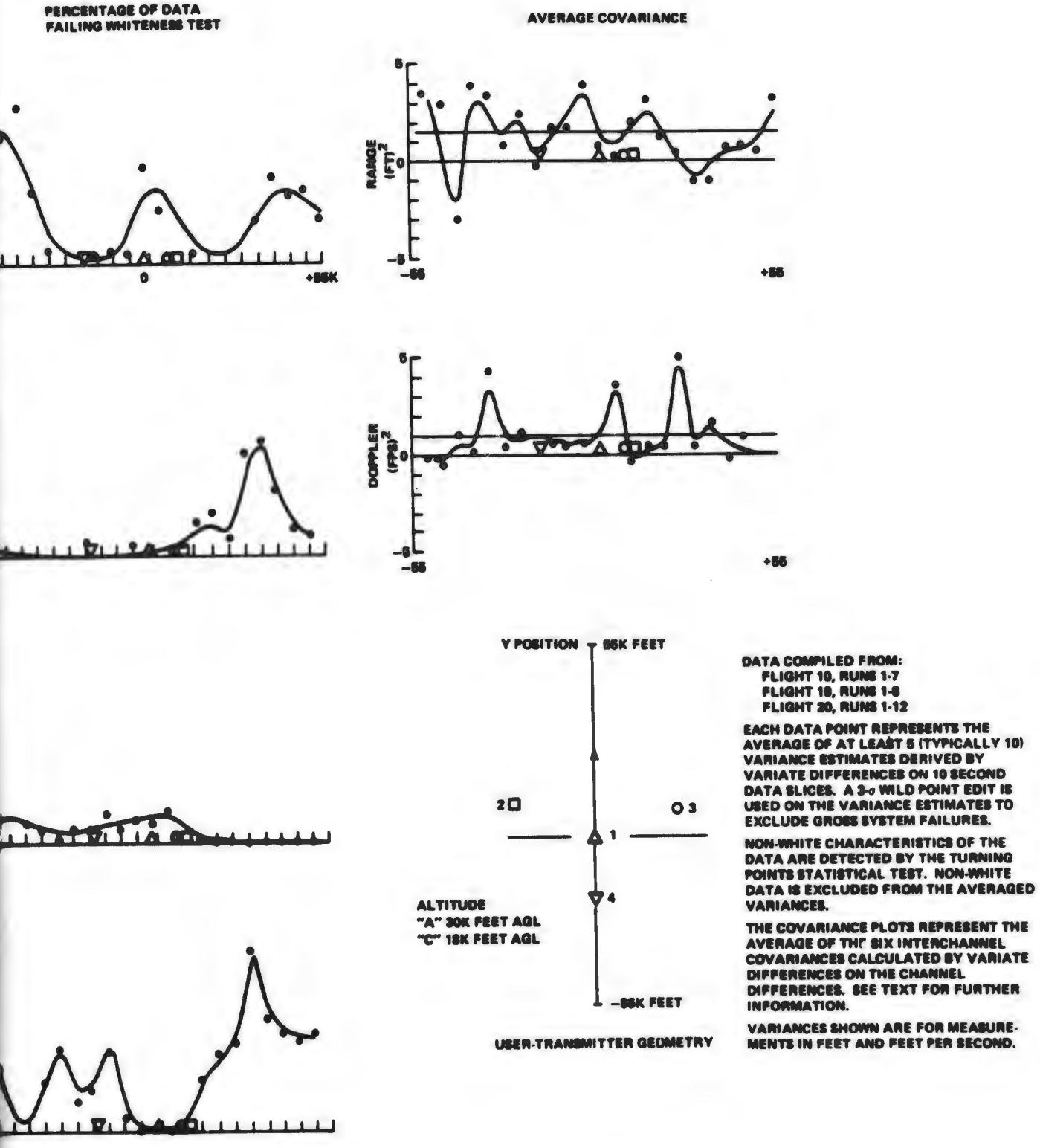

Figure 4-7 Observed Channel Variances and Periodic Content for the HC Airborne Receiver as a Function of User Y Position for "A" and "C" Flight Paths

where PR is pseudo range, PD pseudo doppler and Δt the elapsed time between the samples. The data were tested for randomness by the turning-point whiteness test and was considered oscillatory when the confidence in the random hypothesis declined below 0.10%. Non-random channel measurements are predominantly due to specular multipath and, therefore, the plots of Figures 4-6 and 4-7 indicate the amount of multipath observed in the data.

Referring to these figures, the typical values of channel measurement variances are evident, but strong dependencies with user Y position also present themselves. Specifically, channels 1 and 4 (those transmitters which the aircraft flew directly over) exhibit ground multipath characteristics, since both σ_R^2 and non-randomness increase as the user moves away from the transmitter. This phenomena is particularly noticeable in channel 4 and is discussed further in Section 6. We also note an increase in oscillatory tendencies when the user is directly over channels 1 and 4 transmitters. This is due to multipath from the back-lobes of the uplink antennas. The oscillatory effects of ground multipath from the offset transmitters 2 and 3 are not as predominant as those from 1 and 4 since the change in geometry is not as severe for the offset channels and the diffuse effects of aircraft multipath are more pronounced for side-incident signals.

The linear GDOP analysis was used (see Section 3) to project the observed measurement errors into the navigation solution domain (that is, X, Y, Z trajectory errors). Table 4-2 shows the random error predictions in nav solution coordinates for the overall σ_R and $\sigma_{\dot{R}}$ measurements determined from the test data as discussed in Subsection 4.1.1.

The GDOP analysis assumes: (1) zero inter-channel covariance, and (2) equal measurement error magnitudes. While the first assumption has been verified with the flight data, the second, according to Figures 4-6 and 4-7 cannot be fully supported. Thus there is a deviation between the predicted errors shown in Table 4-2 and the measured data shown in Figures 4-6 and 4-7. This deviation appears as a separation from the predicted curves in Figure 4-8. The effect is most predominant for the area navigation test, in the area north of the center transmitter.

Table 4-2 Predicted Random Error in Navigation Solution (Ft and fps), Field Tests

		Static Navigation Solution								(Two-State) Filtered Solution					
Field Test	Y Coordinate, K Ft	σX	σY	σZ	σB	$\sigma \dot{X}$	$\sigma \dot{Y}$	$\sigma \dot{Z}$	$\sigma \dot{B}$	σX	σY	σZ	$\sigma \dot{X}$	$\sigma \dot{Y}$	$\sigma \dot{Z}$
AREA NAV, X=0, Z=30K	50	5.0	33.9	18.2	51.3	.42	2.8	4.1	4.3	Not Processed	-	-	-	-	-
	30	4.0	4.4	29.4	27.0	.34	.38	2.4	2.2	3.3	6.0	8.6	.27	.50	.72
	0 (SALT)	3.8	5.9	18.2	15.9	.32	.49	1.5	1.3	3.7	4.8	1.75	.31	.40	.15
	-30	4.9	21.5	25.4	30.3	4.1	1.8	2.1	2.5	4.4	3.9	4.7	.37	.33	.40
	-50	6.2	52.9	32.9	59.4	.52	4.4	2.8	5.0	-	-	-	-	-	-
ILS, X=0 Z=APPROACH	8	18.9	318.0	45.5	111.0	.74	9.8	2.1	9.6	-	-	-	-	-	-
	2	3.0	6.8	4.2	5.9	.25	.57	.34	.49	2.5	2.4	3.2	.21	.21	.27
	0 (FLARE)	2.6	5.1	3.1	1.7	.22	.20	.28	.14	2.5	2.5	3.1	.21	.21	.26
	-2	2.9	18.0	7.5	15.2	.29	1.5	.62	.12	2.8	2.2	3.6	.22	.18	.30
	-8	25.8	473.0	75.0	170.0	2.1	40.0	.83	.17	-	-	-	-	-	-

This table summarizes the standard deviation of the navigation solution parameters. The data are obtained by propagating the σR and $\sigma \dot{R}$ measurements (3.0 ft and 0.25ft/sec respectively) through the appropriate geometry transformations at the selected X, Y, Z aircraft locations shown to yield the σX, σY, σZ, σB, $\sigma \dot{X}$, $\sigma \dot{Y}$, $\sigma \dot{Z}$, $\sigma \dot{B}$ values at these aircraft locations.

4.2 BIAS ERRORS

Steady-state errors (i.e. constant or very slowly varying errors) in pseudo-range measurements proved to be, by far the most significant source of navigation inaccuracy. Several aspects of the test system were not completely understood at the outset of the field tests, and these hampered the progress of the test program:

- Signal path delay measurements, accurate to one-billionth of a second, are extremely difficult to make in an uncontrolled desert environment. Measurements of this quality are absolutely essential for the calibration algorithms in the navigation solution

- Receiver interchannel time delay offsets (channel delay mismatch) are very difficult to control. Several interchannel time delay effects became evident during the testing. (See Section 4.2.1)

- The effect of a steady-state pseudo-range error is very pronounced for the WSMR test geometry. The navigation solution filters are based upon a zero mean error assumption which is theoretically achieved by reducing the actual steady-state error to insignificance or accomplishing the equivalent by performing the appropriate modelling. If the steady-state errors are not removed, the filters indeed remove much of the solution noise as intended but can do nothing to reduce the steady-state error. Due to the small scale of the test geometry, steady-state errors are magnified by GDOP in the solution domain, in effect overshadowing any benefits gained by filtering in attempting to improve the users computed position estimate.

The discussion of steady-state errors is divided into the following two broad categories:

- Errors due to the ground calibration configuration (these errors are peculiar to the field tests and would not be directly reflected in operational system performance since the satellite system has a significantly different calibration configuration)

- Errors due to user vehicle and equipment characteristics (which are similar in the test system and operational systems)

A summary of the results of the steady state error analysis, is presented in Section 4.4.

Perturbation Analysis

Before treating the steady-state error sources, an analysis of the effect of this type of error on the performance of the system is given for both the solution and measurement domains. The presence of steady-state error is recognized as a departure of the navigation solution trajectory from the WSMR BET (in the solution domain). The magnitude of the corresponding errors in the measurement domain is evaluated by comparing the navigation solution and BET slant ranges.

Corresponding to every point in the time series of the BET trajectory data, let the slant ranges be given by r_{ibe}, i = 1, 2, 3, 4. The navigation solution * derived

---

*621B navigation solution consists of static and filtered trajectories.

OBSERVED RANDOM ERROR IN 621B POSITION TRAJECTORY WITH GDOP PRES
(AREA NAVIGATION TESTS) (HC)

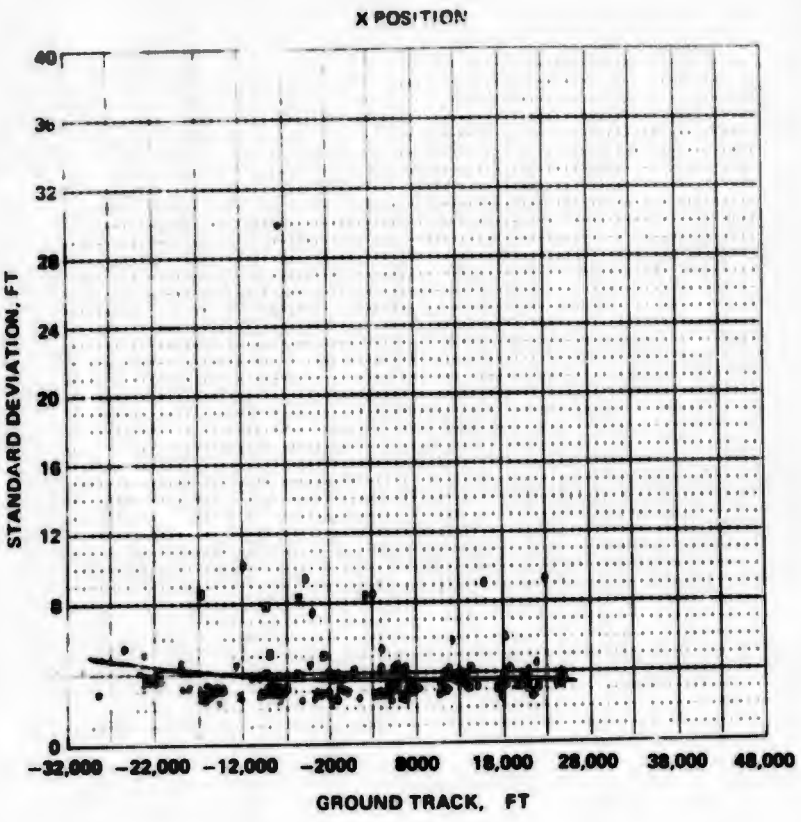

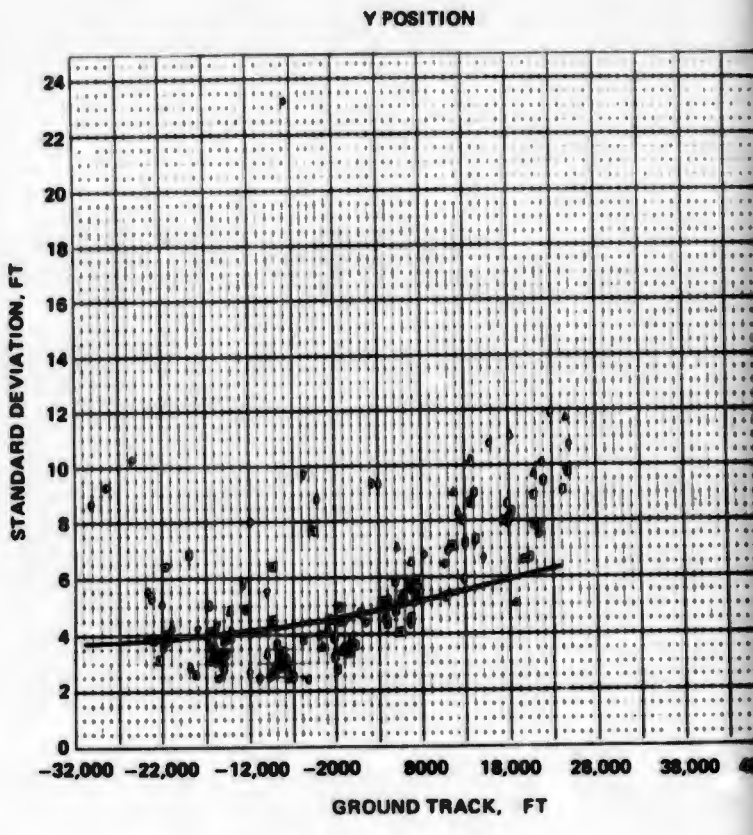

PLOTS SHOWN OBSERVED STANDARD DEVIATIONS OF TWO-STATE FILTERED SYSTEM TRAJECTORY ABOU
ABCISSA IS USER Y POSITION. DATA COMPILED FROM FLIGHTS 17, 18, 19, 20, 22. SOLID LINE ON EACH PLO
"DYNAMIC" GDOPS WITH σ_R = 3 FEET. MULTIPATH CONDITION AT NORTHERN PART OF THE RANGE (Y > 0

OR IN 621B POSITION TRAJECTORY WITH GDOP PREDICTIONS
S) (HC)

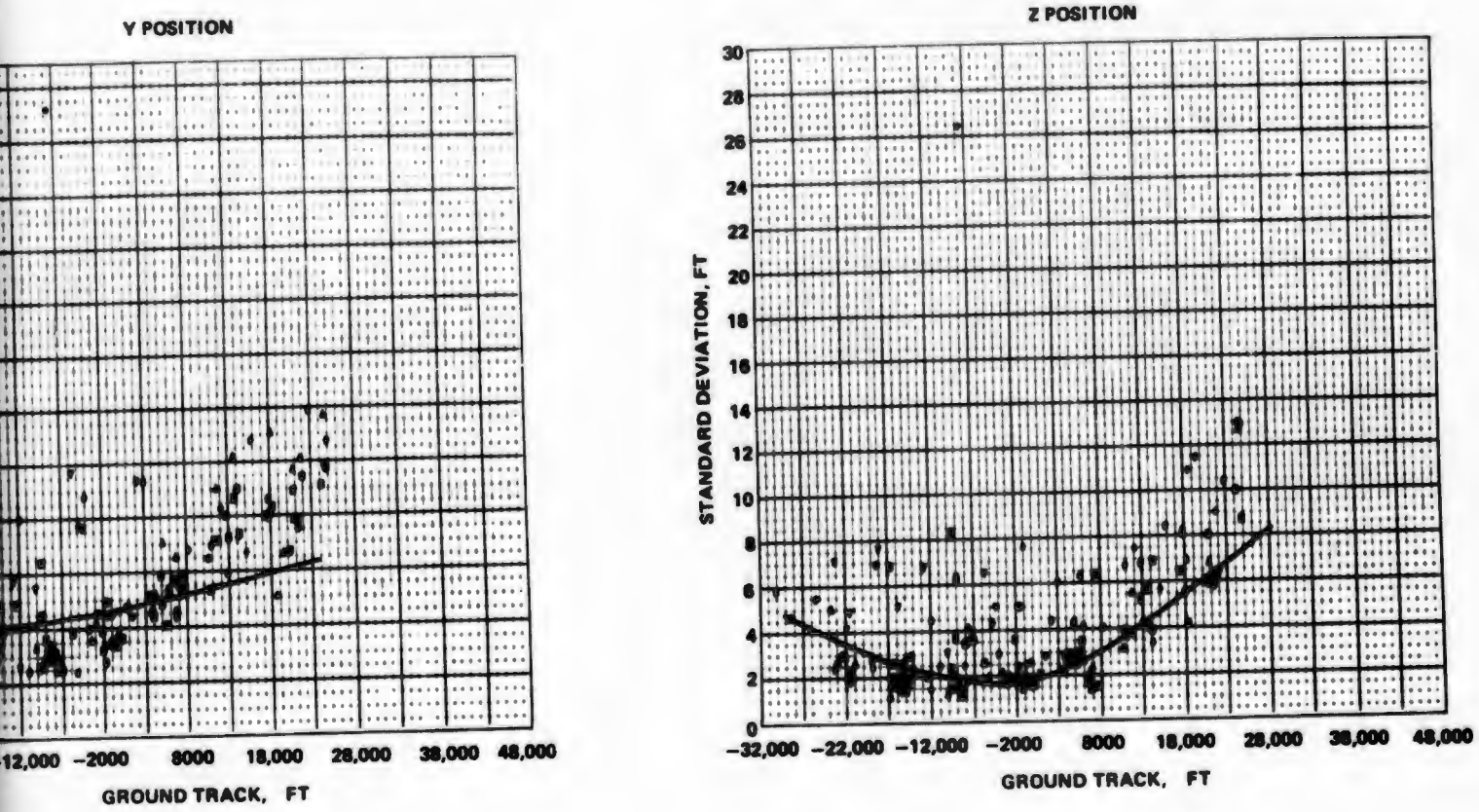

F TWO-STATE FILTERED SYSTEM TRAJECTORY ABOUT WSMR REFERENCE TRAJECTORY.
FLIGHTS 17, 18, 19, 20, 22. SOLID LINE ON EACH PLOT IS PREDICTED ERROR BASED ON
ONDITION AT NORTHERN PART OF THE RANGE (Y > 0) IS MOST EVIDENT ON Y ERROR PLOT.

Figure 4-8 Observed System Random Error as a Function of User Y Position for Two-State Filtered HC Data in Area Navigation Tests

OBSERVED RANDOM ERROR IN 621B POSITION TRAJECTORY WITH GDOP
***ILS TESTS) (MRL)**

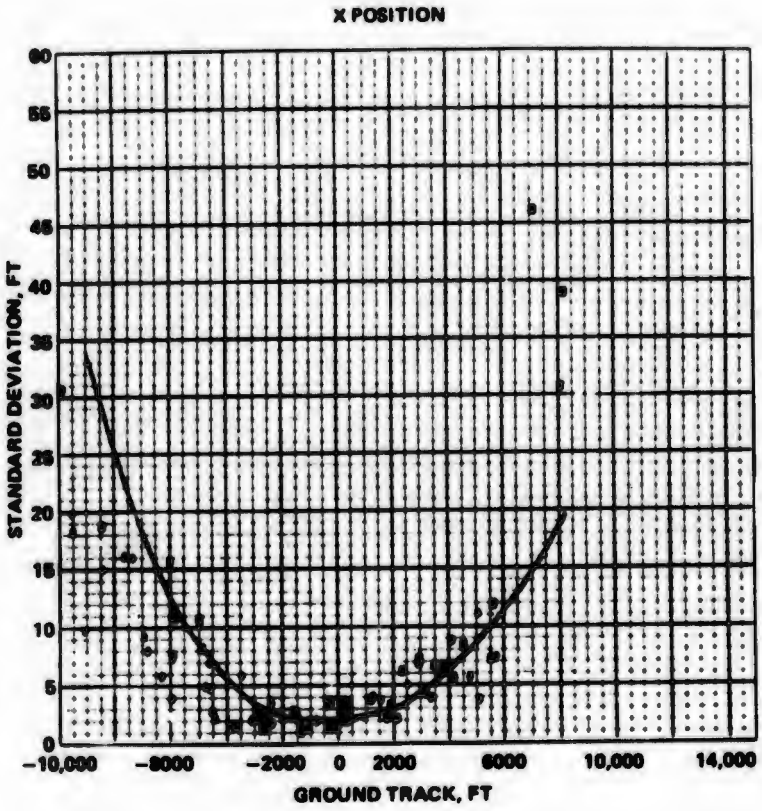

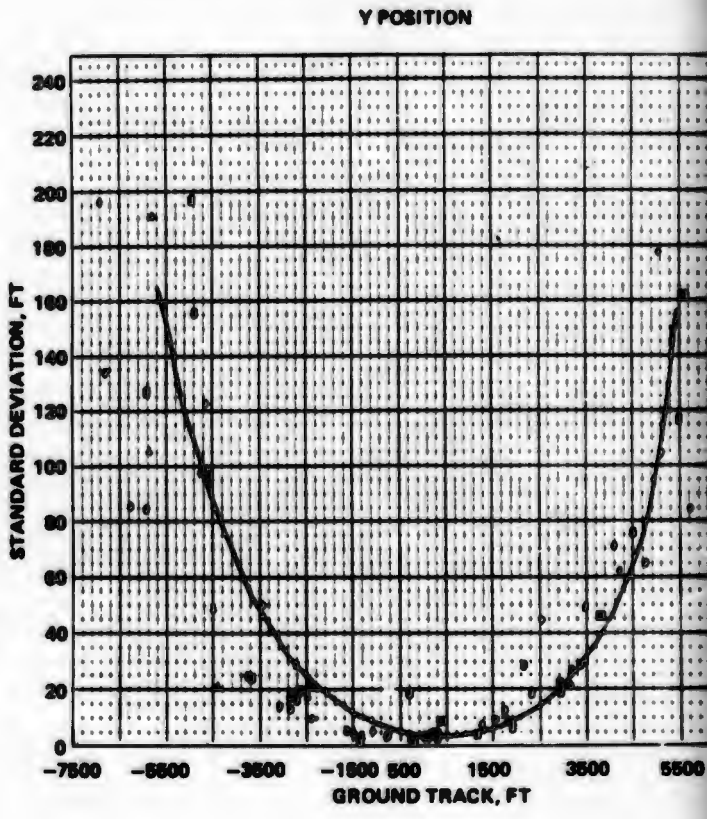

PLOT SHOWS OBSERVED STANDARD DEVIATIONS OF STATIC SYSTEM TRAJECTORY ABOUT
ABCISSA IS USER Y POSITION (ALONG APPROACH PATH). DATA COMPILED FROM FLIGHTS
PLOT IS PREDICTED ERROR BASED ON "STATIC" GDOPS WITH σ_R = 3 FEET.

RROR IN 621B POSITION TRAJECTORY WITH GDOP PREDICTIONS

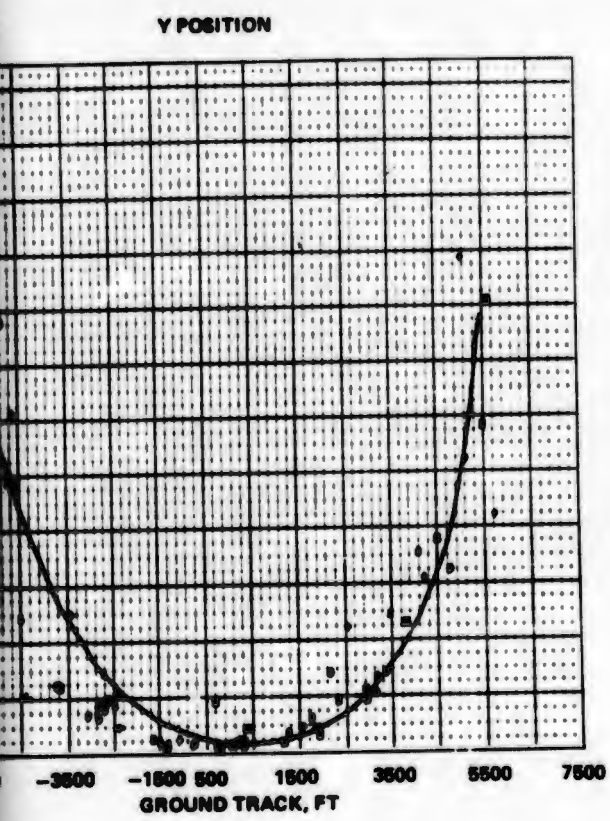

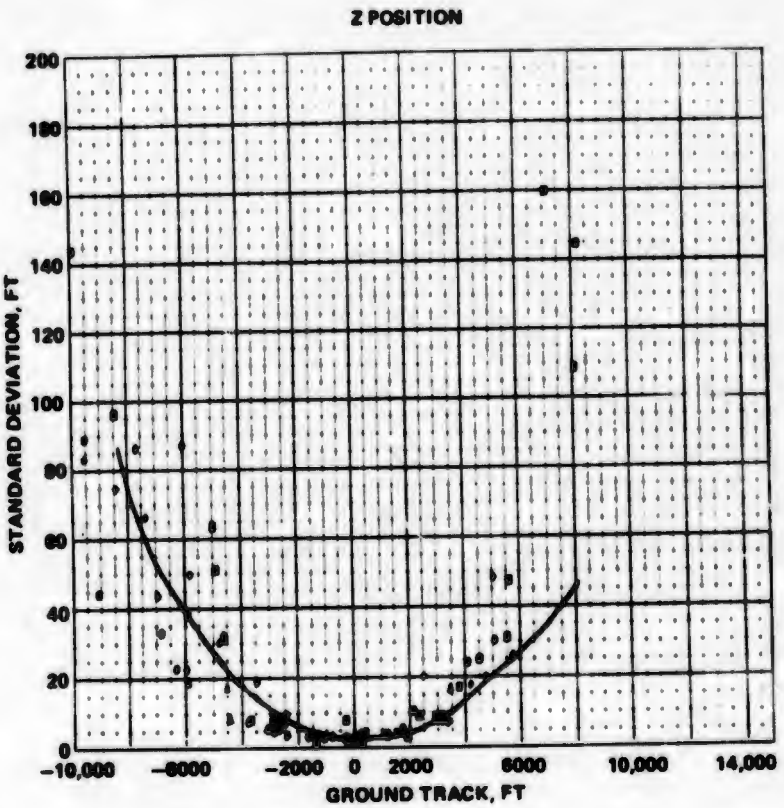

VIATIONS OF STATIC SYSTEM TRAJECTORY ABOUT WSMR REFERENCE TRAJECTORY.
PPROACH PATH). DATA COMPILED FROM FLIGHTS 25, 27, 29, 31. SOLID LINE ON EACH
STATIC" GDOPS WITH σ_R = 3 FEET.

Figure 4-8 Observed System Random Error as a Function at User Y Position for Static MRL Data in ILS Tests (Concluded)

from the four pseudo-range measurements yields the test vehicle trajectory and the system clock bias, B. From the definition of pseudo range,

$$R_i = r_i + B \tag{1}$$

with B known, a comparison of r_{ibe} and r_i yields the uncompensated steady-state error residuals,

$$\delta B_{usi} = r_{ibe} - r_{ij} \tag{2}$$

These residuals are easily identifiable and measurable when compared to one of the four receiver channels. Therefore, to obtain the sensitivity of navigator position as a function of interchannel steady-state residuals we examined the sensitivity of the range difference solution.**

If one selects arbitrarily channel one (i.e., i = 1) as the reference, the sensitivity equation given in Section 3 becomes modified, i.e.

$$(\gamma_{11} - \gamma_{ij})\delta Y_j = \delta B_{usi} - \delta B_{us1} = \delta B_{usi1} \tag{3}$$
$$i = 1,2,3,4; \quad j = 1,2,3.$$

In matrix form Eq. (3) becomes,

$$\underbrace{\begin{bmatrix} \gamma_{11}-\gamma_{21} & \gamma_{12}-\gamma_{22} & \gamma_{13}-\gamma_{23} \\ \gamma_{11}-\gamma_{31} & \gamma_{12}-\gamma_{32} & \gamma_{13}-\gamma_{33} \\ \gamma_{11}-\gamma_{41} & \gamma_{12}-\gamma_{42} & \gamma_{13}-\gamma_{43} \end{bmatrix}}_{A} \underbrace{\begin{bmatrix} \delta Y_1 \\ \delta Y_2 \\ \delta Y_3 \end{bmatrix}}_{\delta \bar{Y}} = \underbrace{\begin{bmatrix} \delta B_{us12} \\ \delta B_{us13} \\ \delta B_{us14} \end{bmatrix}}_{\delta \bar{B}_{us1}} \tag{4}$$

Solving for $\delta \bar{Y}$

$$\delta \bar{Y} = A^{-1} \delta \bar{B}_{us1} \tag{5}$$

Equation (5) relates the linear perturbation sensitivity of the three dimensional navigator position coordinates to uncompensated system steady-state errors referred to transmitter 1 or channel 1.

Typical entries of the sensitivity matrix (A^{-1}), defined in Eq. (5), at 30,000 ft AGL over the center transmitter for the aera navigation geometry are:

$$A^{-1} = \begin{bmatrix} -0.7997 & 0.8746 & -0.0537 \\ 0.5715 & 0.4265 & -1.4143 \\ 1.6234 & 1.7378 & 1.4011 \end{bmatrix} \tag{6}$$

To assess the trajectory perturbation as a function of interchannel steady-state residuals Eq. (5) and (6) are computed at a number of points along the trajectory, (which is

---

**Other techniques may be used, i.e., normalized linearly weighted sums, etc., but were not selected for this analysis, since the range difference technique is simpler and provides satisfactory accuracy.

reasonable in the absence of singularities in Eq. (5). With an interchannel residual of 14 ft in channel 1–4, i.e. $\delta B\mu_{12} = 0$, $\delta B\mu_{13} = 0$, and $\delta B\mu_{14} = 14$ ft, the trajectory perturbations are given in Figures 4–9, 4–10 and 4–11. For this idealized analysis, the elimination of the bias would, of course, reduce all residuals to zero.

The uncompensated interchannel steady state residual in channels 1–4 causes severe tilt (rotation and translation) in the Z and Y trajectory coordinates and a slight translation in the X trajectory coordinate. This effect is exhibited in Flight 19, run 05 and shown in Section 2. When the pseudo-range measurements are compensated for the interchannel steady-state residuals, the Z trajectory follows the WSMR BET with reduced bias error, as shown in Figure 2-3.

Appendix A shows the results of a comparable analysis performed on the solution domain perturbation of user position with unity errors in the various channels.

Steady State Position Error Coupling Into Velocity

In the field test system implementation, the relatively small distances between the user (aircraft) and the transmitters creates a non-negligible position-velocity coupling effect which may not be negligible.

The sensitivity equations relating the steady-state position and velocity errors were given in Section 3 as:

$$\underbrace{\begin{bmatrix} \Gamma_{11} & \Gamma_{12} & \Gamma_{13} \\ \Gamma_{21} & \Gamma_{22} & \Gamma_{23} \\ \Gamma_{31} & \Gamma_{32} & \Gamma_{33} \\ \Gamma_{41} & \Gamma_{42} & \Gamma_{43} \end{bmatrix}}_{\bar{\Gamma}_1} \underbrace{\begin{bmatrix} \delta Y_1 \\ \delta Y_2 \\ \delta Y_3 \end{bmatrix}}_{\bar{Y}} + \underbrace{\begin{bmatrix} \gamma_{11} & \gamma_{12} & \gamma_{13} \\ \gamma_{21} & \gamma_{22} & \gamma_{23} \\ \gamma_{31} & \gamma_{32} & \gamma_{33} \\ \gamma_{41} & \gamma_{42} & \gamma_{43} \end{bmatrix}}_{\bar{\gamma}_1} \underbrace{\begin{bmatrix} \delta V_1 \\ \delta V_2 \\ \delta V_3 \end{bmatrix}}_{\bar{V}} + I\delta\dot{B} = \underbrace{\begin{bmatrix} \delta\dot{R}_1 \\ \delta\dot{R}_2 \\ \delta\dot{R}_3 \\ \delta\dot{R}_4 \end{bmatrix}}_{\dot{\bar{R}}} \tag{7}$$

$$\Gamma_{ij} = \frac{1}{r_i}\left[(V_j - \dot{X}_{ij}) - \gamma_{ij}\dot{r}_i\right] \tag{8}$$

Steady-state measurement errors in the system couple into $\Delta\dot{\bar{Y}}$ as shown in Eq. (5) above. This in turn couples into range rate via Eq. (7). During the area navigation tests, $\dot{X}_{ij} = 0$, and the relative magnitudes of the quantities in Eq. (8) make

$$\Gamma_{ij\,max} \simeq 0.02 \quad \text{for all i and j}$$

which are negligible.

During the ILS flights, however, the user-to-transmitter distances are much smaller than in area navigation. In addition the fourth transmitter is in a tethered balloon making $\dot{X}_{4j} \neq 0$ and the coupling between steady-state range and range rate errors is no longer negligibly small. The relative magnitudes of Γi_j in this case are:

$$\max[\Gamma_{1j} \simeq \Gamma_{2j} \simeq \Gamma_{3j}] \simeq 0.1$$

$$\Gamma_{4j\,max} = \frac{V_j - \dot{X}_{4j}}{r_4} \simeq 0.2$$

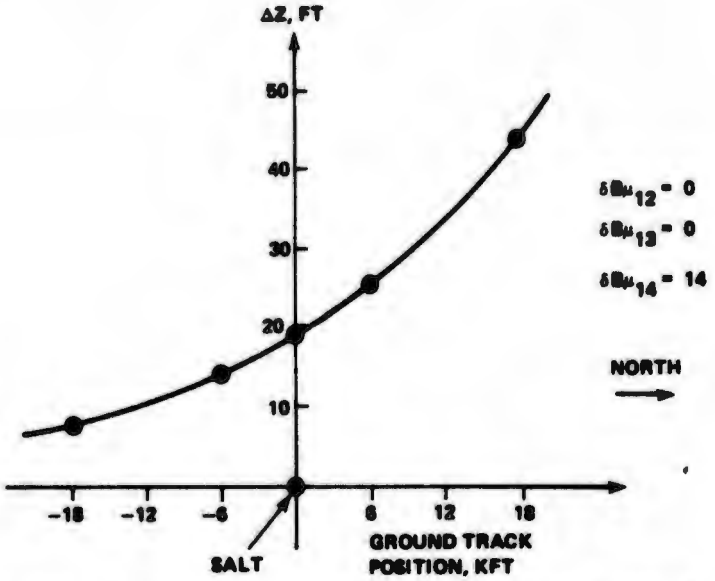

Figure 4-9. The Effect of Interchannel Bias Residuals on Z-Coordinate

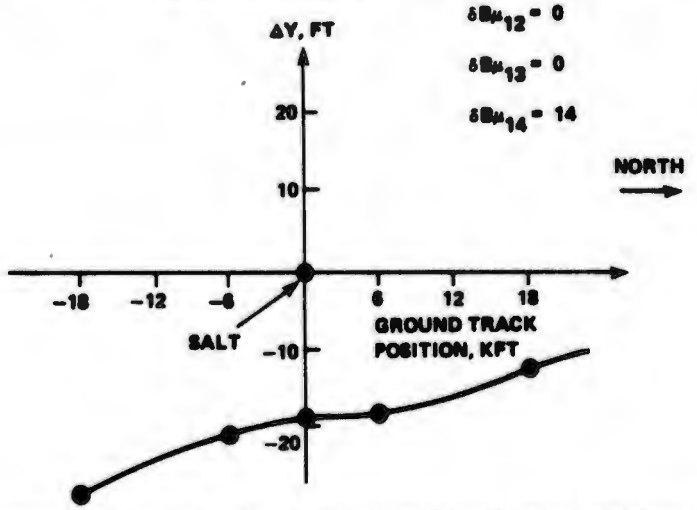

Figure 4-10. The Effect of Interchannel Bias Residuals on Y-Coordinate

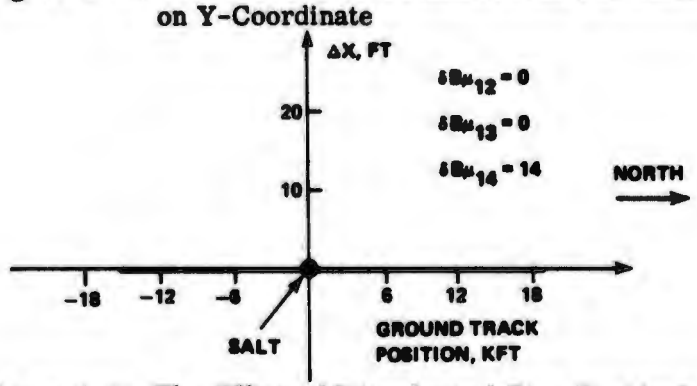

Figure 4-11 The Effect of Interchannel Bias Residuals on X-Coordinate

During the ILS flights, great care was exercised to eliminate steady-state range bias errors. As a matter of fact, the ILS flight solution domain residuals do not exhibit strong bias trends. Hence the position to range rate coupling, if any, is very small and is not discernible in the data.

It is interesting to note at this point, that in an actual system the contribution of Γi_j is practically zero since the r_i's are very large in a satellite-to-user geometry.

4.2.1 Ground Calibration System Errors

The calibration link is defined as the signal path from the transmitters to the calibration receiver located at the MCS site. The effective signal path length, expressed as a propagation time in nanoseconds, had to be precisely measured to obtain the necessary constants used in the calculation of the navigation solution (see Section 3.1). The radiated signal path portion of the calibration link was measured with the ground components of the test system stabilized by two cesium beam frequency standards. These measured path lengths were combined with the rf cable path length measurements to establish the total calibration link delay quantities used in the navigation algorithm. Cable propagation time delays were measured by a substitution technique in the rf link, and also with a time domain reflectometer.

Conceptually, the 621B system can be used to measure rf signal delay by adding the link to be measured to an existing link between the transmitter output and the receiver input, and noting the change in coarse and fine range readings obtained from the combination of the two links from the readings obtained before the link addition. The change in readings represents the additional signal propagation time from transmitter to receiver as a result of the additive link. This measurement technique is called "substitution." In practice, there are two basic problems that must be solved. One problem is that the receiver and transmitter frequency sources are not phase locked. Thus the receiver and transmitter are, in effect, drifting relative to each other and the link path length appears to be changing. This deficiency introduces an uncontrollable, unknown error which must be eliminated to obtain path length measurement accuracies on the order of 1 nanosec. Fundamentally this deficiency can be corrected by using one oscillator to drive both the receiver and transmitter. (All frequencies and timing are derived from one 5 MHz. oscillator within the receiver. This is also true for the transmitter.) In practice, however, one 5 MHz oscillator cannot be used because there are a few miles between the ends of the link of interest. Thus, two accurate and stable oscillators are required, one each for the transmitter and the receiver. The basic requirement on these two separate oscillators is that they be equivalent to two phase-locked oscillators.

The other basic problem is that the normal coarse range output of the receiver is unusable (without some form of computer data processing) because it is not referenced to a fixed time in the stored code period. This is resolved by using the signal from the receiver self-test code generation circuitry to initiate an external counter operating at the code rate (10 MHz), and a signal from the code tracking loop to stop the counter at a time related to the time of receiving the transmitted signal. This implementation provides a method of obtaining a coarse range without resorting to computer processing. This coarse range count method requires that the self-test code be employed for the delay measurements.

The resulting test set-up is shown in Figure 4-12. The two stable, accurate oscillators are Hewlett Packard portable cesium beam frequency standards. The coarse range count is obtained by using an external counter that is gated as described

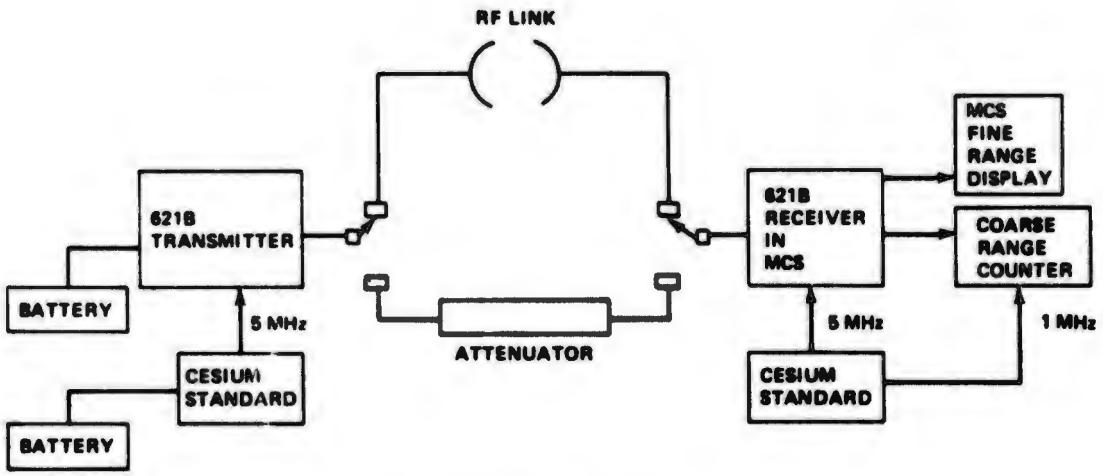

Figure 4-12 Link Delay Measurement Setup

above. In addition the 10 MHz clock in the counter is derived from the same cesium standard which is used to drive the receiver thus insuring that the counter and receiver are synchronized. The attenuator in the rf direct connection is adjusted to establish the same signal level at the receiver for both the reference and link measurements. This equalization eliminates possible path length measurement errors resulting from receiver signal processing sensitivity to signal amplitude.

A reading is obtained from the equipment by combining the coarse range count established on the external counter with a fine range count available from the receiver (see Figure 4-13). The coarse range count interval (10 MHz) is equivalent to 100 nanosec of range delay. The fine range count resolves the coarse range to 0.5 nanosec making precise readings possible.

The procedure used during the test program to perform the rf link path length measurement by the substitution technique can be described by reference to the configuration shown in Figure 4-12. The transmitter and receiver are directly connected to obtain a reference reading. The transmitter and its cesium standard are then transported, while operating continuously, to the other end of the link to be measured and another reading is obtained at the calibration receiver.

Basically the delay in the link is the difference between the two readings. However, there is a relative change in phase between the two oscillators because they are not phase locked, and because there is a substantial amount of time required to travel between the ends of the link to be measured. To account for this, another reference reading is obtained by transporting the cesium standard and transmitter back to the receiver, and connecting the two together directly again. A single reference value is then obtained by interpolating the two reference readings to the time of measurement at the other end of the link. A straight line interpolation is used (an acceptable method as will be shown later in the analysis of error sources). The interpolated value is then subtracted from the reading obtained over the link. This difference value is the path length of all components included in the link measurement. Signal path length values determined by this technique are referred to as "cesium measurements".

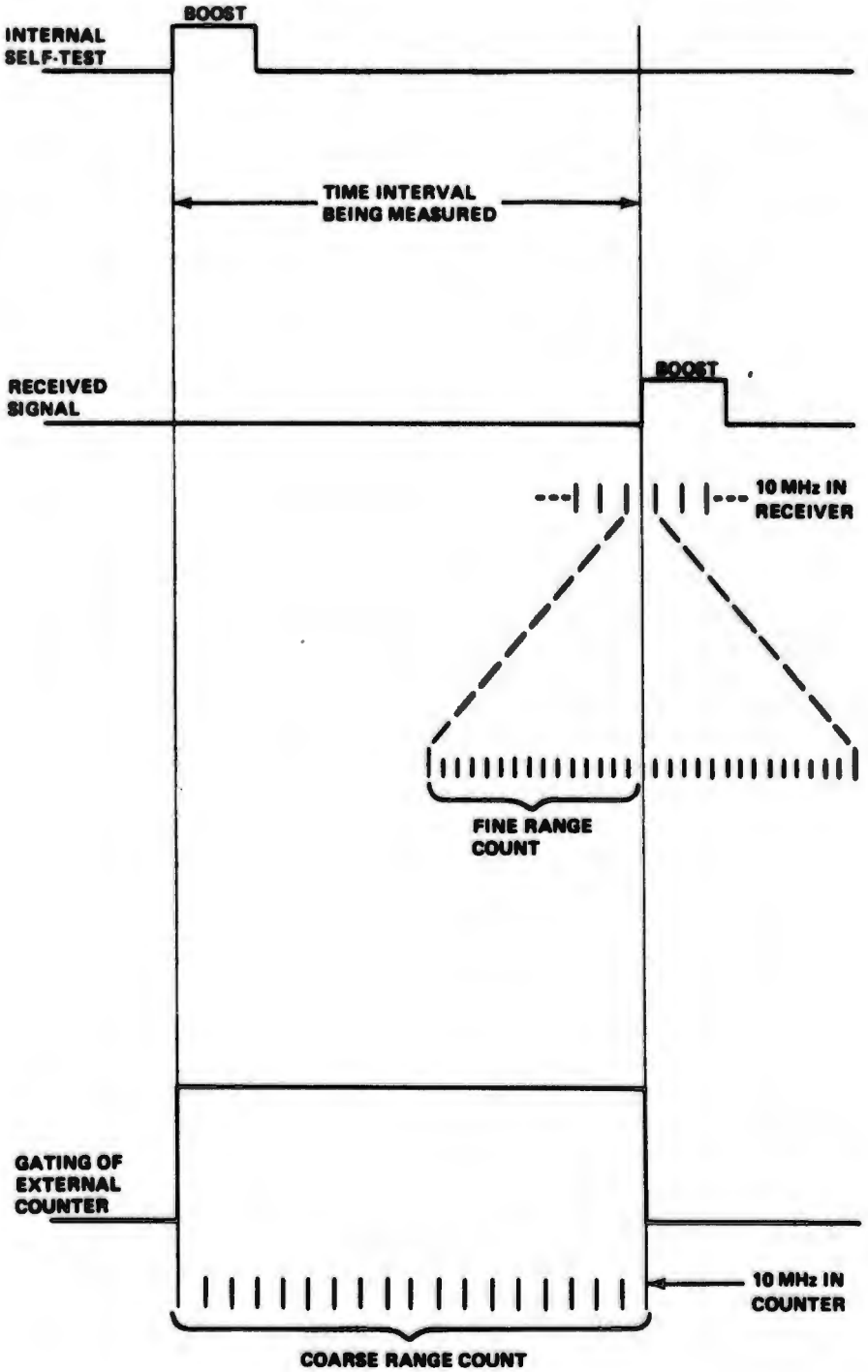

Figure 4-13 Cesium Test Coarse and Fine Range Measurement

The cesium measurements for the A uplink antenna-to-MCS path are tabulated in Table 4-3. Included are the link loss recorded during the cesium test, the number of measurements in the data set, and the 95% confidence range. This range is determined by using the students-t distribution for small samples, and is comparable to the $\pm 2\sigma$ range for large samples.

Table 4-3 Cesium Delay Measurements "A" Uplink to MSC

Link	Date, 1972	Delay[4] Nanosec	95% Range	Link Loss, db	No.[3] of Measurements
SC-50	(1) 6/9	22417.6		94	1
	6/8,9	33.6	± 2.3	97	11 (S)
	10/17	27.3	± 2.8	96	7
	10/18	27.9	± 1.8	95	8
	(2)11/15	24.9	± 1.5	93	6
WC-50	(1) 6/10	32387.8		Varying	1
	6/12	84.2	± 3.0	117	4
	7/21	88.8	± 3.9	90	3
	(2) 11/10	78.2	± 3.9	98	6
SALT	(1) 6/10	7330.0	± 8.1	Varying	3
	6/12	37.5	± 1.7	91	5
	7/10	34.6	± 0.8	90	7
	7/11	35.8	± 0.8	90	10
	7/12	36.9	± 0.5	90	8
	10/31	37.8	± 0.6	91	8
	(2)11/13	30.7	± 1.9	90	7
EC-50	(1) 6/9	18156.9	± 2.1	96	5
	7/14	58.0	± 1.1	98	4
	7/17	57.9	± 2.2	98	8
	7/18	58.1	± 1.5	99	10
	7/20	58.9	± 1.2	99	3

Notes:

(1) Field measurements excluded the transmitter Spiroline. Data was corrected for transmitter Spiroline delay and loss.

(2) For field measurements the transmitter Spiroline was replaced by a 65 ft RG-214 cable. Data was corrected for test cable and transmitter Spiroline delay and loss. Fine range readings contained excessive variations of 13 nanosec. Typical data has 2 nanosec.

(3) Listed is the number of drift corrected measurements, except those marked (S) are simple differences.

(4) The delay includes transmitter and MCS Spiroline, and the uplink antenna flex cable.

From a cesium measurement precision standpoint, the delays in data sets marked (1) and (2) are less accurate than the other data. Two sets of the (1) type are the result of a single measurement and a third was taken under unexplained varying signal level conditions. The type (2) data sets consisted of fine range readings with excessive, unexplained variations. These variations were much larger than those expected from the characteristics of the cesium oscillators and are considered to be due to either an undetected receiver malfunction or to an instability in the external amplifier used to boost the cesium standard's frequency output to match the signal drive required by the receiver.

Substantial variations in the path length measurements are present in all except the EC-50 data. The SC-50 data and most of the SALT data show a consistent link loss which eliminates the likelihood that link multipath changes are the source of the problem. The WC-50 data show a widely varying link loss indicating that the delay changes may be due to link multipath changes. However, it is believed that the varying link loss was the result of a poor connection. Furthermore, the envelope detector (see Volume II, Section 3.3.3) when used with the transmitting dish antenna, indicated the complete absence of multipath on WC-50.

The link delay is plotted versus time in Figure 4-14. The probable cause of the delay variations is the presence of mismatched conditions which produce apparent changes in the link delay when the cable configuration is changed. These mismatches may be occurring at one or both ends of the link. Under these conditions a change in the cable between the uplink antenna and the test transmitter, or, a change in the cable between the MCS Spiroline and the receiver input, could each produce a different result in the cesium delay measurements. This conclusion is supported by the June data in Figure 4-14 which shows a significant change in delay for data with different transmitter cable configurations. For example, the June SC-50 data obtained from two different cable configurations show a change of 16 nanosec. The November data also show a substantial change in delay for a different transmitter cable configuration. Salt Site shows a change of 7 nanosec between the October and November data, and, WC-50 shows a change of 10.5 nanosec between the July and November data, all representing different cable configurations as the only variable. The conclusion is also supported by the small delay variations within a cluster of data. Each cluster was measured with the same cable configuration and reveals the excellent repeatibility which can be obtained of the basic cesium measurement technique. The clusters are the July Salt Site data (three sets), the July EC-50 data (four sets), and the October SC-50 data (two sets).

This effect may produce variations in the measured link delays while the actual delays from the uplink antenna input to the MCS remain constant. Under these conditions the true monitor link delays are not accurately determined by the cesium tests.

An analysis of flight results from flights 17-23 indicates that for the A uplink antenna-to-MCS path, the June type 1 measurements most accurately reflect the actual path length. This conclusion is obtained from the following argument.

Flights 17-20 used the A uplink antenna-to-MCS configuration at all sites. An analysis of the navigation solution trajectory from these flights compared to the WSMR reference trajectory was conducted along the lines discussed in Section 4.2. The errors in the navigator trajectory were converted into errors on the line-of-sight between the aircraft and transmitters, i.e. into steady state errors in range (measurement domain). This analysis showed that the range (or pseudo range since the terms are used interchangeably here) errors referred to channel 4 were:

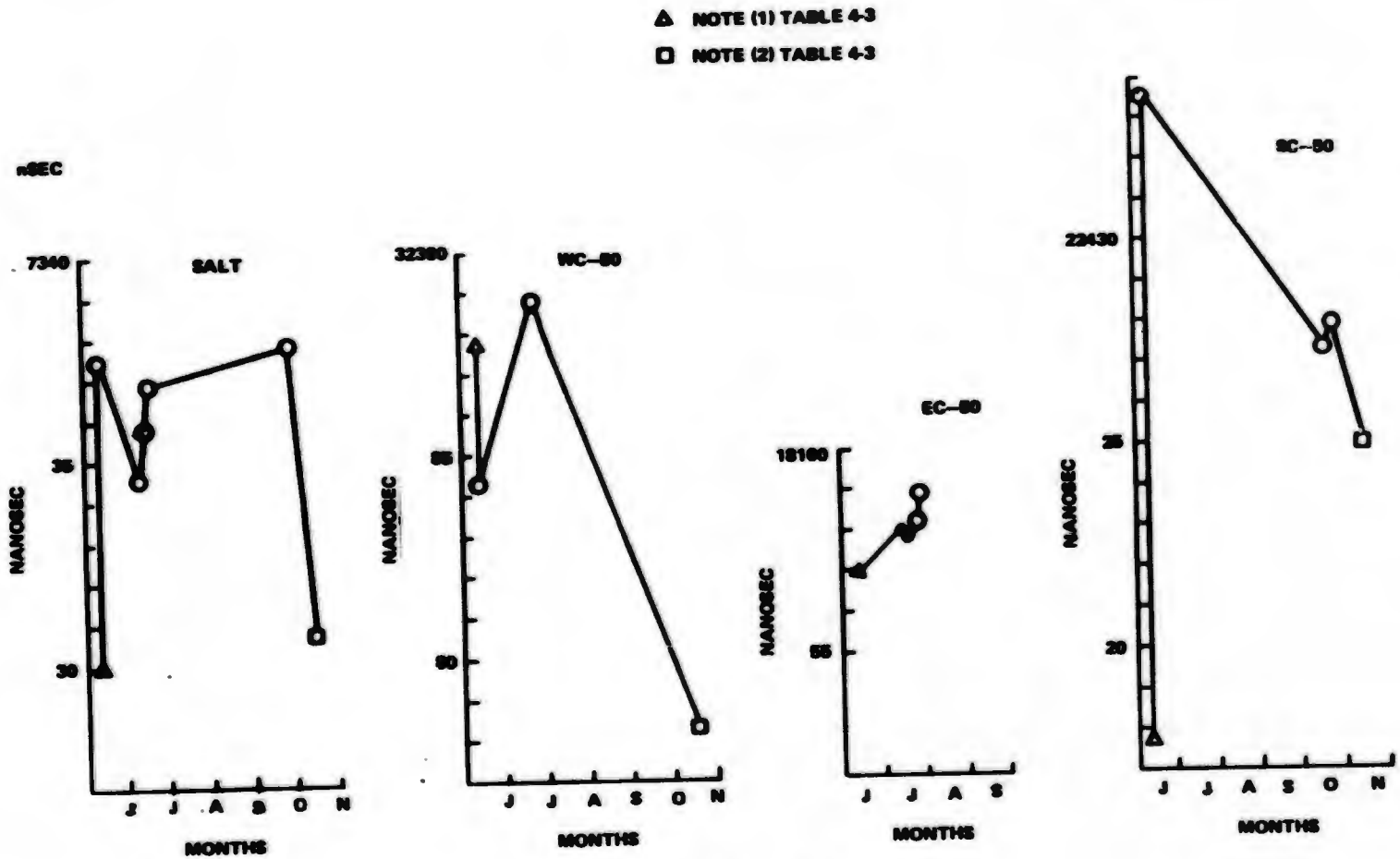

Figure 4-14 A Uplink to MCS Delays vs Time

$$R_{1-4} = -14.0 \text{ ft}$$
$$R_{2-4} = -14.2 \text{ ft}$$
$$R_{3-4} = -14.4 \text{ ft}$$

This can be interpreted two ways. Either channels 1, 2 and 3 are essentially error free, and channel 4 has approximately 14 ft of steady-state errors or the errors are distributed among the channels in such a way to make it appear as if channel 4 contains all the error. There are other techniques available for analyzing these errors, but none of them can definitively distribute the errors properly among the channels and therefore do not resolve which of the two interpretations are correct. The cesium measurements used to produce the trajectories of flights 17-20 (giving the errors shown above) correspond with the average value of the data given in Table 4-3 excluding type (1) data, which was obtained at the time of these flights; June and July. Thus the cesium measurements used in determining these solutions were:

Ground Link	Cesium Test Measurement, Nanosec
Salt (Ch. 1)	7336.1
WC-50 (Ch. 2)	32386.2
EC-50 (Ch. 3)	18158.2
SC-50 (Ch. 4)	22433.6

Including the data from flights 22 and 23 with data from 17-20 makes it possible to resolve which of the interpretations of the error given above are correct. Flight 22 used only the B uplink antenna-to-MCS configuration at all sites (see Appendix C for cesium measurements of the various ground site configurations). The trajectory analysis for this flight showed the following system range errors:

$$R_{1-4} = -1.0 \text{ ft}$$
$$R_{2-4} = 8.0 \text{ ft}$$
$$R_{3-4} = 0.5 \text{ ft}$$

Flight 23 used D uplink antenna-to-MCS signal paths on channels 2 and 3, and A uplink antenna-to-MCS configurations on channels 1 and 4. The range errors computed for these flights were

$$R_{1-4} = -19.5 \text{ ft}$$
$$R_{2-4} = -14.5 \text{ ft}$$
$$R_{3-4} = -24.0 \text{ ft}$$

Each antenna configuration, A, B and D has an associated path length measurement obtained from the cesium beam substitution technique. By rearranging the presentation of system range errors from flights 17-23, Table 4-4 is obtained. The range errors are strongly related to the antenna configuration at channel 4. In addition, flight 23, which antennas at channels 2 and 3 (D path) lengths) does not eliminate the apparent 14 ft error in channel 4. Therefore, the conclusion is that the hypothesis of the errors being distributed among all the channels is not the right one, since if this were the case, Flight 23 having different links on channel 2 and 3 should change the distribution. Flight 22, on the other hand, produces a new channel 4 path measurement for the B configuration, which does remove the 14 ft error. The error has, therefore, been localized to the channel 4 A uplink antenna-to-MCS path length measurement.

Reexamining the cesium measurements for the channel 4 A path in Figure 4-14 we see that the type (1) measurement in June was 22417.6 nanosec compared to the average of non-type (1) June measurements which was 22433.6 nanosec, a difference of 16 nanosec. Using the type (1) measurement at channel 4 will eliminate the bulk of the 14 ft error. Also, using the type (1) measurements at the other sites will not materially alter the values already used in the solution, a desirable result since our trajectory analysis showed these channels were essentially error free already.

Table 4-4 System Range Errors From Flights 17-23 Related to the Channel 4 Antenna Configurations

System Range Errors Computed from a Trajectory Analysis	Antenna Configuration at Channel 4, SC-50	
	A	B
ΔR_{1-4}, ft	-14.0, -19.5	-1.0
ΔR_{2-4}, ft	-14.2, -14.5	8.0
ΔR_{3-4}, ft	-14.4, -24.0	0.5

4.2.1.1 Error Sources in Calibration Link Measurements

System Noise

The fine range reading is perturbed by overall system noise. The noise is estimated at $\sigma = 0.2$ nanosec for the average of ten readings as used in the cesium tests. The estimate is computed from fine range data obtained during the cesium tests.

Differences in Cesium Frequency Standards

The cesium beam frequency standards are not phase locked together for the link measurement. The mean fine range is perturbed by variations in the difference between the two cesium frequency standards. Analysis of laboratory test data obtained with the two cesium standards used in making the link measurements indicates that the difference contains both random error and long term drift (see Figure 4-15). The random error in each reading has $\sigma_{cr} = 2.3$ nanosec. A drift correction process which calibrates the difference in the two cesiums before and after each link measurement eliminates the bias error.

A key consideration in determining the accuracy available from the cesium link measurements concerns the accuracy in the estimate of the drift between the two cesiums at the time of link measurement. As can be seen from Figure 4-15, the drift of the two cesiums is not constant. At the time the cesiums are effectively hooked together by directly connecting the receiver and transmitter, an accurate measure of the offset between the cesium oscillator phases can be obtained. This procedure enables a calibration of the drift between the two cesiums before and after the link measurement.

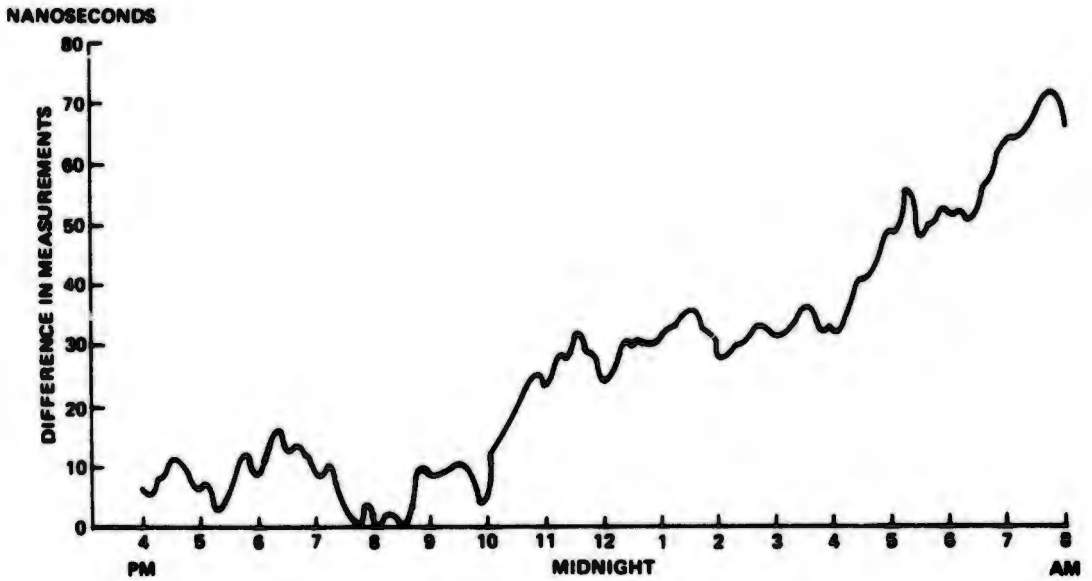

Figure 4-15 Cesium Lab Data December 14 and 15, 1971

A variety of techniques were studied to determine the most effective estimation procedure. It was found that a linear interpolation of the calibration points to the time of the link measurement gave the most accurate estimate of the value of cesium oscillator phase offset. The estimate $\hat{\phi}_1$, of the cesium oscillator phase offset, ϕ_1, is

$$\hat{\phi}_1 = \phi_1 + \frac{t_1 - t_1}{\Delta t} \Delta\phi$$

$$\Delta\phi = \phi_2 - \phi_1$$

$$\Delta t = t_2 - t_1$$

where ϕ_1, ϕ_2 - are the cesium oscillator phases at the calibration points (transmitter and receiver hooked directly together)

t_1, t_2 - are the calibration point times

$\hat{\phi}_i, t_i$ - is the estimated cesium oscillator phase offset at the time of link measurement (t_i) which always occurs between t_1 and t_2

The accuracy of this estimate was studied using a phase drift history obtained in the laboratory by connecting the two cesium beam frequency standards, used for the field testing, together and recording the relative phase drift over a period of 16 hours. This phase history is shown in Figure 4-15. The estimation error, $\epsilon\phi_i$ was dedermined by computing the difference between the oscillator phase offset and the linearly interpolated phase offset at 15-minute intervals.

$$\epsilon\phi_i = \phi_i - \hat{\phi}_i$$

The 15-minute intervals represent a typical travel time in the actual field test between the calibration readings at the MCS (ϕ_1, ϕ_2) and the readings at the other end of the link to be measured. Figure 4-16 shows the generalized technique for obtaining the phase offset estimation error. The rms value of $\epsilon\phi_i$ computed from the laboratory test data is 2.5 nanosec. The measurement error was decreased by averaging 8 to 10 readings of ϕ_i. Therefore, the rms value of the average estimation error, $\bar{\epsilon}\phi_i$,

$$\bar{\epsilon}\phi_i = \frac{1}{n}\sum_n \epsilon\phi_i \quad \text{is 0.8 nanosec.}$$

Occasionally, problems occurred during the field tests which made it impossible to calibrate the cesium oscillator phase offsets both before and after the link measurement. Only one of the calibration values, ϕ_1 or ϕ_2, was available. Thus the linear interpolation scheme could not be applied. Under these conditions, a simple difference was used to estimate the link measurement.

The normal link measurement was determined by

$$\hat{D} = \beta - \bar{\hat{\phi}}_i$$

where: β is the reading obtained at the receiver when the transmitter is at the other end of the link (true length = D) to be measured, $\beta = D + \phi_i$

$\bar{\hat{\phi}}_i$ is the averaged value of the linearly interpolated oscillator phase offset

When one of the calibration readings was not available the link measurement was determined by

$$\hat{D} = \beta - \phi_1$$

or

$$\hat{D} = (D + \phi_i) - \phi_1$$

The laboratory data (Figure 4-15) was examined to determine the error in estimating ϕ_i by using the value ϕ_1, $\delta\phi_i = \phi_i - \phi_1$. By employing the same 15-minute intervals used in the previous analysis, the rms value of $\delta\phi_i$ was found to be

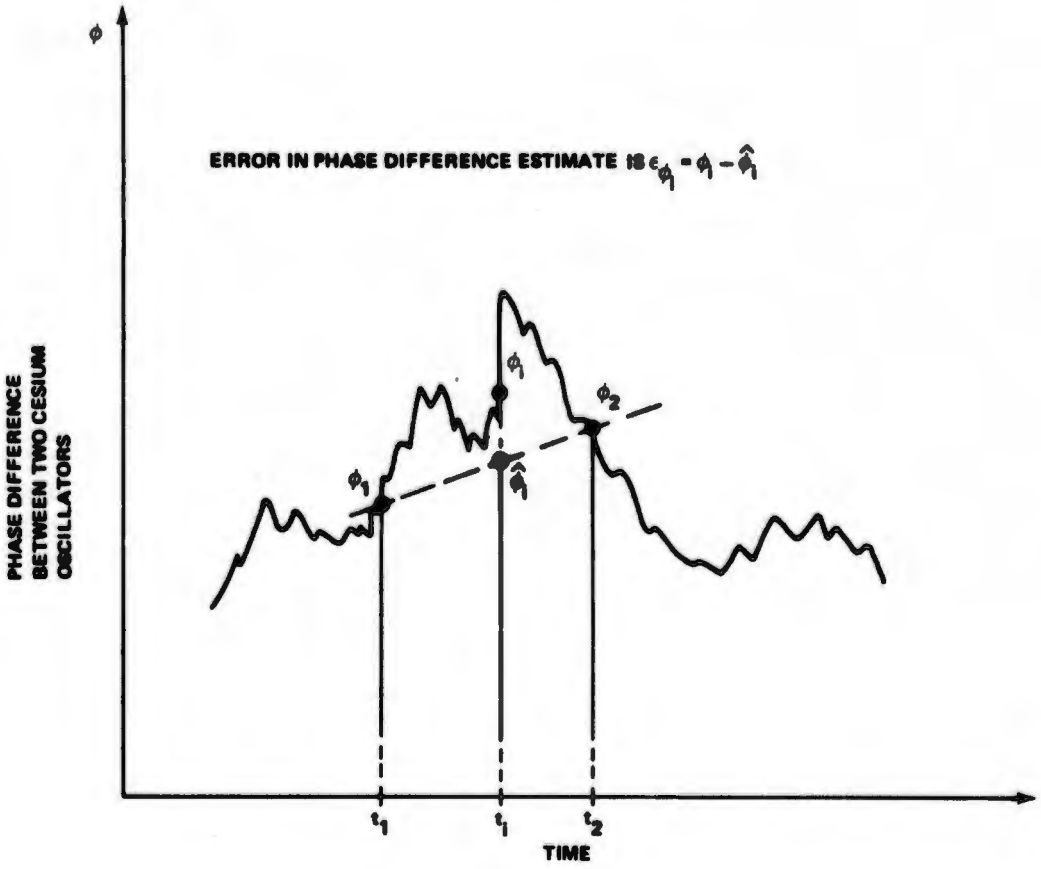

Figure 4-16 Linear Interpolation of Cesium Measurement

4.3 nanosec. Thus this technique causes errors about twice as large as the linear interpolation scheme.

Circuitry Variations

The mean fine range may be perturbed by variations in the transmitter and receiver circuitry. The high-frequency aspects of this source are included, above, in overall system noise, and bias errors would be eliminated by the drift correction process. However, this source may produce low frequency noise with an unknown error contribution.

Coarse Range

The potential error via one count jumping in coarse range is eliminated by selecting receiver/coarse counter cesium cables such that the leading edge of the coarse count gate is approximately midway between the 10 MHz clock pulses being counted. See Figure 4-16.

In addition, the ambiguity in coarse range count is resolved by establishing the fine range transition point prior to performing the cesium test. This is accomplished after setting up for a reference measurement by "free running" the crystal oscillator in the receiver cesium standard and observing the transition point, that is, the fine range count at which the coarse range changes by a count of one. This information was used to determine the correct value for the coarse range count during the cesium test.

Frequency Accuracy

The frequency accuracy of the cesium standards is $\pm 1 \times 10^{-11}$. Since the time interval being measured (Figure 4-16) has a maximum value of about 3 sec, the frequency accuracy translates to a measurement accuracy of $3 \times 1 \times 10^{-11}$ which is ± 0.03 nanosec, maximum.

External Error Sources

Since the 621B navigation solution employs measured calibration link delays, the characteristic by which an external error source is identified is its stability with time. That is, if all external elements exhibited the same constant characteristics during delay measurement and during flight tests, there would be no effect from external error sources.

Multipath

Changes in link multipath conditions may produce an apparent change in delay. Since the stability of multipath conditions is not known, the error contribution of multipath changes is unpredictable. However, during link delay measurements the link loss was constant within one or two decibels. Thus, it is unlikely that there were significant delay changes due to multipath.

Mismatch

The ground transmitter output, transmission line (cable, connectors) and antenna subsystem are designed to minimize reflections and prevent large bias errors from entering into range measurements. These errors should be calibrated out by

cesium measurements on the ground links. However, subsequent demating and mating of cables may produce an apparent change in delay. This effect was not evident in most of the field data since a given cable configuration produced perturbations for repeated measurements that were "expected" due to the cesium characteristics.

The calculation of the mismatch effect is based on the simple model shown in Figure 4-17. The initial signal, e_{f_2}, and the first outgoing reflected signal, e_{r_c} may be treated as the direct and reflected signals in the single-reflection multipath model (see Section 9.8.1). The reflection coefficient is related to the ratio of the signals, e_{r_c}/e_{f_2} and the differential delay is 2τ. This approach is valid for low VSWR's where the first reflected signal (e_{r_c}) is the only significant reflection.

The effective voltage reflection coefficient in this case becomes

$$R_e = \left(\frac{M-1}{M+1}\right)^2 a^2$$

where M = VSWR and a is the cable loss ratio. For two VSMR's of 4 ($M_1 = M_2 = 4$ in Figure 4-17 the maximum errors occur for cable delays of approximately $\tau = 50\ (1 \pm R_e)$, and with a cable loss of approximately 1db, $R_e = 0.285$. Therefore, the maximum error magnitudes occur at cable delays of 35 and 64 nanosec respectively which place the error at either the maximum of 14.2 nanosec, or the minimum of -14.2 nanosec on the error envelope (see Section 9.8.1). The above computations assumed that the cable loss remained unchanged. This is reasonable for the variety of cables used.

The cable configurations used in these tests, however, are generally changing from site-to-site since most of the test configurations employed permanently mounted cables at each site. Therefore, although an example has been given of the magnitude of measurement error which could occur due to a fault in a single cable typical of those used at WSMR, the actual situation is more complex. We conclude from the cesium measurements made with different cable configurations (Figure 4-14) and from an analysis of the flight data that there were mismatch conditions existing at various times during the testing which introduced errors as much as 16 nanosec into the measurements.

Atmospheric Conditions

Atmospheric effects are a function of temperature, pressure, and vapor pressure which are embodied in N, the refractive modulus (N = index of refraction x 10^6). The effect of a change in N is an increase in signal delay as N increases because of slower propagation velocities. The calibration link delays are affected by variations in N at ground level.

The surface variations at WSMR are presented in Ref. 39 which was prepared for this program by the staff meteorologist at HAFB. The minimum and maximum values of N are 224.08 (April) and 335.01 (July), respectively. Using ΔN=111 and multiplying by the free space delays produced the following maximum changes in nanosec; 0.8 for Salt, 3.6 for WC-50, 2.0 for EC-50, and 2.5 for SC-50.

The reference also presents the value of N, which was calculated from measured parameters, for flights 17-20. In addition, the value of N for each run during the flight is included. This data shows that for Flight 17 at EC-50, N decreased from

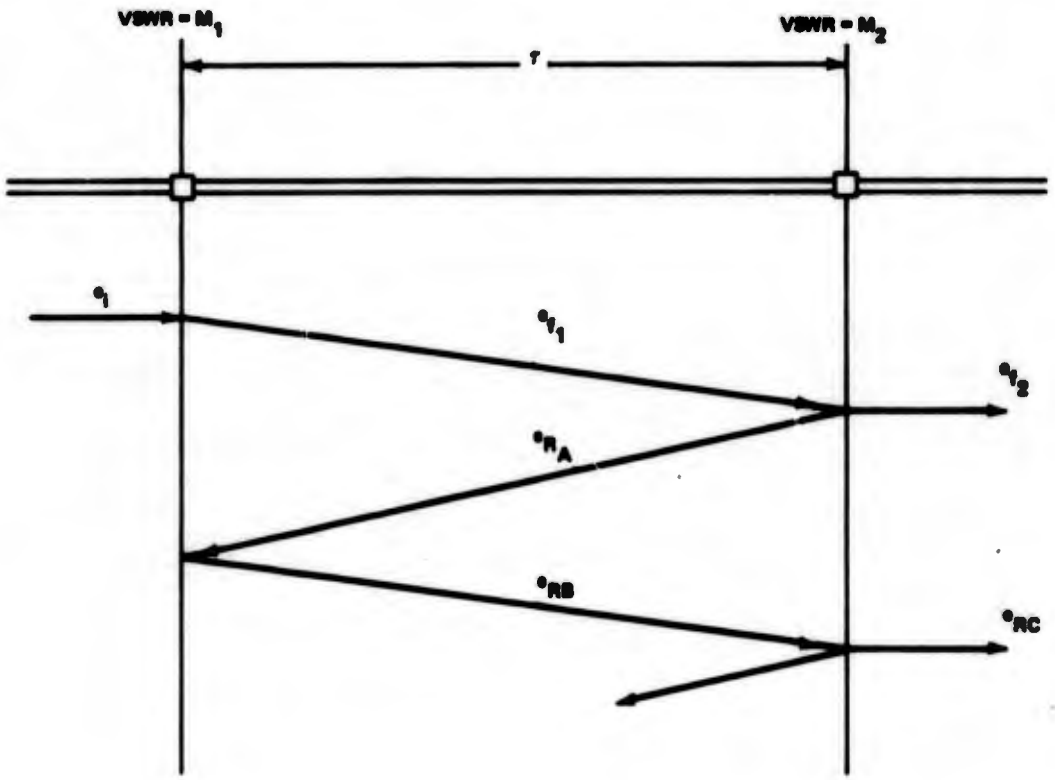

Figure 4-17 Cable Mismatch Effects Model

288.3 for run 1 to 280.1 for run 6, 50 minutes later. This translates to calibration link delay decreases of 0.06 nanosec for Salt, 0.26 for WC-50, 0.15 for EC-50, and 0.18 for SC-50. These data indicate that there may be a variation of a few tenths of a nanosec in actual link delay during the cesium measurements which take approximately two hours for each link.

Attenuators

The attenuators used to reduce the direct connected transmitter signal to the receiver were Narda Microline type 771. Each of these attenuators delays the 621B signal 0.22 nanosec. The variations with time are expected to be only a few percent, maximum, since the delays are fixed by the physical dimensions of the attenuators.

4.2.1.2 Cable Delay Measurement Error Sources

The cesium delay measurements could not fully define the total calibration path delays. The additional cable delay measurements necessary for a complete calibration were made by a cable substitution technique called rf substitution (which measures the delay at the operating frequency) and a time domain reflectometer (which measured delay using the step response which contains, essentially, all frequencies). Thus, two redundant sets of data were available for the short flexible cables at each transmitter and the calibration receiver (rf substitution and TDR). The Spiroline cables at each site (those cables permanently attached to the antenna-pole assembly) were measured with the TDR and by rf substitution and were also included in the cesium measurements.

High confidence Spiroline measurements were available from the redundant data sets. The resultant Spiroline delays are plotted versus time in Figures 4-18 and 4-19 These plots clearly demonstrate the stability of most of the Spiroline cables.

Comparative measurements revealed that cable delays by rf substitution were 2% greater than values obtained with the time domain reflectometer. For example, a 65-ft RG-214 cable measured by rf sbustitution exhibited 101.0 nanosec delay (average of 15 simple differences) while the delay was 99.0 nanosec when measured with the TDR. Since the rf substitution method measures delay at the operating frequency, its results (averaged over many data samples) were taken to be more accurate than the TDR. Thus, all TDR measurements are multiplied by 1.02.

RF Link Substitution

The basic measurement error in cable delay by substitution will be less than that for radiated link delay measurements because the time between readings is considerably shorter. For example, cesium lab data evaluation reveals an rms error of 0.8 nanosec for one minute between reference and measurement. This is about one-fifth of the rms error for the typical 15 minutes between reference and measurement encountered in the radiated link measurements. (The 15 minutes is required to transport the transmitter/cesium to the transmitter site.) Cable measurements may be accomplished in a shorter time since only a change in connection is required to introduce the cable into the measurement set-up. The remaining error sources in the substitution technique are essentially the same as those listed in the previous section for cesium measurements except for the potential effects of variations which are less because of the shorter time between readings.

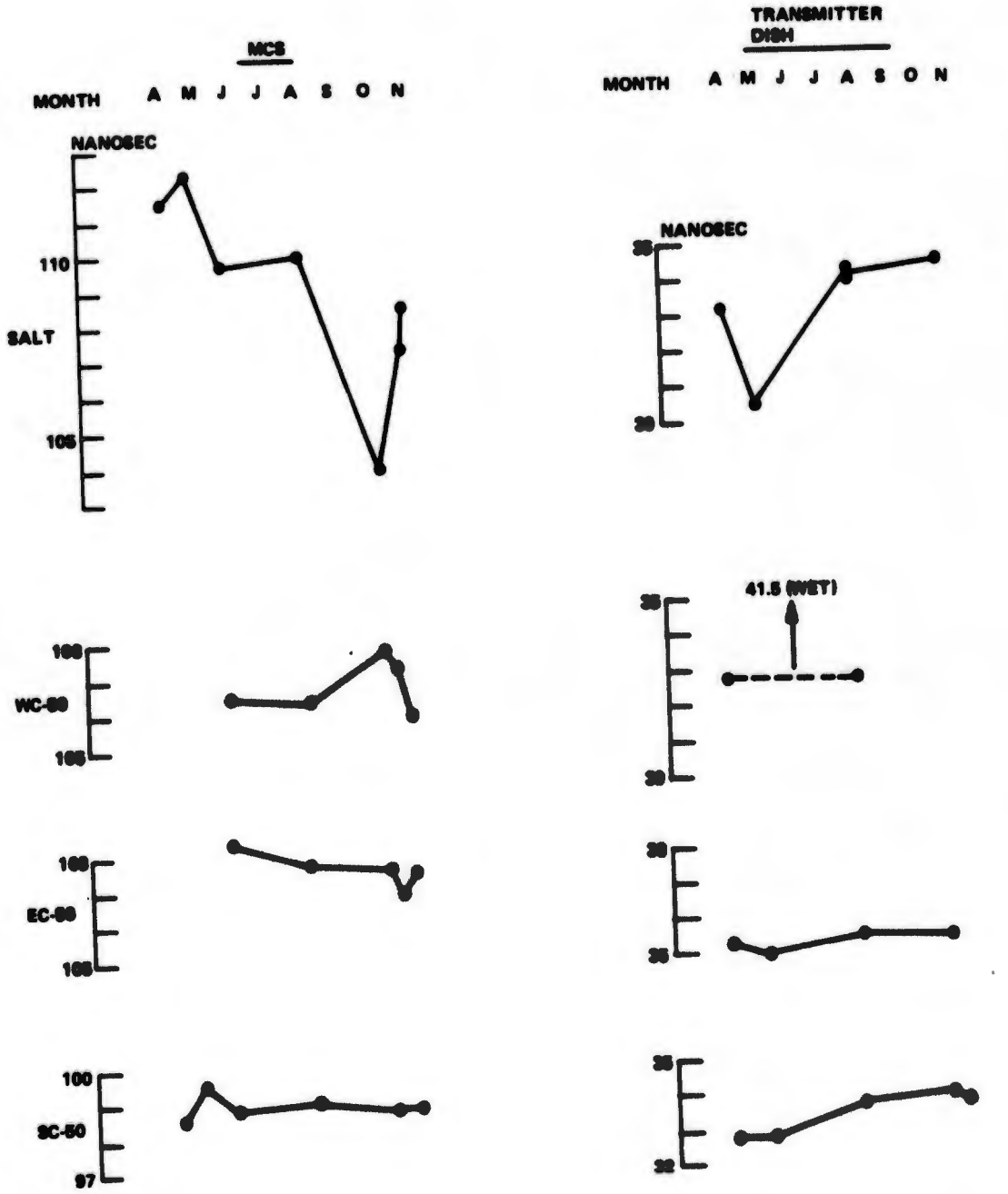

Figure 4-18 Measured Spiroline Delays

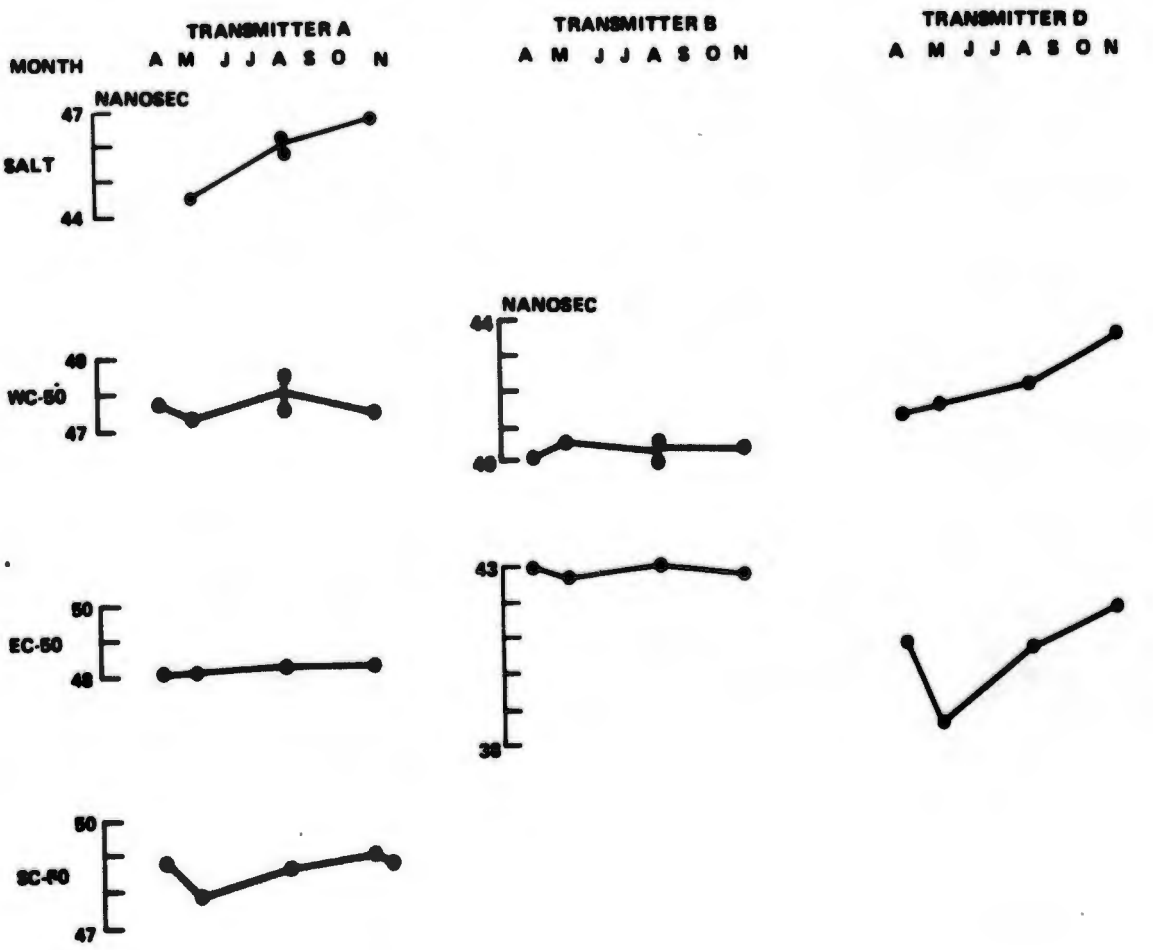

Figure 4-19 Measured Spiroline Delays

Some cable delay data was obtained by using the receiver generated self-test signal. In this case the two-cesium source of error (drift of the two oscillators) is eliminated because a separate transmitter is not employed. The self-test signal is generated in the receiver and derived from the receiver oscillator.

Hewlett Packard Time Domain Reflectometer Measurement Errors

An investigation of the TDR accuracies indicates ±1 nanosec tolerances should be applied to the measurements.

The data plotted in Figure 4-20 and 4-21 show the principal errors which could be expected by using various instrument settings for measurements. For cable measurements, a sweep speed by either 20 nanosec/cm or 50 nanosec/cm was used. All measurements were taken using the DETAIL position. As can be seen from Figure 4-20 there is no appreciable difference (less than 0.2 nanosec) in cable length measurements regardless of the settings of vertical deflection sensitivity, time magnifier, or the DETAIL/NORMAL controls. Using the NORMAL position increases the instability of readings slightly. Similarly the length error associated with sweep speed is insignificant as shown by the differences in Figure 4-20 (sweep speed = 20 nanosec/cm) and Figure 4-21 (sweep speed = 50 nanosec/cm). For the test cable used in these measurements, the length at 20 nanosec/cm is approximately 23.175 nanosec, while at 50 nanosec/cm is approximately 23.075 nanosec, an error of 0.100 nanosec which may be neglected for our purposes.

The measurement instability when using the NORMAL position (Figure 4-20 and 4-21) may be explained by the difficulty in determining the location of the cable ends as seen on the instrument as leading and trailing edges. Figure 4-22 shows data of the test cable leading edge measurement rise time (10% to 90% point) for worst case settings at 50 nanosec/cm. The edge is poorly defined in the NORMAL position, for most settings.

The predominant error in using the TDR is time measurement linearity. Figure 4-23 shows the linearity error for the instrument used during cable measurements made in November. The vertical error scale in nanoseconds applies to the majority of 621B measurements although some measurements were made at settings which increase the error by a factor of 2. As can be seen the error magnitude is variable depending upon actual cable length measured. However, we feel a tolerance of ± 1 nanosec can be safely used based on this data.

The TDR reference spot displayed on the oscilloscope which is used to make the time measurement was also investigated. The following table presents changes in the spot size as a function of instrument settings. This error appears small enough to disregard as long as the DETAIL setting is used.

HP TDR Reference Spot Size

Sweep Speed, Nanosec/Cm	Normal	Detail
20	0.72 ± 0.04 nanosec	0.06 ± 0.04 nanosec
50	1.8 ± 0.04 nanosec	0.15 ± 0.01 nanosec

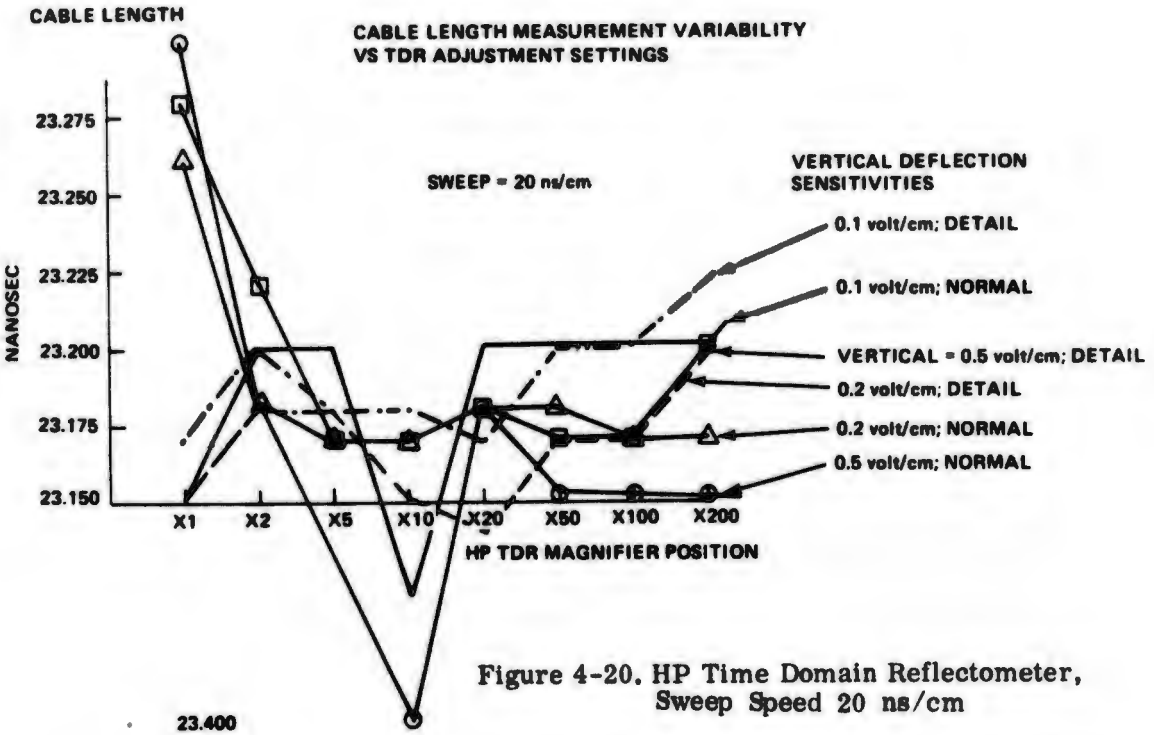

Figure 4-20. HP Time Domain Reflectometer, Sweep Speed 20 ns/cm

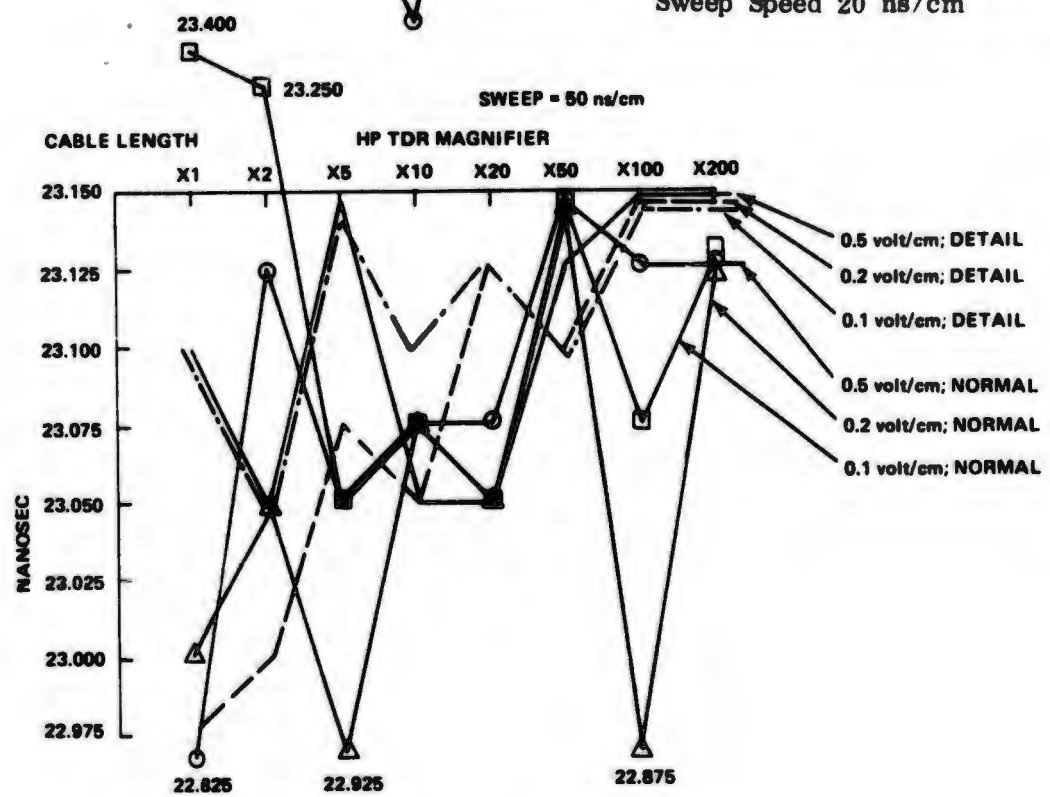

Figure 4-21 HP Time Domain Reflectometer, Sweep Speed 50 ns/cm

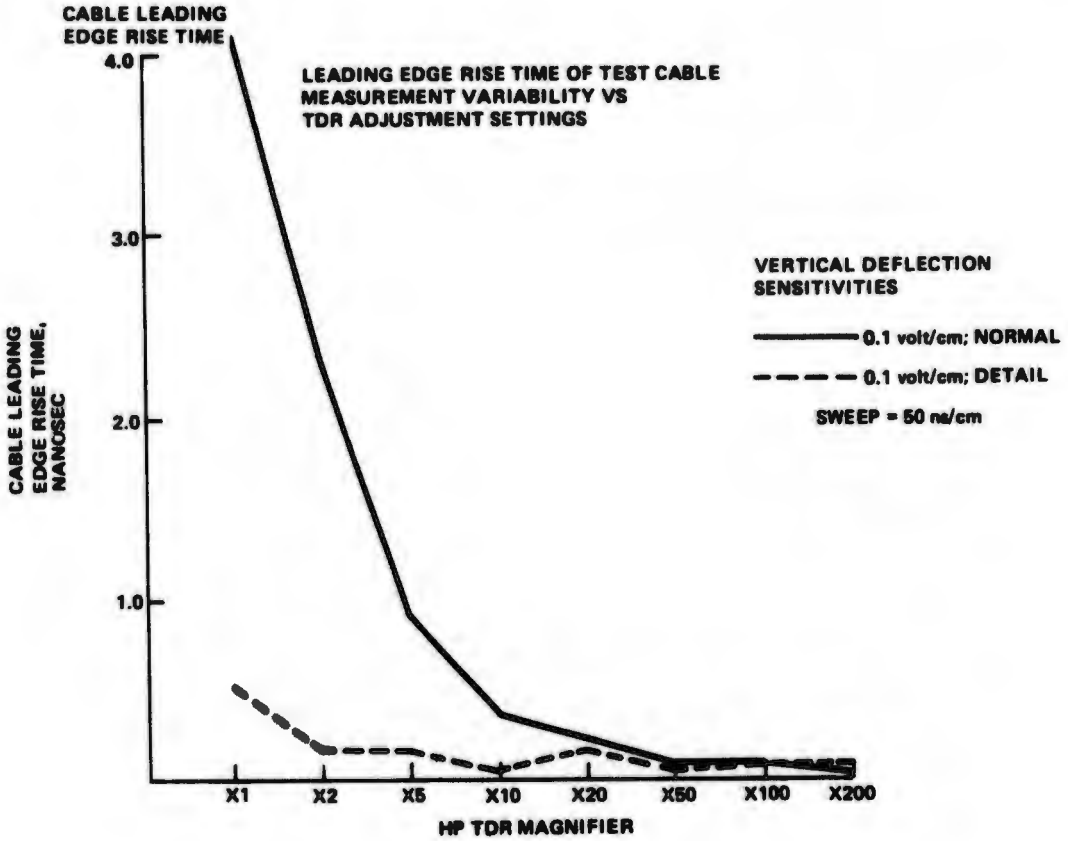

Figure 4-22 HP Time Domain Reflectometer

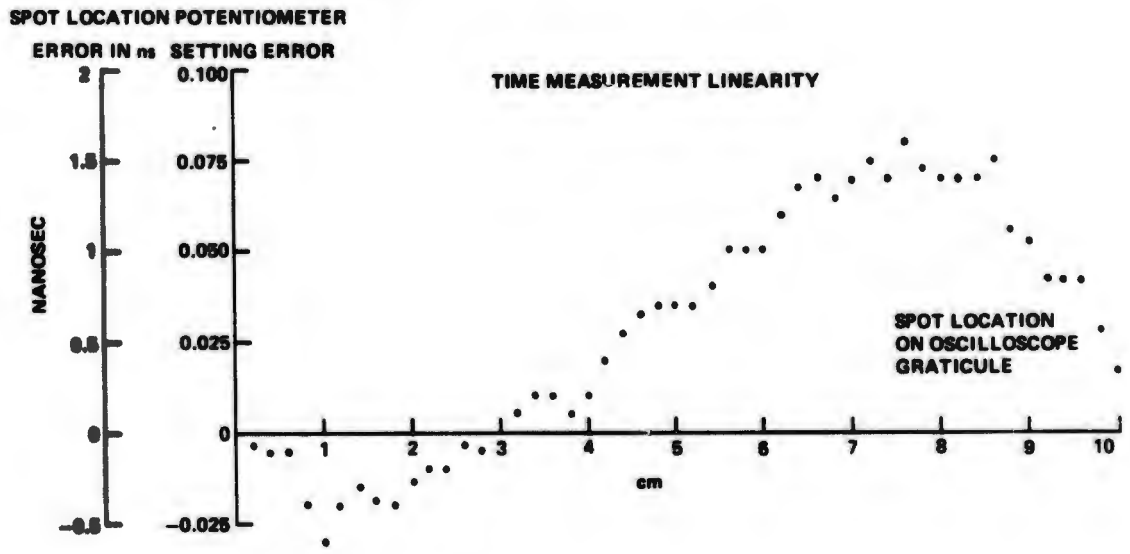

Figure 4-23 Time Measurement Linearity for HP Time Domain Reflectometer

Other settings such as time magnifier or vertical deflection sensitivity do not have any observable effect on spot size.

Moisture Effects

During May moisture was discovered in some of the Spiroline cables and a purging program was started in June. The cables were then purged prior to cesium link and cable delay measurements, and, prior to flight when time permitted. Most of the measured cable delays after May show good stability. The notable exception is the Salt Spiroline at the MCS. This cable is the only one that contains a multi-turn coil (see Figure 4-24).

The delay variations of the Salt Spiroline at the MCS may be the result of varying moisture content in the cable. Purging was not as effective for this cable as it was for other Spiroline cables. This may be related to the fact that the Salt MCS Spiroline is the only cable containing a multi-turn coil. Analysis of the flight data (see page 6-49) shows the error magnitude covered by the varying moisture content to be approximately 6 nanosec.

The Spiroline cable delays prior to June were variable to an unknown extent due to moisture content. This unknown makes the accuracy of the measured calibration link delays and Spiroline delays questionable with respect to any given flight for flights 1 through 15. This factor may have caused the "out-of-bounds" readings in the dish to dish cesium data since the readings all represented excessive delays.

Mechanical and Thermal Effects

The following cable delay variations are estimated on the basis of 120 ft of Spiroline and 20 ft of RG-214 in each calibration link. The temperature change is assumed to be 50°F. The temperature effect is 0.1 nanosec for Spiroline (25 ppm/°C) and 0.1 nanosec for RG-214 (100 ppm/°C). Flexing of RG-214 may cause delay changes up to 0.02 nanosec (500 ppm). There are no effects of humidity on RG-214.

Overall Performance of the Cesium Beam Measurement Technique

- 50-Mi Area
  - The capability of the cesium measurement method was not realized
  - There is a substantial uncertainty in the measured calibration link delays due to effects that were not a linear function of the length of the rf cable between the transmitter and the antenna. The uncertainty may be as high as ± 10 nanosec
  - Early cesium measurements (prior to June 1972) contained additional uncertainty due to time varying Spiroline cable delays resulting from moisture in the cables
  - The MCS Spiroline cable for the Salt link exhibited delay variations throughout the program

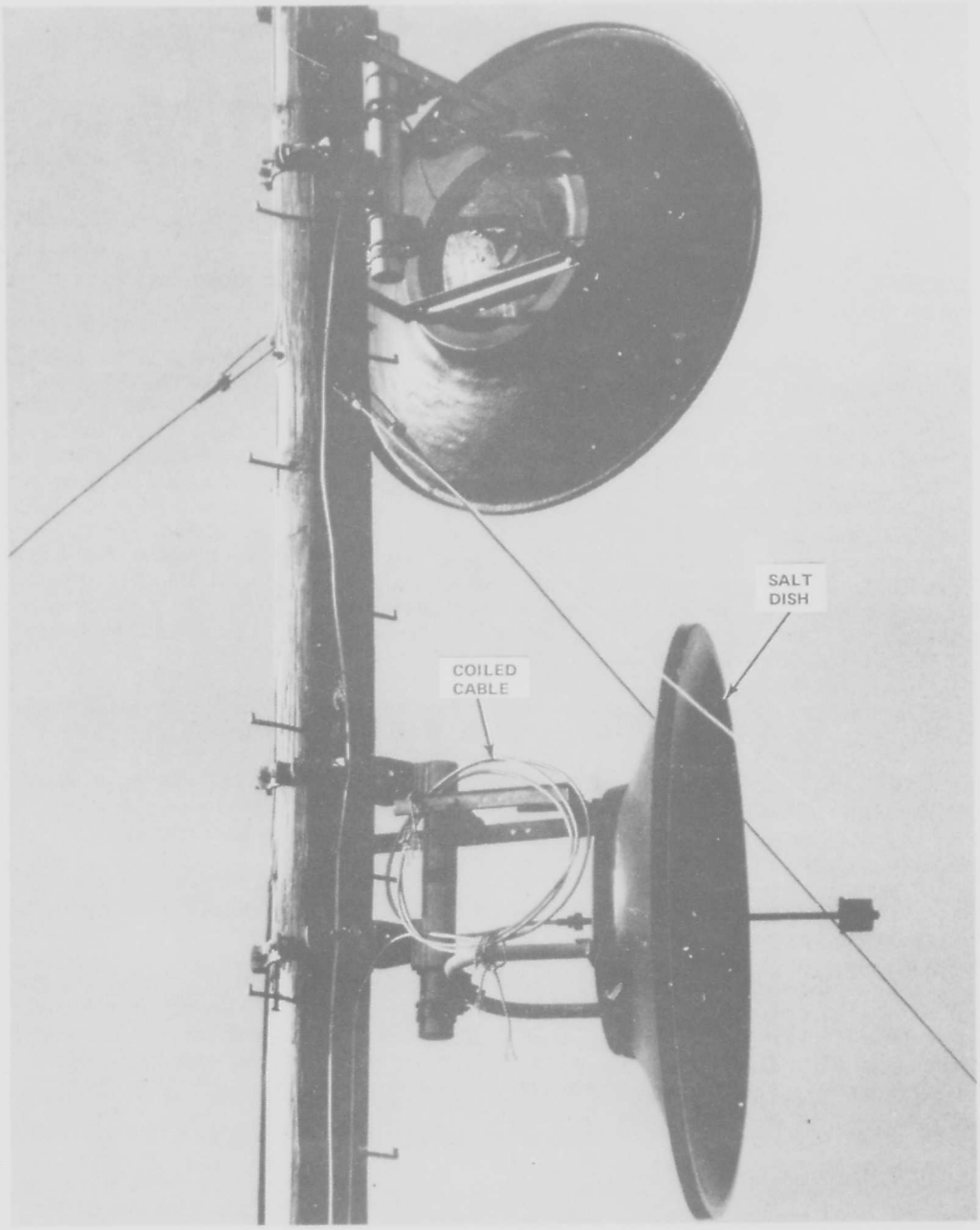

Figure 4-24 Salt Spiroline at MCS

- Northrop Strip - The capability of the cesium measurement method was realized

- General - The repeatibility potential of the cesium measurement method was demonstrated. The data show repeatibility within 1 nanosec when the measurements are made with the same cable configuration.

4.2.1.3 Uplink Antenna Delay Errors

The ground transmitting antenna arrays cause a distortion of the transmitted signals as a function of the antenna look angles. The distorted signal envelopes are perceived by the correlation receiver as apparent signal delays.

The relative delays of the uplink antennas were measured on an antenna range in Bethpage, New York during December 1972. The transmitting and receiving antennas were each mounted on towers at a height of 58 ft separated by 86 ft. The set-up is shown in Figure 4-25. The transmitter and receiver were operated in the self-test code, and both were operated from the 5 MHz source in the receiver to eliminate oscillator differences. The transmitter uplink signal was split to provide a hardwired reference signal to the receiver. Receiver channel 2 responds to the uplink antenna signal and channel 4 responds to the hardwired reference signal. The delay of the uplink antenna was obtained by measuring the phase difference between the channel 2 and 4 fine range outputs (50 KHz) on a two-channel oscilloscope. The fine range equivalent time base on the oscilloscope was 5 nanosec/cm and the jitter was averaged, visually, to obtain a reading to the nearest one-half nanosec. The jitter was approximately 2 nanosec peak-to-peak.

A single plane cut was made on each uplink antenna to measure the delay variation over the range of look angles equivalent to a flight path. Two flight paths were considered which extended from 50,000 ft north of Salt to 50,000 ft south of Salt. Both flight paths were oriented north-south and directly over Salt. One was at 30,000 ft AGL and the other at 18,000 ft AGL. The computed antenna angles are shown in Table 4-5 to the nearest degree. They are presented in terms of deviations from boresight with respect to compass directions at WSMR.

The measurement process was refined to minimize antenna range multipath and equipment drift.

Antenna range multipath was evident when comparing two sets of data from the same cut on an antenna, where the two data sets were obtained with different antenna orientations on the antenna range. One data set was obtained with the north side of the antenna o the right and the other set with the north side of the antenna to the left, when facing the transmitting antenna from the receiving tower.

Early tests were performed using an omni (aircraft) receiving antenna. The antenna range multipath was reduced considerably by changing to an RCP helix antenna with about a 40^{o} beamwidth. The remaining effects are minimized by averaging the two data sets and smoothing the curve. In much of the data the two sets are within 1 nanosec with occasional points separated by more than 2 nanosec.

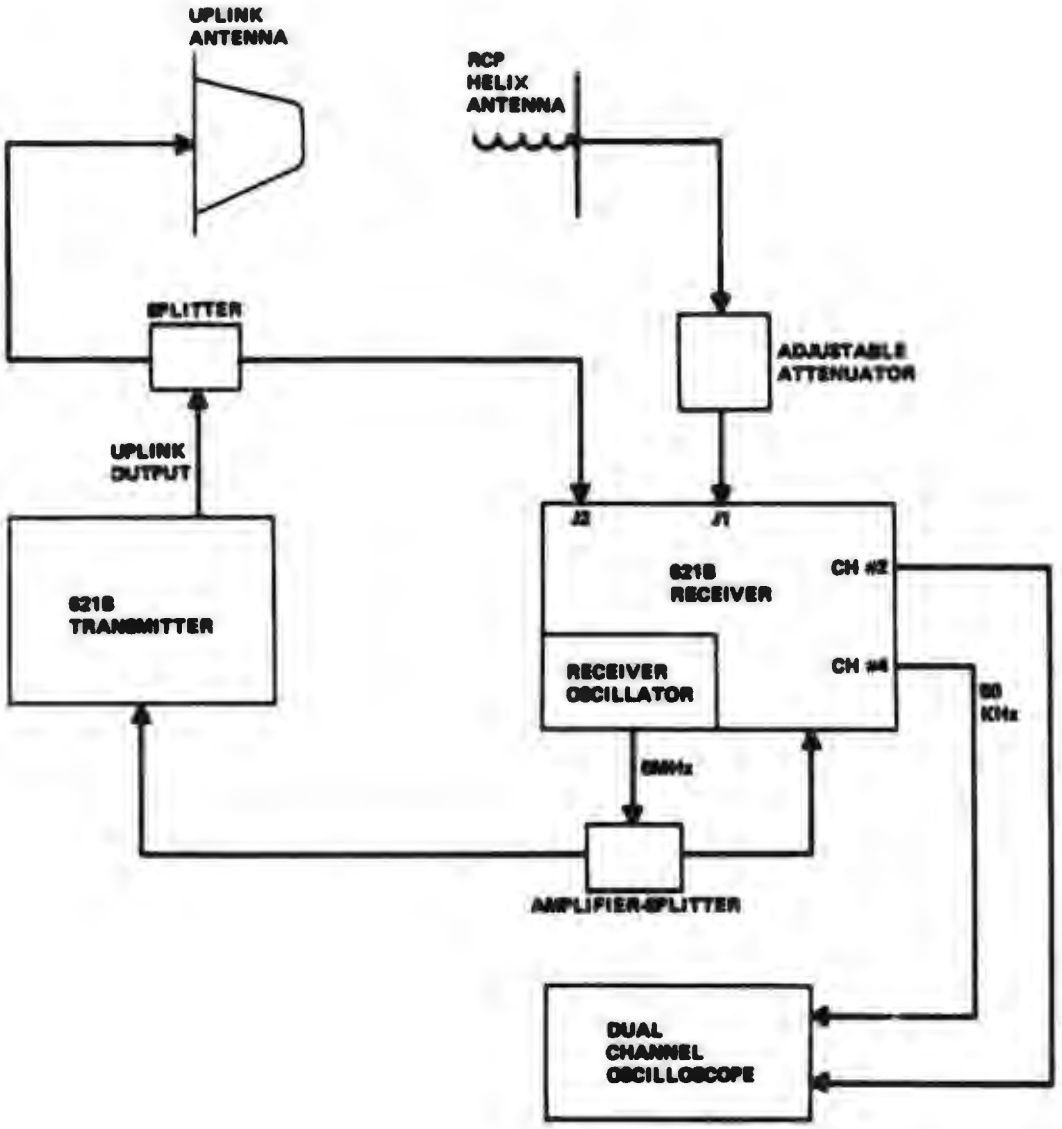

Figure 4-25 Set-Up for Antenna Delay Measurements

Table 4-5 Antenna Angles for Two Flight Paths Over Salt, in Degrees From Boresite

Uplink Antenna Serial No.	Link	30 Kft Altitude			18 Kft Altitude		
		Degrees East or West	North	South	Degrees East or West	North	South
2	Salt	0	59	59	0	70	70
3	WC-50	5 West	64	53	9 East	73	66
4	EC-50	7 East	63	55	7 West	73	67
6	SC-50	4 East	46	67	7 East	60	76

Equipment drift effects were noted in repeating some of the data. The repeated data contained the same curve with a bias. The curves were adjusted on the basis of comparison data taken on boresite for all antennas in a short period of time (two hours). The typical data collection time for one cut (two data sets) is one hour.

The measured data is presented in Figures 4-26, 4-27 and 4-28. The delays are presented in terms of the measured, bias corrected, numbers. These numbers are relative to an arbitrary constant.

The effect of the antenna delay error processed by the airborne receiver on the navigation solution is shown in Figures 4-29 and 4-30. Figure 4-29 shows the time history of the residual error obtained by differencing the navigation solution with the WSMR BET ($z = z - z_{BET}$). The navigation solution in this figure is computed ignoring any antenna delay error effects. Thus the antenna error is present in the solution and causes a distortion of the z coordinate position. Figure 4-30, on the other hand, has the antenna delay error effect corrected out of the solution. This was accomplished by constructing a piece-wise linear fit to the measured delay errors shown in Figures 4-26, 4-27 and 4-28 and correcting the solution accordingly. The aircraft is located over Salt (center transmitter) at t = 16 on the plot. At this point the antenna correction has improved the z position residual from -20 ft (Figure 4-29) to -10 ft (Figure 4-30), indicating that the antenna delay error causes approximately 10 ft distortion in the z direction.

The effect of the antenna delay error on the calibration receiver is small since there is no variation in look angle in this case. The variation in physical signal delay in the antenna time is unknown. However, it is expected that this effect is also small because it is a function of the dimensional stability of the antenna components. There is a potential change due to small angular movements of the antenna as a result of tolerances in the antenna mount. From a study of the data taken during February 1973 in Bethpage and the measurements at WSMR, it is concluded that antenna movement did not have significant effect on Salt, EC-50, and SC-50 calibration link delays. This conclusion is based on the fact that antenna movements were probably less than 2^{o}, and the Bethpage measurements showed an insensitivity to 5^{o} movements. Furthermore, analyses (single-reflection multipath) and uplink antenna measurements reveal that apparent delay changes are nearly always accompanied by an apparent change in signal level, which would result in a change in link loss (see Section 9), while the WSMR measurements revealed an essentially constant link loss between different sets of measurements.

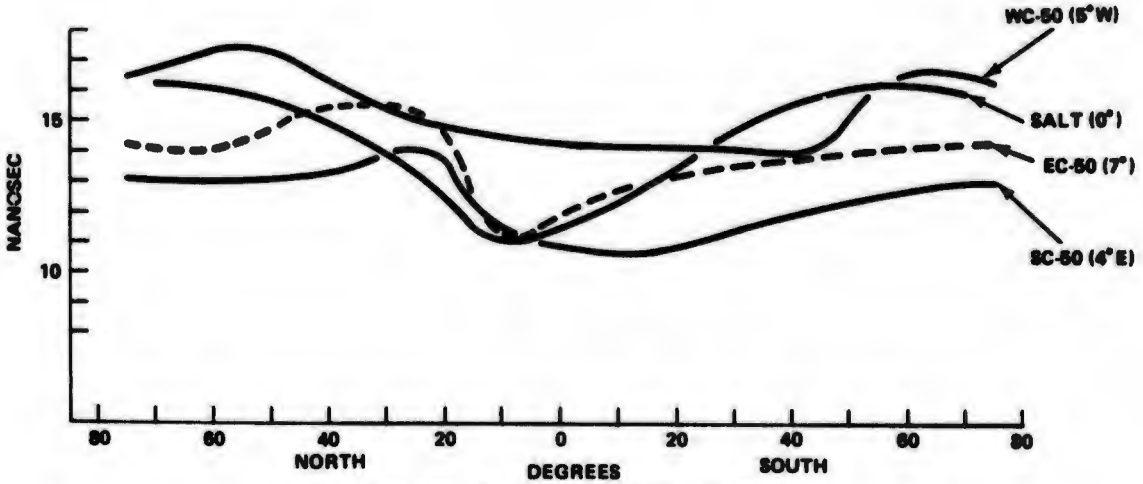

Figure 4-26 Antenna Delays for 30K Ft. Altitude

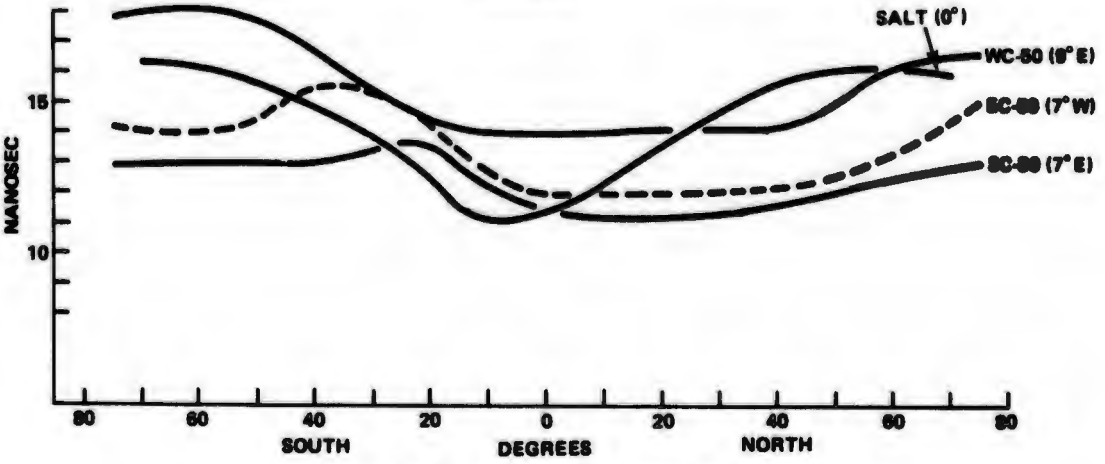

Figure 4-27 Antenna Delays for 18K Ft. Altitude

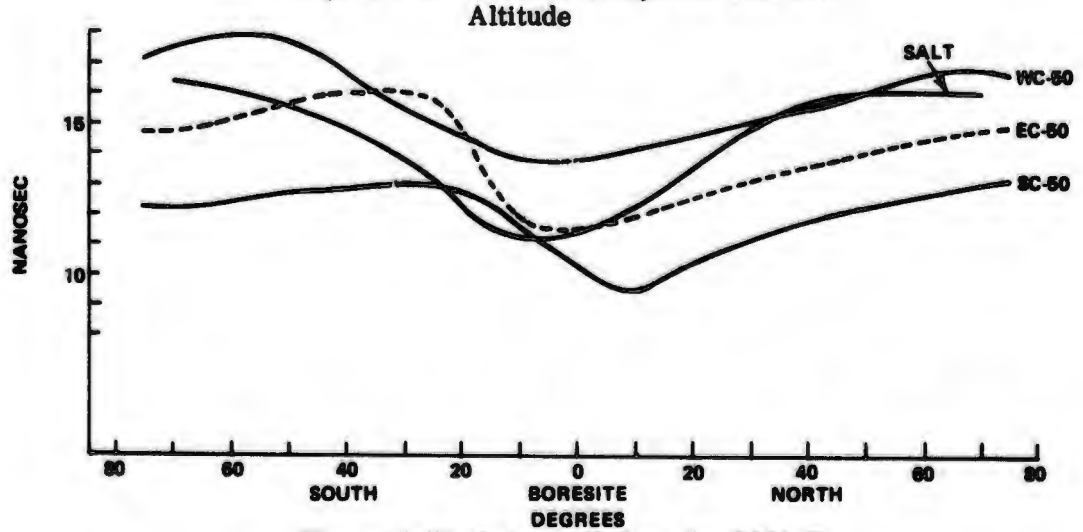

Figure 4-28 Antenna Delays for 3000 Ft. Altitude

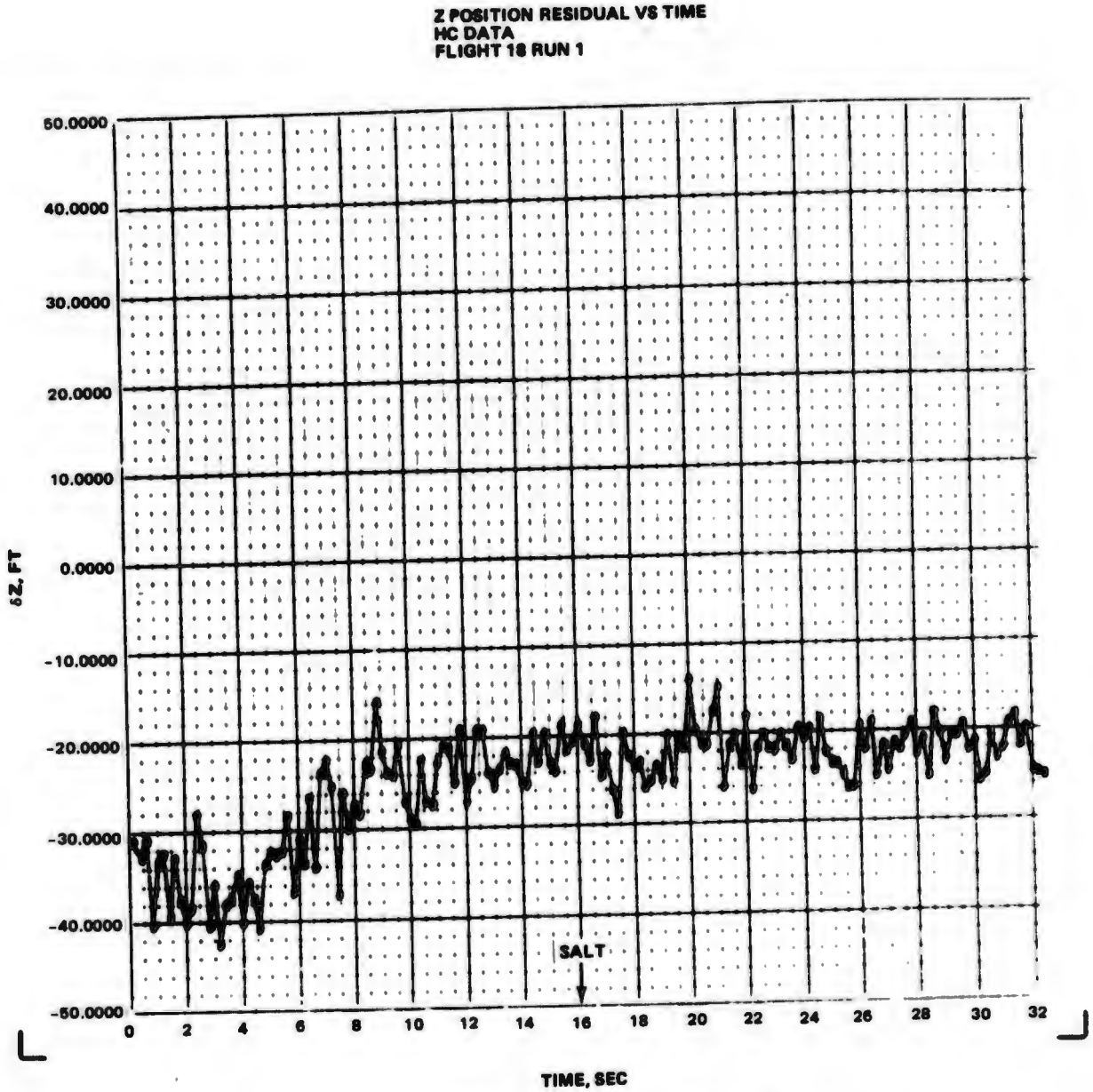

Figure 4-29 No Corrections for Observed Antenna Delays (Case 1)

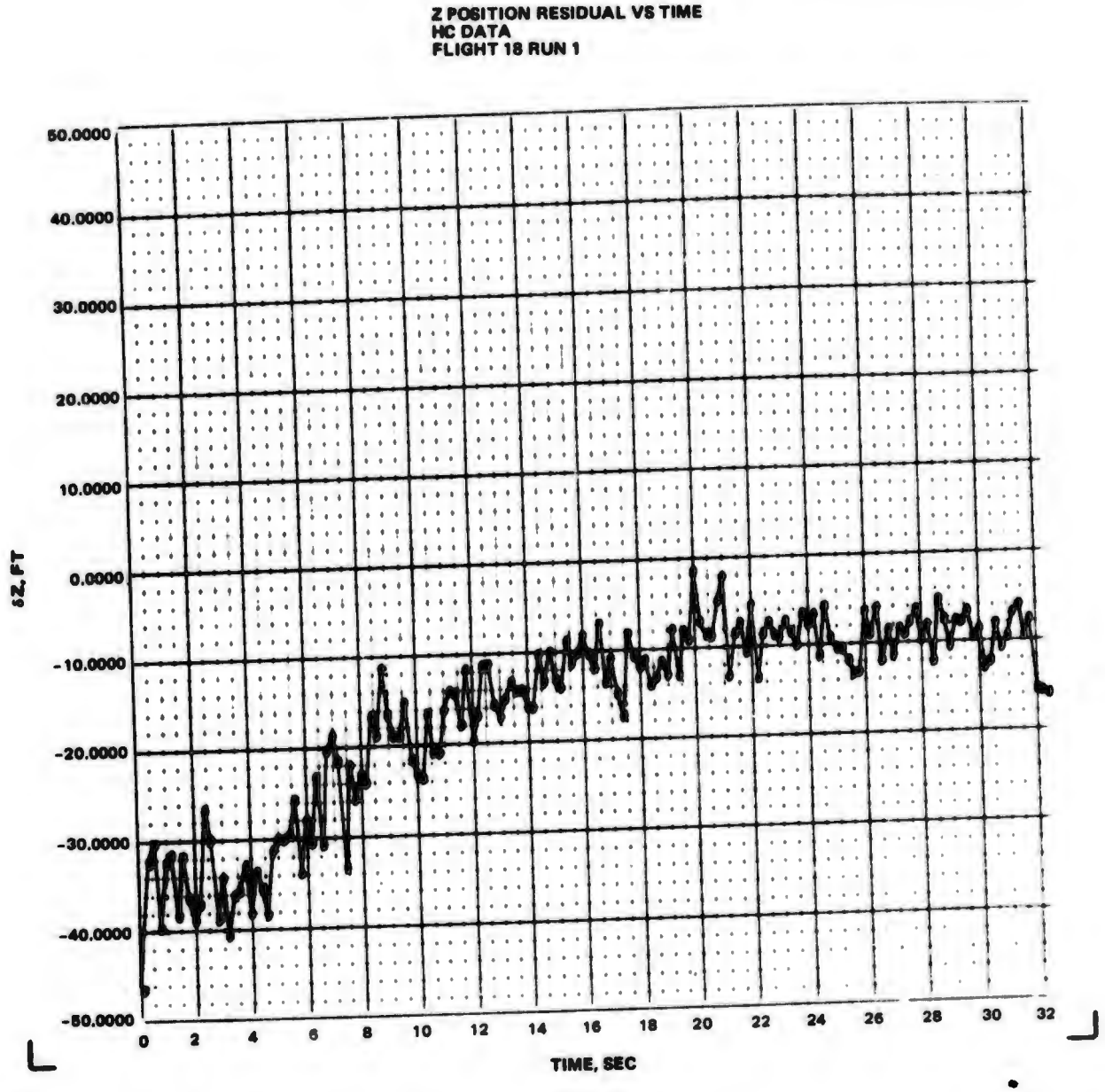

Figure 4-30 Antenna Delays Modelled

4.2.1.4 Transmitter Error Sources

Transmitter Low Power Attenuator Errors

The transmitter contains a built-in 2-stage attenuator to control the output level of the long code portion of the uplink signal. The attenuator range is 0 to 60 db controlled in steps of 1 db from 0 to 10 db, and in steps of 10 db for 0 to 60 db, thereby enabling any setting within 1 db by proper adjustment of the two controls. The attenuator was found to be ineffective at settings greater than approximately 25 db due to rf leakage paths bypassing the attenuator. The leakage path causes two errors to develop:

- The signal is not attenuated by the value set on the attenuator controls
- The signal now composed of a direct signal through the attenuator and a leakage signal slightly displaced in phase, appear to the receiver as multipath and causes pseudo-range tracking errors.

The performance of the attenuators in each of the four transmitters, for both signal attenuation and effective delay errors, is shown in Figures 4-31 to 4-34. This error source only affects data from flights 1-15 due to the configuration of the ground system. The effect on the solution is variable since various settings were used throughout this flight period. The magnitude of the average error is approximately 3 nanosec.

Transmitter Internal Delay Error

The transmitters have a built-in signal delay which causes the uplink signal output to be nominally 200 nanosec later than the monitor link output. The delay is implemented in the transmitter by sending the uplink signal through two additional shift register stages which are advanced with a 100 nanosec shift clock (Figure 4-35). This delay was necessary to avoid interference of the uplink and monitor link signals received at the MCS. In order to properly reference the data received at the MCS site to the transmitter site uplink antennas, all the delay elements, including the internal transmitter delay, between these two locations must be accurately known.

It was very difficult to obtain an accurate measurement of the effective transmitter delay. Four separate techniques were utilized to perform this measurement. Two of these utilized an oscilloscope to display the uplink and monitor link outputs simultaneously. A measurement of the delay was obtained directly from the two wave forms. The other two methods used the receiver processors to obtain the range readings of both outputs from which the delay was determined by subtracting the two ranges. Practically speaking, the latter two techniques give more reliable results since it is not possible to determine by inspection precisely at which point the receiver will track a waveform. Therefore, the individual observing the waveforms uses his own judgement in determining what reference points on the waveform are suitable when measuring the relative delay between the uplink and monitor link outputs. This introduces an additional error in the measurements. A sketch of the equipment set-up for the four measurement methods is shown in Figure 4-36.

Each measurement method gave slightly different results. In addition the measurements showed a variability for each of the techniques, of 5-10 nanosec (best case). This situation could not be tolerated in evaluating the overall system results, since the nominal 200 nanosec delay between uplink and monitor link outputs had to have a

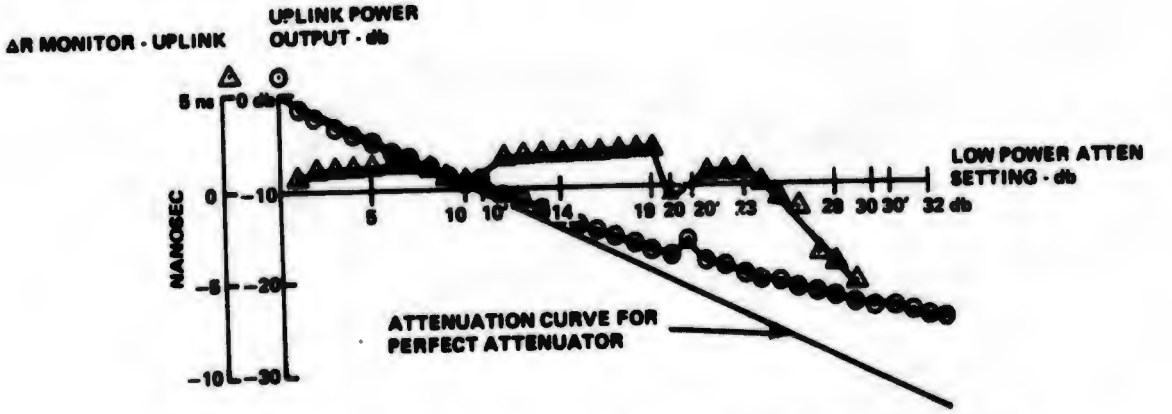

Figure 4-31 621B Transmitter Low Power Attenuator Linearity and Transmitter 1 Range Error Sensitivity vs Attenuator Setting

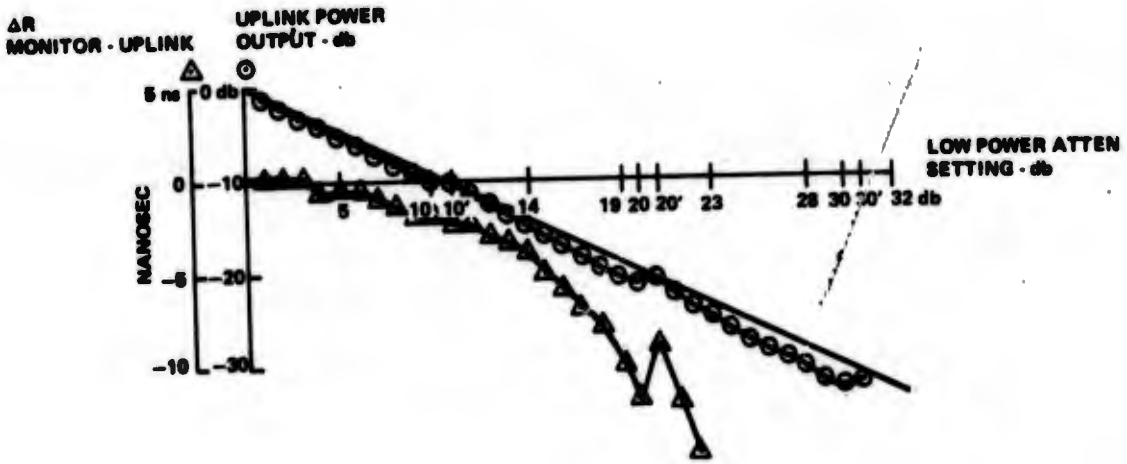

Figure 4-32 621B Transmitter Low Power Attenuator Linearity and Transmitter 2 Range Error Sensitivity vs Attenuator Setting

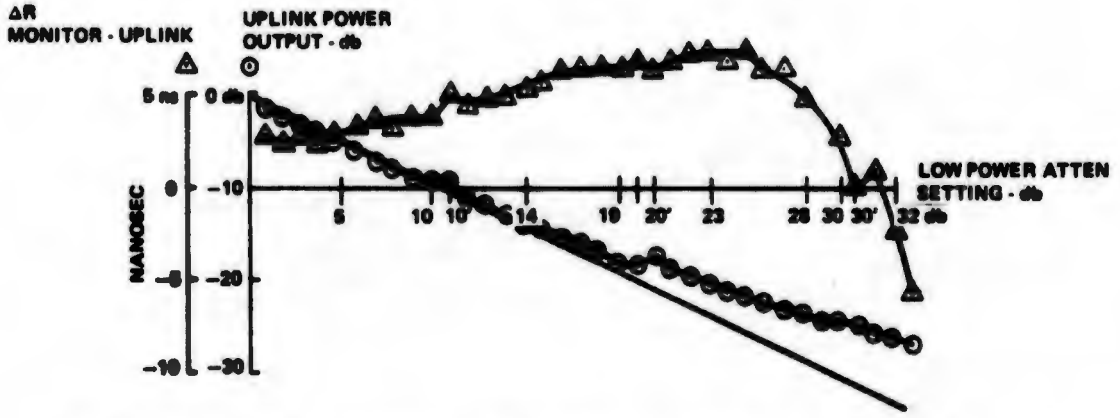

Figure 4-33 621B Transmitter Low Power Attenuator Linearity and Transmitter 3 Range Error Sensitivity vs Attenuator Setting

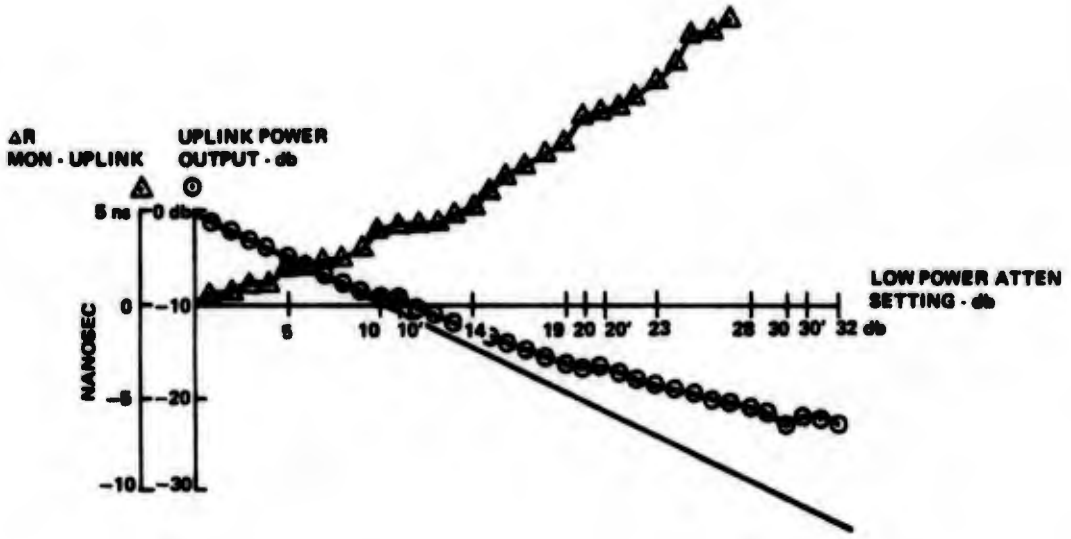

Figure 4-34 621B Transmitter Low Power Attenuator Linearity and Transmitter 4 Range Error Sensitivity vs Attenuator Setting

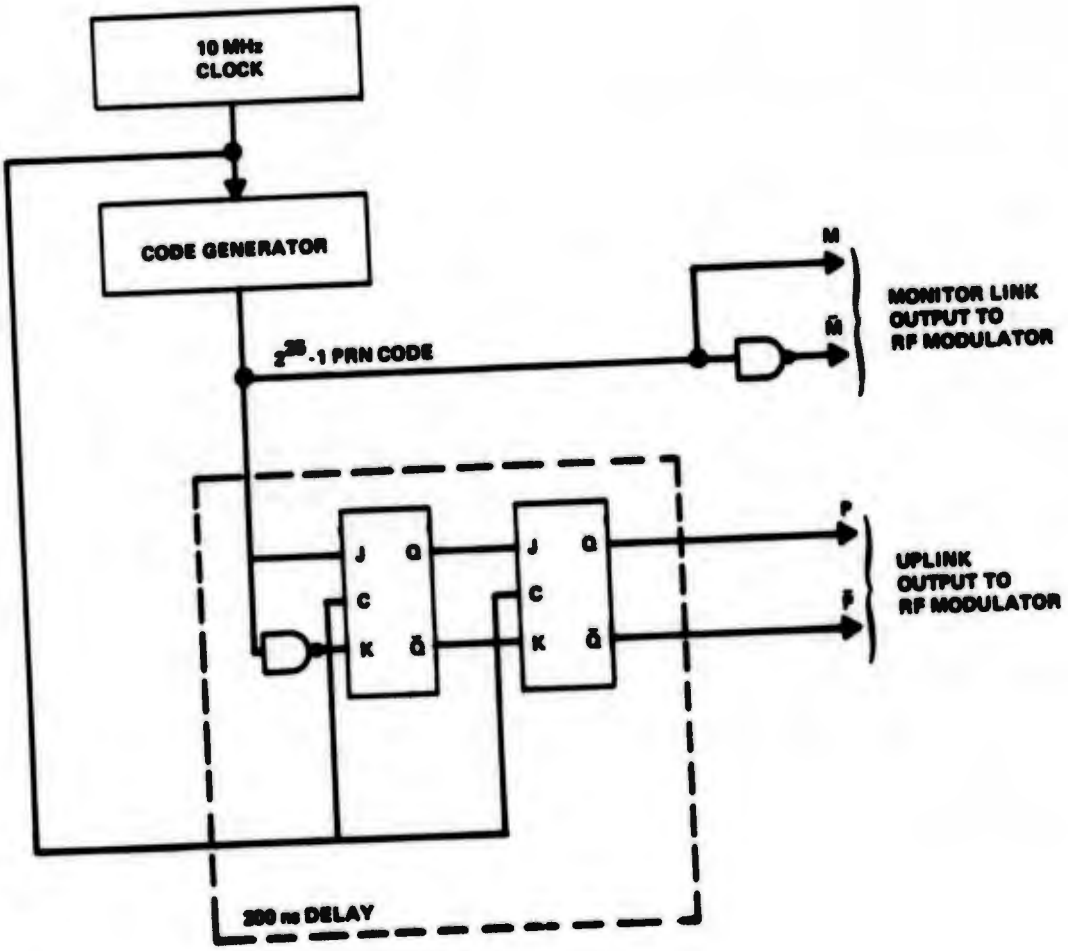

Figure 4-35 Functional Schematic of Transmitter 200 Nanosec Uplink Signal Delay

MEASUREMENT TECHNIQUE

1. DOUBLE CABLE/OSCILLOSCOPE

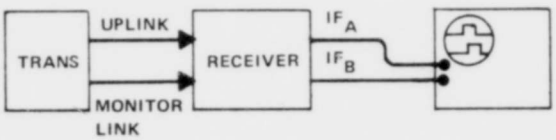

TRANSMITTER OUTPUT WAVEFORMS ARE OBSERVED AT THE RECEIVER IF OUTPUT

2. SINGLE CABLE/OSCILLOSCOPE

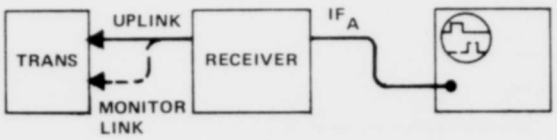

TRANSMITTER OUTPUT WAVEFORMS ARE OBSERVED AT THE RECEIVER IF OUTPUT. A SINGLE CABLE IS USED TO FIRST LOOK AT THE UPLINK, THEN THE MONITOR OUTPUT. THIS ELIMINATES CABLE LENGTH VARIABILITY (A PROBLEM IN THE DOUBLE CABLE TECHNIQUE) FROM THE MEASUREMENT.

3. DOUBLE CABLE/RECEIVER RANGE

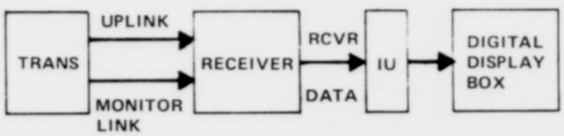

TRANSMITTER OUTPUTS ARE PRESENTED IN BINARY FORM ON THE DIGITAL DISPLAY BOX. THE MEASUREMENT IS MADE BY SUBTRACTING THE UPLINK PSEUDO RANGE FROM THE MONITOR LINK PSEUDO RANGE.

4. SINGLE CALBE/RECEIVER RANGE

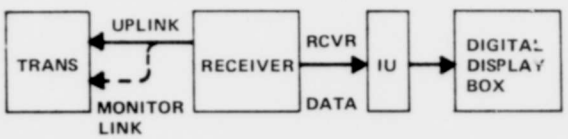

TRANSMITTER OUTPUTS ARE PRESENTED IN BINARY FORM ON THE DIGITAL DISPLAY BOX. A SINGLE CABLE IS USED TO FIRST LOOK AT THE UPLINK, THEN THE MONITOR LINK OUTPUT. THIS ELIMINATES CABLE LENGTH VARIABILITY (A PROBLEM IN THE DOUBLE CABLE TECHNIQUE) FROM THE MEASUREMENT.

Figure 4-36 Transmitter Internal Delay Measurement Set-Up

tolerance of less than 2 nanosec. This error source is present in all the data from flights 1-15, which is the primary reason why the data from these flights is unsuitable for accuracy analysis. The ground system was reconfigured after flight 15 to eliminate the monitor link output and therefore remove this error source. (See Section 3.1.)

Over a period of one month an investigation of this delay was conducted at the field laboratory at Holloman AFB. It was during this period that the four measurement techniques evolved. A composite plot of the delay measurement data for each transmitter obtained from the four measurement methods is shown in Figures 4-37 to 4-40. Each data point presented is the average of at least ten readings thereby removing system noise as a variable. The delay data from transmitter 1, Figure 4-37, shows the best stability. However, even this performance is not sufficient. A reading taken at 9:00 AM on 6/4/72 showed a stable value of 236 nanosec, while a reading taken at 12:00 PM on the same day showed a stable value of 241 nanosec. Other transmitters showed similar variations.

The factors affecting the internal transmitter delay stability are not fully understood. Some of the problem undoubtedly lies in the inherent difficulty in making a measurement of this type in a field laboratory. Other aspects of the problems are associated with both the transmitter circuitry and the sensitivity of the tracking loop performance in the receiver to certain types of external influences. A summary of the major error producing mechanisms that were investigated is presented in Table 4-6. Since we were able to eliminate this delay from the system operation, the investigation was eventually dropped.

4.2.1.5 Error Resulting From Transmitter Antenna Location Uncertainty

A potential error is introduced into the navigation position solution because of the uncertainty in the location of each transmitter antenna used in the area navigation and Northrop Strip testing. The antennas were located by an optical traverse surveying technique which resulted in errors of ± 3 in. Uncertainties in antenna (signal origin) position contribute directly to system ranging errors. The resulting error is constant from flight to flight since the position uncertainty does not change with time. The ground calibration system does not have this potential error source because calibration path length delays are derived using rf measurement techniques which do not depend upon surveyed antenna location.

ILS testing required a balloon-borne transmitter, three ground transmitters and a receiving site all utilizing omni antennas. The surveyed position of each of the four omni antennas located on the ground has the same ± 3 in position uncertainty as discussed above. The balloon transmitter omni attached to the balloon transmitter package was tracked during each flight by four cinetheodolites. The cine data was converted into balloon antenna position and velocity by WSMR. The balloon antenna position for flight 25 has a 10 ft uncertainty, while flights 26 through 31 have a 5 ft uncertainty, as reported by WSMR. After reviewing the cine balloon data from flight 25, it was decided to rearrange the cines in order to upgrade the quality of the balloon antenna position data while keeping the quality of the aircraft BET at 5 ft uncertainty. This equipment change accounts for the improvement in balloon data after flight 25.

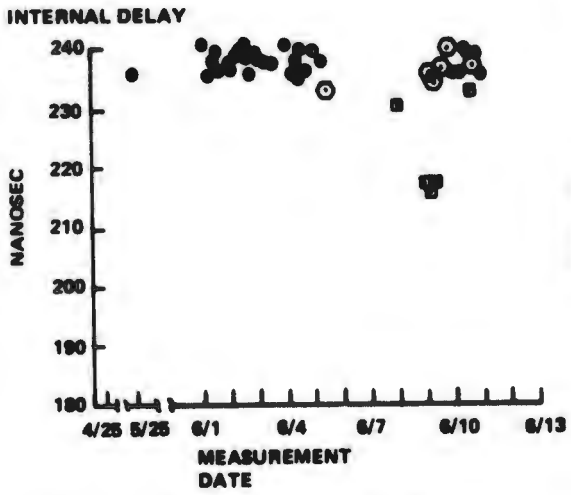

Figure 4-37 Transmitter 1 Internal Delay Measurements Monitor Output-Uplink Output vs Measurement Date

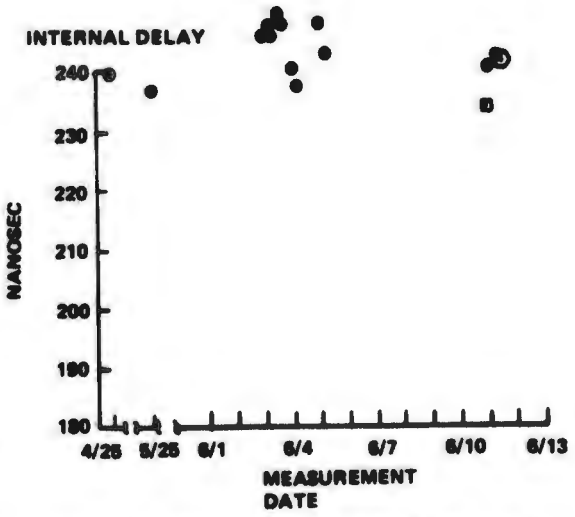

Figure 38 Transmitter 2 Internal Delay Measurements Monitor Output-Uplink Output vs Measurement Date

TRANSMITTER INTERNAL DELAY MEASUREMENTS

LEGEND

SYMBOL	TEST TECHNIQUE	DISPLAY USED FOR MEASUREMENT
●	SINGLE CABLE	RECEIVER COARSE & FINE RANGE (LIGHT BOX)
■	DOUBLE CABLE	RECEIVER IF ON OSCILLOSCOPE
▲	SINGLE CABLE	RECEIVER IF ON OSCILLOSCOPE
⊙	DOUBLE CABLE	RECEIVER COARSE & FINE RANGE (LIGHT BOX)

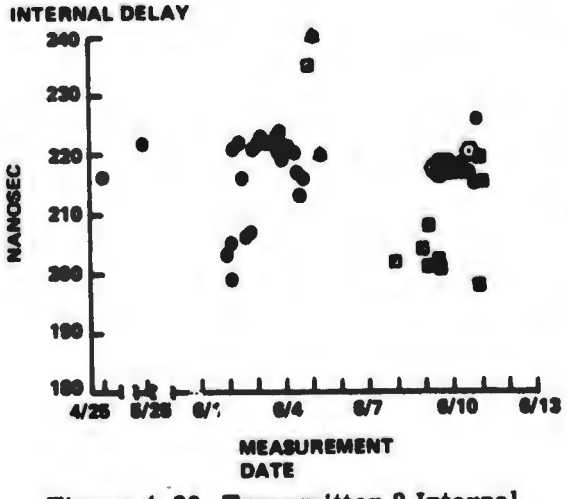

Figure 4-39 Transmitter 3 Internal Delay Measurements Monitor Output-Uplink Output vs Measurement Date

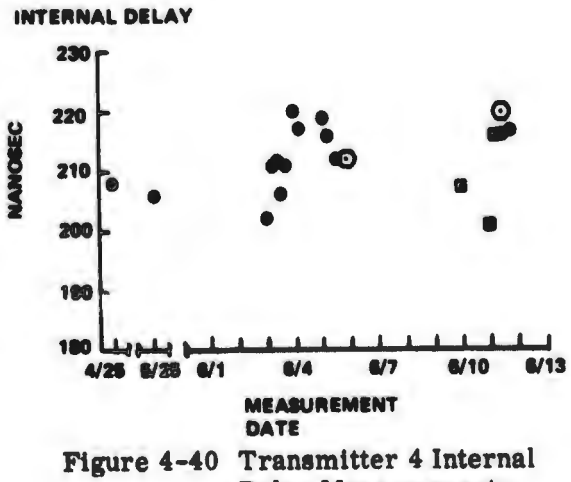

Figure 4-40 Transmitter 4 Internal Delay Measurements Monitor Output-Uplink Output vs Measurement Date

Table 4-6 Major Error Producing Mechanisms Investigated

Factors Affecting the Transmitter Internal Delay and/or Its Measurements	Observations of the Effect
1. Transmitter Internal Case Temperature	An abbreviated test showed no measurable temperature dependence over a range of 80°–110° F (measured near the code generator module). However, we did note a shift in the delay measurement during the first hour of transmitter operation of approximately 3 to 6 ns.
2. Transmitter RF Amplifier Adjustment	Small adjustments in the RF amplifier affect the symmetry of the spread spectrum signal which in turn affects the tracking point of the receiver processors. The change in processor tracking point can be large, > 10 ns.
3. Transmitter Power Supply Voltage Variations	Supply voltage variations affect the RF amplifier chain in effect making small operating adjustments similar to effect #2 above.
4. Transmitter Low Power Attenuator Setting	RF leakage around the attenuator causes a second uncontrolled signal path (a form of multipath) forcing the receiver processor to attempt to track a multiple signal. Tracking errors > 5 ns can result.
5. Output Port Termination	In using the single cable measurement technique, the unused output port is unterminated. Investigation of various ways of terminating this port showed very small shifts in the delay measurement, < 1 ns.
6. Cable Mismatch	Cabling used in the test set up was constantly changing. Mismatch errors cause multipath type signals with their attendant errors. This effect was not investigated.
7. Stray RF Leakage	Since the receiver is very sensitive, stray RF leakage from the transmitter (located in the same room for these tests) can be serious multipath type problem. Even though precautions were taken to avoid this problem, we have occasionally noted 1-2 ns errors.

4.2.1.6 Error Sources at the Calibration Receiver Site

MCS Dish Antenna Interaction

The receiving antennas at the MCS site are parabolic dishes mounted on two poles spaced about 100 ft apart. Each pole has two antennas. (See Volume II for general configuration.) The orientation of the antennas and the relative locations of the transmitters makes it possible for a signal to arrive at the receiver via multiple routes from the various antennas at the MCS. Therefore, the receiver can be processing the correct signal which was routed from the MCS antenna assigned to the transmitter of interest, while at the same time be processing this transmitter signal via a different MCS antenna. These signals arrive at the receiver displaced in time by the extra distance the false signal must travel in going through the wrong antenna. The receiver is, in effect attempting to track a multipath signal. Generally, the dimensions of the antenna system at the MCS place the signal at least 100 nanosec apart. In addition, the narrow beamwidth of the parabolic antennas, approximately 8^{o}, provides additional signal rejection.

Investigations of this error source showed that the undesired signals were always at least 20 db lower than the desired signal at the input to the receiver. The worst case receiver tracking error caused by the undesired signals was one nanosecond maximum.

MCS Hybrid Power Combiner

The four signals are summed at the MCS by a hybrid power combiner before entering the reciever. The hybrid combiner consists of resistive elements. Although the power combiner showed very good insertion loss balance among the four ports (7 to 7.5 db), there was a slight variation in signal delay through the device. Measurements of signal delay made at the MCS using the calibration receiver showed that the maximum delay differential delay between signal paths was 0.5 nanosec.

Calibration Receiver

The calibration receiver was identical to the HC airborne receiver. Since their performance was very similar, a single discussion of the error sources for this unit is presented in Section 4.2.2. However, the calibration receiver error magnitudes are generally less than those associated with the airborne receiver because signal dynamic effects are eliminated on the ground. The calibration receiver steady-state pseudo-range errors are estimated to be less than 3 nanosec worst case with random components of approximately 0.5 nanosec.

4.2.2 Airborne User Errors

The steady-state measurement errors in the user equipment are substantially smaller than those associated with the ground system. Slowly varying steady state errors of 4 to 8 ft are observed in the flight data on a per-run basis. While certain components of these variations are due to ground-related phenomena (such as uplink antenna apparent delay), some are associated with the airborne user.

Some of the steady-state errors associated with the user are readily modelled. These include tropospheric error and. for dynamic geometries, loop tracking errors.

Range errors due to refraction are caused by variations in the velocity of propagation, which in effect retards the signal, yielding an error in the range measurement. The error is a function of the change in atmospheric refractivity along the signal propagation path caused by the average change in the atmospheric parameters of temperature, water vapor and pressure with height above the earth's surface, and the incident angle of the traversing electromagnetic wave.

The refractive index profile is determined from radio sonde measurements and modelled at $N = N_0 e^{-k_0 h}$ where N is the refractivity, related to the refractive index n, $N = (1-n)\ 10^{-6}$ and h is the height above sea level, measured in feet. Average values of the parameters at Holloman AFB, for the time period of interest are $N_0 = 270$ and $k_0 = 3.577 \times 10^{-5}$.

The true range between the i^{th} transmitter and the user is defined as the straight line distance between them:

$$r_i = \sqrt{(\bar{Y} - \bar{X}_i) \cdot (\bar{Y} - \bar{X}_i)}$$

The actual pseudo range measurement is not made along this line, but along the path of least delay. This range to the user is given by the integral of the index of refraction over the ray path:

$$r_{ei} = c \int_s \frac{n(h)}{c}\, ds$$

where c is the speed of light.

The atmospheric range correction to remove the tropospheric error is:

$$\Delta r_i = r_i - r_{ei}$$

where:

$$r_i = c \int_s \frac{ds}{c}$$

It is reasonable to neglect the variation of n with h, and the differential path length is given by

$$ds = dh \csc E = \frac{r_i\, dn}{(Z_y - Z_{xi})}$$

where E is the ground elevation angle and Z_{Xi} is the Z position of the i^{th} transmitter in 621B coordinates.

Evaluating the correction term

$$\Delta r_i = -\frac{10^{-6} r_i N}{(Z_y - Z_{xi}) k_0} \left[\exp(-k_0 h_{xi}) - \exp(-k_0 h_y)\right]$$

where h_{xi} are the transmitter altitudes. The residual error affecting the solution is a function of time variation of N which was not modelled. The residual errors are approximately 1 ft 1σ .

For third order loops used in the correlation receiver implementations (both code and carrier loops) the errors in range and range rate are a function of range acceleration and range jerk. The error magnitudes will depend on the relative proximity of the aircraft to the transmitters, aircraft maneuvers and aircraft velocity. The range error shown in Figure 4-41 follows the shape of the slant range jerk dynamics. These data were generated by a computer simulation of a linearized third order phase locked loop. Figure 4-41 shows the range error for simulated flight at 300 ft AGL, which passes directly over the transmitter. The aircraft speed is 570 fps. The loop dynamics effects produce a short term disturbance on the computed trajectory. These errors are not modelled in the navigation solution. They contribute a bias error approximately equal to $\Delta R = 16 \epsilon_{code}$ and $\Delta \dot{R} = 0.1 \epsilon_{carrier}$ where ϵ_{code} and $\epsilon_{carrier}$ are the phase error output respectively, in radians for the code and carrier loops. At 30,000 ft AGL these errors are not significant (less than 0.0004 and 0.001 fps).

In the ILS flight test, the aircraft passes much closer to the transmitters than in area navigation. However, the errors still remain insignificant. A discussion of the effects of the loop dynamic error for ILS tests can be found in Section 7.

Tropospheric and Multipath Doppler Measurement Biases

The doppler measurements are obtained in the receivers by averaging (differencing) the doppler over a 100 ms counting interval. The result is the average range rate over the sample interval. This is equivalent to deriving range rate by differencing two range samples per time interval. Therefore, the tropospheric correction for doppler is the difference between two tropospheric corrections;

$$\Delta \dot{R}_{ij} = \frac{\Delta R_i - \Delta R_j}{\Delta t_{ij}} \qquad (1)$$

The contribution of Eq. (1) becomes significant at low ground elevation angles where the tropospheric corrections exhibit the steepest slope with ground track distance measured from a ground transmitter.

The multipath contribution to doppler measurements exhibits a monotonic functional behavior with distance similar to the tropospheric doppler contribution, but with larger magnitudes. In addition, the mechanism causing the multipath doppler bias is different (see Sections 4.3 and 9). Multipath doppler is caused by the rate of change of differential delay due to aircraft's motion which creates a beat between the direct and specularly reflected signals. The resultant composite signal phase varies with time. The rate of change of phase induces an error in the carrier tracking loop creating a doppler bias in the measurements (see Section 4.3).

Both kinds of steady-state measurement errors propagate into the velocity solution via the sensitivity matrix relating the measurements to the user vector velocity. Figure 4-42 shows the Z-velocity residual between the navigation solution and the WSMR reference, which has been averaged over small regions of the flight path,

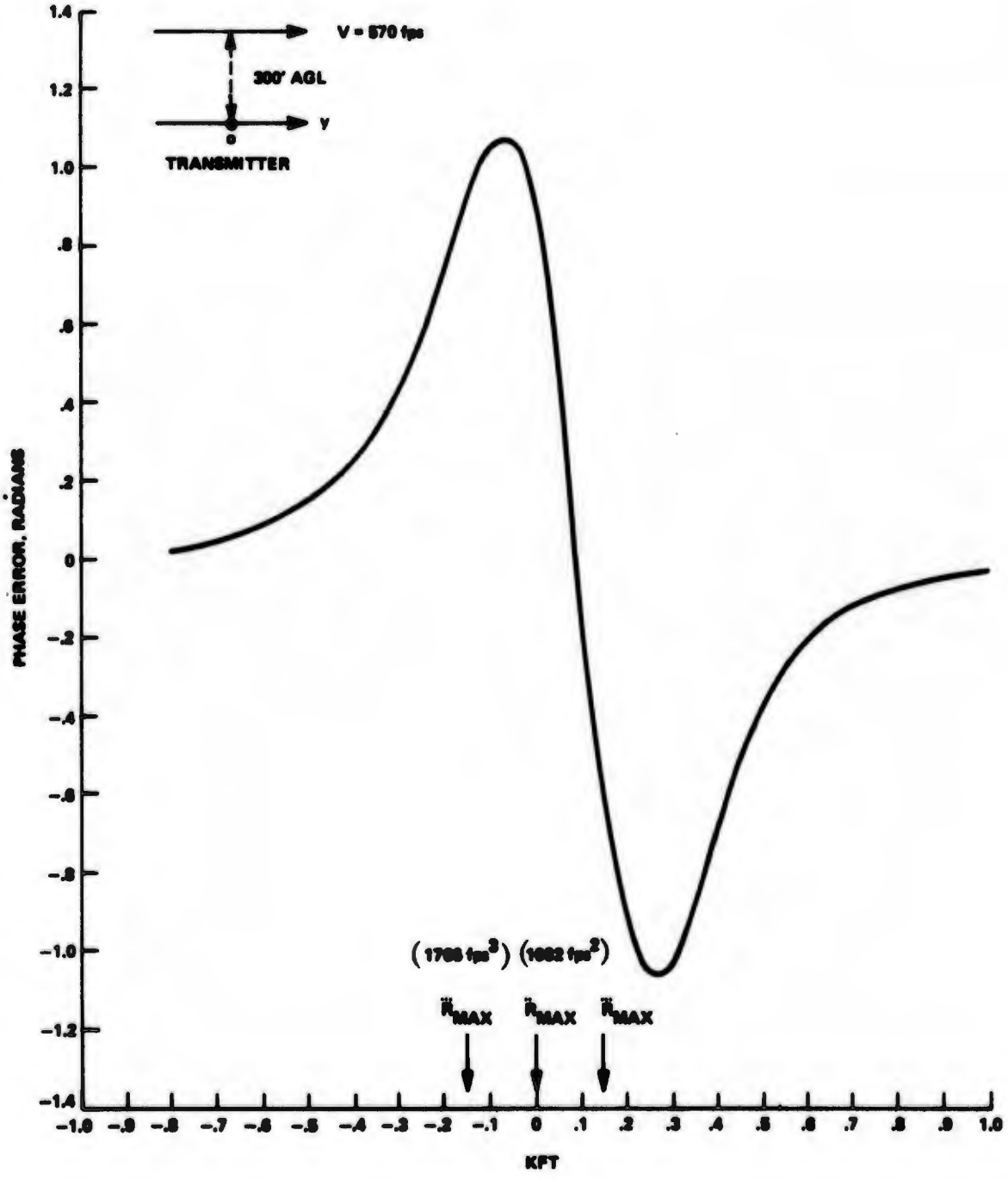

Figure 4-41 Hazeltine Carrier Loop Phase Error Response @ 123 dBm

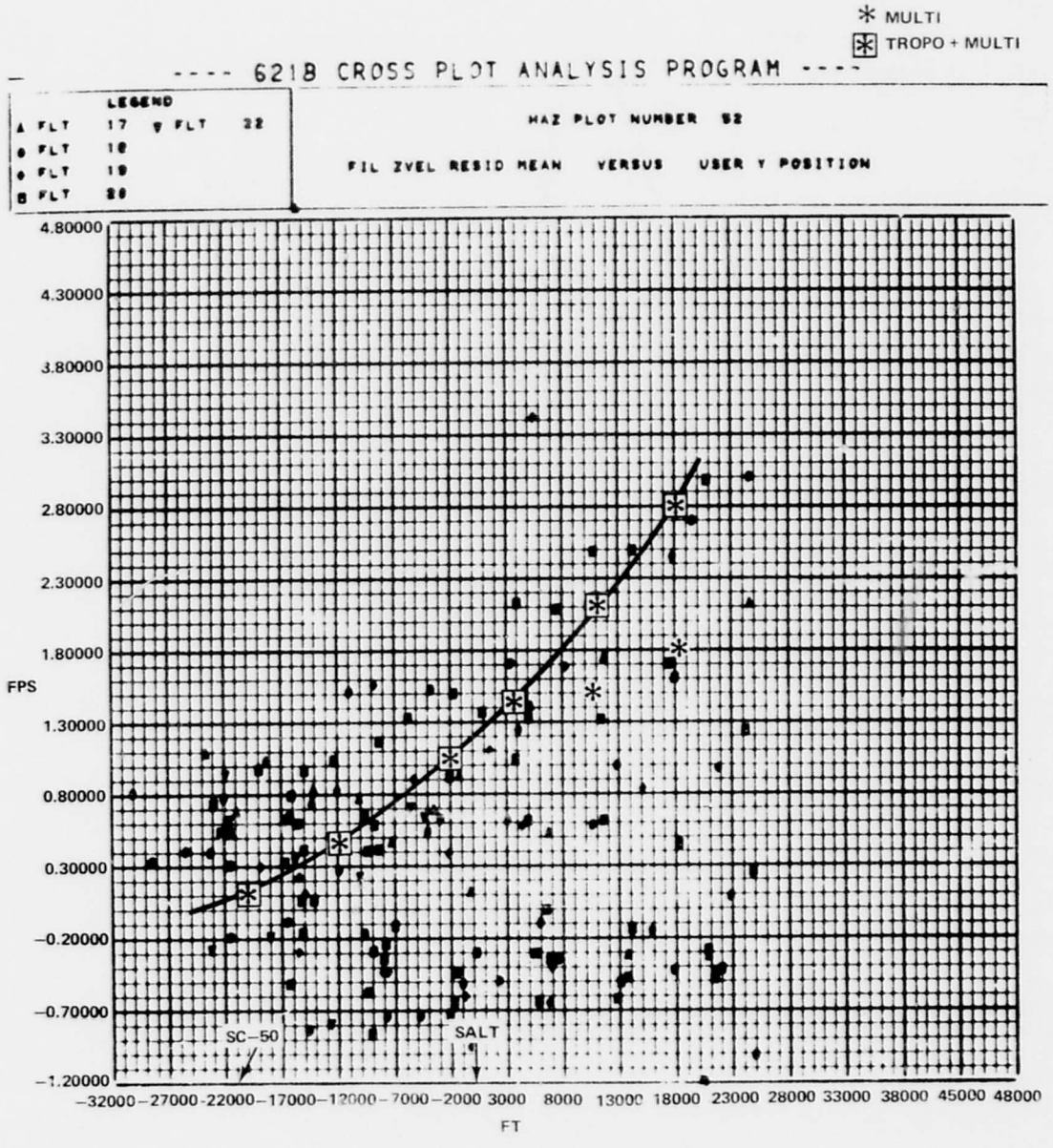

Figure 4-42 Predictable Effects of SC-50

versus user Y-position (ground track distance), for the HC receiver data. The technique of averaging the residual errors over small regions of the flight path highlights the trend of the error by reducing the noise content.

The significant upward trend in the data points is caused by multipath and tropospheric doppler contributions from transmitter SC-50 located at approximately -20,000 ft on the abscissa. Superimposed on these data is a theoretical curve derived by computing values of the Z-velocity errors caused by multipath and tropospheric doppler measurement biases in channel 4 (SC-50). The theoretical curve of Z-velocity bias change was obtained by a perturbation analysis (discussed in Section 4.2). The tropospheric doppler contribution becomes significant only when the aircraft is more than 33,000 ft away from SC-50, as shown in Figure 4-42. The composite curve of the multipath and tropospheric doppler contribution shown on the figure has good agreement with the actual data trend. The spread of the data points at the bottom of the Figure 4-42 are in part caused by similar effects from the other transmitter sites. Transmitters WC-50, EC-50 and Salt create predominantly diffused multipath doppler biases resulting in a random spread of Z-velocity residuals. The tropospheric doppler contribution from these stations is very small and the multipath predominates.

Figure 4-43 shows similar data from measurements derived from the MRL receiver. An analysis similar to that done above for the HC receiver locates the theoretical multipath and tropospherical doppler bias contributions above the scatter of data points. This is caused by a peculiarity of the MRL receiver discussed in detail later in Section 4.5. Basically, range acceleration along the line-of-sight to the transmitters causes an apparent doppler measurement bias error because the receiver implementation produces the doppler output shifted in time from the actual measurement. Thus the true doppler value at the time of receiver output has changed from the measured value due to a slant range acceleration. When this error is combined with the multipath and tropospheric range rate errors, the composite curve shows good agreement with the data in Figure 4-43.

Range Error Contributed by Code Asymmetry

The distortion (asymmetry) of the code or modulation envelope can cause significant steady state errors in the receiver code tracking loop. Asymmetry of the modulation envelope (code) may be caused by bandlimiting, phase nonlinearity and multipath.

Each of the receivers was observed to be sensitive to this effect to some degree. The transmitters were not identical as far as this distortion is concerned which resulted in each code tracking loop measuring a slightly different value of pseudorange. Test data showing this effect for each receiver is presented in Figures 4-44 to 4-52. These curves show the steady state interchannel error, e.g., channel 2 - channel 1 error, when all four channels are locked to a single transmitter. There is a substantial difference in tracking signals from transmitter 1, for example, compared to tracking transmitter 4 as seen on Figure 4-44. At a signal level of -115 dbm, this difference is approximately 2 ft. An examination of the remaining figures shows that the effects vary from channel to channel among the three receivers. For the test system equipments, the maximum error resulting from the distortion of the code or modulation envelope is 4 ft.

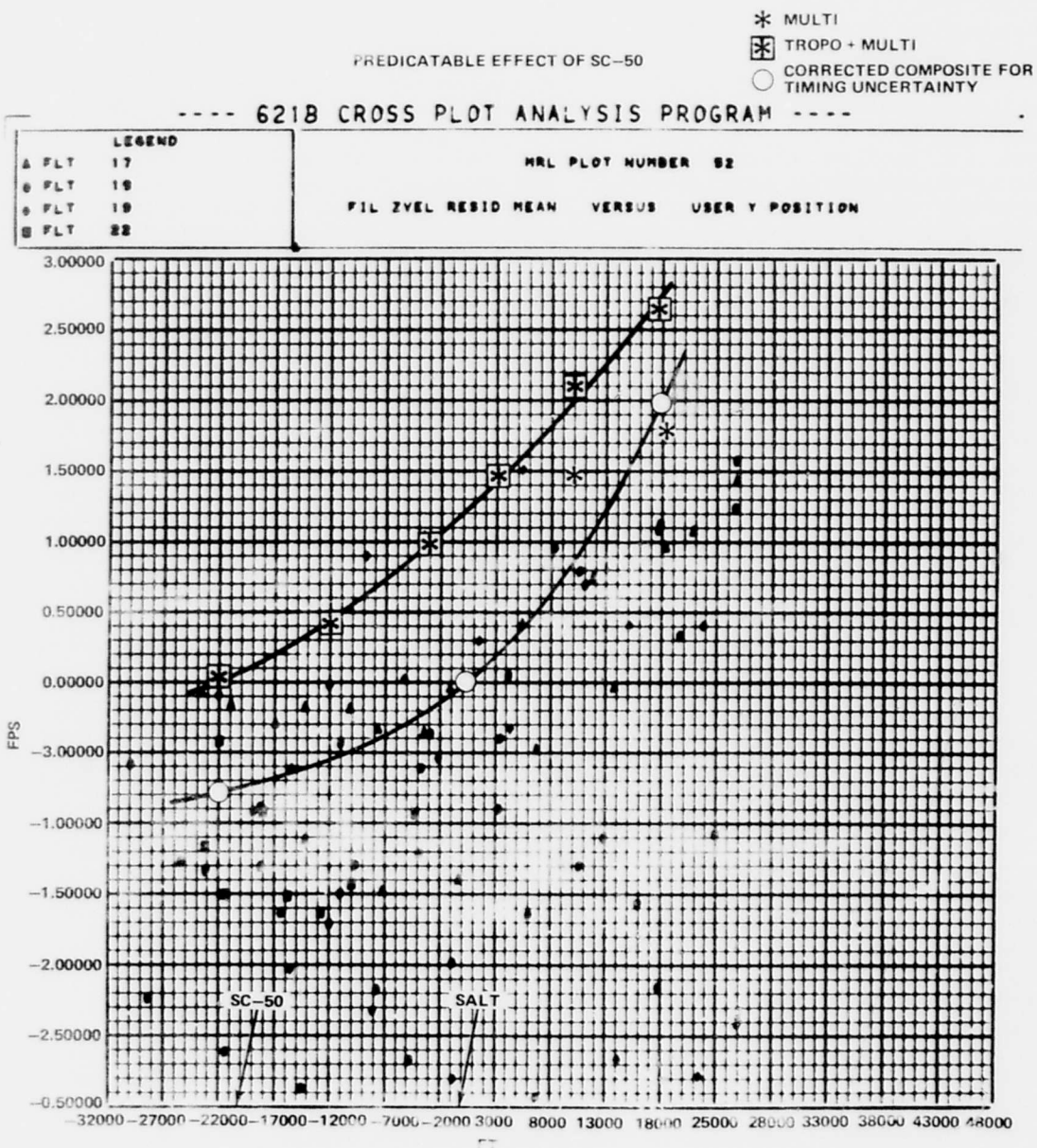

Figure 4-43 Predictable Effects of SC-50

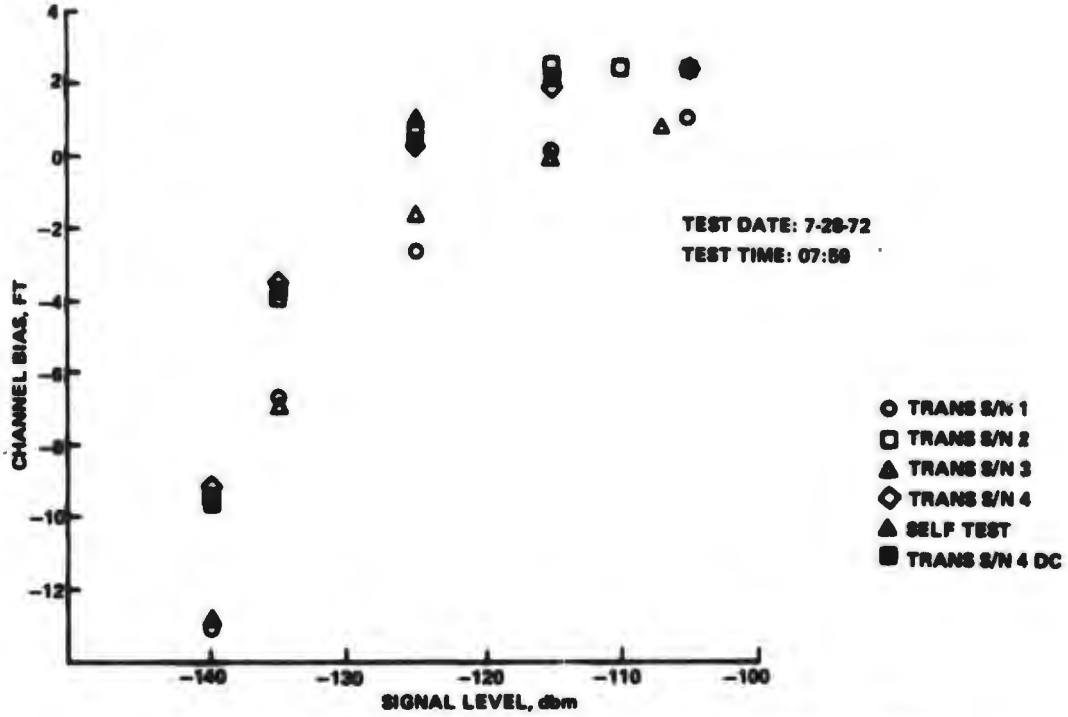

Figure 4-44 Ground Test Flight 49 HAZ Receiver 1 Bias Shift Data Channel 2-1 vs Signal Level

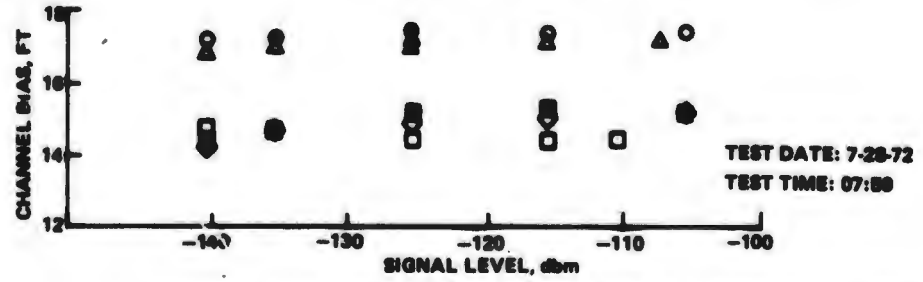

Figure 4-45 Ground Test Flight 49 HAZ Receiver 1 Bias Shift Data Channel 3-1 vs Signal Level

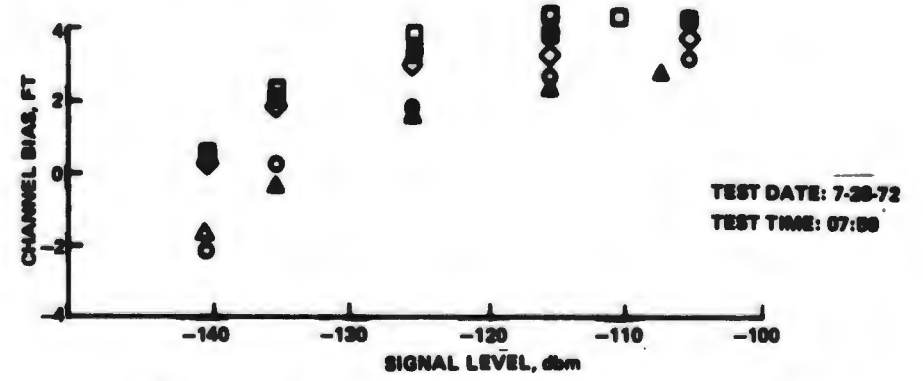

Figure 4-46 Ground Test Flight 49 HAZ Receiver 1 Bias Shift Data Channel 4-1 vs Signal Level

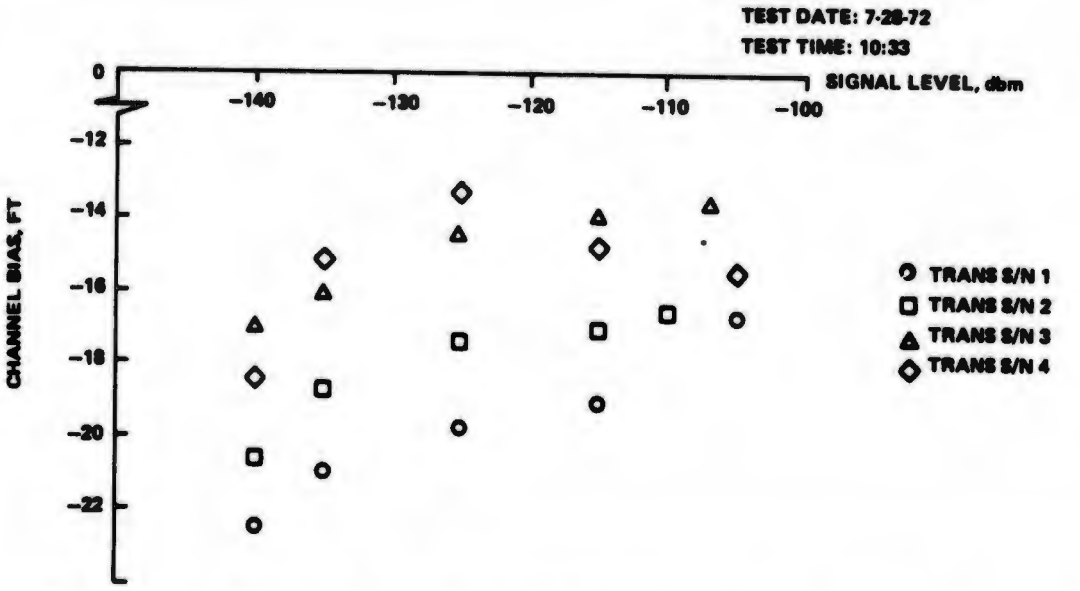

Figure 4-47 Ground Test Flight 50 HAZ Receiver 2 Bias Shift Data, Channel 2-1 vs Uplink Signal Data

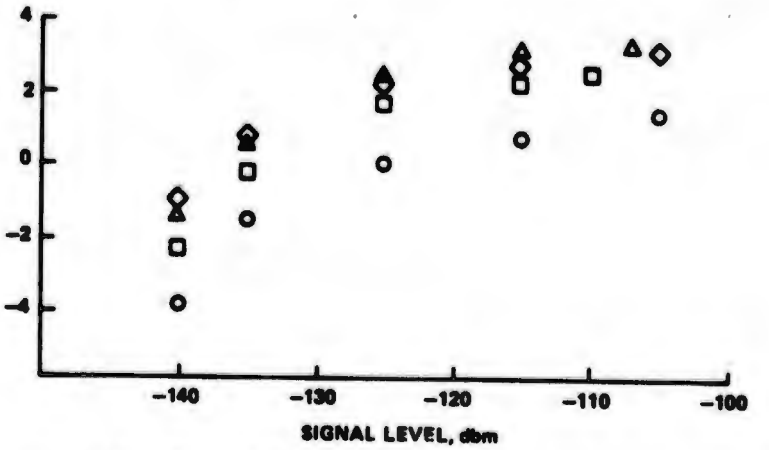

Figure 4-48 Ground Test Flight 50 HAZ Receiver 2 Bias Shift Data, Channel 3-1 vs Signal Level

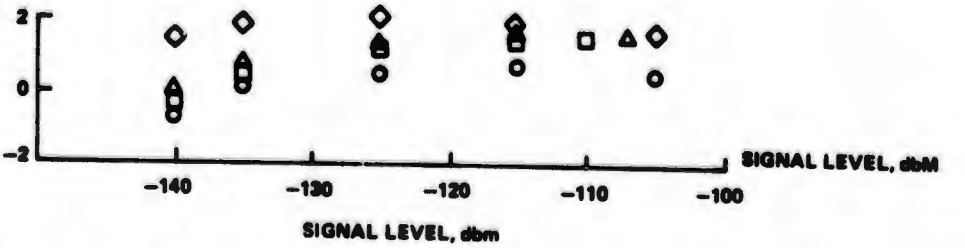

Figure 4-49 Ground Test Flight 50 HAZ Receiver 2 Bias Shift Data, Channel 4-1 vs Signal Level

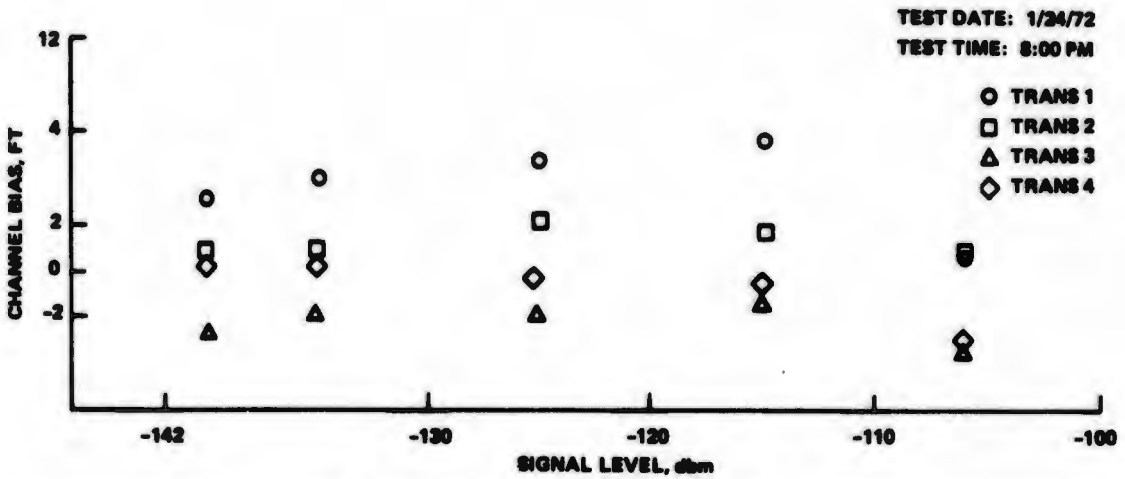

Figure 4-50 Ground Test Flight 68 MRL Receiver Bias Shift Data, Transmitter/ Receiver Synchronized, Channel 1-2 vs Signal Level

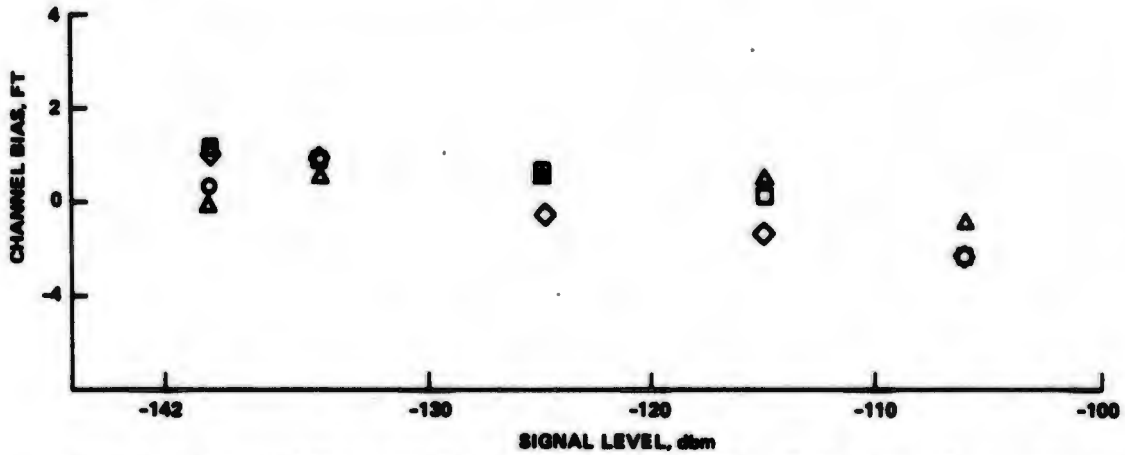

Figure 4-51 Ground Test Flight 68 MRL Receiver Bias Shift Data, Transmitter/ Receiver Synchronized, Channel 1-3 vs Signal Level

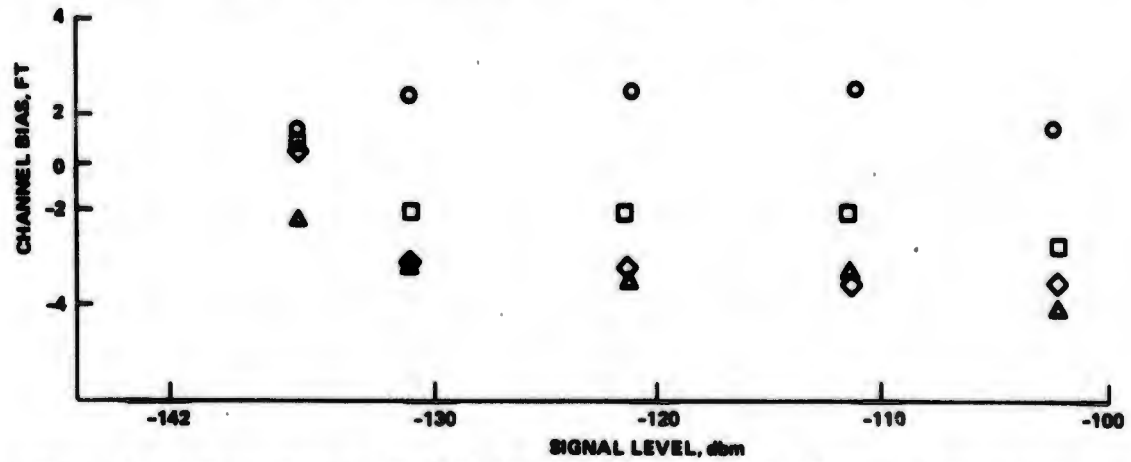

Figure 4-52 Ground Test Flight 68 MRL Receiver Bias Shift Data, Transmitter/ Receiver Synchronized, Channel 1-4 vs Signal Level

Range Error Sensitivity to Received Power Level

The HC receivers exhibited a steady-state range measurement error which was functionally dependent on the received signal level. The same figures used above, Figures 4-44 to 4-52, show this dependence for all the receivers on signal level. The magnitude of this error varies among the receiver channels as shown in Figures 4-44 and 4-45, channels 2 and 3 (with respect to channel 1) for HC receiver 1. Channel 2 of this receiver consistently showed the poorest performance as a function of signal level. A measurement variation of 10 ft was typical between signal levels of -110 dbm and -140 dbm. Channel 3 on the other hand, Figure 4-45, shows almost no variation in range measurement as a function of signal level.

The MRL receiver generally was far less sensitive to received power level than was the HC receiver. Figures 4-50, 4-51 and 4-52 show the interchannel range measurement steady state errors for the MRL equipment. Although there is some sensitivity to transmitted signal (range error contributed by code symmetry), these figures show very little dependence on the signal level.

Range Channel Error From Channel Mismatch

The implementation of the receivers enables correction for delay mismatches through the four channels due to manufacturing tolerances and different signal path lengths resulting from the mechanical packaging arrangement. The mismatch correction is implemented in the HC equipment in a manner that allows a detailed inspection of the process. Figure 4-53 shows the channel delay mismatch data used for HC receiver 1 for flights 10 and 17. Channel 4 delay is used as a reference, and the other three channel delay variations with respect to channel 4 are computed. Small variations in this data are present within a flight. The variations generally amount to about 1 or 2 nanosec.

It is not clear whether these variations represent real physical phenomena, or if they represent a measurement error and the channel delay mismatches are essentially constant. The large scale mismatches, for example, channel 1 4 nanosec and channel 3 $\approx$ -11 nanosec, are real phenomena. They represent the difference in construction and/or packaging of these processors. The 1 to 2 nanosec small scale variation of a channel, however, is a different matter. For example, the data may be in error because the characteristics of the self-test signal, and not the channel characteristics, are changing.

Associated with this problem is the software techniques for calculating the values of the channel delay mismatches. A variaty of data anomalies are eliminated so that the calculation is performed only when the data from the receiver is valid. For example, the channels must be locked and the channel outputs must have settled before calculations are performed. The calculation is performed by a fading memory filter which generally gives a better result than could be obtained by a simple unfiltered calculation. However, if the filter memory has a bad data point, the final result may be unrepresentative of the true channel delay mismatch. Such an occurrence is in the data from flight 20. Figure 4-54 shows the channel delay mismatch data used by the navigation solution for the HC receiver. These data are a result of combining the individual channel delay calculations from the ground calibration receiver and the HC airborne receiver. The test procedure called for channel mismatch calculations once per run for the airborne data, and four times per flight for the ground calibration receiver. A bad point was accepted by the software filter from the ground calibration receiver which produced a 4 ft error. On run 7, another bad point was

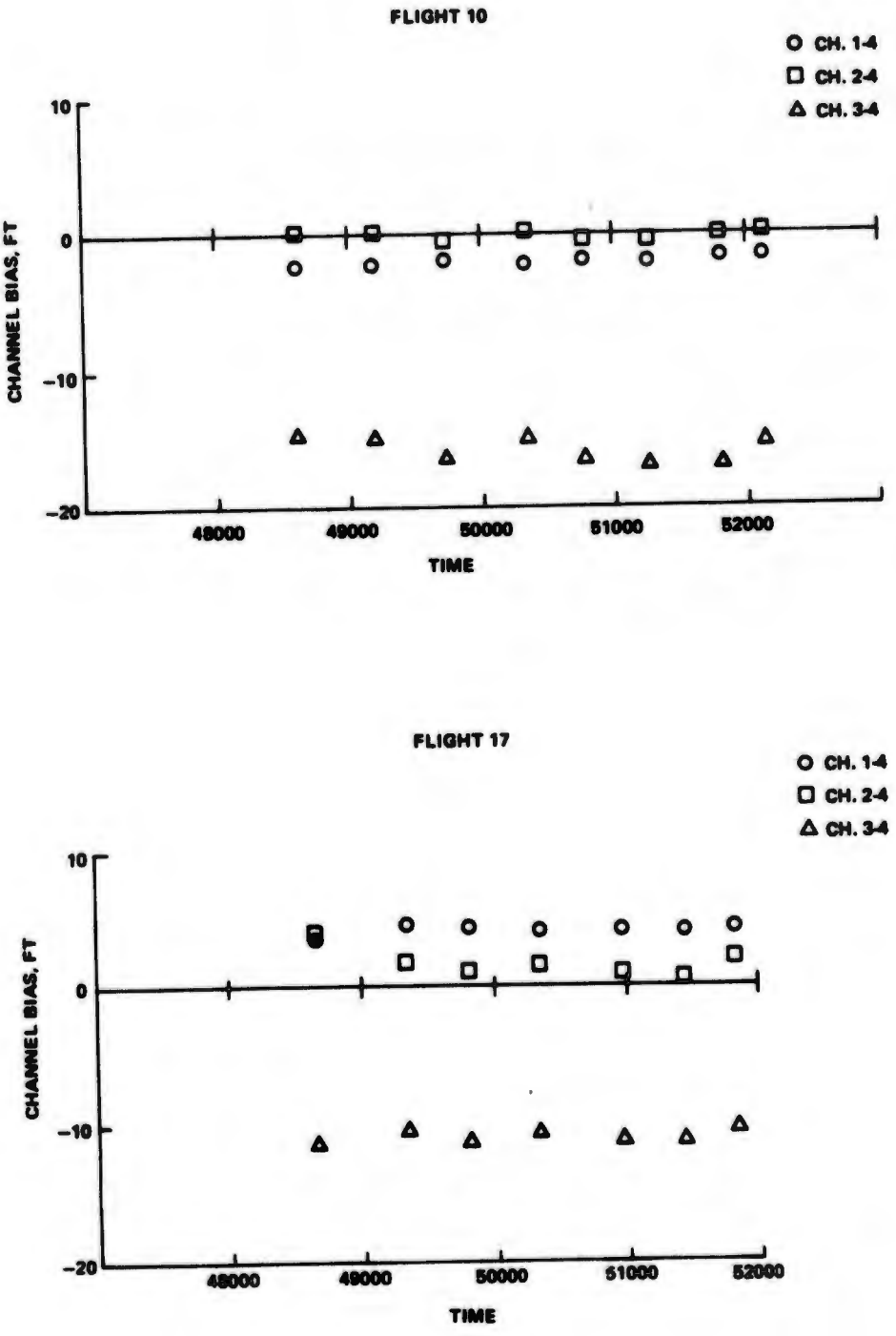

Figure 4-53 Hazeltine Receiver Channel Bias Calibrate Cycle, Receiver 1

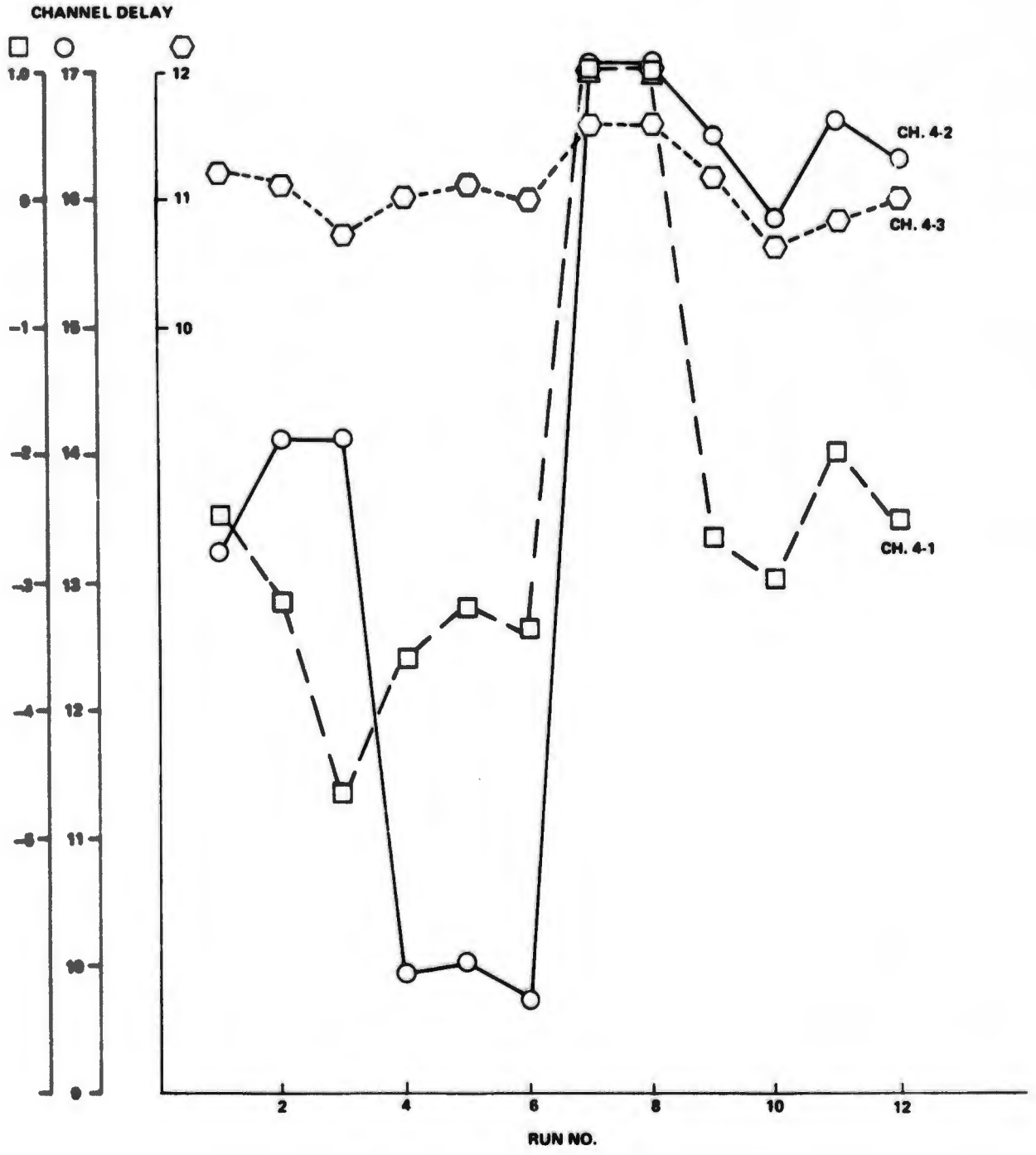

Figure 4-54 Flight 20 Composite Channel Delay Data Used in Solution for HC Receiver

processed resulting in a 3 ft error in the opposite direction. Although these errors rarely happen, the software routine may sometimes produce errors by accepting bad data points.

The overall channel delay mismatch data for the two HC receivers for flights 1-23 is shown in Figure 4-55. The values presented are the average delays for each flight. The large changes in value are the result of installing different processor units in the receiver. The small variations in value are the result of the errors discussed above.

4.3 PERIODIC ERRORS

Those error sources characterized by significant discrete frequency components (i.e., not white) cause periodic disturbances both in the measurement and the navigation solution. An example of a periodic disturbance is partly diffused, partly specular multipath.

Multipath disturbances caused by ground reflections become significant in one portion of the area navigation A flight path. A sharp increase in channel 4 variance, plus a pronounced oscillatory tendency in the data occur when the aircraft is in the vicinity of 20,000 ft north of Salt Site. At this point the look angle to channel 4 is about 37^{o} and the signal reflections from SC-50 cause ground multipath errors in both receivers.

Figures 4-56 and 4-57 show the observed standard deviations of the residual, $\delta R4\text{-}1$, computed by

$$\delta R_{4-1} = (R_4 - R_1)_{\text{nav solution}} - (R_4 - R_1)_{\text{WSMR}}$$

versus the elevation angle from transmitter 4 to the aircraft. There is an almost linear slope of this data of about 2 ft (1σ) per 60^{o} of elevation angle for HC and 1.2 ft (1σ) per 60^{o} for Magnavox. The data actually contains significant quantities of periodic components throughout this region. These appear noise-like due to the high aircraft velocity and the inability of the standard deviation calculation to differentiate the periodic components from the noise. Figures 4-58 and 4-59 show an analysis of a portion of the trajectory data from Flight 19, Run 5 for the MRL and HC receivers respectively. A correlogram and an amplitude spectrum distribution for the channel 4-1 residuals computed as shown above indicate the presence of relatively strong periodic components in the data. This data sample is from a region approximately 4500 ft north of Salt Site. The spectral components are typical of the data along this portion of the flight path. (Note: the navigation solution data used in this analysis is an output of the two-state filter).

Multipath errors are experienced mainly at low elevation angles where the signal received at the user's receiving antenna is the resultant of the direct signal path through the atmosphere and a reflected signal path from the earth's surface and/or from the aircraft's structure. The effect of a multipath signal on the receiver measurement performance is dependent upon many variables. The primary receiver variables are the sensitivity of the technique for measuring range (tracking the signal) to signal multipath and the frequency and relative amplitude of false signal presented to the tracking loops, which is dependent upon design variables such as signal processing bandwidth and gain control. The multipath signal strength at the aircraft is primarily dependent upon ray path, the transmitting antenna design and the antenna height above the earth's surface. Other factors which affect the multipath signal are the receiving antenna design and its location on the aircraft, the signal polarization and frequency, and the signal modulation characteristics.

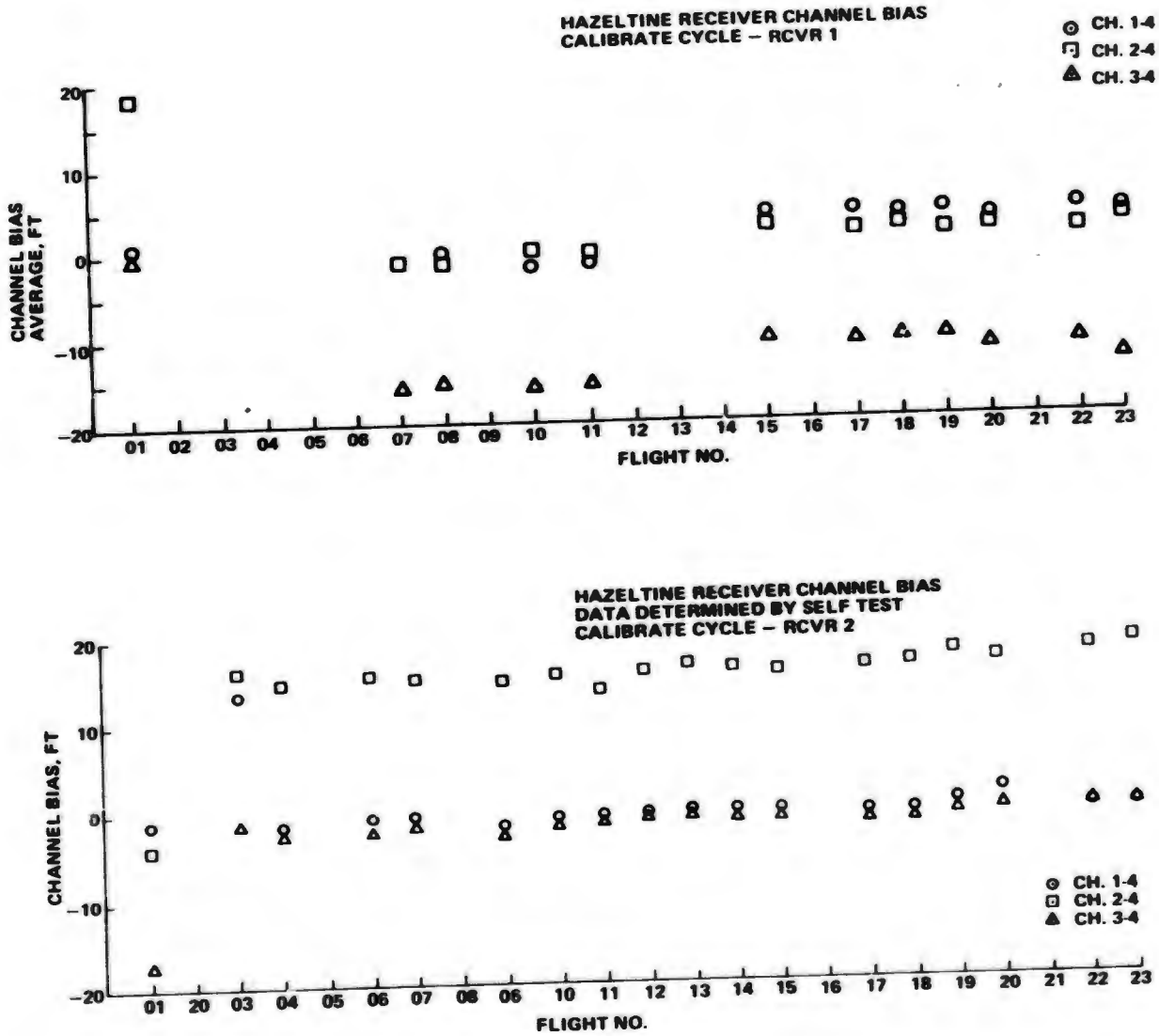

Figure 4-55 Hazeltine Receiver Channel Bias

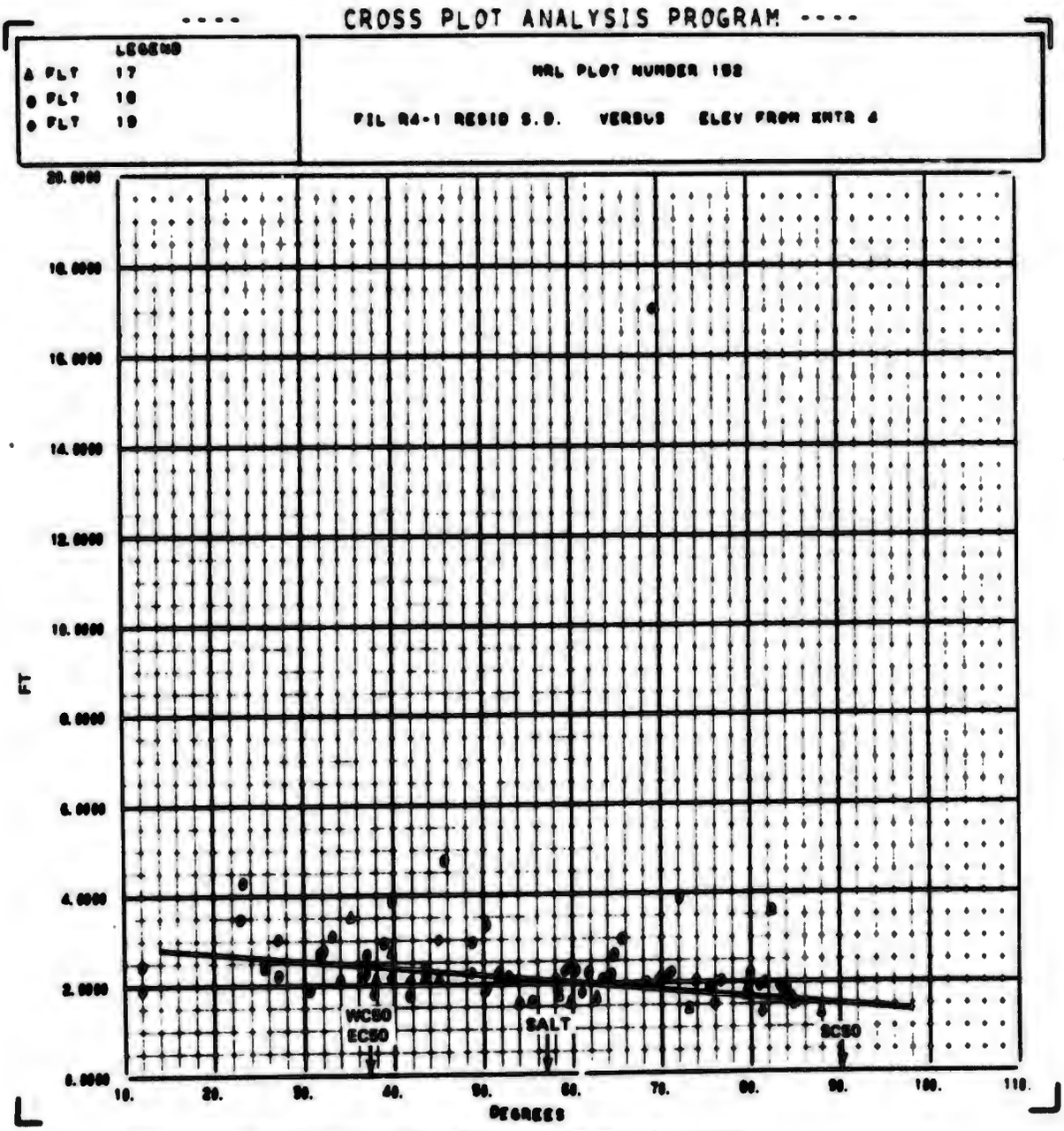

NOTE: CHANNEL 4 MINUS CHANNEL 1 RESIDUAL σ VERSUS ELEVATION ANGLE FROM CHANNEL 4 SHOWING INCREASED NOISINESS WITH Y POSITION NORTH OF SALT (MRL)

Figure 4-56 MRL Standard Deviation

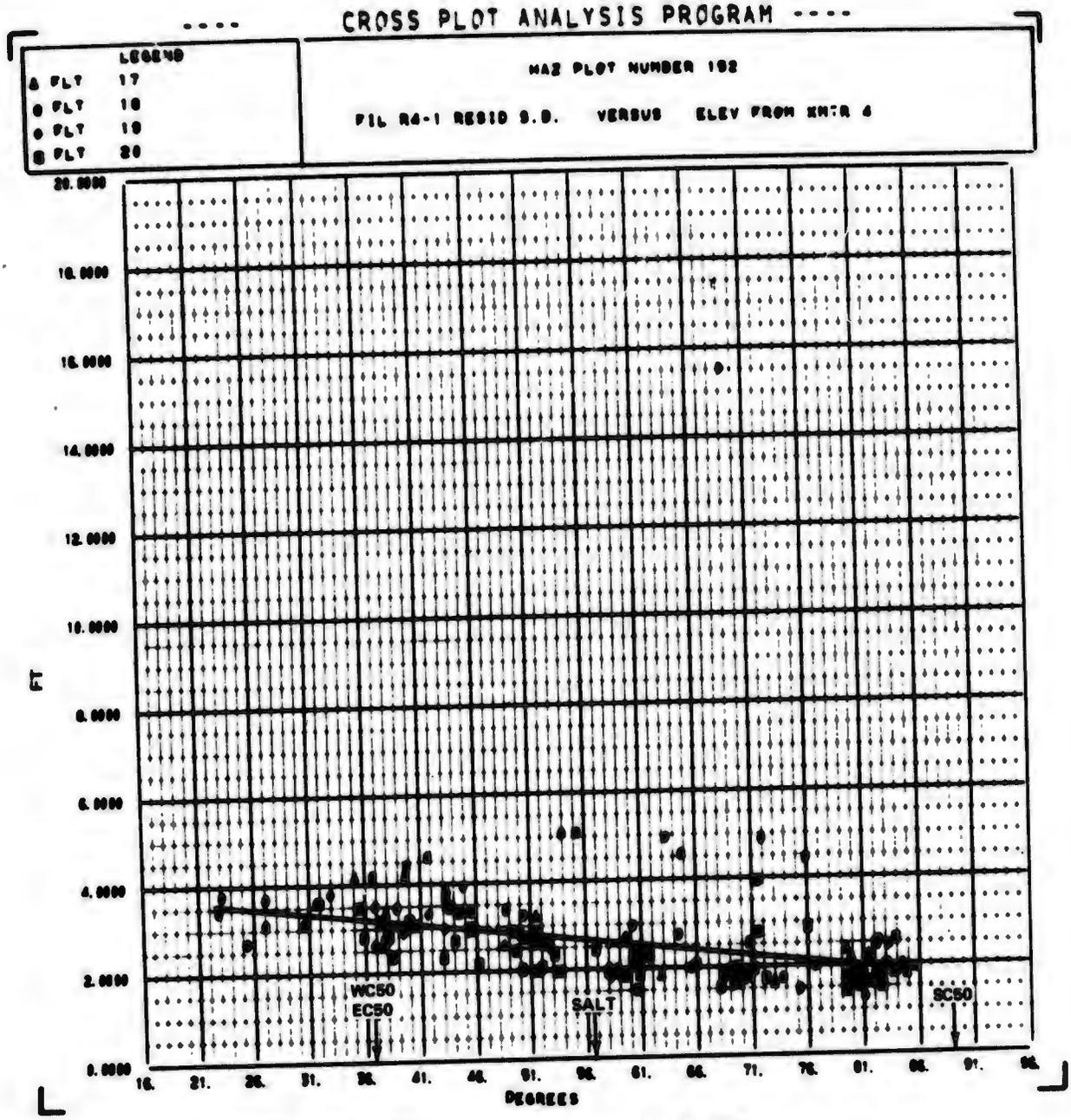

NOTE: CHANNEL 4 MINUS CHANNEL 1 RESIDUAL σ VERSUS ELEVATION ANGLE FROM CHANNEL 4 SHOWING INCREASED NOISINESS WITH Y POSITION NORTH OF SALT (HAZELTINE)

Figure 4-57 HAZ Standard Deviation

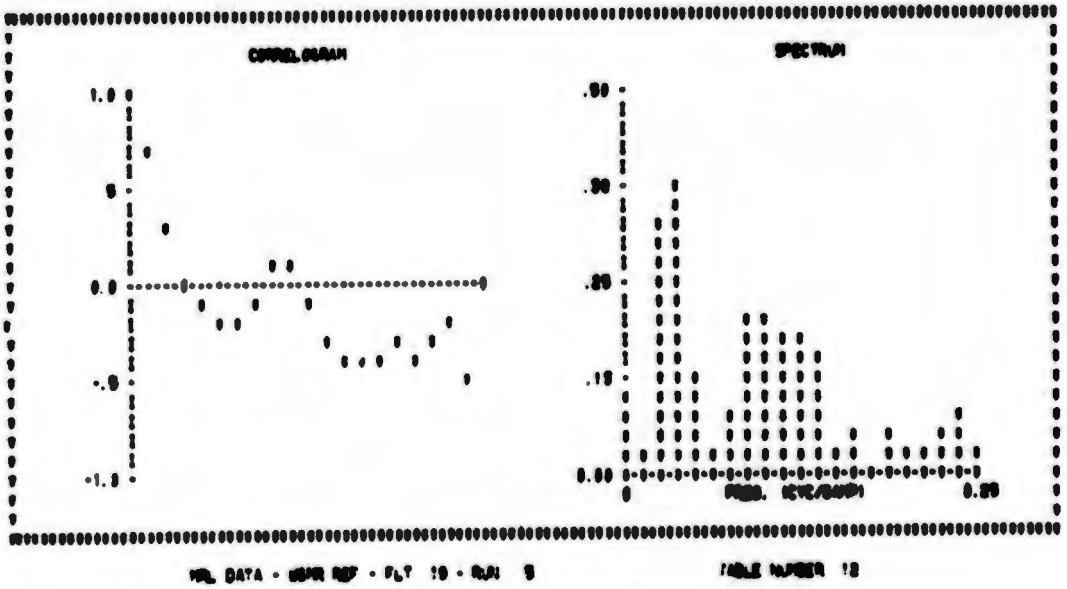

Figure 4-58. Spectrum Analysis Plot, MRL Data

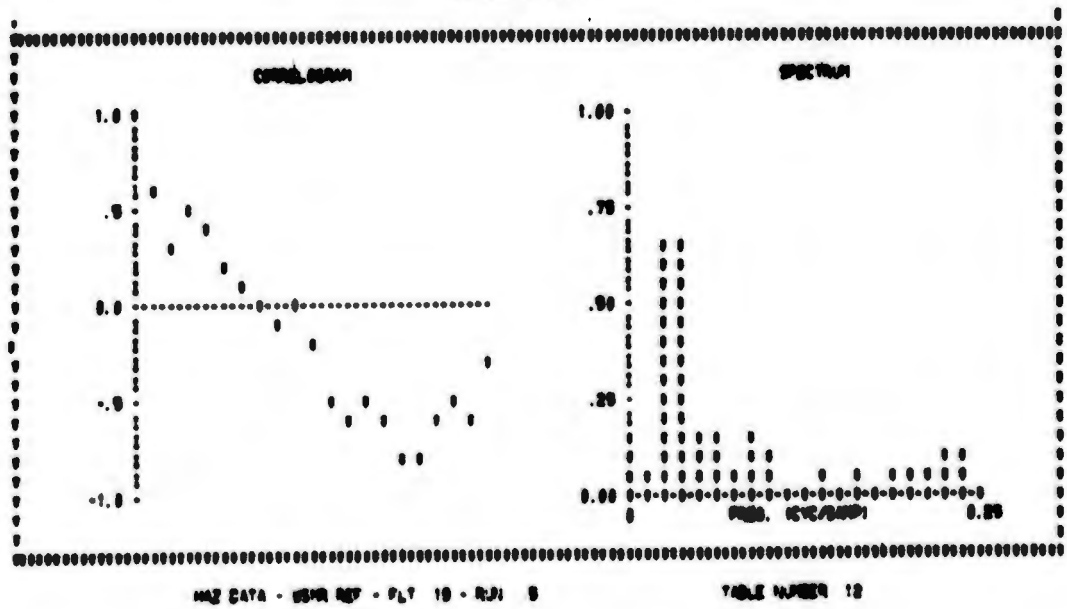

Figure 4-59 Spectrum Analysis Plot, HAZ Data

The range and range rate errors are a function of the geometry dependent system (time varying propagation channel caused by aircraft's motion) and the receiver design. The significant aspects of the receiver design affecting multipath sensitivity are the received signal power, pseudo noise code characteristics, carrier and code tracking loop noise bandwidth, and the code tracking loop discriminator transfer function (see Section 9 for a more detailed discussion).

Multipath can cause both bias and random errors in the measurement of pseudo range and pseudo doppler depending on the properties of the propagation medium. The multipath errors in the system demonstration and ILS tests can be attributed to:

- Errors in ground-to-aircraft links (both diffuse and specular)
- Error due to aircraft structure (predominantly diffuse)
- Errors on the calibration links (specular).

Range Error

The multipath range bias error characteristics of the correlation receiver in terms of the received signal characteristics is given by:

$$\Delta R_m = \begin{cases} d\,\dfrac{R_1}{1+R_1}\,, & d < 50(1+R_1) \\ (150-d)\,\dfrac{R_1}{2-R_1}\,, & 50(1+R_1) \le d < 150 \\ 0\,, & d \ge 150 \end{cases}$$

where

$$R_1 = R\cos\left[\frac{2\pi}{\lambda}\,d - \phi\right]$$

R is the magnitude of the voltage reflection coefficient for either vertical or horizontal polarization

λ is the wavelength (ft)

d is the differential delay (ft)

ϕ is the phase angle (rad.) for either vertical or horizontal polarization. The specular multipath contribution to range error was found to be approximately 2 ft.

Range Rate Error

The changing system geometry causes a beat between the direct and specularly reflected signals, called the differential doppler or fade frequency. The rate of change of phase between the direct and interfering signals can be shown to be

$$\dot{\alpha} = \frac{\Delta\omega R[R+\cos(\Delta\omega t+\phi)]}{R^2+2R\cos(\Delta\omega t+\phi)+1} \qquad (1)$$

where $\Delta\omega = \frac{2\pi}{\lambda}\,\dot{d}$ is the differential delay or fade frequency and $\dot{d}$ is the rate of change of differential delay.

Eq. (1) can be expanded in a Fourier series of form

$$\dot{\alpha} = \Delta\omega \sum_{i=1}^{\infty} (-1)^{n+1} R^n \cos[n(\Delta\omega + \phi)] \tag{2}$$

In terms of the carrier tracking loop parameters, the velocity error is

$$\Delta\dot{R}_u = \frac{\lambda}{2\pi} (\Delta\omega) \sum_{i=1}^{\infty} (-1)^{n+1} R^n P_{B_L}(\Delta\omega) \cos[n(\Delta\omega t + \phi)] \tag{3}$$

$$P_{B_L}(x) = \begin{cases} 1 & |x| \leq B_L \\ 0 & \text{otherwise} \end{cases}$$

where B_L is the one-sided loop noise bandwidth of the carrier tracking loop. Note that Eq. (3) shows the effects of bandlimiting on velocity error, i.e. if $n\Delta\omega > 2\pi B_L$ there is no error in velocity due to multipath.

The multipath contribution to range rate error is significant. It was found to be on the order of 0.6 fps at the worst flight/transmitter geometries.

Errors in Ground-to-Aircraft Links

These errors are characterized by diffuse reflections for high elevation angles and specular reflections for low elevation angles. The diffuse reflections are rejected by the aircraft antenna which is right hand circularly polarized while the reflected signal is left hand circularly polarized.

At low elevation angles, the antenna on the aircraft does not provide polarization discrimination of the reflected signals. Multipath in this case is characterized by a fade frequency which is a function of the velocity and height (AGL) of the aircraft, transmitting antenna height (AGL) and relative look angles. These errors are identifiable by spectral analysis of the data.

Errors Due to Aircraft Structure

The multipath in this case is a function of the relative placement of the antenna with respect to the aircraft structure. The errors are highly diffuse and rapidly changing with the attitude of the aircraft. These errors have a noiselike effect on the data.

4.4 SUMMARY OF BIAS AND PERIODIC ERRORS

Table 4-7 gives a summary of the magnitude of the observed and theoretically predicted systematic errors. The approach taken in summarizing the bias errors provides a good estimate of the magnitude and relative significance of the biases. A rigorous treatment of bias errors is given in Section 6, where the location and sign of each bias error in the system is identified for flights 17-23.

The most significant steady-state errors are the interchannel biases, cesium time delay measurements, uplink antenna apparent signal delays and transmitter attenuator leakage. These four sources of systematic errors contribute 18 ft of the total 19.3 ft of the root sum squared (rss) errors.

Table 4-7 System Steady State and Periodic Errors

	Hazeltine		MRL		Remarks
	ΔR	$\Delta \dot{R}$	ΔR	$\Delta \dot{R}$	
A. Aircraft Rcvr					
1. Interchannel Biases					
(a) Power Level Variation	12	N.A.	0.5	N.A.	Maximum
(b) Spectral Distortion	0.5	N.A.	0.5	N.A.	Estimated Minimum
(c) Other	1	N.A.	N.A.	N.A.	Calib Cycle
2. Dynamics	0	0	0	0.4	Maximum
3. Clock Error	0.1	0	0.1	0	
B. Up-Link					
1. Multipath	2	0.6	2	0.6	Maximum
2. Antenna Delay	4*	N.A.	4*	N.A.	Over Salt
3. Troposphere	0	0.3(1)	0	0.3(1)	(1) Not Modelled
C. Transmitter					
1. Spectral Distortion	4	N.A.	1	N.A.	Maximum
2. Attenuator Leakage	5□/0.5△	N.A.	5□/0.5△	N.A.	□Fits 1 Thru 15 △All Other
3. Cable Length Uncertainty	2	N.A.	2	N.A.	
4. Mismatch	0.1	N.A.	0.1	N.A.	
D. Cal Receiver					
1. Interchannel Biases					
(a) Spectral Dist	0.5	N.A.	0.5	N.A.	Estimated Minimum
(b) Ant Interaction	1	N.A.	1	↓	
2. Cable Length Uncertainty	2	N.A.	2	↓	
3. Power Combiner	0.5	N.A.	0.5	↓	
4. Mismatch	0.1	N.A.	0.1	↓	
E. Cal-Link Propagation					
1. Refraction	3	0	3	0	
2. Cesium Time Delay	12	0	12	0	
3. Multipath	3	0	3	0	Slow Variation (Not Calibrated)
Total (RSS)	19.5	0.67	14.7	0.77	

*Note: Applicable to Fits other than 17 thru 20 where it is modelled.

The user vector position errors, $\Delta\bar{S}_i$, determined by a comparison of the solution to WSMR data for all test data from flights 17-23 in a region bounded by GDOP $\leq$ 10 (representing realistic geometries which may be encountered in an operational system) have been averaged to form a total solution mean error,

$$\Delta\bar{S}_m = \frac{1}{N}\sum_{i=1}^{N}\Delta\bar{S}_i$$

where N is the total number of samples in region with GDOP's $\leq$ 10, (approximately 10,000 points) and

$$\Delta\bar{S}_i = \sqrt{\Delta x_i^2 + \Delta Y_i^2 + \Delta Z_i^2}\ .$$

The total solution mean error for the two sets of data obtained from the HC and MRL user receivers on these flights was found to be 38.9 ft and 31.6 ft respectively. The rss values of the measurement errors in Table 4-7 were found to be related to the total solution mean error for both receivers by a factor of two.

This result lead to the conclusion that an average value of the navigation solution sensitivity to measurement errors over the total measurement and solution domains is approximately 2.

The predominant source of periodic error in the system is multipath. While there are two major sources of periodic errors, multipath reflection and loop dynamics, multipath was found to be the most significant, causing approximately 2 ft range error and 0.6 fps error in range rate measurements, with slant range acceleration contributing an error of 0.4 fps maximum in range rate in the MRL receiver due to a timing mechanization problem (see Section 4.5).

4.5 SYSTEM CLOCK PERFORMANCE

The test system contained seven principal oscillators. Each of the four transmitters and each of the three receivers contained one primary oscillator. The test system precision, and to a lesser extent, the accuracy, depend greatly on the behavior of these oscillators.

During the 621B experiment program, the four channel clocks of the calibration receiver in the MCS were monitored whenever a data flight took place. An examination of this data provides not only valuable insights into the performance of the clocks themselves but also furnishes useful clues to the causes of system anomalies which could frequently be related to clock anomalies.

4.5.1 Oscillator Stability

The calibration receiver data obtained during flight represents the time history of the four transmitter oscillators measured against the calibration receiver oscillator. The carrier tracking loop data (pseudo-doppler output of the receiver) is a direct

measure of the transmitter vs calibration receiver oscillator frequency offset. Changes in the carrier loop output represent either real changes in the transmitter or receiver oscillator frequency or anomalous carrier loop performance. Since the rf carrier and the PRN code modulating the carrier are generated coherently in the transmitter, it is possible to determine carrier loop anomalies in the calibration receiver by comparing the carrier loop output with the code loop output. For purposes of this discussion, the two loops operate independently. A change in either the transmitter or receiver oscillator will be reflected in the output of both loops. An error developing in either loop will show up only in that loop output thus isolating loop failures from oscillator behavior.

The recorded data from flights 1-23, area navigation configuration, have been analyzed for oscillator behavior. Two general observations will be made; one regarding the basic oscillator stability and the other regarding aberrant oscillator behavior.

As far as the clock oscillator performance itself is concerned, we can say as a general observation that, when operating normally, all clocks evidenced acceptable stability. Out-of-spec short-term conditions usually occurred as the result of some malfunction in the circuitry, the power supply or the environment. The oscillator drift rates were low, and were also generally very linear during the monitoring period. We examined the clock data in detail for only two flights, 20 and 22, which seemed typical of all flights in which the clocks operated normally. The drift rate specification was $\Delta f/f < 5 \times 10^{-10}$/day.

Since the drift data was normally taken only during the approximately 1.5 hours of the actual flight, we linearly extrapolated to a 24-hour period, which we feel is justifiable because of the highly linear drift rate characteristics exhibited. On virtually every flight showing normal oscillator operation, the drift rate and drift direction is the same. This is true in spite of the fact that the oscillators had been turned on anywhere from 12 to 24 hours before the test flight. The effect of this is to be sampling the data at different intervals after oscillator start up and always finding virtually the same result. Thus while the linear extrapolation of data from 1.5 to 24 hours may at first seem extreme, in fact we have supporting evidence gathered during various 1.5 hour samples of the 24-hour period that the normal oscillator behavior is practically a straight line drift. The 24 hour drift data for the four receiver channels is presented below.

Channel	$\frac{\Delta f}{f}$ Flight 20	$\frac{\Delta f}{f}$ Flight 22
1	1.1×10^{-8}	2.4×10^{-8}
2	1.1×10^{-8}	5.9×10^{-9}
3	3.5×10^{-8}	1.5×10^{-8}
4	0	3.9×10^{-9}

Visual examination of the clock data for other normal operation flights confirmed that the above clock performance is very typical of that exhibited during the entire experiment program. Figure 4-60 shows the oscillator records for flight 20 obtained from the MCS calibration receiver.

4.5.2 Oscillator Failures

The ground system oscillators exhibited various types of failures during the test program. Some failures could be classed as catastrophic. These prevented the computation of a valid navigation solution. Other failures were more graceful and, for various reasons, did not prevent computation of the navigation solution.

Flight 3 data shows a good example of a graceful failure of the calibration receiver oscillator. In this case (Figure 4-61) all 4 channels show similar problems which isolates the cause to the receiver oscillator. The failure probably is a result of a malfunctioning oscillator oven control. This type of behavior does not destroy the navigation solution. The effect is to greatly increase the computed clock bias rate (B). However, the solutions are structured so as to allow this as long as the clock bias acceleration (B) term remains very low.

Another type of oscillator failure is shown in Figure 4-62. In this case, which occurred during flight 11, the transmitter 3 oscillator developed a severe instability. Comparison of the carrier loop output with the code loop output confirms that the problem is not associated with the receiver but rather is present on the input signal. This type of failure is caused by a noisy oscillator control voltage. The oscillator is self-contained with the control voltage developed within the unit. This type of problem was normally traced to a failed element in the control voltage circuit.

Because of the method used in computing the navigation solution, oscillator behavior of this type has only minimal effect on the solution. The calibration receiver data is brought into the solution with the airborne data once per second. Since these frequency excursions are occurring in the tracking loops at both receivers, by subtracting the two sets of data (the process used to synchronize the system via software) at a rate of 1 cps removes most of this effect.

One other type of oscillator failure is significant in this test program. Properly speaking, this is not an oscillator failure, but rather a failure in the MCS frequency module which provides the required receiver frequencies derived from the primary oscillator. Figure 4-63 shows data from flight 7. The frequency module is indicating incipient failure in run as shown by the noise burst. This problem is only affecting the carrier loop since no similar phenomena can be seen in the code loop output. This type of failure is generally catastrophic in the computation of the navigation solution, although the example given in Figure 4-63 is not too severe since the frequency module has not fully failed.

4.3.5 User Clock Analysis

During the field tests, the pseudo ranging technique of passive user navigation was used to derive the aircraft's trajectory. This method, as explained earlier (Section 3), allows the user to deterministically compute the phase and frequency offsets between his reference clock and the system time base which, in our case, is the MCS clock. Ideally these offsets, called the pseudo-range and pseudo-doppler clock biases, are well behaved functions of time and therefore may be used to improve the user's trajectory data (i.e. a two-state filter) or provide a degraded three-measurement mode of navigation (Ref. 33). In order to fully exploit the desirable characteristics of the clock biases, the user must be aware of system bias errors (for the clock bias quantities are dependent on geometry just as the X, Y, Z trajectory coordinates) and he must also keep changes in common-mode system errors within tolerance (since the clock calculations are affected by common errors even though the X,Y,Z calculations are not).

If we assume stable oscillators (no drift), the user's clock bias rate is a constant with time

$$\dot{B} = \text{(user's clock frequency)} - \text{(system clock frequency)} + \text{(error terms)} = k$$

Likewise the user's pseudo-range clock bias is a straight line in time

$$B = \text{(user's initial clock phase)} - \text{(system initial clock phase)} + \text{(error terms)} + \dot{B}t$$

where t is generalized time. These relationships are derived in Ref. 1. We establish, then, the following model

$$B(t) = N(0, 0.0005) \qquad \text{(normal random variable)}$$

$$\hat{B}(t) = B(t - \Delta t)$$

$$\hat{B}(t) = B(t - \Delta t) + \dot{B}(t - \Delta t)\,\Delta t$$

and we are interested in a quantitative measure of how well the test data corresponds to this model. The two-state Kalman filter employs this clock model. The outputs of this filter were used to perform this analysis.

Figure 4-64 shows the MCS received pseudo-doppler data versus time for flight 19, run 4, a typical run. These data represent the transmitter clock frequency relative to the MCS clock frequency and show very high short term stability for all five oscillators. Noise content of less than 0.1 fps is apparent for all channels and small drifts, barely detectable on channels 1 and 3, are less than 0.01 feet per second. These drifts are clearly smaller than modelled, so we expect good filter performance. Figure 4-65 verifies this prediction for the Hazeltine data, but shows a model offset for the MRL case.

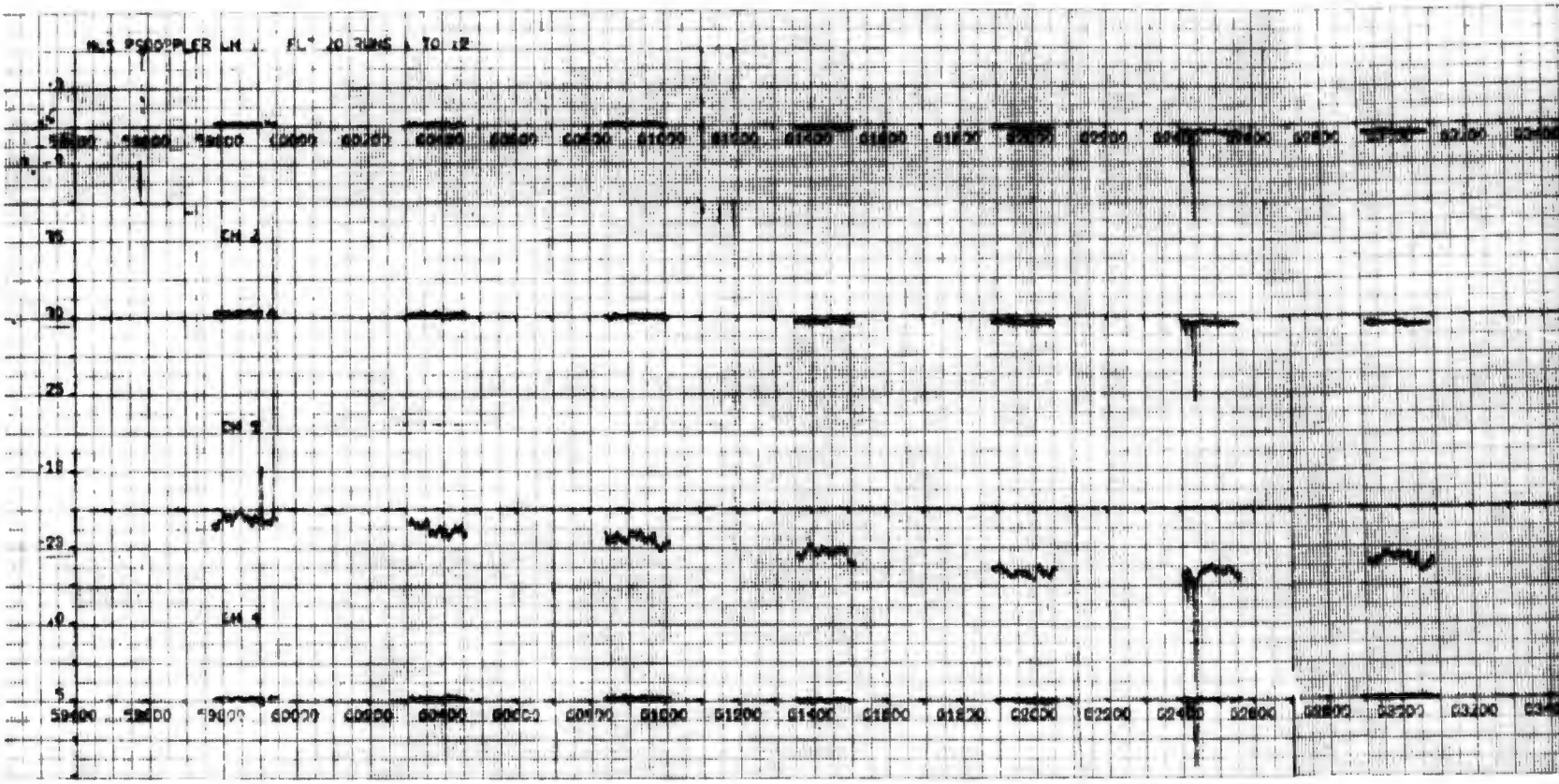
M.S. DOPPLER LM
FL° 20 RUNS A TO Z
CH 4
CH 2
CH 1

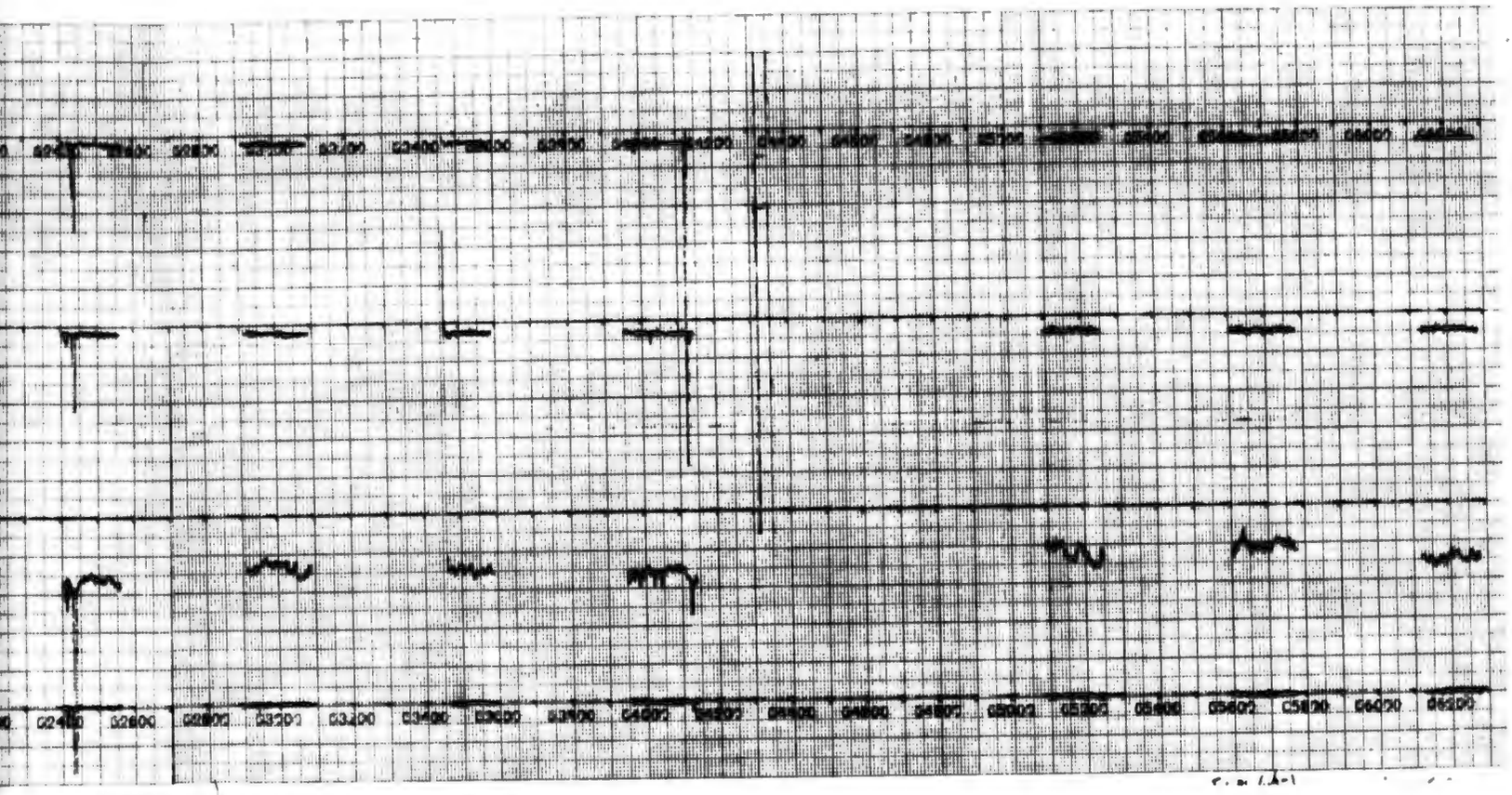

Figure 4-60 Flight 2 Oscillator Records

2

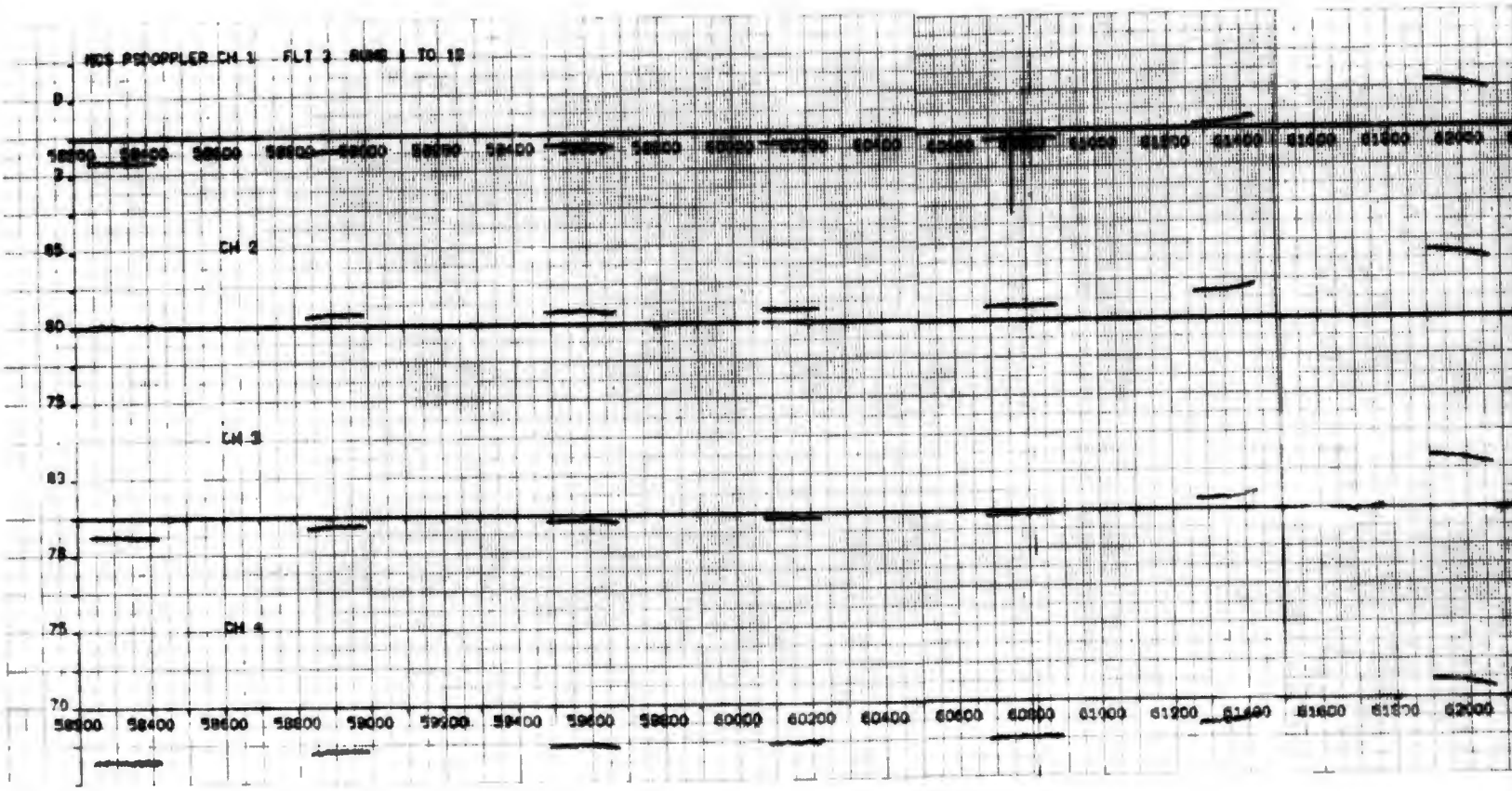
MCS DOPPLER CH 1 - FLT 2 RUNS 1 TO 12
CH 2
CH 3
CH 4

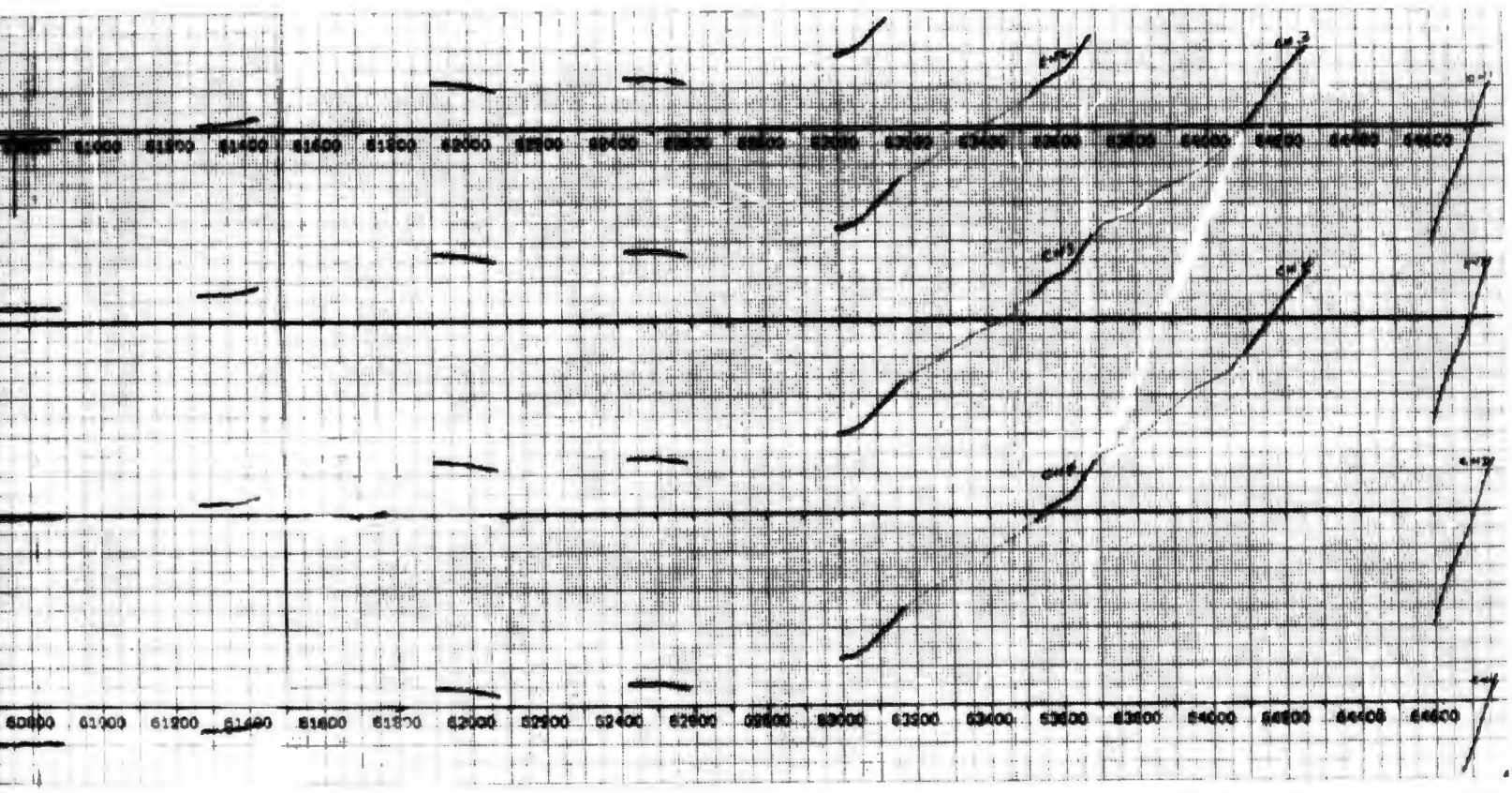

Figure 4-61 Flight 3 Oscillator Records

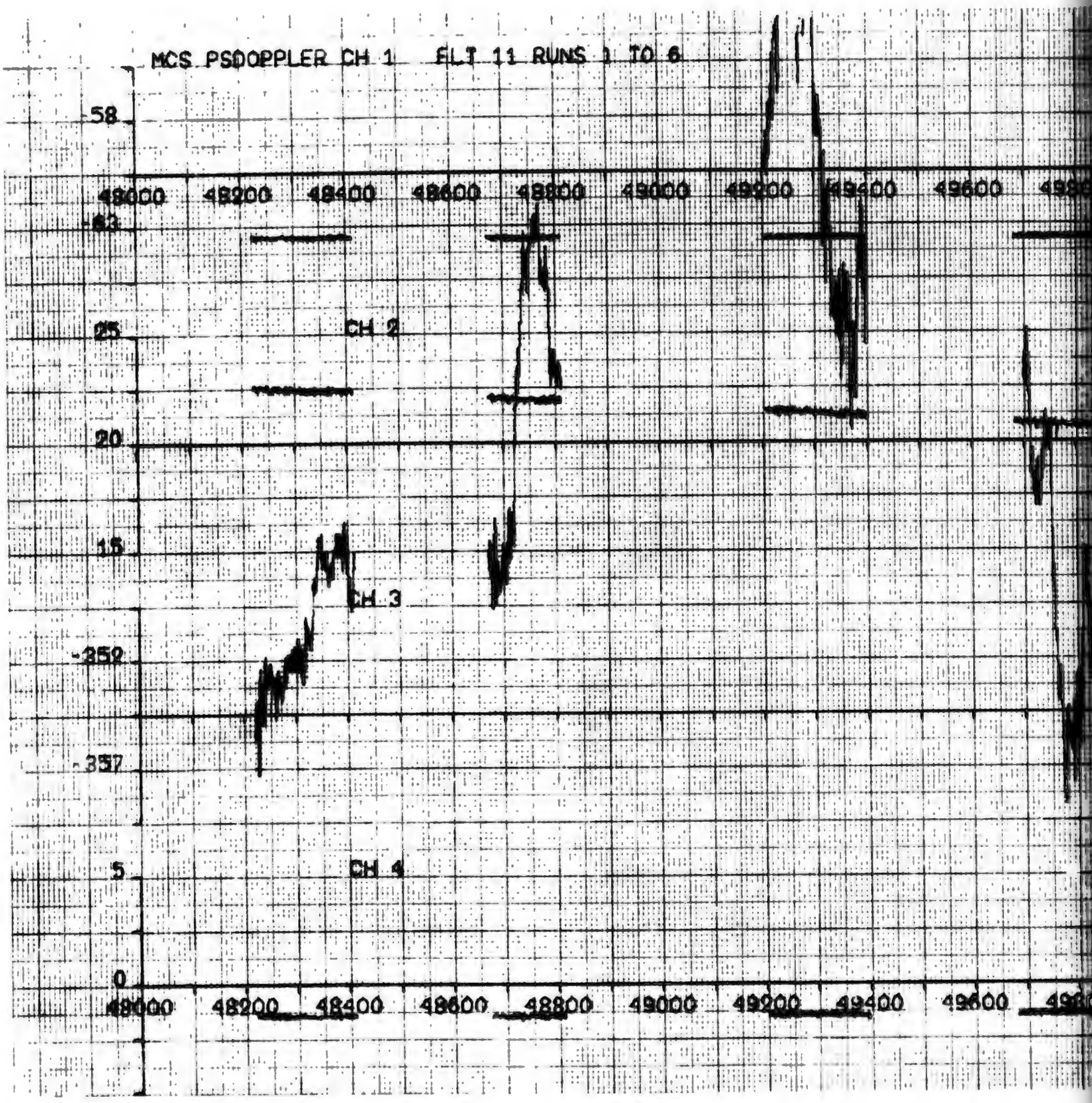
MCS PSDOPPLER CH 1 FLT 11 RUNS 1 TO 6
58
48000
48200
48400
48600
48800
49000
49200
49400
49600
-63
25
CH 2
20
15
CH 3
-352
-357
5
CH 4
0
48000
48200
48400
48600
48800
49000
49200
49400
49600

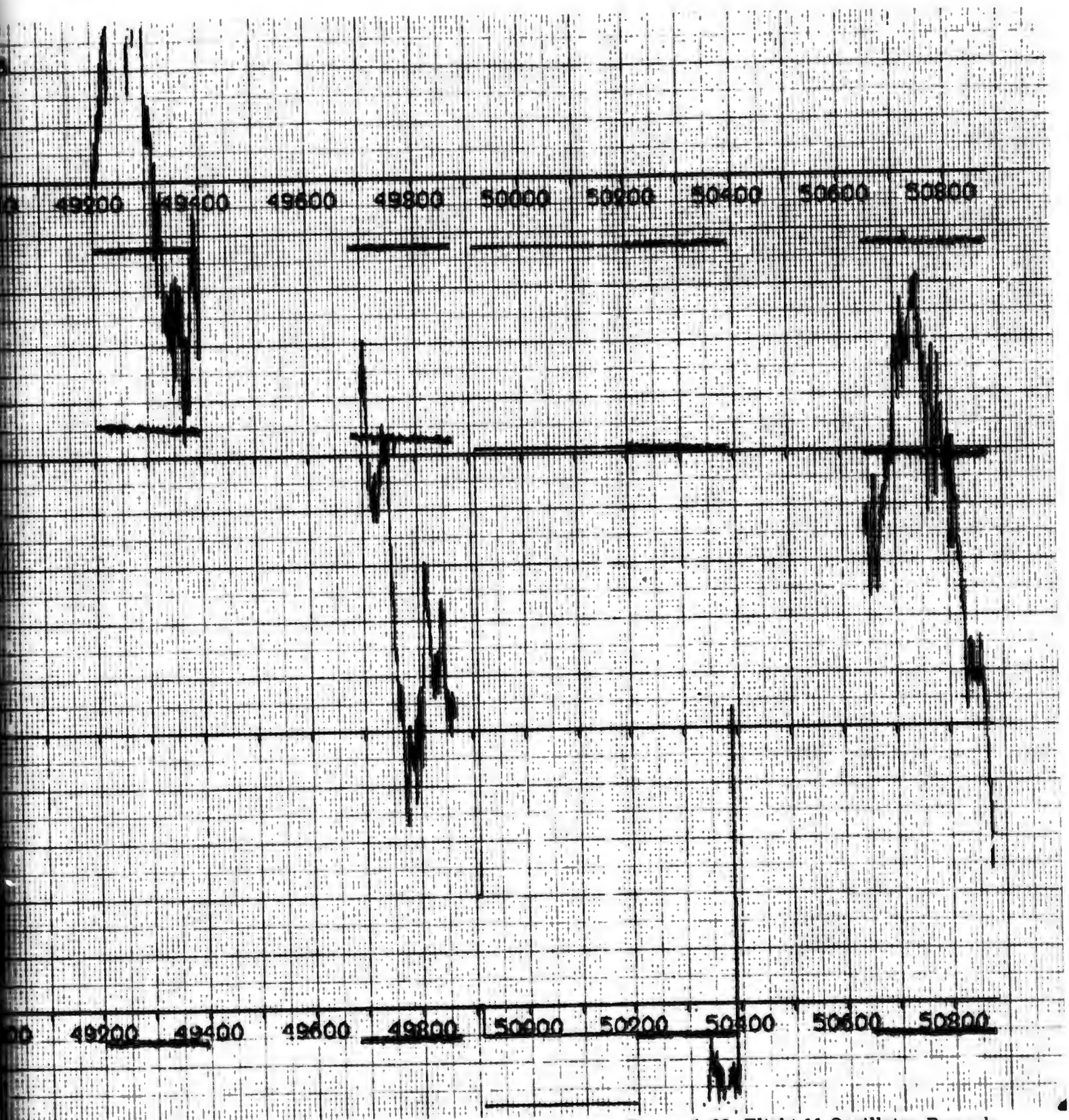

Figure 4-62 Flight 11 Oscillator Records

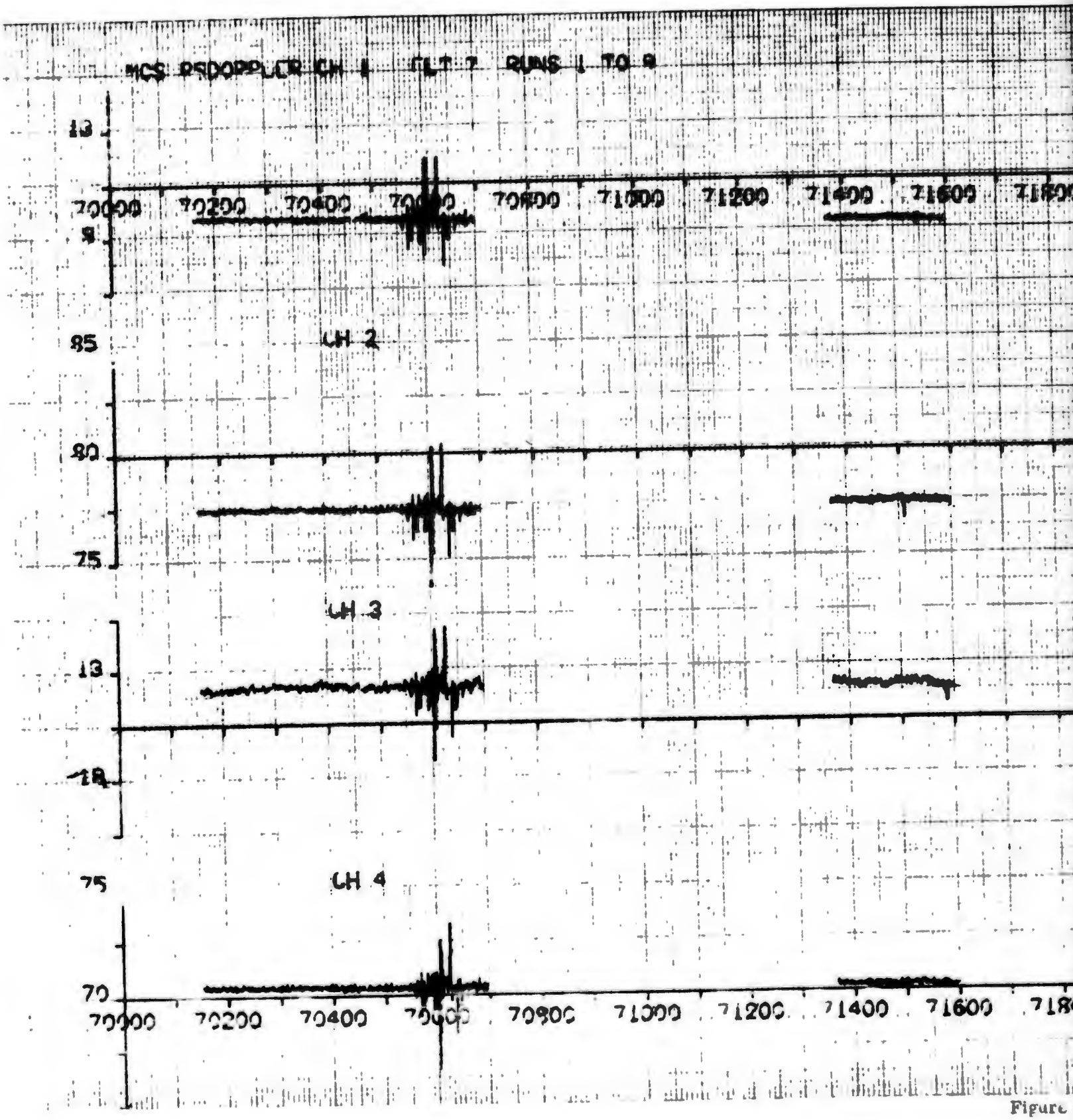
MCS RSDOPPLER CH 1 FLT 7 RUNS 1 TO 8
13
70000
70200
70400
70600
70800
71000
71200
71400
71600
8
85
CH 2
80
75
CH 3
13
-18
75
CH 4
70
70000
70200
70400
70600
70800
71000
71200
71400
71600

Figure

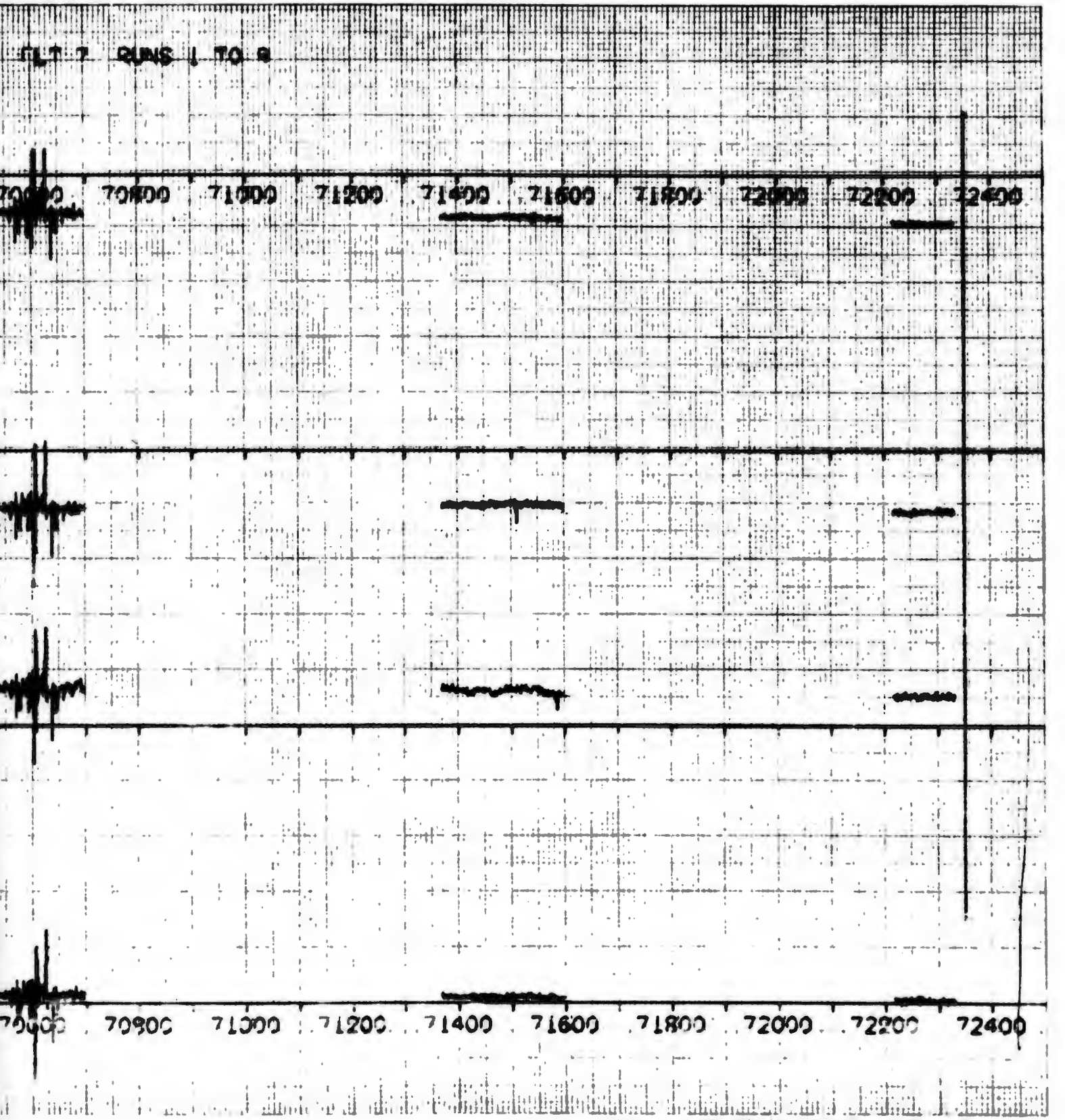

Figure 4-63 Flight 7 Oscillator Records

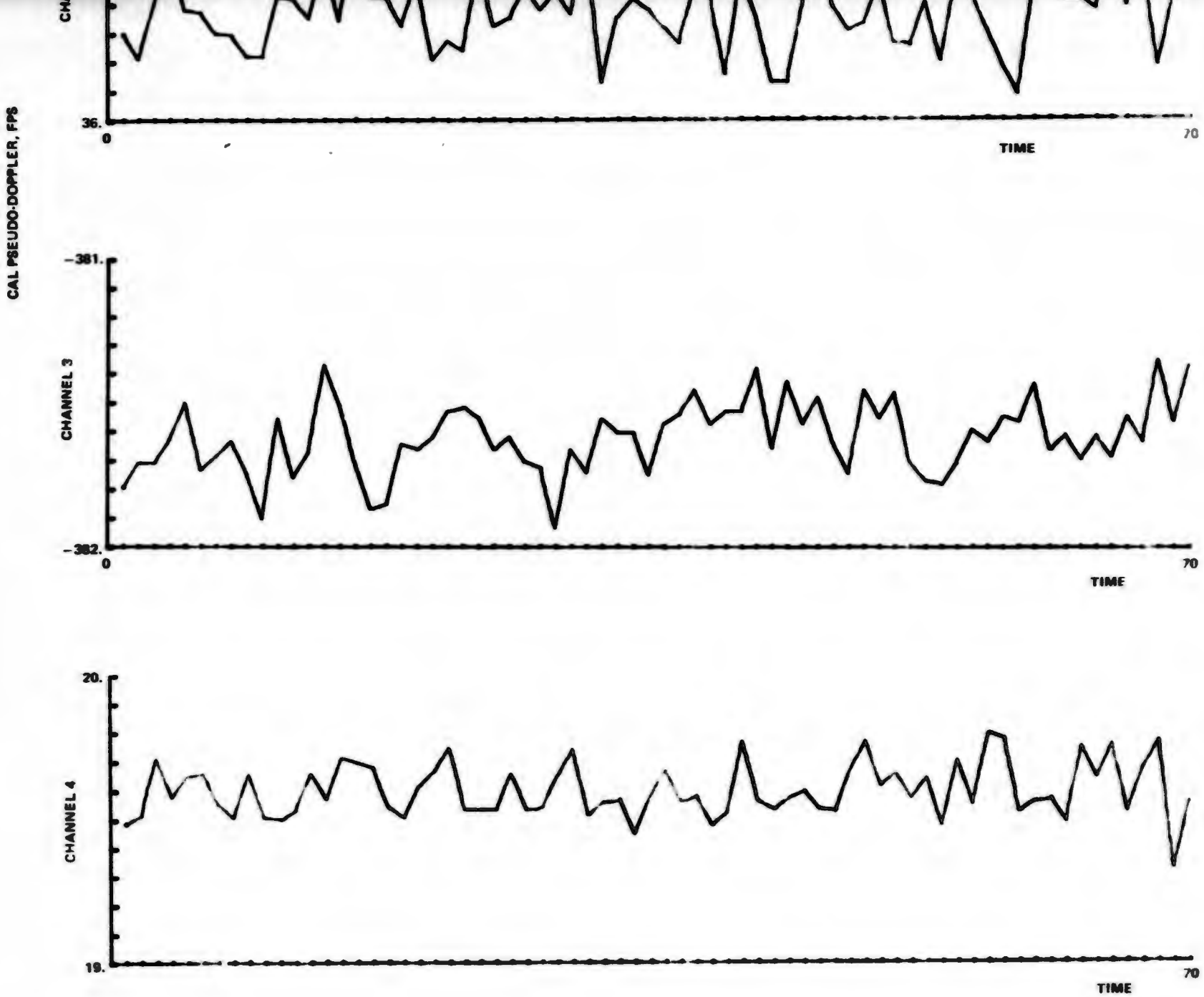

Fig. 6.4-5 CAL Pseudo-Dopplers for Flt 19 Run 4 Showing Good Stabili

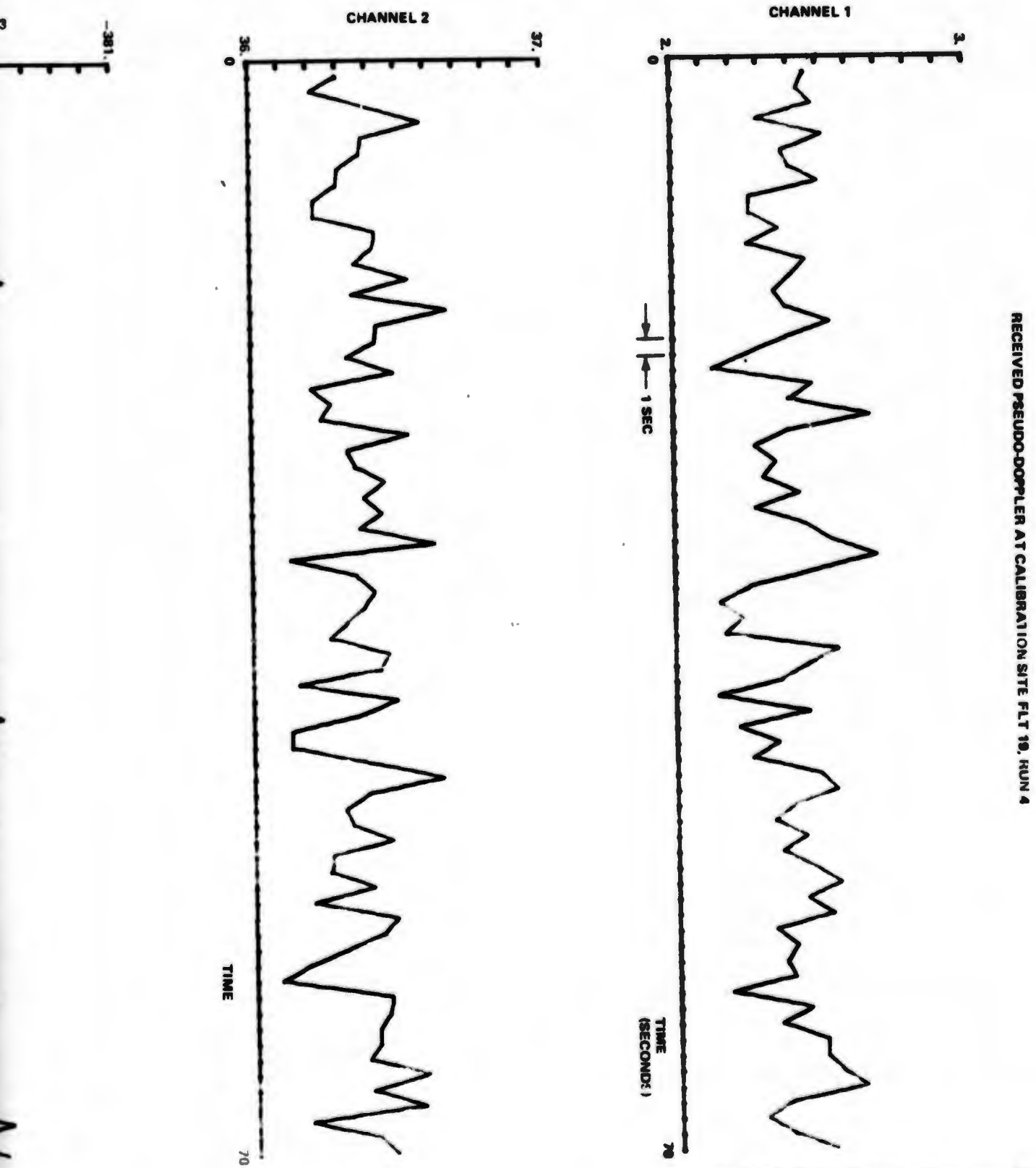

Figure 4-64 CAL Pseudo Dopplers for Flight 19, Run 4 Showing Good Stability

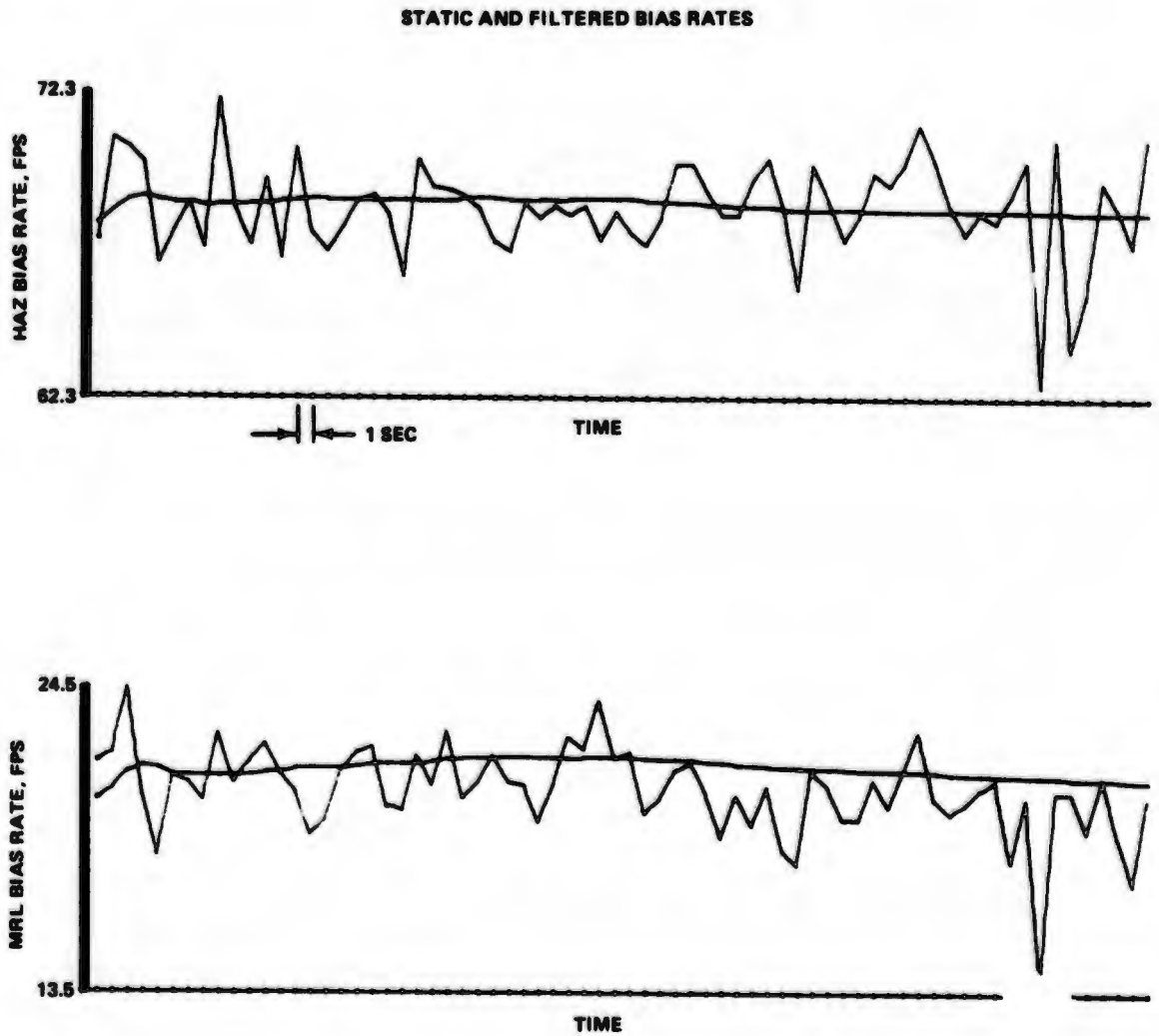

Figure 4-65 HAZ and MRL Bias Rate Measurements for Flt 19, Run 4 Showing MRL Drift

Since both Hazeltine and Magnavox user equipment are operated simultaneously, and receive the same transmitted signal, the drift in the MRL clock bias rate must be unique to the MRL user receiver. The observed drift in B, which is, for this run, greater than 0.035 feet per second squared is highly unlikely for user clock instability. This effect is due to an implementation problem in the MRL receiver whereby the receiver range rate output is not referenced in time to the other outputs.

Specifically, the HC and MRL systems are implemented differently for the measurement of pseudo doppler. This results in an overall 50 ms time mismatch for the MRL data as shown by the timing diagram below.

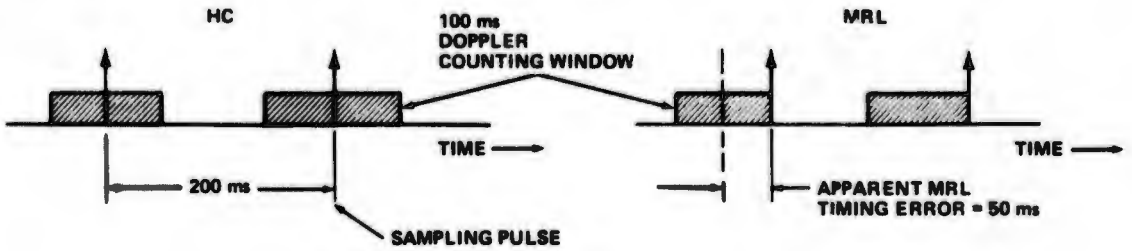

The pseudo-doppler data for the HC receiver is effectively sampled and time tagged in the center of the 100 ms doppler averaging window. This is accomplished by positioning the doppler averaging window precisely over the data sampling pulse. The MRL receiver implementation however, has the sampling pulse at the end of the 100 ms averaging window. Thus the doppler value which represents the data at the center of the averaging window, is erroneously located at the end of the averaging window. To first order, the velocity measurement error induced by the MRL timing error is proportional to the user's range acceleration

$$\delta v = \ddot{R}\,\Delta t \; + \text{ higher order terms}$$

and may reach a maximum of 0.8 fps for the area navigation "A" flight path.

The user clock performance is summarized in Figures 4-66 and 4-67 which are scatter diagrams of the B and $\dot{B}$ model deviations for the two user receivers. The bias rate deviations emphasize the MRL offset and also show a larger standard deviation of the MRL data ($\sigma_{\Delta\dot{B}} = 0.59$ for HC, $\sigma_{\Delta\dot{B}} = 0.65$ for Magnavox). The clock bias model deviations also show larger MRL variation, and further a correlation between the two receivers is noted. This correlation is due to common external effects such as MCS clock drift and channel propagation variations, and may be removed by a rotation of axis. After rotating, indicated in Figure 4-66 by the (zero intercept) regression of HC on MRL, the observed standard deviations are: $\sigma_{\Delta B} = 2.0$ for HC and $\sigma_{\Delta B} = 6.8$ Magnavox. We conclude that better MRL results for the filtered navigation solutions are achievable with a more stable user clock.

4.5.4 Inherent Range Rate Redundancy

The navigation system, being configured with both range and range-rate capability, provides a certain inherent redundancy. A back-up mode of operation can be provided in case of failure of the range rate functions. The ranging output

can provide range rate by differentiation. We investigated this aspect for a ground system operation where the calibration receiver was producing range, but due to a failure in the frequency module, could not provide range rate. A test case of different techniques for smoothing the $\frac{dr}{dt}$ data was run using data from the early parts of flight 17. Since the ground system data is characterized by $\dot{r}$ constant, and all higher order terms are essentially equal to zero, a first order digital smoothing algorithm was chosen. Figures 4-68 and 4-69 show the results which can be obtained. Figure 4-68 contains the ranging data converted to range-rate by:

$$\dot{R}_t = \frac{R_t - R_{t-1}}{\Delta t}$$

$$\dot{R}_{ts} = \dot{R}_t + \frac{\Delta t}{\Delta t + \tau} [\dot{R}_t - \dot{R}_{t-1}]$$

where R_t, R_{t-1} are the calibration receiver values of pseudo range at t and t -1.

Δt calibration receiver data sampling interval

τ adjustable smoothing time constant - the best value for the ground system data has been empirically found to be 4

$\dot{R}_{ts}$ smoothed value of pseudo range rate.

The pseudo range-rate data obtained from the carrier loop is shown in Figure 4-69 for comparison with the derived pseudo range rate data ($\dot{R}_{ts}$) obtained from the code loop.

There is very good agreement between these curves for this case, which represents normal operation of the oscillators in the ground system. For abnormally high oscillator drift rates, one may want to implement a filter of more sophistication. However, the concept remains the same and failure mode redundancy is available in the system.

An extension of this concept could be applied to users not requiring very high accuracy velocity data. In this case, the range rate data could be provided by the implementation of techniques similar to those described above to derive the data from the range output of the code loop. It would seem that hardware simplification, and resultant lower cost per unit, could be obtained in this way since the carrier loop digitizer and associated I/O would be eliminated.

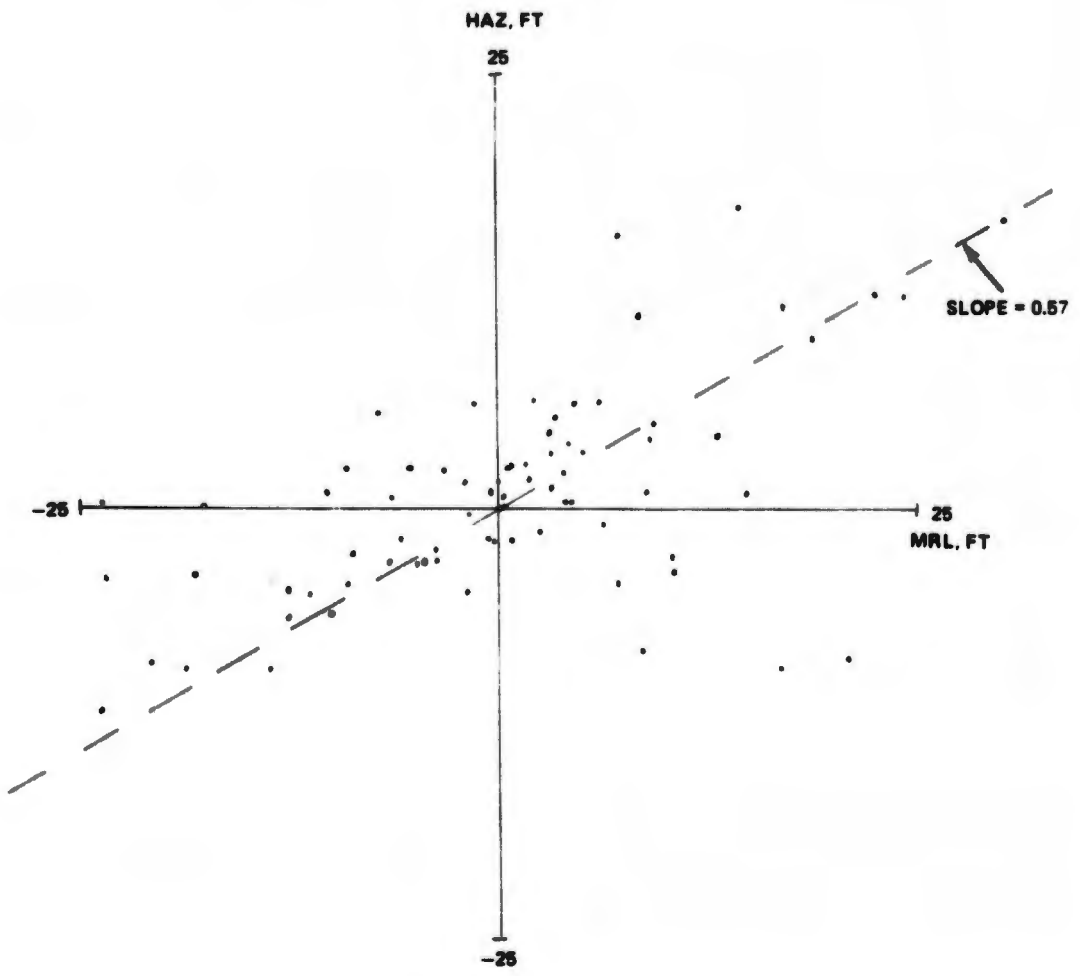

Figure 4-66 Scatter Diagram of HAZ and MRL B Deviations Flight 18, Runs 3-7, Flight 19, Runs 4-8

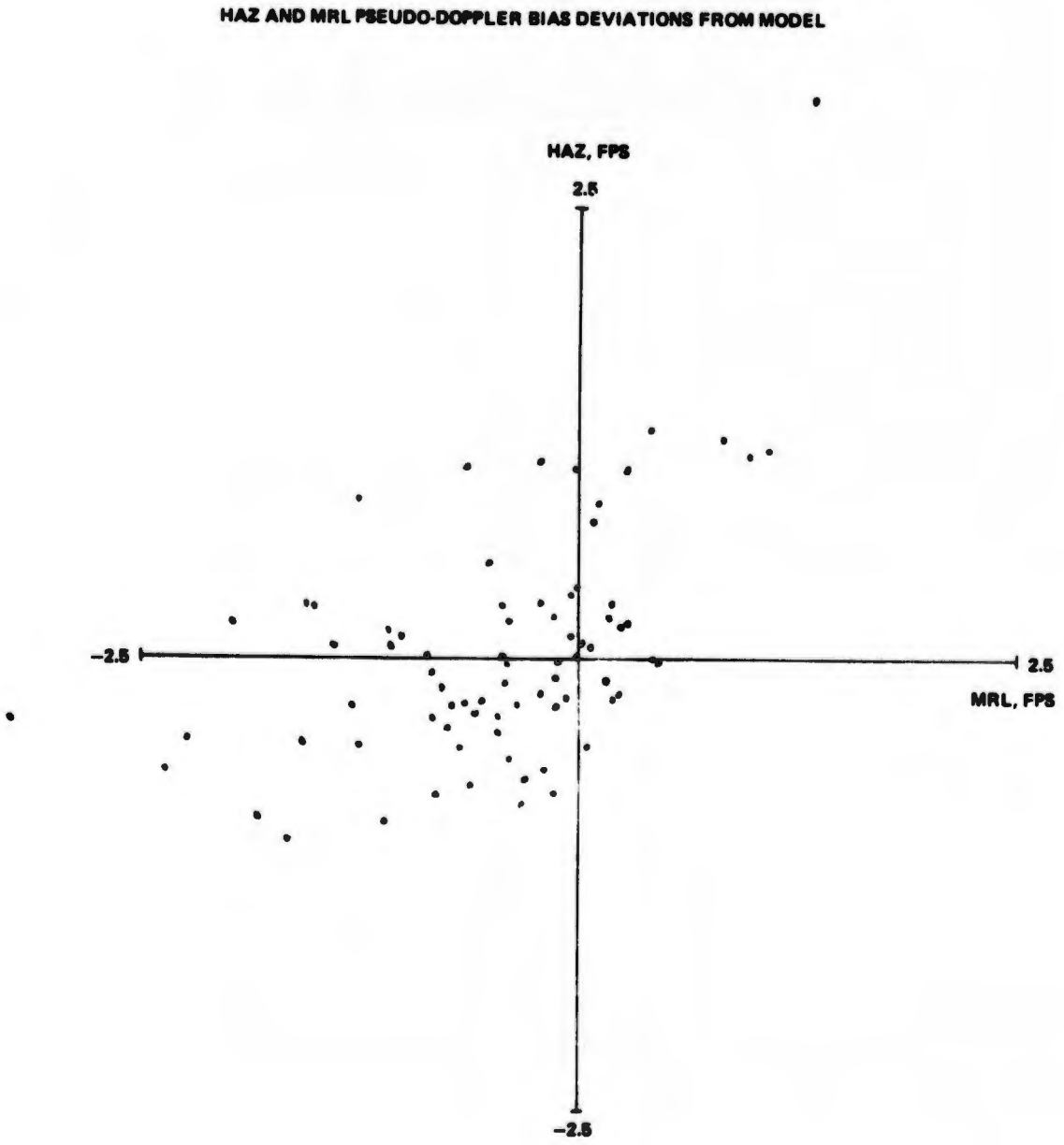

Figure 4-67 Scatter Diagram of HAZ and MRL $\dot{B}$ Deviations. Flight 18, Runs 3-7, Flight 19, Runs 4-8

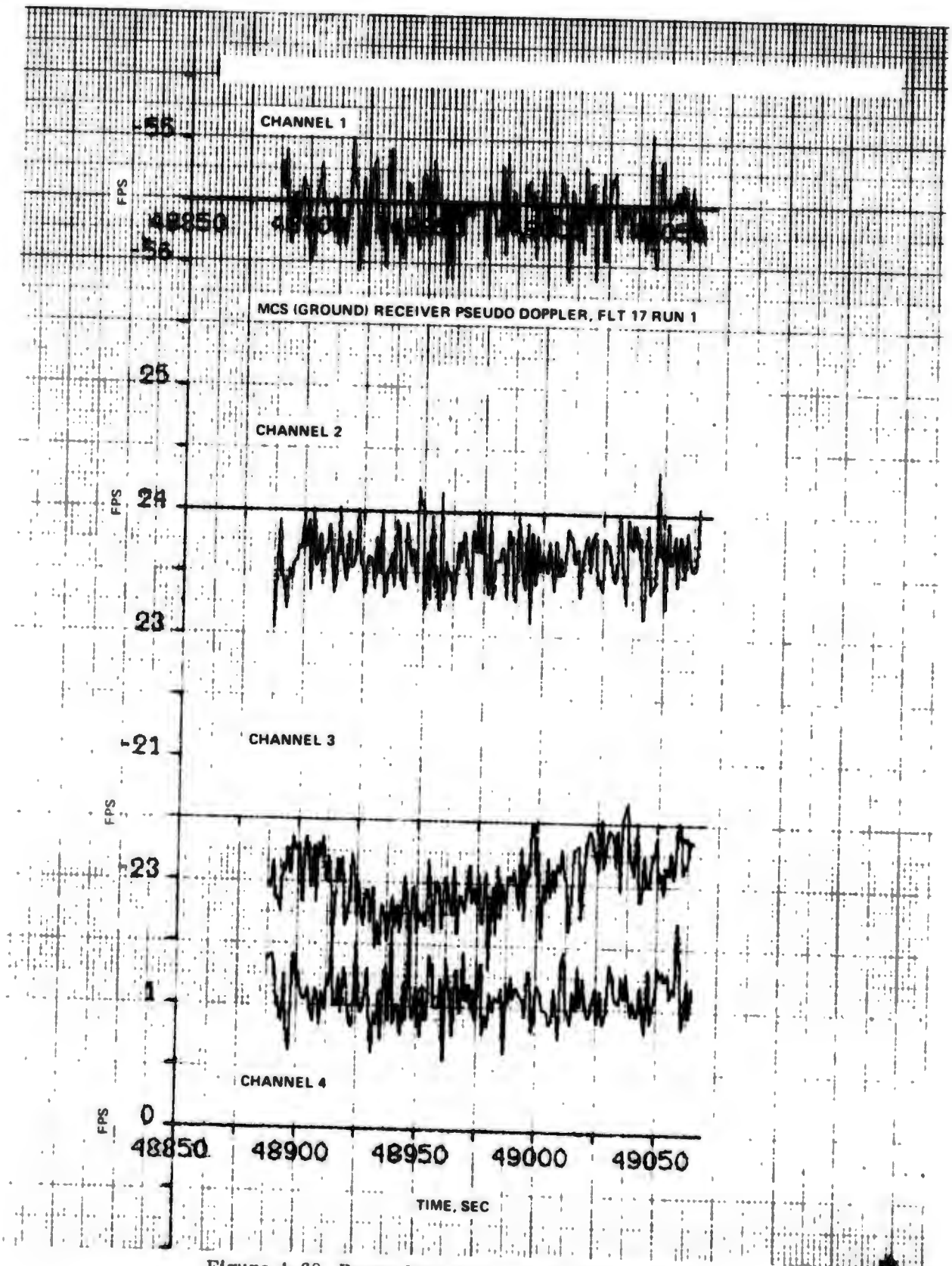

Figure 4-68 Range Data Converted to Range Rate

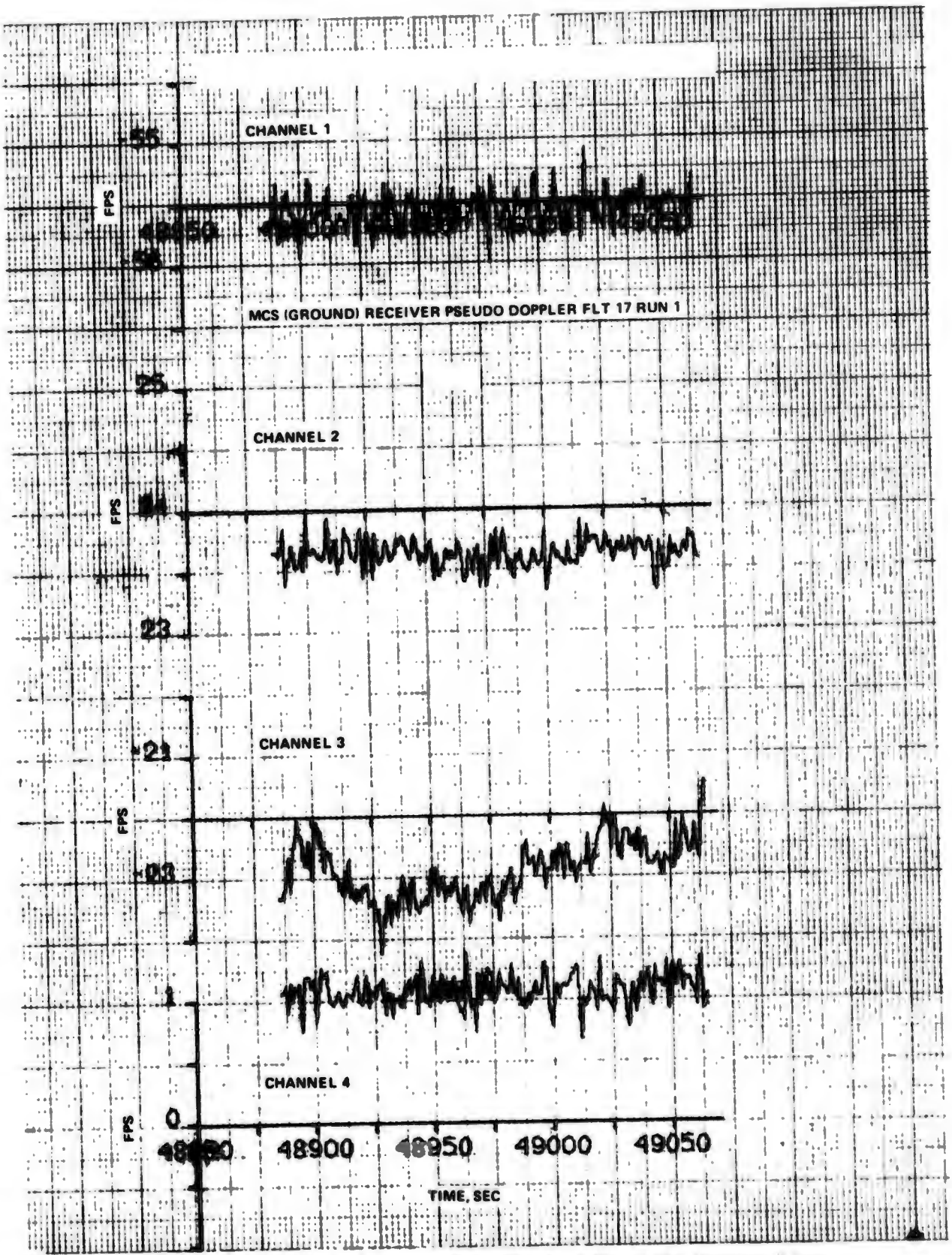

Figure 4-69 Pseudo Range Rate Obtained From the Carrier Loop

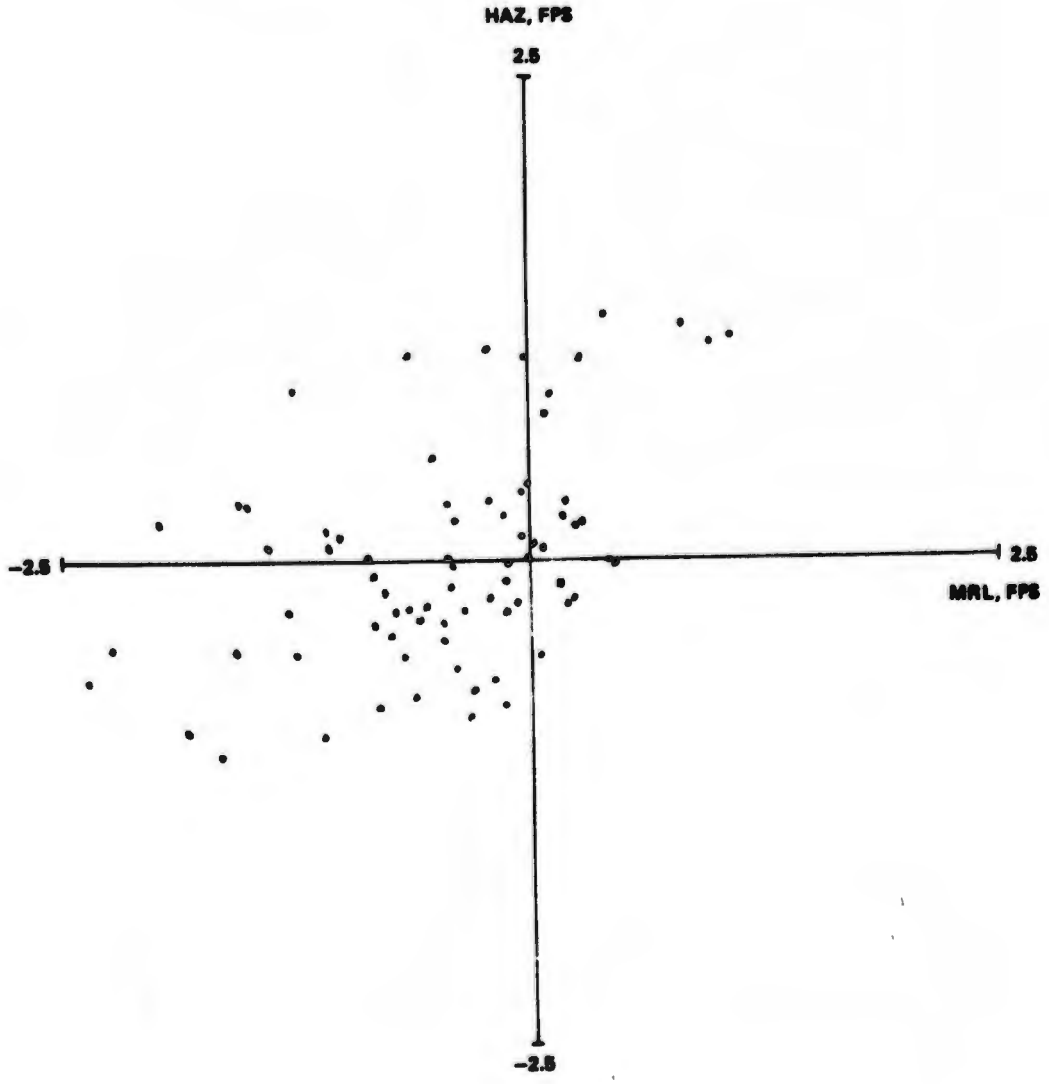

Figure 4-71 Scatter Diagram of HAZ and MRL B Deviations. Flight 18, Runs 3-7, Flight 19, Runs 4-8

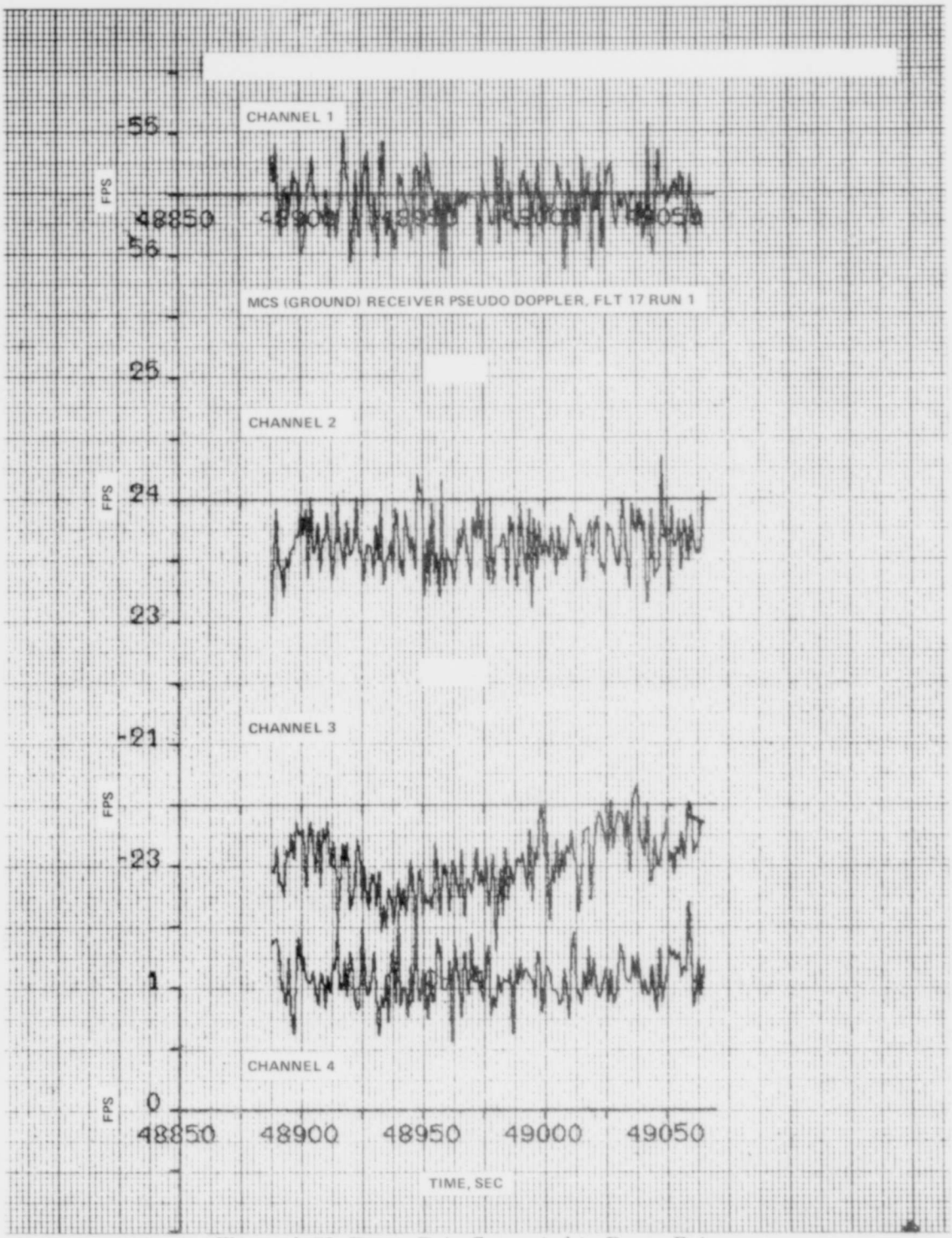

Figure 4-72 Range Data Converted to Range Rate

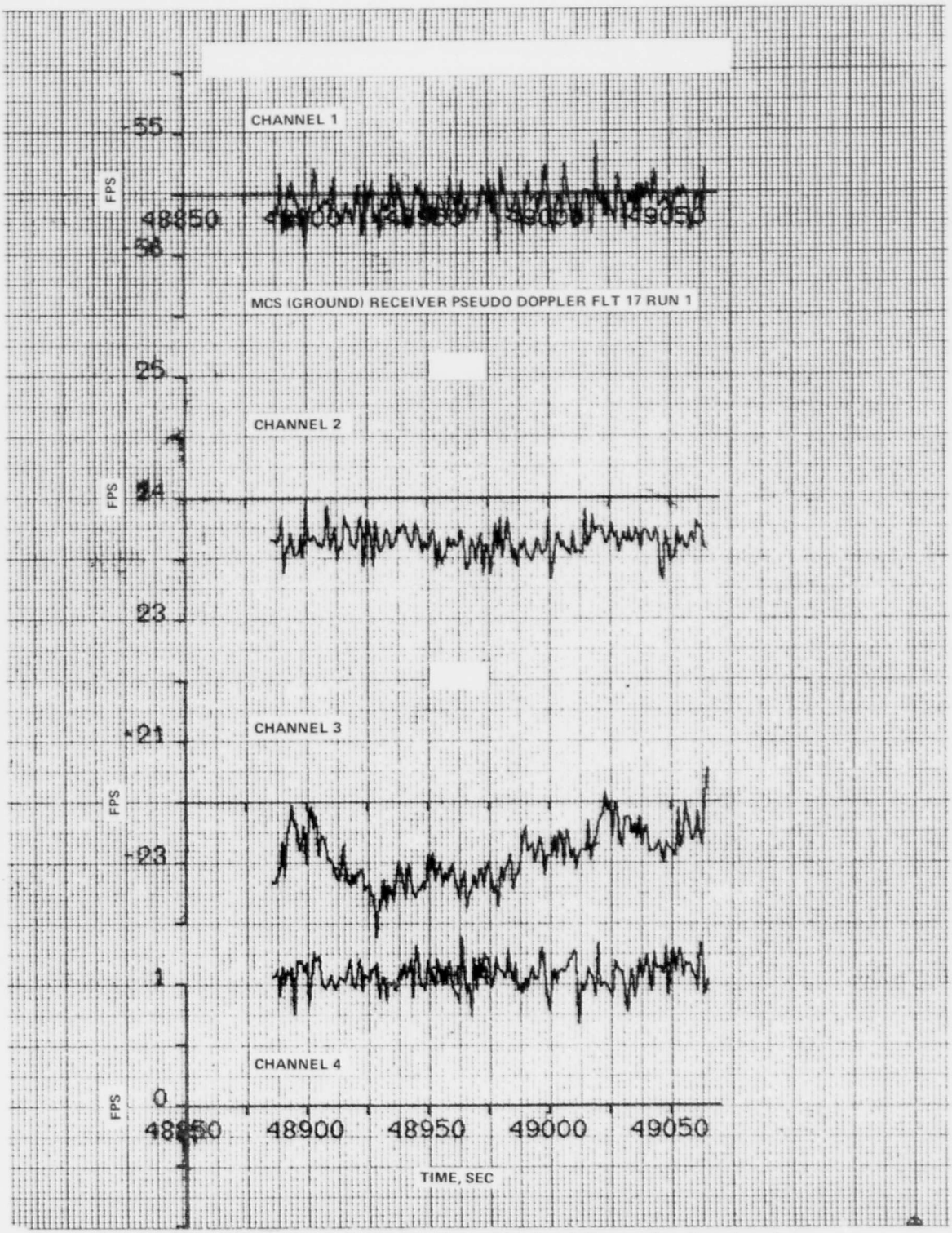

Figure 4-73 Pseudo Range Rate Obtained From the Carrier Loop

where R_t, R_{t-1} are the calibration receiver values of pseudo range at t and t -1.

Δt calibration receiver data sampling interval

τ adjustable smoothing time constant - the best value for the ground system data has been empirically found to be 4

$\dot{R}_{ts}$ smoothed value of pseudo range rate.

The pseudo range-rate data obtained from the carrier loop is shown in Figure 4-73 for comparison with the derived pseudo range rate data ($\dot{R}_{ts}$) obtained from the code loop.

There is very good agreement between these curves for this case, which represents normal operation of the oscillators in the ground system. For abnormally high oscillator drift rates, one may want to implement a filter of more sophistication. However, the concept remains the same and failure mode redundancy is available in the system.

An extension of this concept could be applied to users not requiring very high accuracy velocity data. In this case, the range rate data could be provided by the implementation of techniques similar to those described above to derive the data from the range output of the code loop. It would seem that hardware simplification, and resultant lower cost per unit, could be obtained in this way since the carrier loop digitizer and associated I/O would be eliminated.

SECTION V

TEST DATA, FLIGHTS 1-15

The Flight Test Program started in the 50-mi area of White Sands Missile Range (WSMR), New Mexico. The ground transmitters were configured for the Area Navigation tests in which they simulated a symmetric Y constellation. The first portion of the flight test program, covering flights 1-15, was spent gaining basic knowledge about the system performance. Flights 1-7, surfaced the major hardware and software system problems. Even though the navigation solutions were not very accurate (~150 ft errors) during this period, the system was functioning well enough at this point to begin a study of the error components. By the completion of flight 7, we had experienced the whole range of equipment problems and had developed correction techniques to insure reliable equipment operation. Although some equipment failures continued to occur (see Section 7), our ability to keep the system functioning during tests resulted in greatly improved data collection over that obtained in earlier flights.

The test results were not very consistent throughout this period. The problems we encountered were due partly to the test systems and partly due to our lack of knowledge about the behavior of the error components, especially those associated with the ground system. Laboratory testing of both the ground and airborne system components allowed us to locate the source of major errors by flight 15. The findings indicated that the effects of ground system instability were so severe that basic changes were made to the ground system set-up before the next flight group, flights 17-23, was initiated. Flights 1-15 are thus considered system development flights.

5.1 FLIGHT DATA OVERVIEW

The predominant error in the system data for flights 1-15 is the pseudo-range steady-state error introduced by the ground system. Our method of "software synchronizing" the four transmitters using the calibration station requires the complete and accurate knowledge of the signal propagation time from the output of the uplink antenna at the transmitters to the output of the calibration receiver (see Section 3). The signal paths between the transmitters and the calibration receiver contained an assortment of RG-214 and Spiroline cabling, cable connectors, signal attenuators, as well as the free-space medium and transmitting and receiving antennas. Also, for the early flight group, a propagation delay was introduced in the transmitter between the aircraft and calibration links to insure that the calibration receiver would not acquire the uplink signal. The complexity of the calibration links (also called the monitor links) made it very difficult to establish the true value of the total calibration path delay. Any measurement error in this delay strongly affects the quality of the navigation solution. The desert environment of WSMR caused further complications since the propagation characteristics of the link elements seemed to change with temperature and humidity.

The system shakedown effects are readily observable by comparing the test system and WSMR reference navigation trajectories. Figure 5-1 shows an overview of pseudo-ranging steady-state errors by presenting system-WSMR interchannel range differences as a function of flight number. The range difference data is used since these quantities are independent of transmitter-user geometry and do not con-

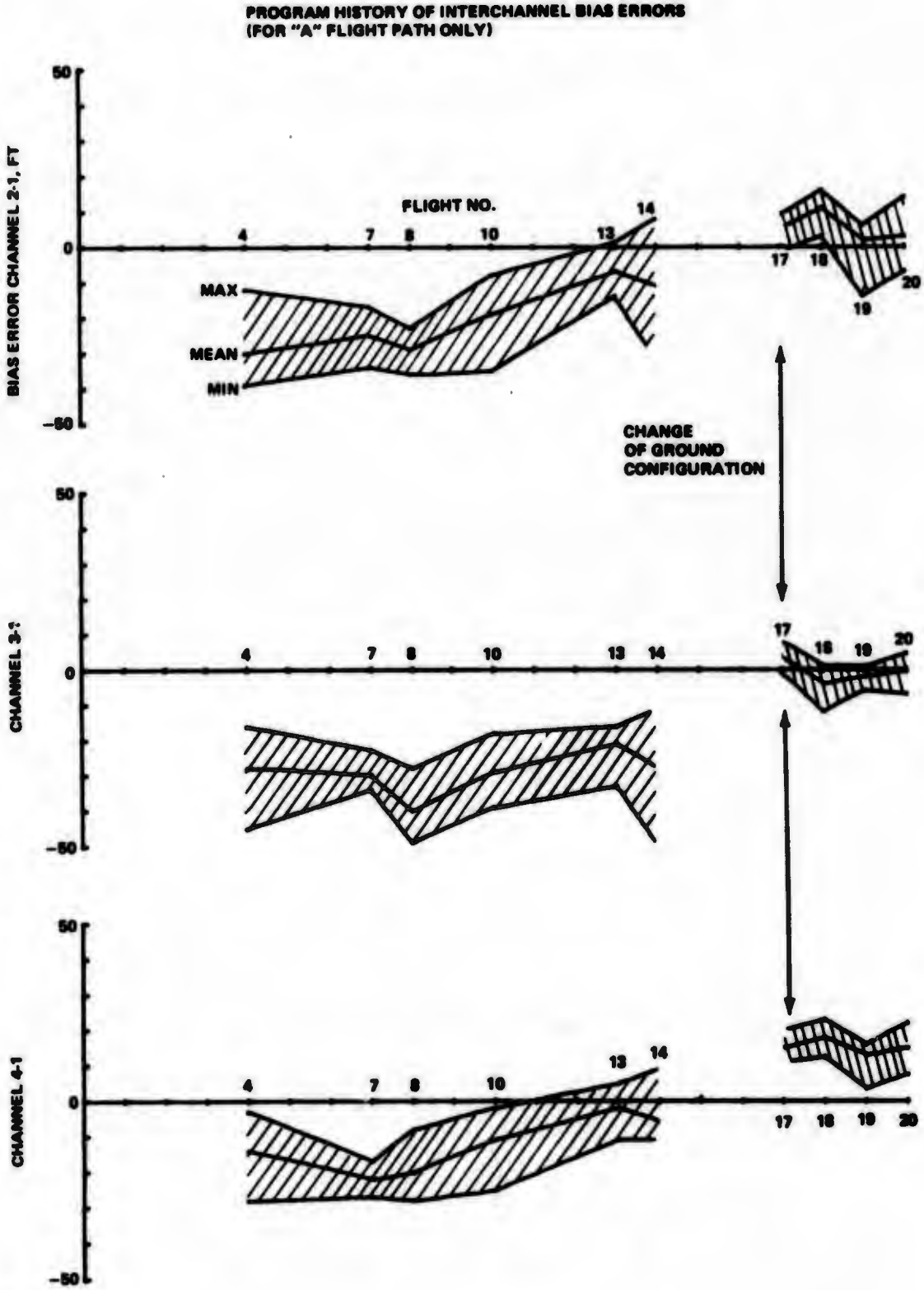

Figure 5-1 Interchannel Bias Error vs Flight Number

tain the influence of GDOP's (the Geometric Dilution of Precision, or GDOP, is explained in Section 3.2).

Referring to Figure 5-1, a long term trend of decreasing error is detectable but in general, the entire group shows unacceptable errors and great variability.

The corresponding data from the next flight group, flights 17-23, is presented on the same plot to show the distinct improvement obtained by reconfiguring the ground system. The later flights were flown with the calibration receiver locked to the uplink signal, thus eliminating the effect of cabling, antenna and internal delays at each transmitter (see Section 3).

Although deterministic conclusions about the location of the steady-state errors cannot be made from Figure 5-1 alone, it seems probable that channel 1 is in error since all three interchannel differences show similar trends (the same effect could occur if channels 2, 3 and 4 were in error simultaneously, but this is less likely than an error on channel 1 only). The bulk of these errors is in the ground components of the system since a comparison of the trajectories from the two airborne receivers shows relatively small differences. In Figures 5-2 through 7 the differences between the Hazeltine and Magnavox navigation trajectories and the WSMR reference trajectory are plotted versus time for the middle portion of run 2 of flight 10. While there is considerable disagreement between the navigation system and reference trajectories, the two system trajectories (HC and MRL) are relatively close to each other. Since both user receivers utilize the same ground calibration data to compute their respective trajectories, we conclude that the major portion of the steady-state errors are in the ground data.

The instability in the ground system was unexpected. Care had been exercised in the selection of antennas and cabling to keep the rf path losses low. The antenna beamwidths and transmitter dual output were designed to prevent interfering signals at both the Mobile Calibration Station (MCS) and the aircraft. In addition, careful site selection minimized the potential link multipath effects. Furthermore, a path length measurement technique, the cesium measurement (see Section 4.2.1), was devised to make sure the signal path length was known in the event that multipath effects were disturbing the link. However, in spite of these precautions, path length measurements made in the field showed variable delays, which we were not always able to explain.

For example, a measurement of the channel 1 transmitter internal delay between the uplink output and the monitor link output made between flights 7 and 8 indicated a delay of 194 nanosec. A similar measurement made after flight 15 indicated a delay of 236 nanosec. Both measurements were obtained by the same technique. There was a change made to the transmitter hardware during this period which could have affected this delay, but not, theoretically, to such a large extent. The interchannel errors plotted in Figure 5-1 use the 236 nanosec value throughout. If we had incorporated the 194 nanosec value for the early flights, they would have been 236 - 194 = 42 nanosec more in error.

5.2 FLIGHT DATA ANALYSIS

The analysis of the system data from the early flight group is purposely limited in scope since its quality is degraded by the problems in the ground and flight systems discussed above. This data set has served well, however, in uncovering the basic problem areas in the test set-up and equipment. Therefore no discussion of random and periodic errors is attempted here, but rather left for later sections. Our primary interest here lies in presenting the insights gained about the calibration data. Both the flight and ground

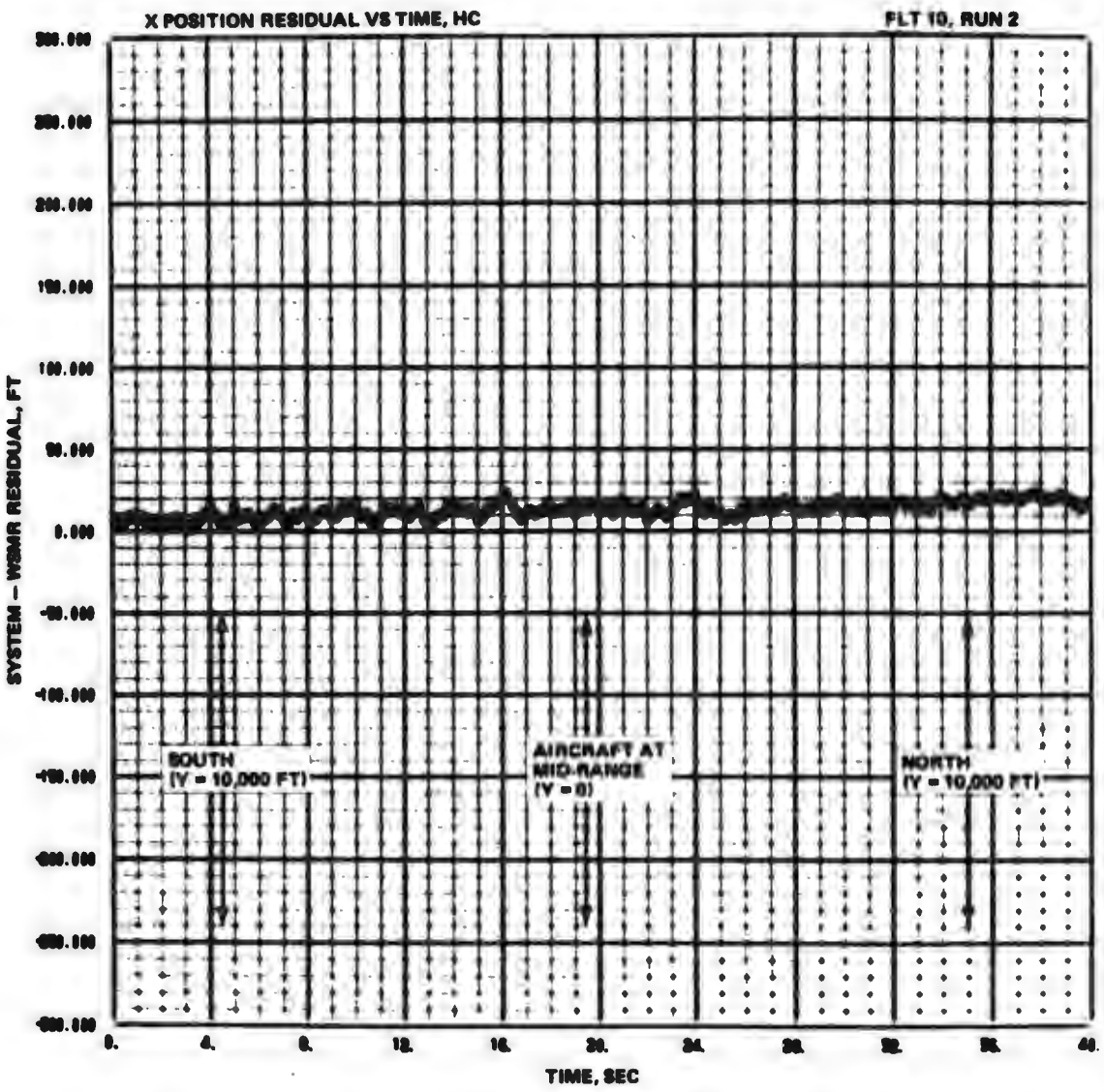

Figure 5-2 Hazeltine Trajectory Error vs Time for Two-State Filtered Navigation Solution Showing Large Steady State Errors

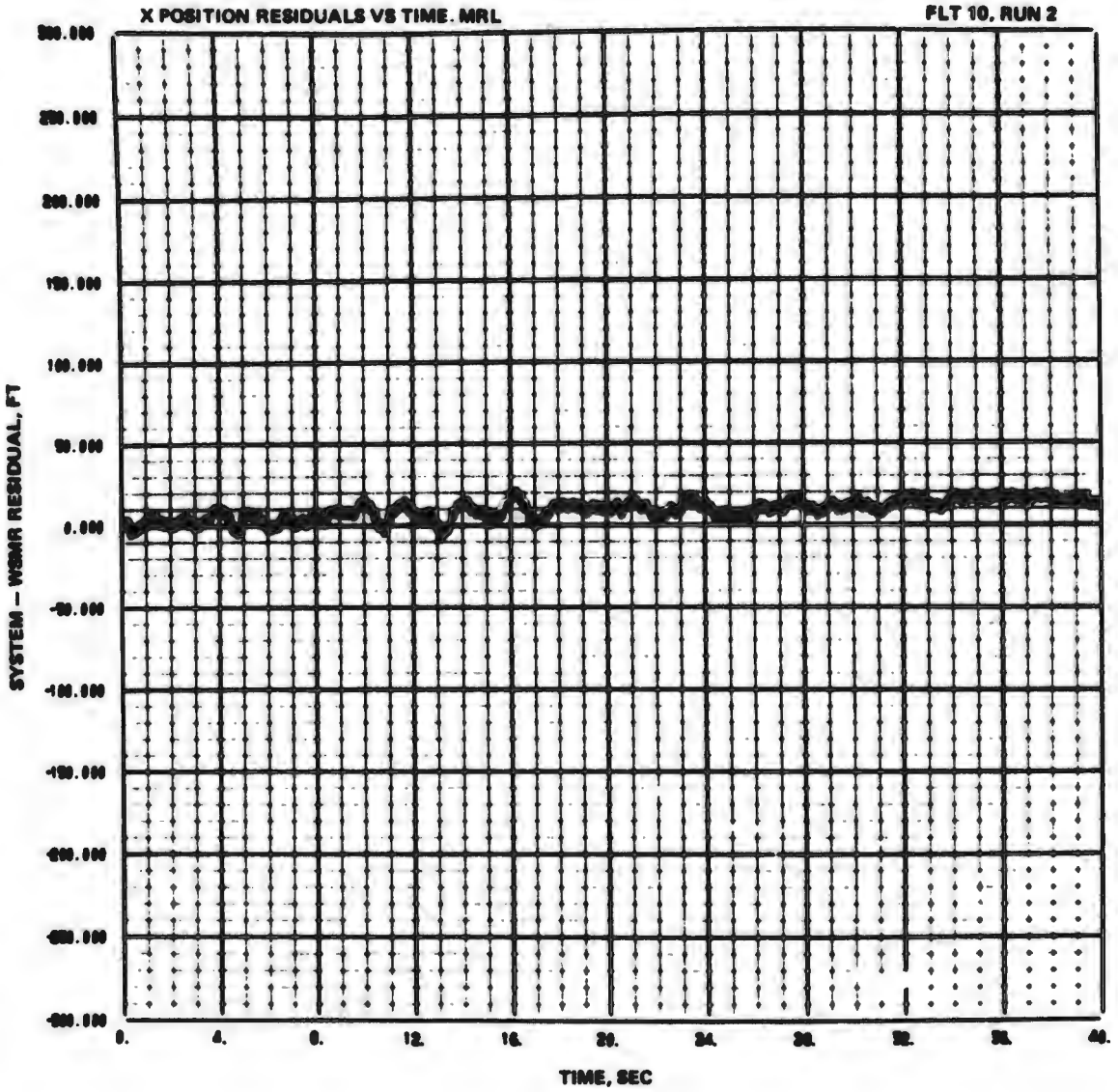

Figure 5-3 Magnavox Trajectory Error vs Time Showing Poor Agreement With WSMR Reference But Good Agreement With the Hazeltine Trajectory

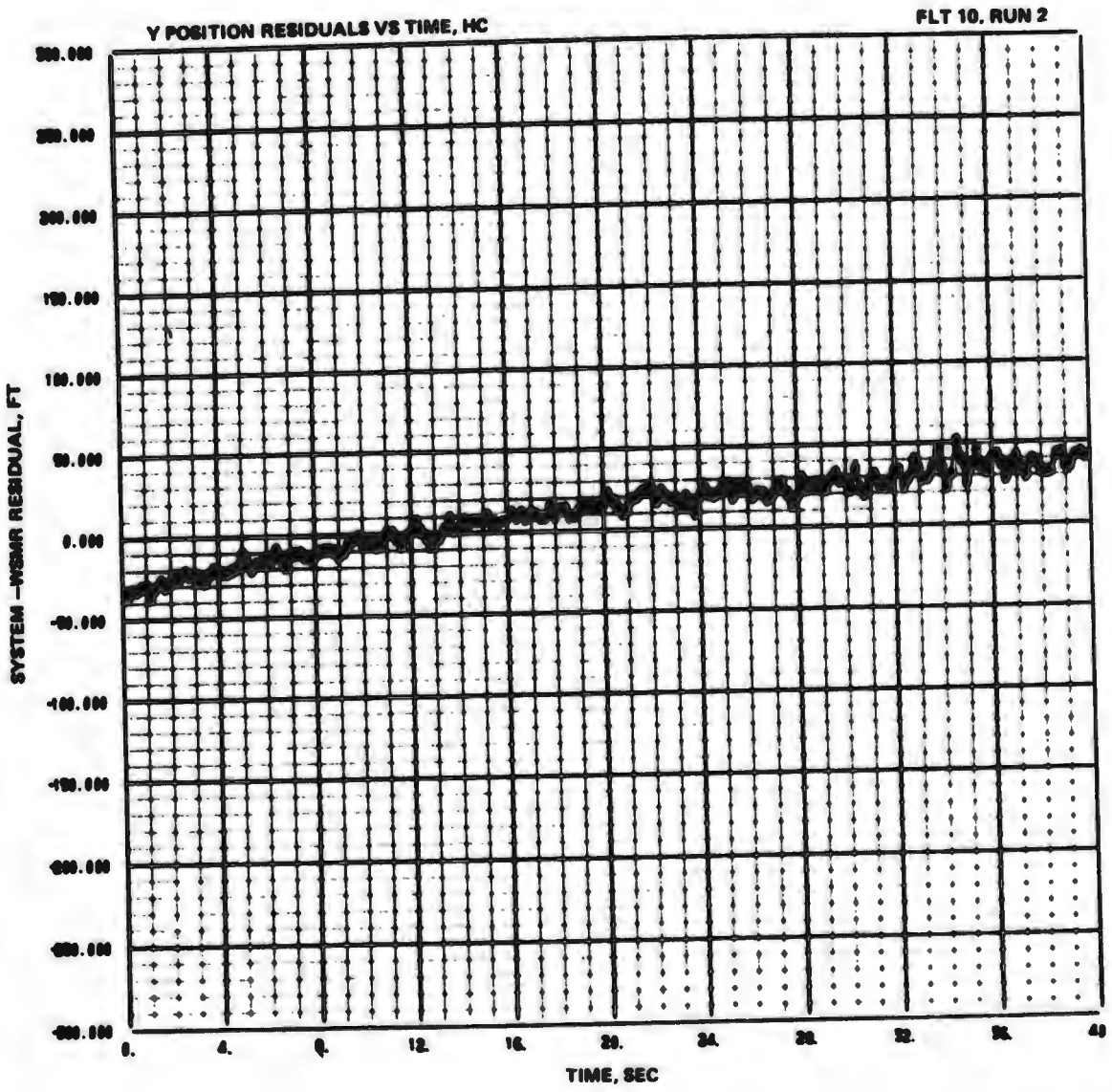

Figure 5-4 HC Trajectory Error vs Time Showing Characteristic Slope Evolving From Steady State Pseudo-Range Error and User-Transmitter Geometry Change

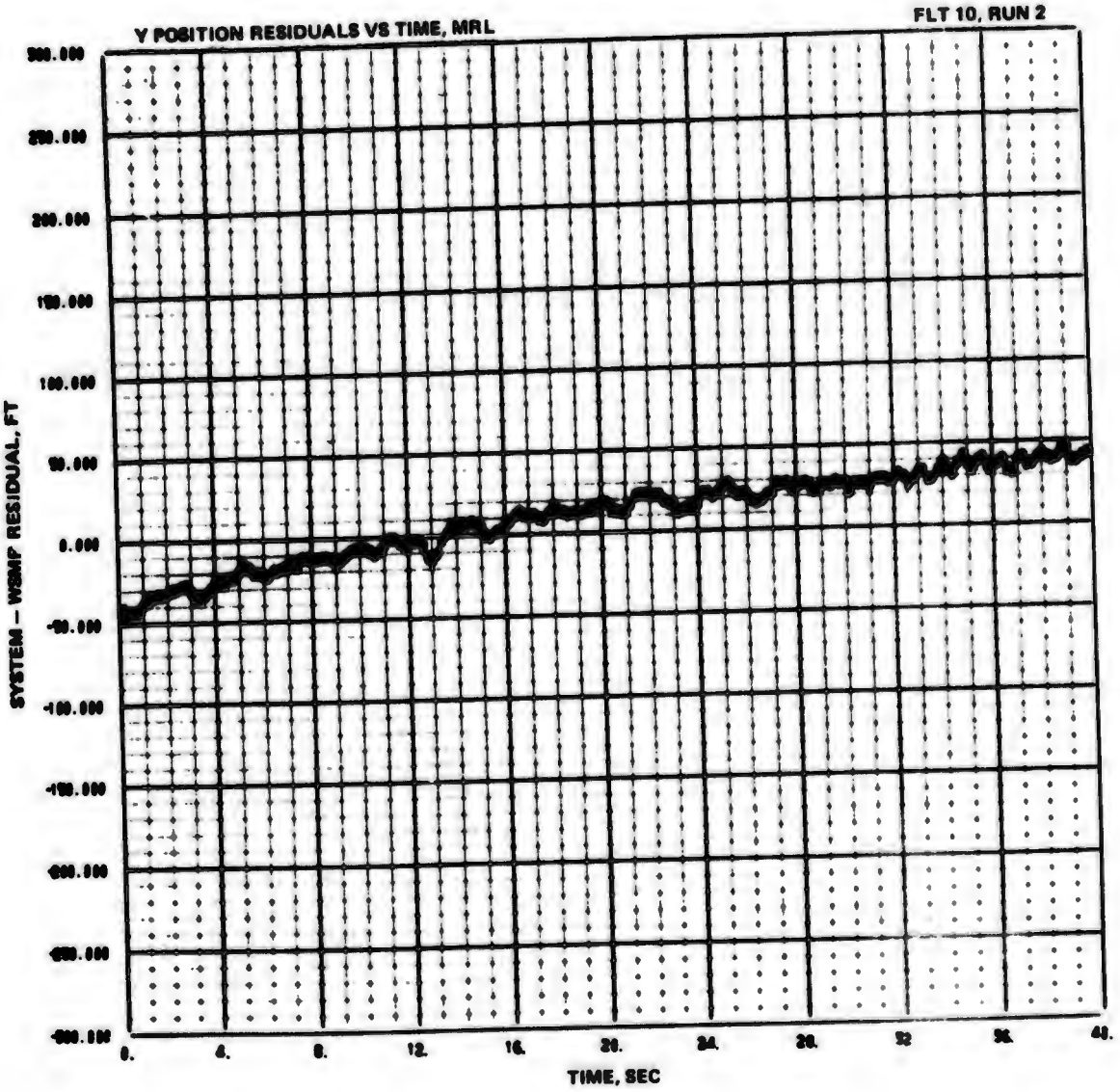

Figure 5-5 MRL Trajectory Error vs Time

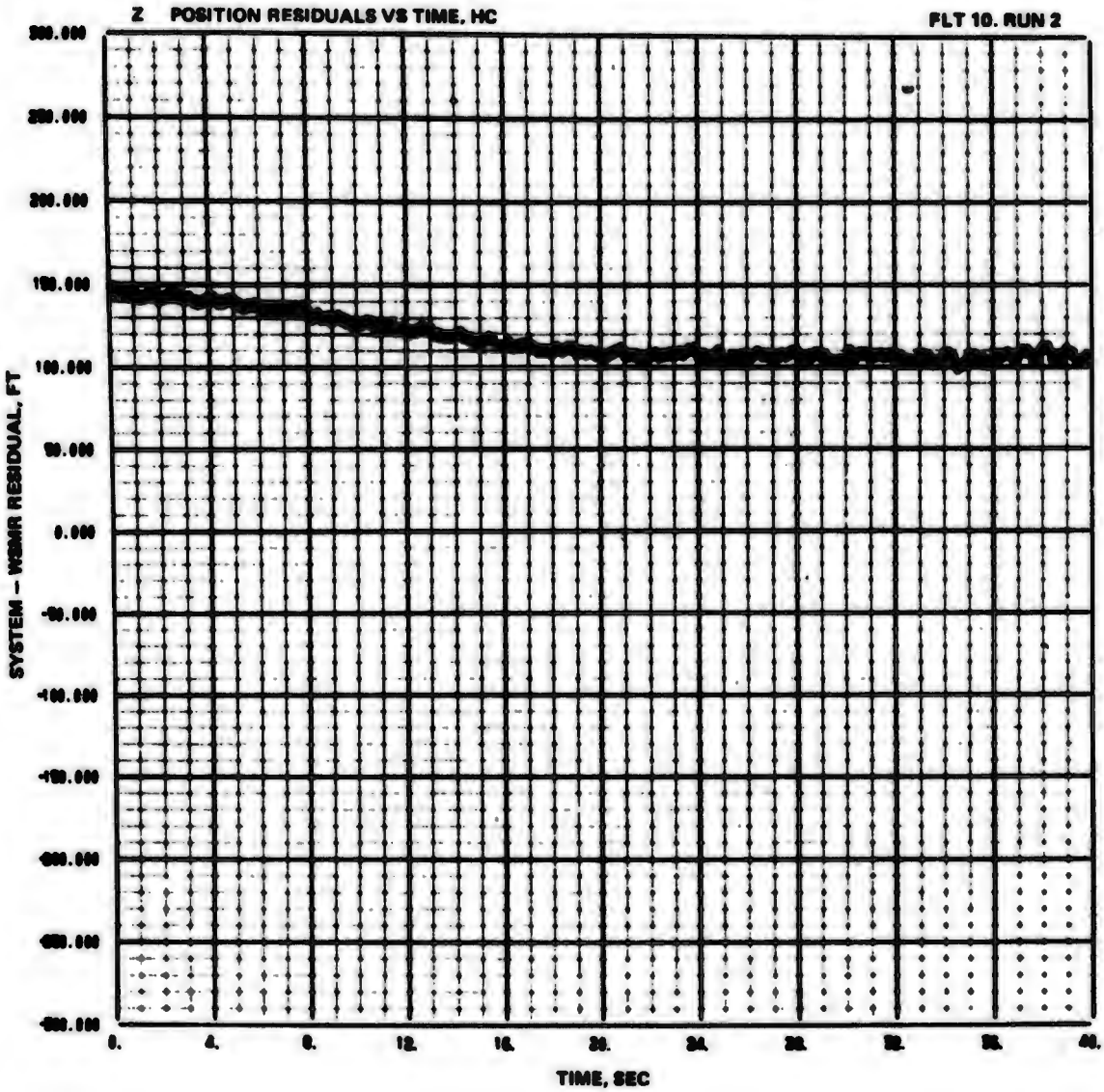

Figure 5-6 HC Trajectory Errors vs Time

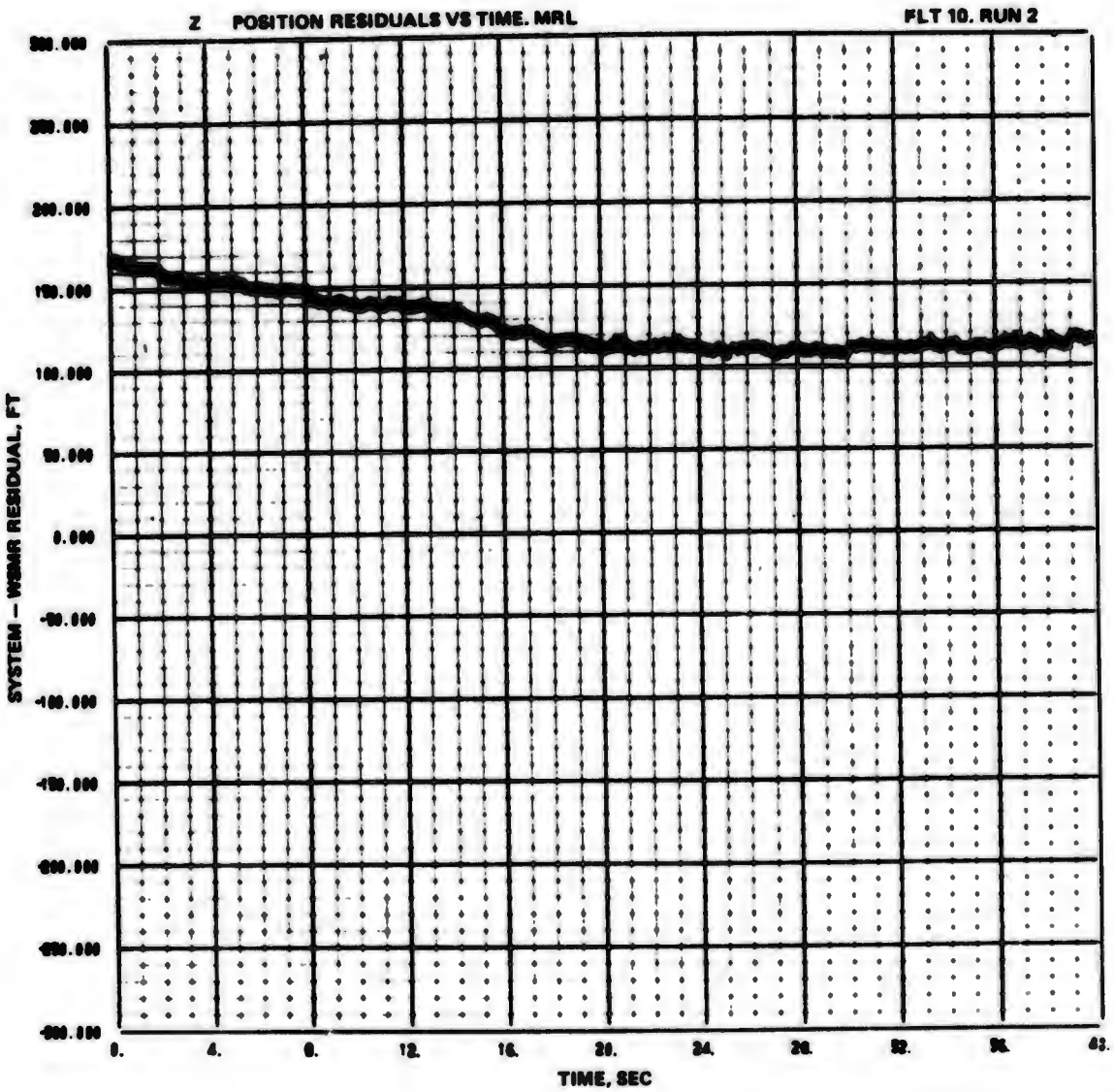

Figure 5-7 MRL Trajectory Error vs Time

measurement data were used for this purpose.

The analysis approach used was as follows:

- We chose one flight from the group as typical and utilized its data only; thus eliminating to some degree data variability
- We eliminated the effects of known error sources
- We used range difference and X, Y, Z residuals between the system and WSMR trajectories to determine, as nearly as possible, an estimate for channel steady state errors
- We reviewed the calibration measurement data taken in the field in light of the predicted channel errors and attempted to pinpoint the sources of error.

Flight 10 was chosen as a typical flight from the early flight group since its interchannel errors are approximately equal to the average of these errors over all the flights from the 1-15 group (see Figure 5-1). Further, the reference trajectory from WSMR is advertised as "good" and the flight is composed of seven "A" and "C" runs which show no noticeable anomalies. (For an explanation of "A" and "C" geometry, see Volume II, Section 3.5.3.)

From the outset, two known errors were eliminated. The first was the 42 nanosec steady-state error introduced by the (apparent) mismeasurement of the transmitter number 1 internal delay (see Section 4.2.1.4). The second source of error which is pertinent to the present discussion was discovered much later in the flight test program. This is the apparent delay in the uplink antennas which varies as a function of user "look" angle. Detailed measurements of these delays were made after the flight test program was completed. Since the peak-to-peak variation in the delay correction data is about 8 nanosec (see Section 4.2.1.3 for further details), its effect on flight 10 data is expected to be minimal. This is verified by Figures 5-8 through 5-13 which show the interchannel range residuals for the corrected data. Comparing these values with the flight 10 entries of Figure 5-1, small shifts in the mean values (about 2 ft and 4 ft better in channels 2 and 4, respectively, and about 3 ft worse in channel 3) are evident and there is a decrease in the maximum-minimum range of the data. The time history plots of Figures 5-2 through 7 also present the corrected data.

Based on the observed navigation errors, values were assigned to the steady-state pseudo-range errors for each of the four channels. However, this cannot be done exactly. Our lack of knowledge about the true value of the clock mismatch (computed clock bias) between the user and calibration receivers prevents the deterministic solution of the four pseudo-range error equations. Therefore, relying on our experience with the system some constraints were established which allowed us to estimate the channel errors. For the flight 10 data, the interchannel residual data (of Figures 5-8 through 13) was augmented in two ways:

- We performed an analysis on the X, Y, Z trajectory errors between the system and reference trajectories using the sensitivities of the X, Y, Z errors to each of the four pseudo-ranging errors (these sensitivities are derived from the linear perturbation analysis of the pseudo-range navigation solution and are plotted in Appendix A)
- We applied a confidence factor to each error estimate based on the difficulty and/or variability of propagation delay measurements associated with each channel.

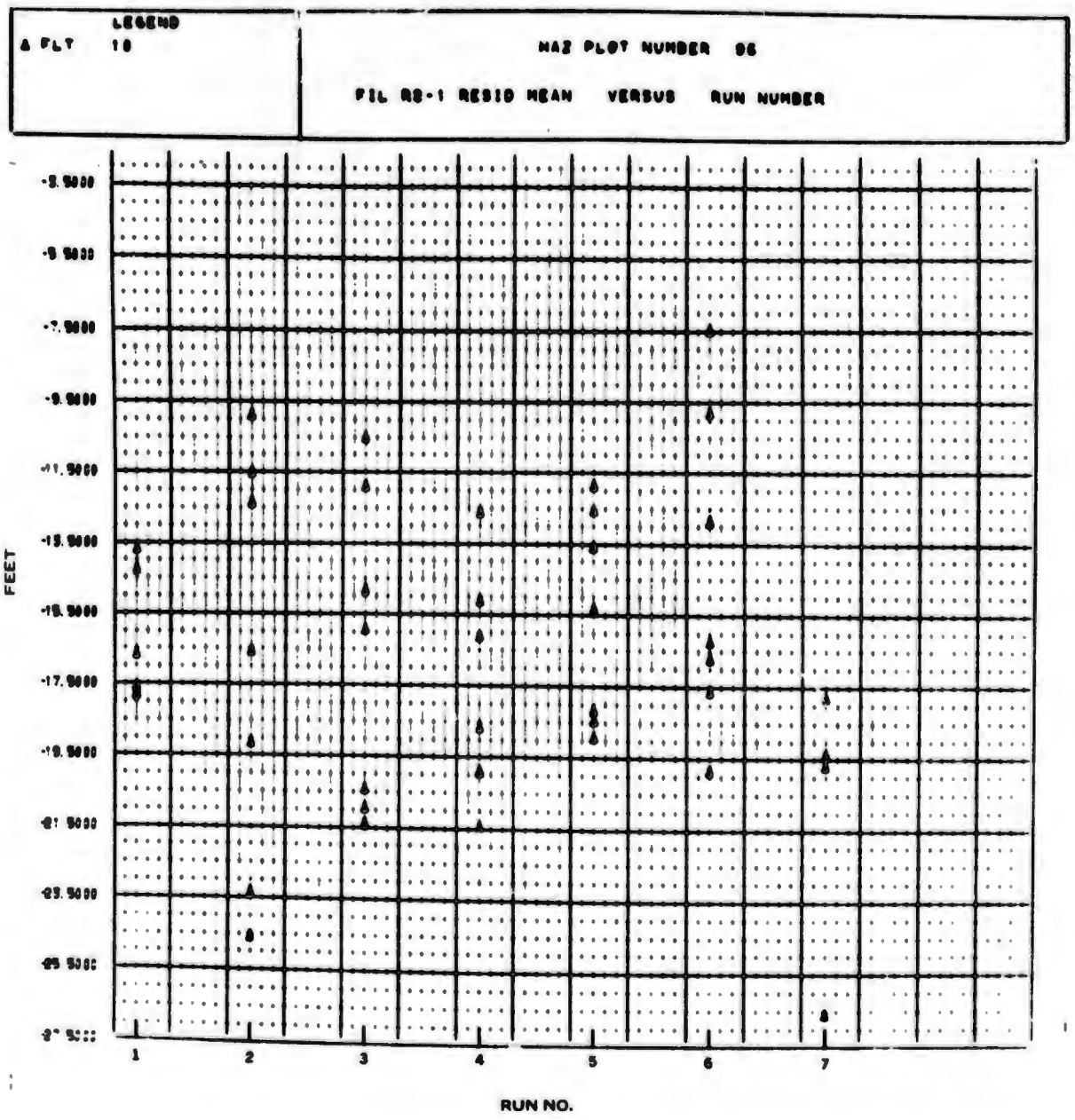

Figure 5-8 HC Interchannel Bias Residuals, Flight 10

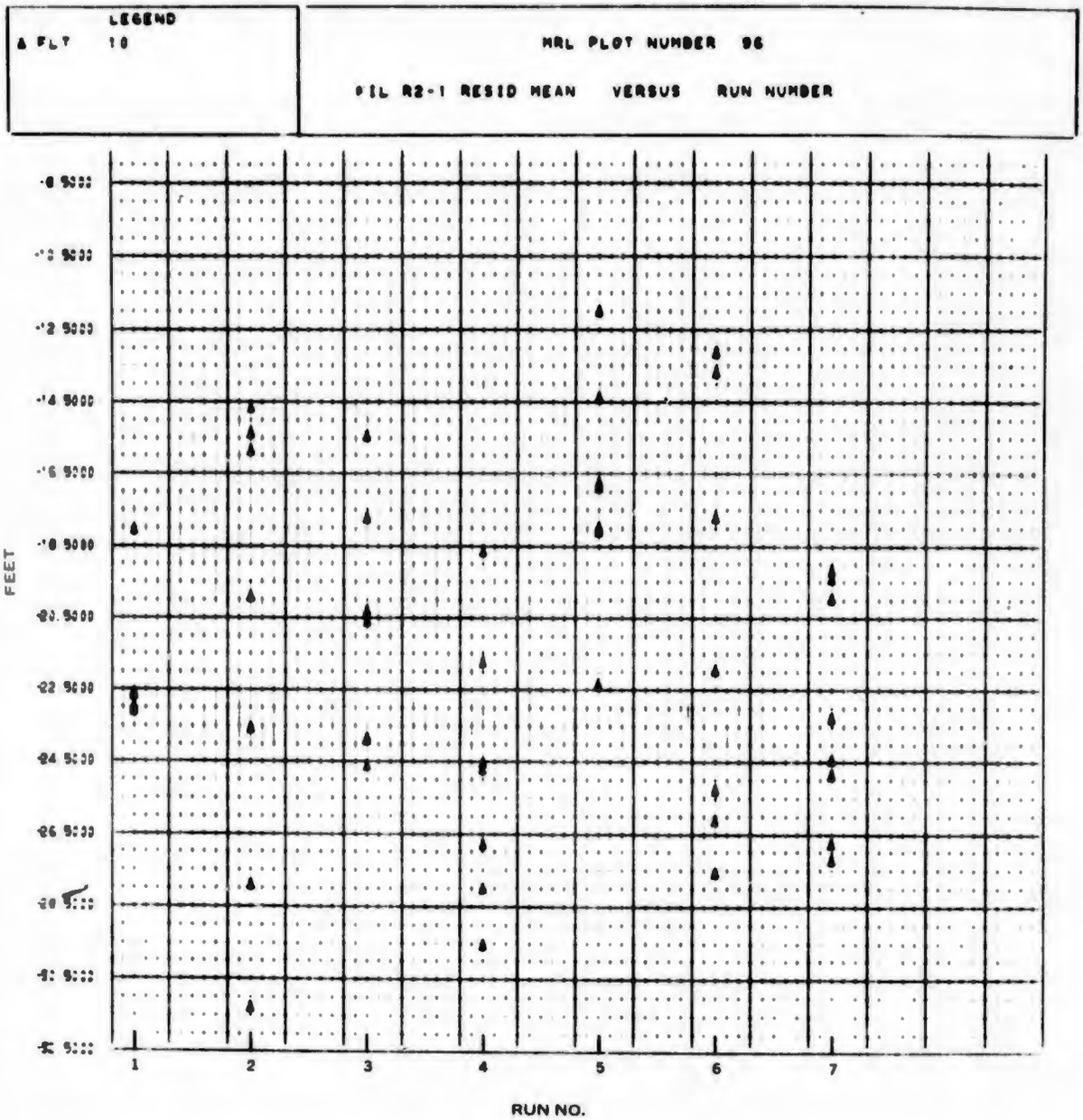

Figure 5-9 MRL Interchannel Bias Residuals, Flight 10

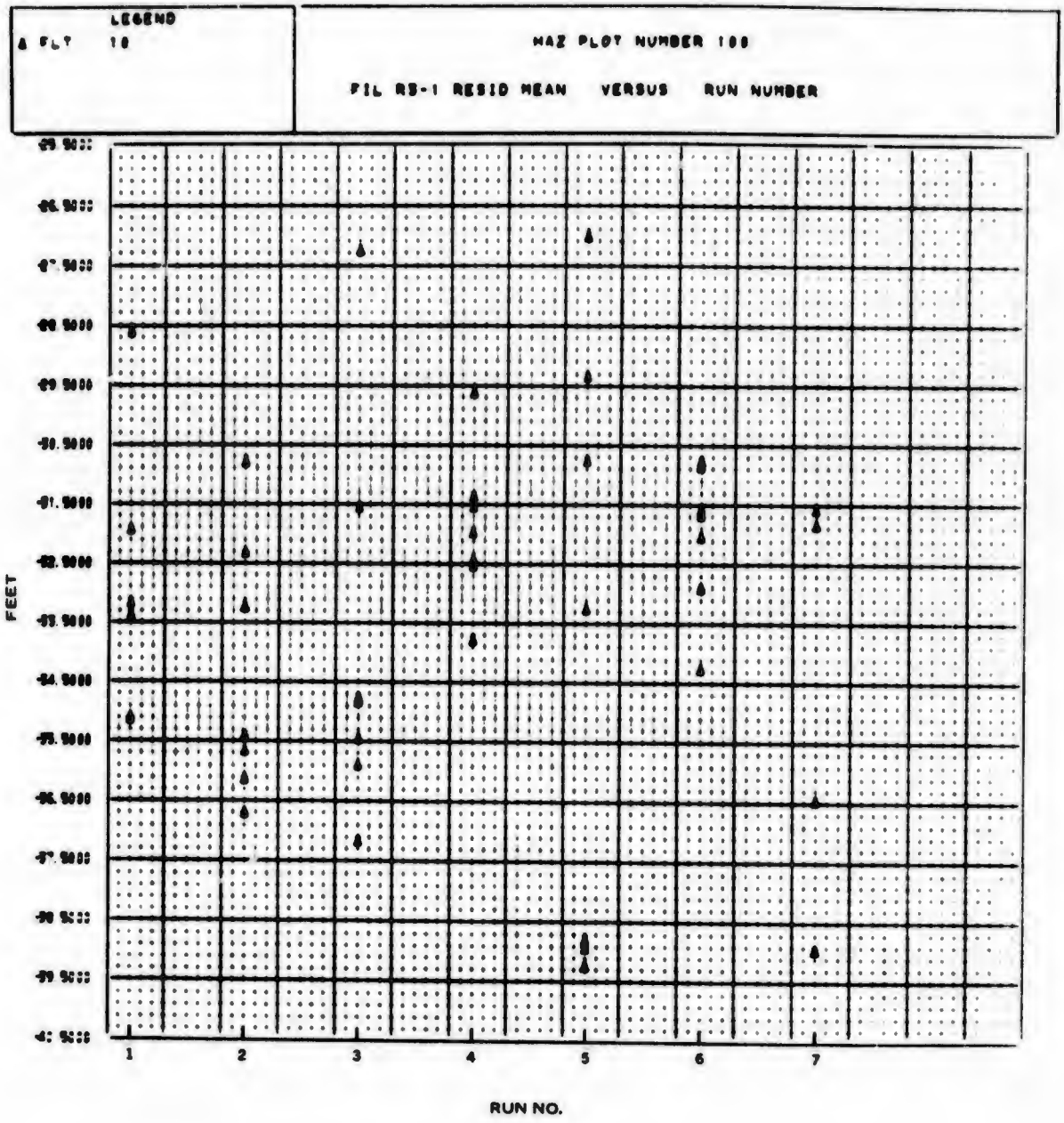

Figure 5-10 HC Interchannel Bias Residuals, Flight 10

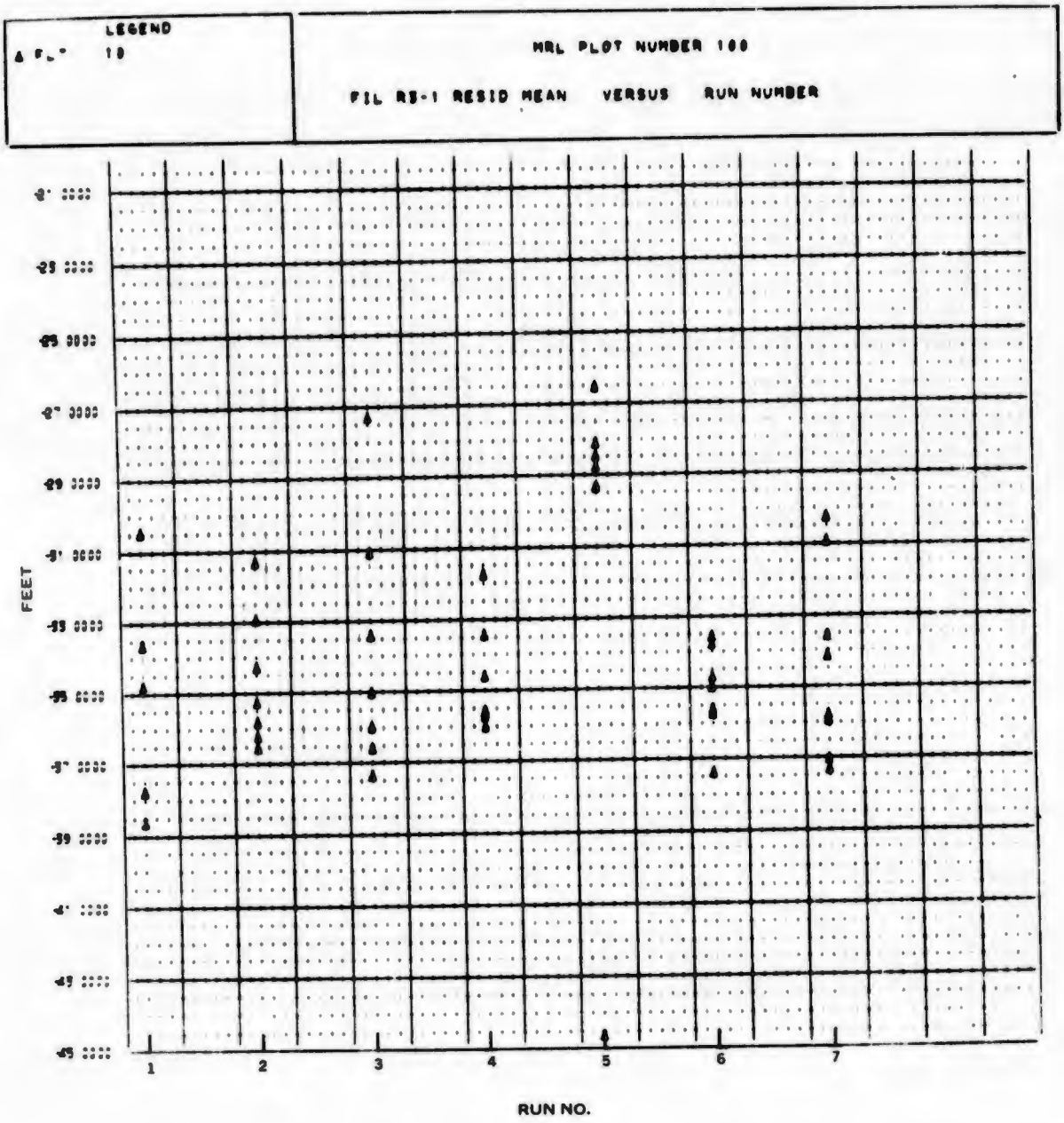

Figure 5-11 MRL Interchannel Bias Residuals, Flight 10

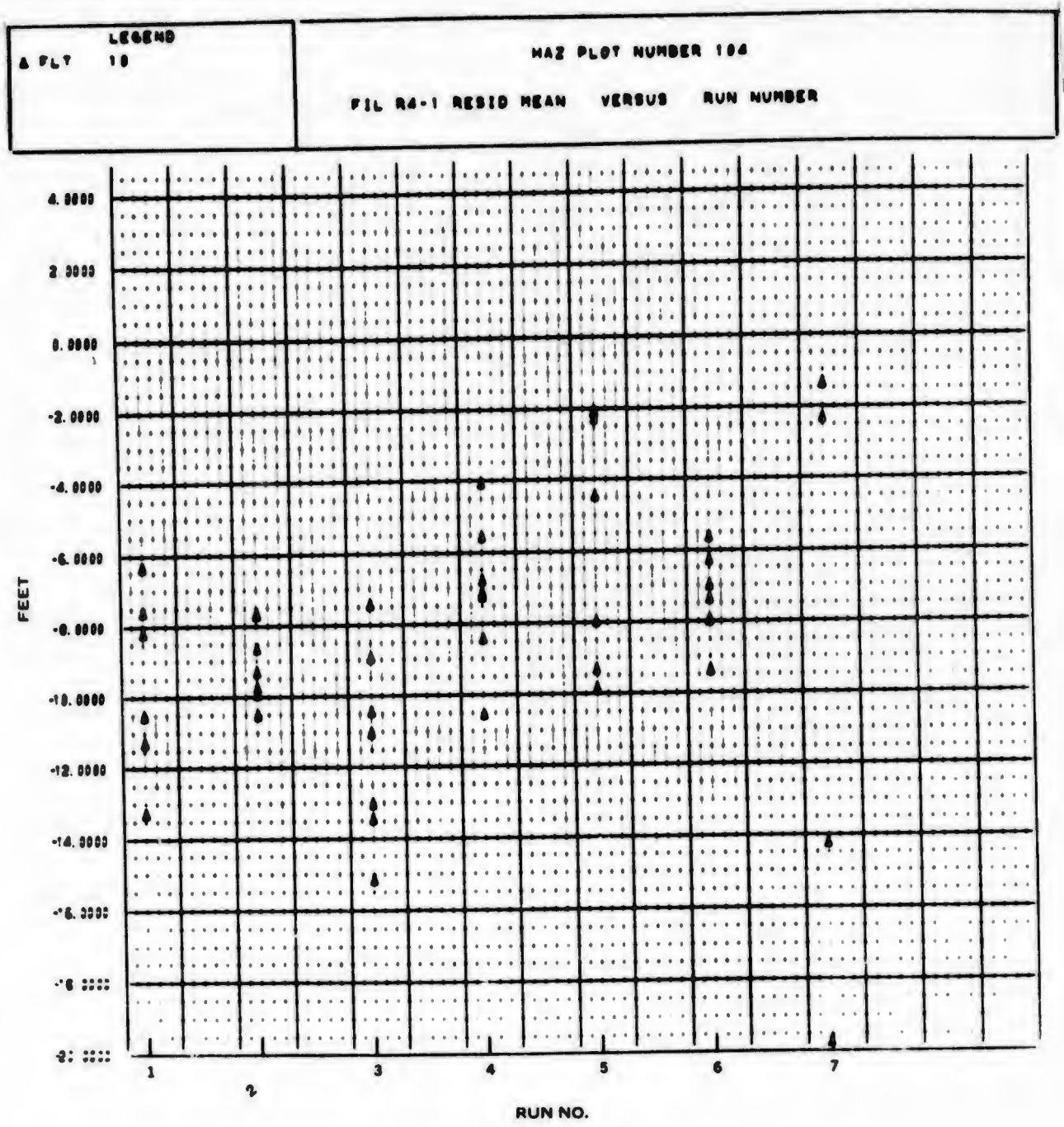

Figure 5-12 HC Interchannel Bias Residuals, Flight 10

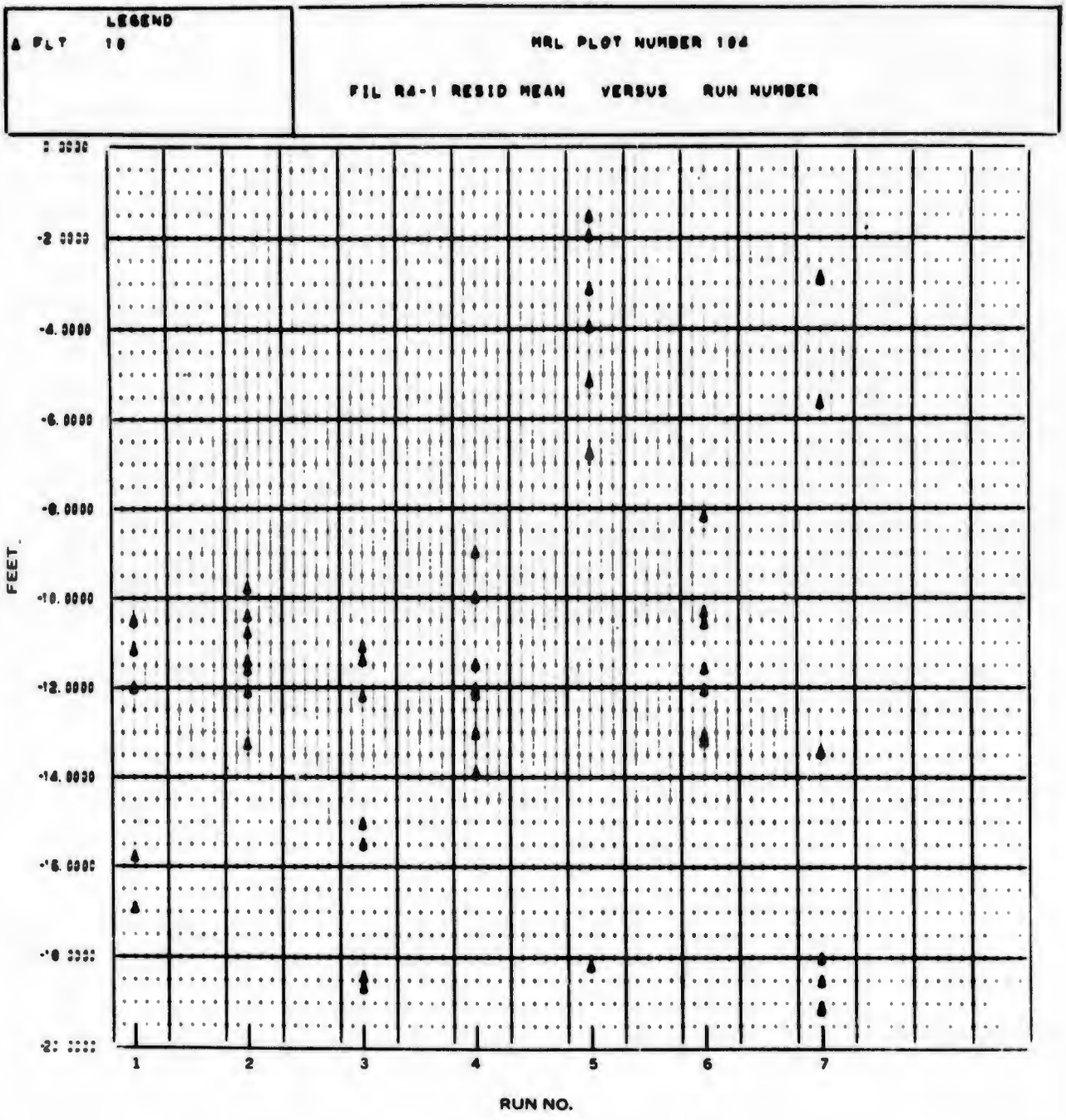

Figure 5-13 MRL Interchannel Bias Residuals, Flight 10

Analyses such as these are not very rigorous. However, they did allow us to quantify the test results and draw some conslusions.

The X, Y, Z coordinate errors and sensitivities are presented in Table 5-1. This table shows the X, Y, Z error observed at three different points on the WSMR test range for run 2 of flight 10. The errors are taken directly from Figures 5-2 through 7. Also presented in this table are the sensitivities of the X, Y, Z errors to errors in pseudo range. Thus, for a user at mid-range, a 1 ft error in channel 1 pseudo-range will cause a 4.8 ft error in the calculated value of Z position. These data were used in conjunction with the interchannel residuals to estimate the individual channel errors. This technique does not add any new information to the problem from the mathematical standpoint, but serves as a redundant data set in the "navigation solution domain" rather than in the "measurements domain".

Inspecting these data in an attempt to assign errors to each channel, the relative confidence in the ground delay measurements associated with each channel were kept in mind. Such "weighting" factors depend heavily on our experience with the system in the field and also demand a high degree of judgement. The relative weighting of the channels are:

- Channel 1 shows, by far, the most measurement variation and therefore earns the least amount of confidence. The 42 nanosec variation in the transmitter internal delay (discussed previously) plus certain delay characteristics of MCS cabling (explained below) make errors as large as 20 ft a distinct possibility

- Measurements taken for the other three channels all show variability, but to a lesser extent than channel 1. Thus our confidence in these channels is slightly higher than in channel 1. Errors as large as 15 ft are reasonable.

The data presented in Table 5-1 represents the navigation errors using our best *a priori* estimates of calibration link delays independent of the flight data. These figures were calculated based on measurement confidence alone and, evidently, do not fully describe the state of the ground system. After applying the added information available in the flight data, the conclusion is (under the constraints discussed above) that:

- The channel errors were approximately:

  - channel 1 - 20 ft
  - channel 2 - no error
  - channel 3 - -10 ft
  - channel 4 - 10 ft

These values produce zero-mean residuals in both the "measurement" and "navigation solution" domains as verified by Figure 5-1 and Table 5-1.

The field calibration measurements were next reviewed in light of these updated channel error estimates. Table 5-2 presents the data showing the delay values presently used to compute the navigation solution and also gives the maximum and minimum measurement values. Referring to this table, the internal transmitter delays between the monitor and uplinks are seen to be the most unstable. The 10 ft error estimates in channels 3 and 4 are obviously possible considering the range of

Table 5-1 Observed Coordinate Errors and Sensitivities, Flight 10, Run 2

OBSERVED COORDINATE ERRORS AND SENSITIVITIES
FLIGHT 10, RUN 2

COORDINATE	OBSERVED ERROR	CHANNEL SENSITIVITIES 1	2	3	4
---14K FEET SOUTH--- (X,Y,Z)=(-1576,-17801,30711)					
X	2 FT.	-0.1	0.9	-0.9	0.1
Y	-4	-2.2	0.1	0.4	1.8
Z	16	5.2	-2.2	-2.4	-0.8
---MID-RANGE--- (X,Y,Z)=(-16?7,4,?0711)					
X	11	-0.1	0.8	-0.9	0.1
Y	15	-0.3	-0.5	-0.4	1.4
Z	11	4.8	-1.4	-1.7	-1.5
---14K FEET NORTH--- (X,Y,Z)=(-1696,13655,30693)					
X	16	-0.1	0.8	-0.8	0.1
Y	4?	0.9	-1.1	-1.0	1.1
Z	112	5.5	-0.9	-1.7	-2.6

OBSERVED INTER-CHANNEL BIAS ERRORS ARE ---

(2-1) = -19 (3-1) = -34 (4-1) = -11

PAGE 1

Table 5-2 Ground System Calibration Measurements Applicable to Early Flights (1-15) (Nanoseconds)

Parameter	Chnl	Best Est. w/o Fit Data	Measurements			New Estimates with Fit Data
			Max	Min	Range	
Transmitter	1	-236	-194	-241	47	-238
Internal Delay (1)	2	-240	-234	-250	16	-242
	3	-230	-198	-240	42	-218
	4	-208	-201	-220	19	-218
Free Space Delay and Spiroline Cables	1	7316	7327	7311	13	7312
	2	32384	32394	32379	15	-
	3	18166	18171	18161	10	-
	4	22406	22421	22402	19	-
RG-214 Cables (2)	-	-	-	-	-	-
MCS Spiroline Alone	1	114	115	113	2(4)	-
	2	138	-(3)	-(3)	-(3)	-
	3	143	-(3)	-(3)	-(3)	-
	4	101	101	103	2	-
Xmtr Spiroline Alone(1)	1	-36	-33	-36	3	-
	2	-44	-36	-44	8	-
	3	-39	-38	-39	1	-
	4	-35	-35	-33	2	-

NOTES:

(1) Signs are assigned to give direct relationship between parameter and total calibration delay

(2) All measurements showed good results, minimal variation

(3) Cable length measured once but showed strong insertion loss variations during test program - cables replaced after flight 16

(4) Variations as large as 8 nanoseconds were observed later in the test program

measurement values for these channels. (Refer also to Figures 4-37 through 4-40 which plot the internal transmitter delay values versus measurement data.) Thus it appears that "corrected" values to the channel 3 and 4 transmitter delays could be assigned and that incorporating these new values in the navigation software would show improved test system-WSMR agreement.

Such assignments, however, are invalid for the data available for channel 1. Although great variation is observed in the channel 1 figures, no values were measured which would yield a delay of about 255 nanosec, required to give good system-WSMR agreement. We can only account for 4 nanosec if error in the right direction in channel by noting variations in the free-space delay values. The channel 1 error is evidently stemming from an unobserved error source. The most likely place for this error is the Spiroline cable at both the transmitter and the calibration station. These cables showed wide variations in insertion loss and delay at various times. The cable at the transmitter site was changed after flight 15 for this reason. It is certainly possible that a large delay error could have developed in the cable. (See Section 4.2.1.2 for a discussion of rf cable error sources.) However, there are no measurement data available to support a firm conclusion.

5.3 CONCLUSIONS - EARLY FLIGHTS

The flight data from the early flight group (flights 1-15) served to uncover the large errors (within 15-25 ft) in the ground and airborne systems as well as in the test program software. Since widely varying errors plagued these flights, especially steady-state calibration errors in the ground system, these data are not suitable for system accuracy analysis.

The steady-state errors in the ground component of the pseudo range are by far the most predominant. This is easily determined by comparing the Hazeltine and Magnavox user receiver trajectories which show agreement within 5 to 10 ft. When the system trajectories are compared to the reference trajectory from WSMR, a 20 ft steady-state error is evident on channel 1 and 10 ft errors on channels 3 and 4. The 10 ft errors are attributed to the transmitters by inspecting delay measurement variations, but the 20 ft error in channel 1 is still unexplained.

In summary, flights 1-15 served as developmental flights. The accuracy analysis of the flight data is reserved for the later flight groups 17-23 and 25-31.

SECTION VI

TEST DATA, FLIGHTS 17-23

Flights 17-23 provided test system data in the area navigation enviroment after changes were made to the ground system to eliminate the major sources of error identified during earlier flight tests. The improvement in the stability of the data as a result of the new ground system configuration allowed us to perform an accuracy analysis of these data with confidence. The overall results of this analysis show:

- The test system pseudo-range error (measurement error) components are identifiable. The remaining unexplained mean error residual between the test system and the White Sands Missile Range (WSMR) reference data is approximately 2 ft

- The user navigation position and velocity errors are:

  - For the vector position error (total position error determined from $\Delta S_1 = [(\Delta X^2 + \Delta Y^2 + \Delta Z^2)]1/2$) the mean is approximately 25 ft and the standard deviation is approximately 10 ft

  - For the vector velocity ($\Delta \dot{S}_1 = [\Delta \dot{X}^2 + \Delta \dot{Y}^2 + \Delta \dot{Z}^2]^{1/2}$) the mean $\Delta \dot{S}_1$ is approximately 1.3 fps, and the standard deviation is approximatley 0.6 fps.

A summary of the tests conducted during flights 17-23 is presented in Table 6-1. It is important to view the detailed test results of these flights in light of the specific test objectives. For instance, flights 17-20 were flown at 34,000 ft MSL and 22,000 ft MSL (A and C paths) directly over Salt Site, while flight 22 was flown at 34,000 ft MSL but offset to the east of the transmitter grid (B flight path). These different profiles produced slightly different results. In order to delineate these results and present the underlying causes for the differences, we will be making observations and comparisons of the data from different flights to highlight specific effects. The composite results of flights 17-23 will also be presented from three different viewpoints to point out the effects of various problems which occurred during this flight group and to show the navigation quality attainable with the test system.

The overall system performance during a typical data run is shown in Figures 6-1 and 6-2. These figures depict the aircraft flight path and solution errors for flight 19, run 6 in the X-Y and Y-Z planes. The aircraft flight path is determined from the WSMR trajectory data and is shown as a solid line connecting triangles. For this run the aircraft is flying at 32,000 ft above ground level (AGL), Figure 6-2, and almost along the Y axis, X = 200 ft (Figure 6-1). The four transmitter locations are given in the X-Y plane for reference. At 1 sec intervals along the flight path an error vector is drawn from the WSMR trajectory (triangles) to the test system navigation solution. The error vectors are exaggerated by a factor of 100 to make them visible on the trajectory plot. Thus the aircraft trajectory is plotted at a scale factor of 10,000 ft/box, while the error vectors are plotted at a scale factor of 100 ft/box. The navigation system trajectory can be visualized by connecting the free ends of the error vectors. For this data run, at the north end of the run, Y = 25,000 ft, the

Table 6-1 Flight Conditions for Flights 17-23

Flight	Run	Flight Path	Power Level, dbm
17	1 to 3	34 K ft MSL, Path A over Salt Site, Runs alternate north to south direction	- 120
18	1 to 2	34K ft MSL, Path A, Run direction alternates north to south	- 123
	5 to 7	22K ft MSL, Path C over Salt Site, Runs alternate north to south direction	- 130
19	1 to 6	34K ft MSL, Path A, Run direction alternates north to south	- 123 on runs 1 and 2 - 133 on runs 3 to 6
	7	Descent from 34K ft to 22K ft heading 180°	- 133
	8	22K ft MSL, Path C heading 360°	- 130
20	1 to 12	34K ft MSL, Path A, Run direction alternates north to south	- 123 on runs 1 to 4 - 133 on runs 5 to 9 - 140 on runs 10 to 12
22	1 to 3, 6 to 14	34K ft MSL, Path B offset east of transmitter complex, run directions alternate north-east to south-west	- 123 on runs 1 to 3 - 133 on runs 6 to 10 - 140 on runs 11 to 14
23	3 to 9	7K ft MSL, Path D over Salt Site, Runs alternate north to south	- 115 on runs 3 to 5 - 120 on runs 6 & 7 - 125 on runs 8 & 9

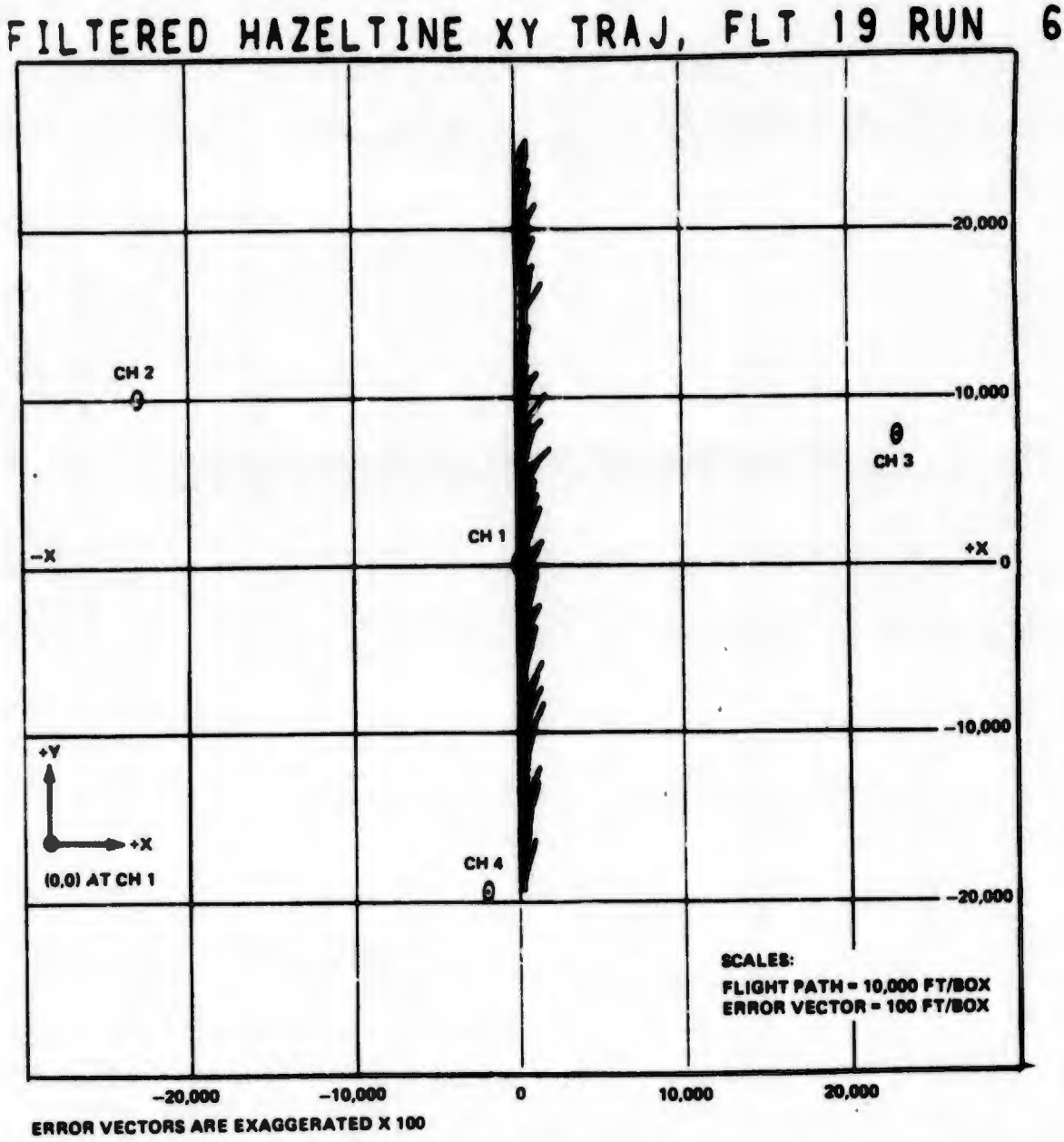

Figure 6-1 Area Navigation Summary Plot

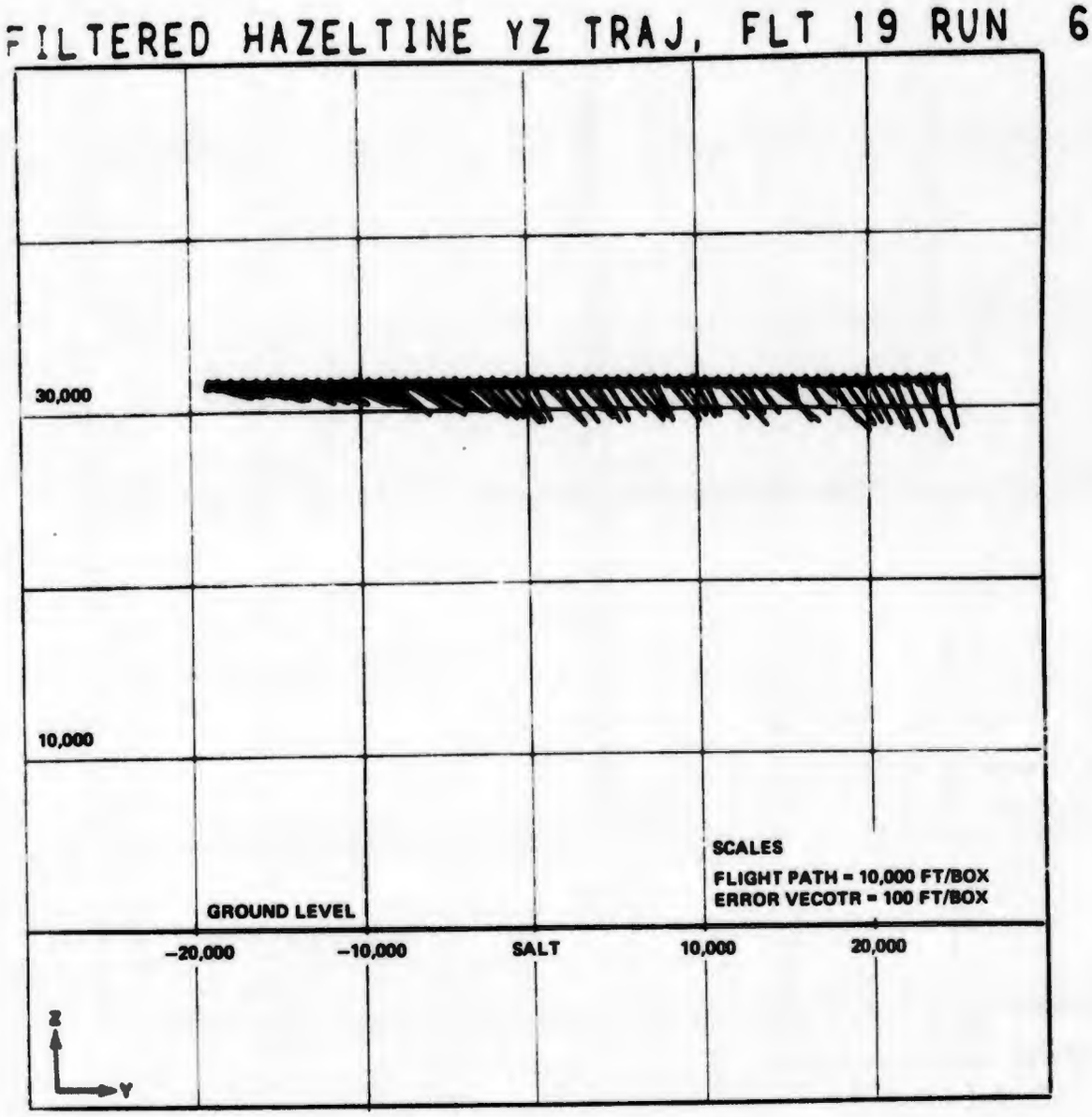

Figure 6-2 Area Navigation Summary Plot

navigation solution is below, slightly to the east (+ X) and north (+ Y) of the WSMR reference which is assumed to be the true position of the aircraft. The exaggerated scale of the error vector shows the solution to be approximately 30 ft below the aircraft position at the north end of the flight path.

The solution data used to generate this error plot was processed through the two-state filter. Therefore, most of the solution noise has been removed resulting in the reasonably well ordered error vectors. The solution error is caused by various steady-state measurement (pseudo range) errors located in the test system which will be described later in this section.

One other point needs to be made about the data in Figures 6-1 and 6-2. The solution vector error is seen to be dependent upon aircraft position (Figure 6-2 in particular). This effect is due to two causes. The steady-state error affecting the solutions used in these figures has some components which are varying slowly with time. These show up as small changes in position error over a flight. The second, and more important cause, is the effect of the linear tranfsormation of the pseudo-range measurements into the user's position solution. The linear transformation, in general, amplifies a measurement error in the process of converting to the solution domain. Since the elements of the linear transformation are a function of the aircraft-to-transmitter geometry, the amplification value changes along the flight path resulting in a varying solution error which in turn is being caused by a steady-state measurement error. (see Section 4.2).

A similar presentation of another data run, flight 19, run 7, is given in Figures 6-3 and 6-4. On this data run, the aircraft descended from 32,000 ft to 18,000 ft above ground level. Figure 6-4 shows a portion of this descent from 27,000 ft to 20,000 ft. The aircraft is at 23,000 ft AGL when passing over Salt Site (Ch. 1) which is at Y= 0. On this run, as in run 6, the solution errors are primarily in the Y and Z directions as shown on Figure 6-4. The cross track error in X is very small as shown in Figure 6-3. The combination of the measurement error distribution in the system and the linear transformation causes the navigation solution to be below the aircraft flight path at the north end of the run (Y = 25,000 ft) and above the navigation solution at the south end of the run (Y = -28,000 ft). These data are typical of the navigation system performance obtained during flights 17-23 prior to making corrections to the data as a result of identifying error mechanisms in this data set.

6.1 DETAILED FLIGHT DATA ANALYSIS

6.1.1 Flight 17

Of the six runs attempted on flight 17, only the first three produced a navigation solution. A system failure occurred at the calibration receiver site after run 3 which prevented post flight software synchronization of the transmitters and thus obviated a navigation solution. Runs 1 to 3 showed typical navigation quality for this flight group. Since the data did not show any unusual behavior, the runs are included in the overall data set statistics but not presented here in detail.

6.1.2 Flight 18

During flight 18, the Hazeltine receiver was operated in two tracking loop configurations, second order and third order. Runs 1 and 2 (tracking loop operating in

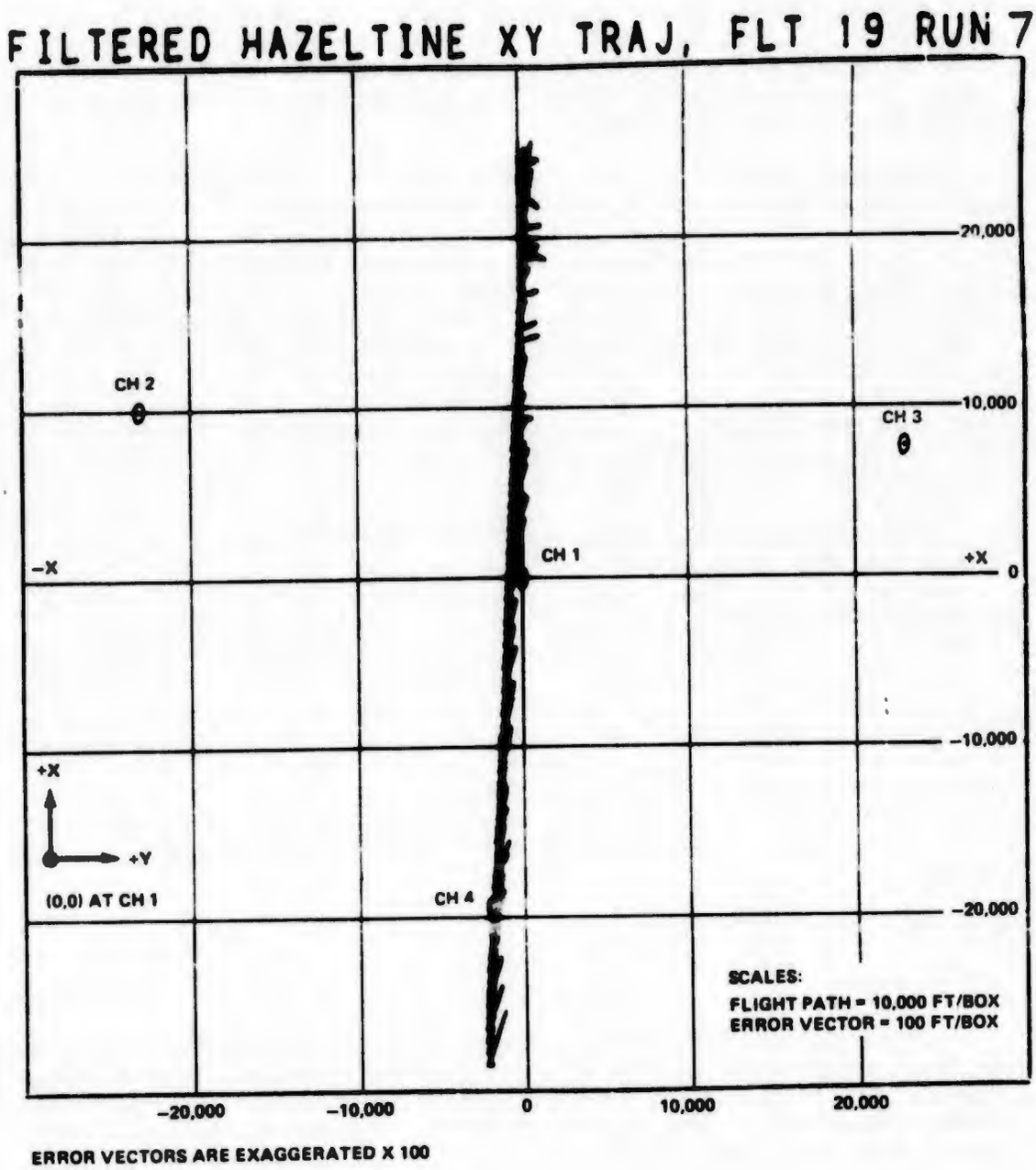

Figure 6-3 Area Navigation Summary Plot

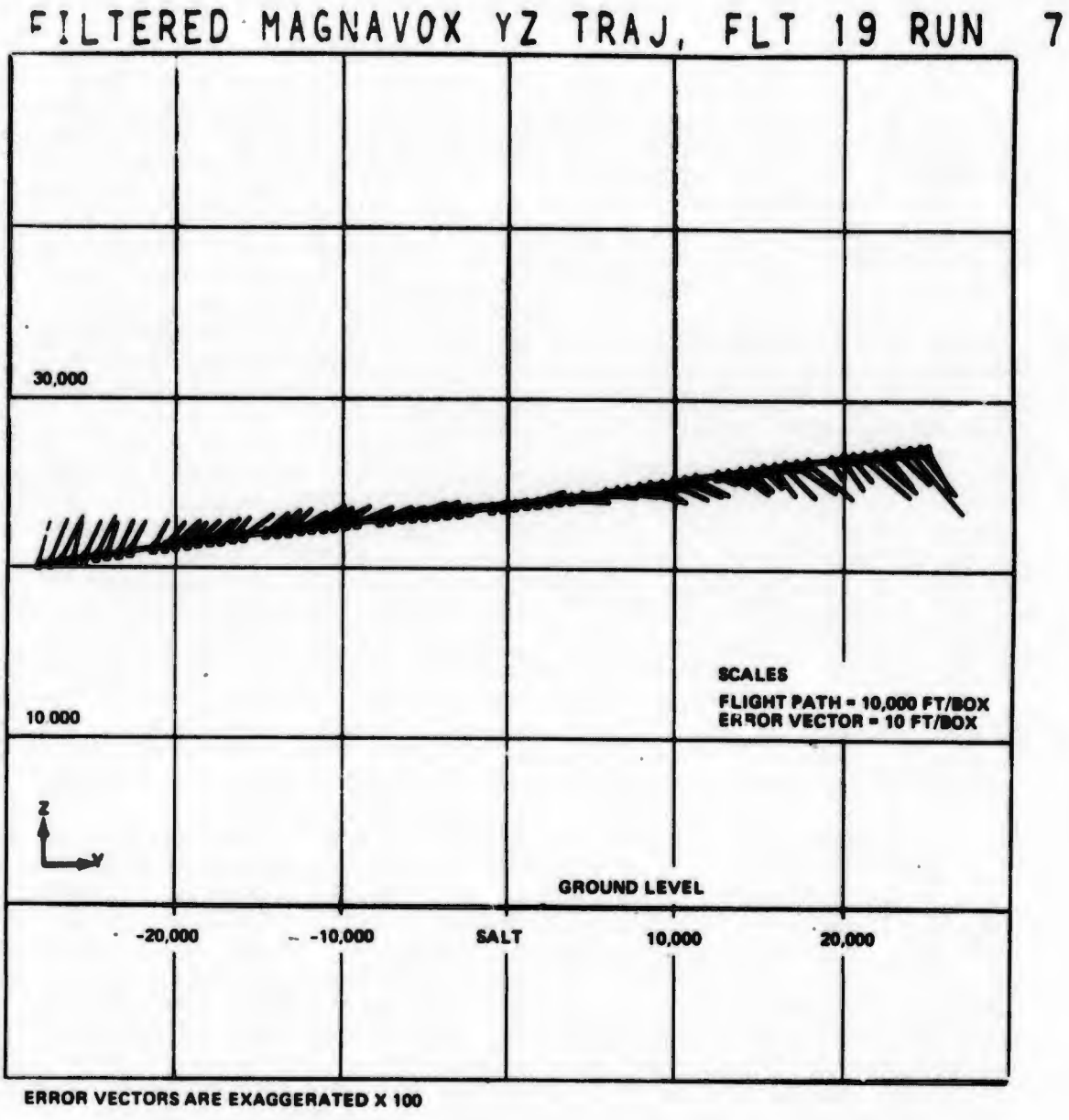

Figure 6-4 Area Navigation Summary Plot

second order) show a significant change in the HC velocity residual (navigation solution compared to WSMR) standard deviations compared to data later in the flight where the loop was operating in third order. Figure 6-5A shows the standard deviation of the HC velocity solution error residual ($\sigma\delta\dot{x}$, $\sigma\delta\dot{y}$, $\sigma\delta\dot{z}$) for both flights 18 and 20. The data are presented in terms of an error band containing the $\sigma\delta\dot{x}$'s etc. which are obtained by partitioning the error residual time series into sequential 50 point samples, and then computing the statistics of each partition. The increased noise content of the data while the receiver is operating in second order loop is evident on the X and Y velocity residuals. On runs 1 and 2, Figure 6-5 shows the $\sigma\delta\dot{x}$ and $\sigma\delta\dot{y}$ magnitudes to be about 1.0 fps, while on the later runs when the receiver is operating in third order loop these quantities are about 0.3 fps. Flight 20 data, presented on the same figure, shows comparable third order loop $\sigma\delta\dot{X}$ and $\sigma\delta\dot{Y}$ performance.

This phenomenon is also evident in the measurements themselves. Figure 6-5B shows the observed standard deviations of the raw pseudo-doppler measurements (ground and user components included) on channels 1 and 3. These σ's are calculated by the variate difference method of variance estimation (see Section 4.1 for further details of the method) and therefore do not require the use of the WSMR reference trajectory. There is an obvious decrease in noisiness at the beginning of run 5, when the receiver was switched to third order operation. The data also show much more erratic behavior on the first four runs than on the later three. Carrier loop noise increases by more than a factor of two when going from third order to second order operation. This increase is evident on all four channels (only channels 1 and 3 are presented in Figure 6-5B), and is expected since the carrier loop bandwidth opens by a factor of 100 in the lower order configuration (about 20 Hz for third order loop, 2 KHz for second order).

The Z-coordinate velocity behavior is different from the X and Y velocities on flight 18. As shown in Figure 6-5A, the Z axis velocity does not respond to the third order command given after run 2. The flight 20 data on this figure show normal third order loop behavior for the Z-coordinate velocity noise. An examination of the measurements (pseudo-range rate) on each of the four channels was made to determine the cause of the Z velocity behavior. This examination indicated that the airborne receiver switched from second to third order loop on channels 1, 2 and 3, but not on channel 4. Due to the position of the aircraft with respect to the transmitters, the transformation of pseudo range-rates into coordinate velocities is such that channel 4 data strongly influences the Z axis, but has small influence on the X and Y axes. Therefore, the malfunction of the second/third order control logic in channel 4 is expected to show up as an error only on the Z-axis coordinate data.

As a matter of side interest, the second/third order test provided some insight to the quality of the velocity residual obtained from the comparison of the navigation solution to the WSMR data. An examination of the velocity residual errors in Figure 6-5A shows that the σ residual errors increase by a factor of 3 when operating in second order tracking loop compared to third order loop. This is interesting since the receiver internal loop noise actually has a much sharper increase from third order to second order operation than the residual error in Figure 6-5A indicates. While the second order loop noise is clearly shown by this figure, the actual receiver third order loop noise is below the basic residual noise level. Therefore, the velocity residual noise level, while the receiver is operating in third order loop, is a result of factors external to the loop such as transmitter oscillator noise, atmospheric scintillation, airframe response to turbulence, and WSMR reference data noise.

Haz DATA

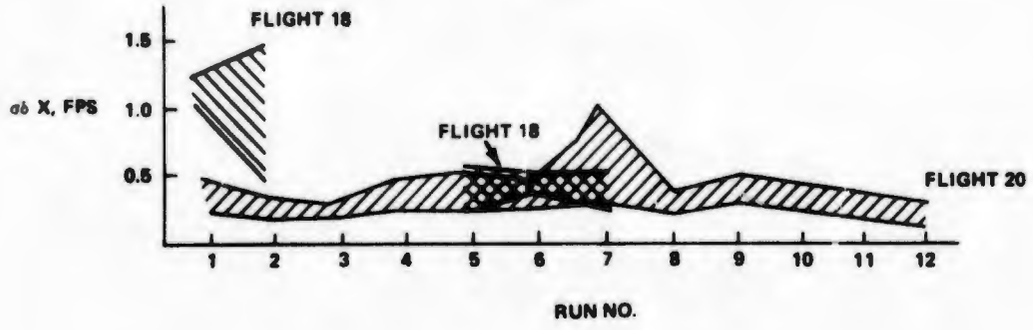

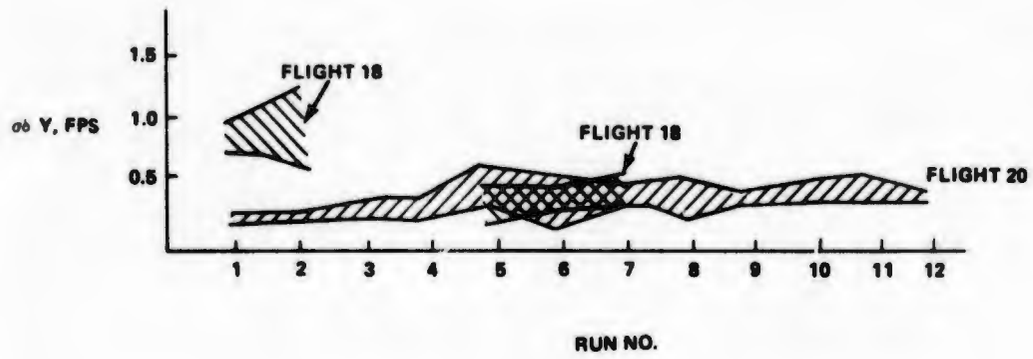

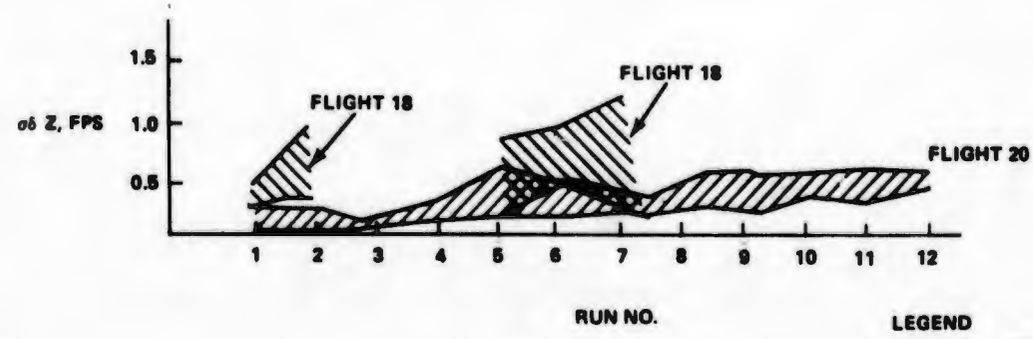

LEGEND

FLIGHT 18

FLIGHT 20

A. VELOCITY RESIDUAL ERRORS ON FLIGHTS 18 AND 20

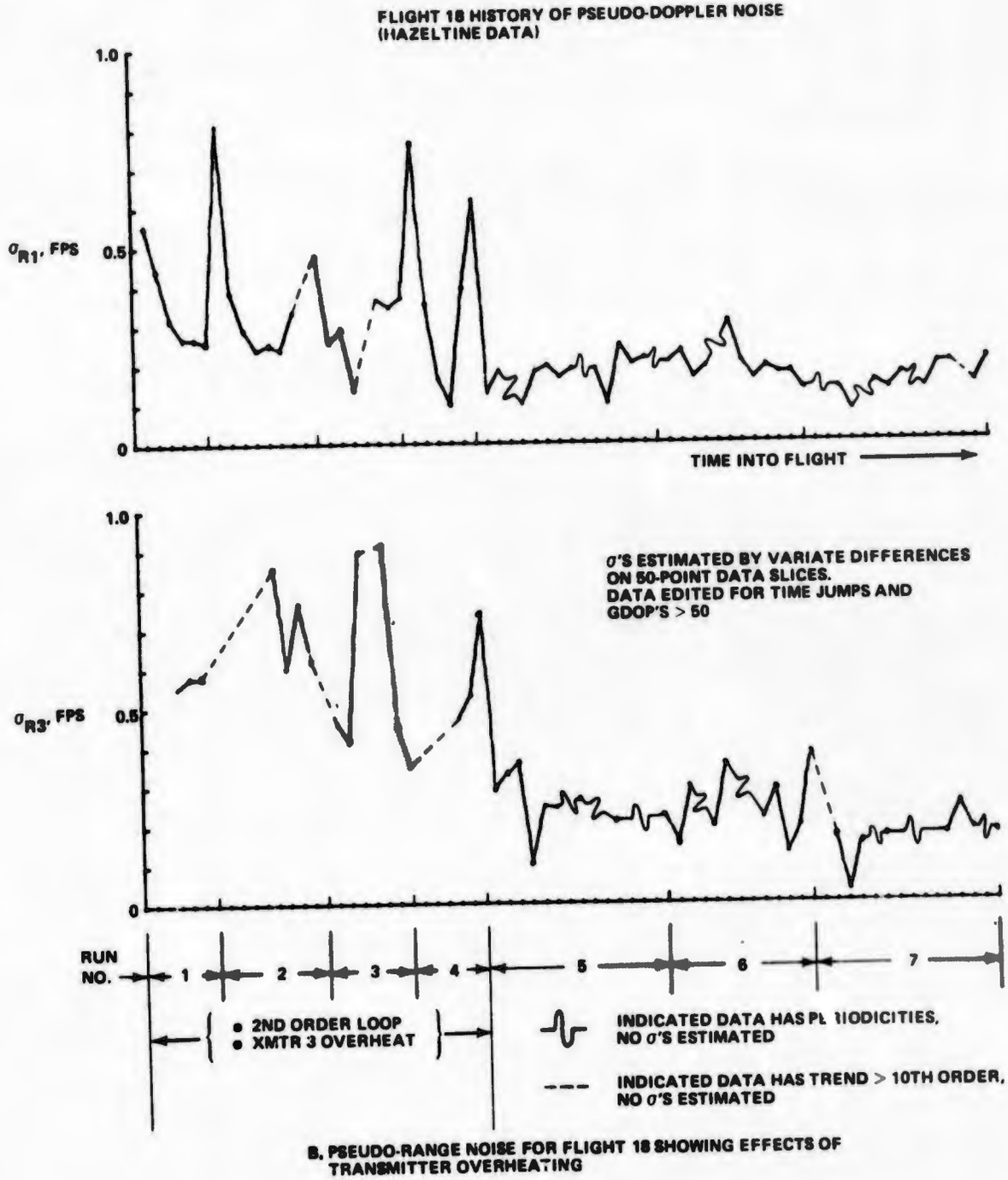

B. PSEUDO-RANGE NOISE FOR FLIGHT 18 SHOWING EFFECTS OF TRANSMITTER OVERHEATING

Figure 6-5 Velocity Residual and Pseudo Doppler Noise Effects For HC 2nd/3rd Loop Operation

Another event which occurred during flight 18 was an equipment failure at EC-50 (Ch. 3). An ac generator operating a transmitter cooling fan at the site failed early in the flight. Since the transmitter electronics are operated off batteries, and the site was unmanned, the generator failure was not immediately detected. When the generator failed, the temperature within the transmitter began to rise because the fan stopped. The transmitter was eventually shut down automatically by an overheat protection switch. The transmitter shut-down alerted personnel at the MCS and a crew went to the site. The transmitter was restarted by cooling the interior of the case with a CO_2 fire extinguisher. The transmitter temperature rise had an noticeable effect on the data. The X-position residual standard deviation ($\sigma_{\delta x}$) is considerably greater during runs 1 and 2 of flight 18, than during runs 5 through 7 as shown in Figure 6-6A. The transmitter was cooled down and restarted just before run 5. Apparently the temperature rise affected the code clock jitter. This is confirmed by Figure 6-6B which shows the pseudo-range σ estimates for channels 1 and 3. Channel 3 errors primarily influence the X-coordinate data and have slight effect on the Y and Z coordinates in the area navigation geometry. Thus this type of problem would be expected to show up mainly in the X-coordinate data.

6.1.3 Flight 19

Referring to Table 6-1, there were eight runs attempted with received signal levels of -123dbm on runs 1 and 2, and levels of -133dbm on the remaining runs. Of the eight runs, six runs produced good navigation solutions.

The Hazeltine receiver had a circuit malfunction in the RF/IF section which permitted receiver operation but at a reduced front end sensitivity. So the receiver was, in effect, tracking a signal lower than -133dbm. However, no quantitative measure of the loss of sensitivity was available. An inspection of the data did not show any effect from this malfunction even though the next flight, flight 20, does produce some measurable effects in the data quality at very low signal levels.

The navigation solution produced from data collected on run 1 was poor. In reviewing the data, we found a partial failure in the calibration receiver which resulted in poor synchronization of the transmitters by the post-flight software. The pseudo-doppler data recorded at the Mobile Calibration Station (MCS) calibration receiver for the first three runs of flight 19 are shown in Figure 6-7. These data represent a measurement of the frequency offset of each transmitter with respect to the calibration receiver master oscillator. The frequency offset data have been converted to an equivalent range rate and plotted as a function of time. (The time scale in this figure is Greenwich Mean Time in seconds.) The large noise spikes appearing simultaneously in the four transmitter measurements in run 1 are due to an intermittant circuit failure common to all four carrier tracking loop channels in the calibration receiver. These noise spikes affect the software synchronization of the transmitters (see Section 3.1); this in turn affects the navigation position errors. The problem in the receiver was corrected after run 1 resulting in acceptable frequency measurements for the remainder of the flight.

Two examples of the navigation quality were presented in Figures 6-1, -2 and 6-3, 4, runs 6 and 7 respectively. Figures 6-1 and 6-2 give the Hazeltine solution and Figures 6-3 and 6-4 give the Magnavox solution. Even though the aircraft flight paths are not the same for these two runs, (run 6 HC data is level at 34,000 ft MSL, run 7 MRL data is a descent from 34,000 to 22,000 ft MSL), the difference in flight path geometry does not fully account for the solution differences exhibited by

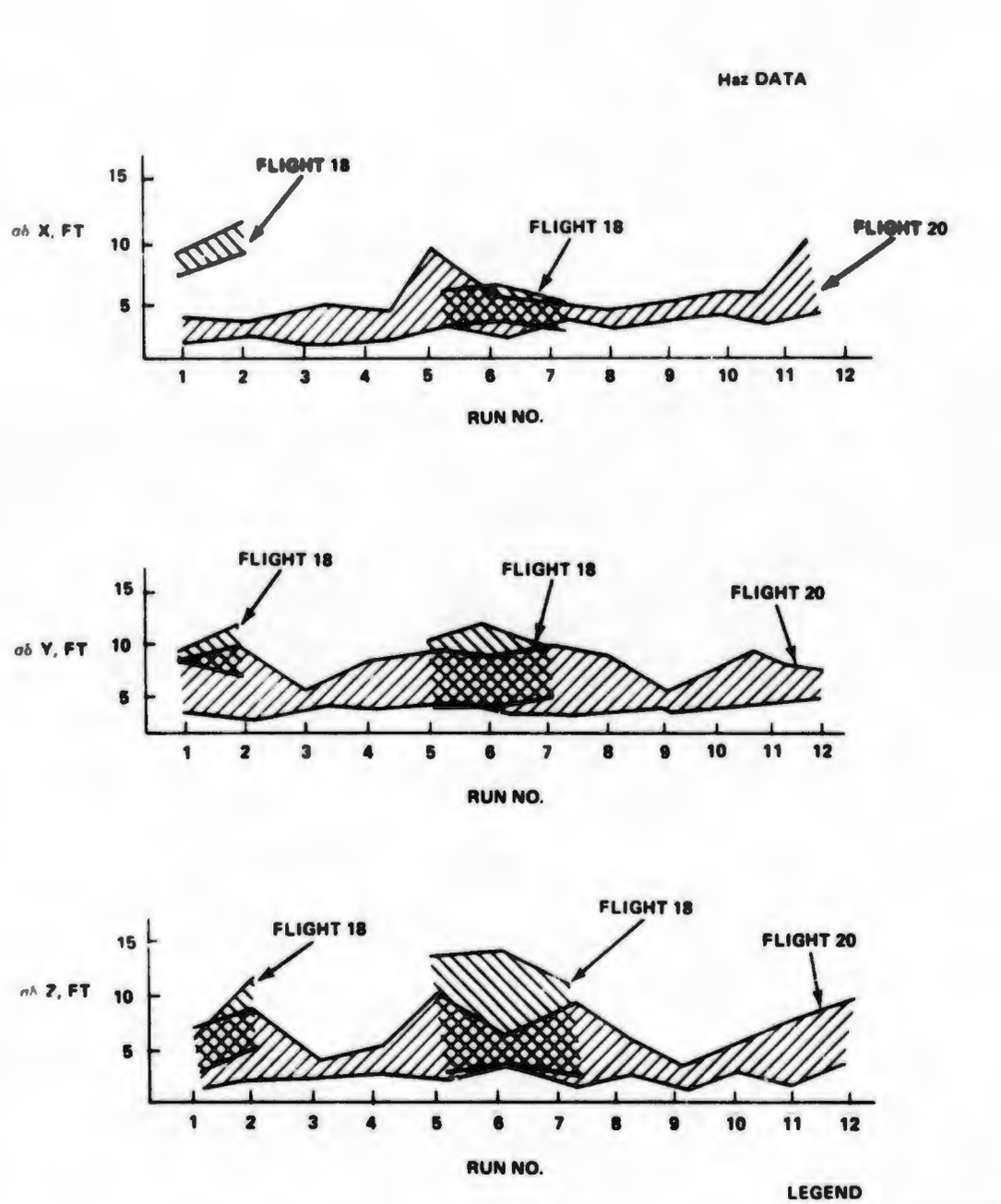

FIG. A X, Y, Z RESIDUAL STANDARD DEVIATION FOR FLIGHTS 18 AND 20

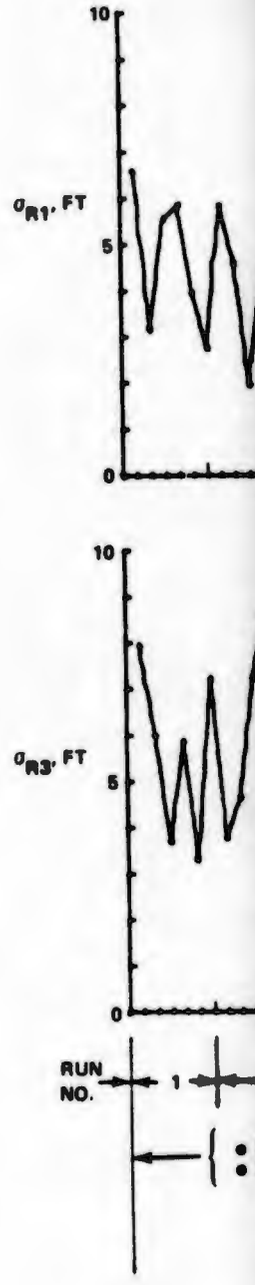

HT 20

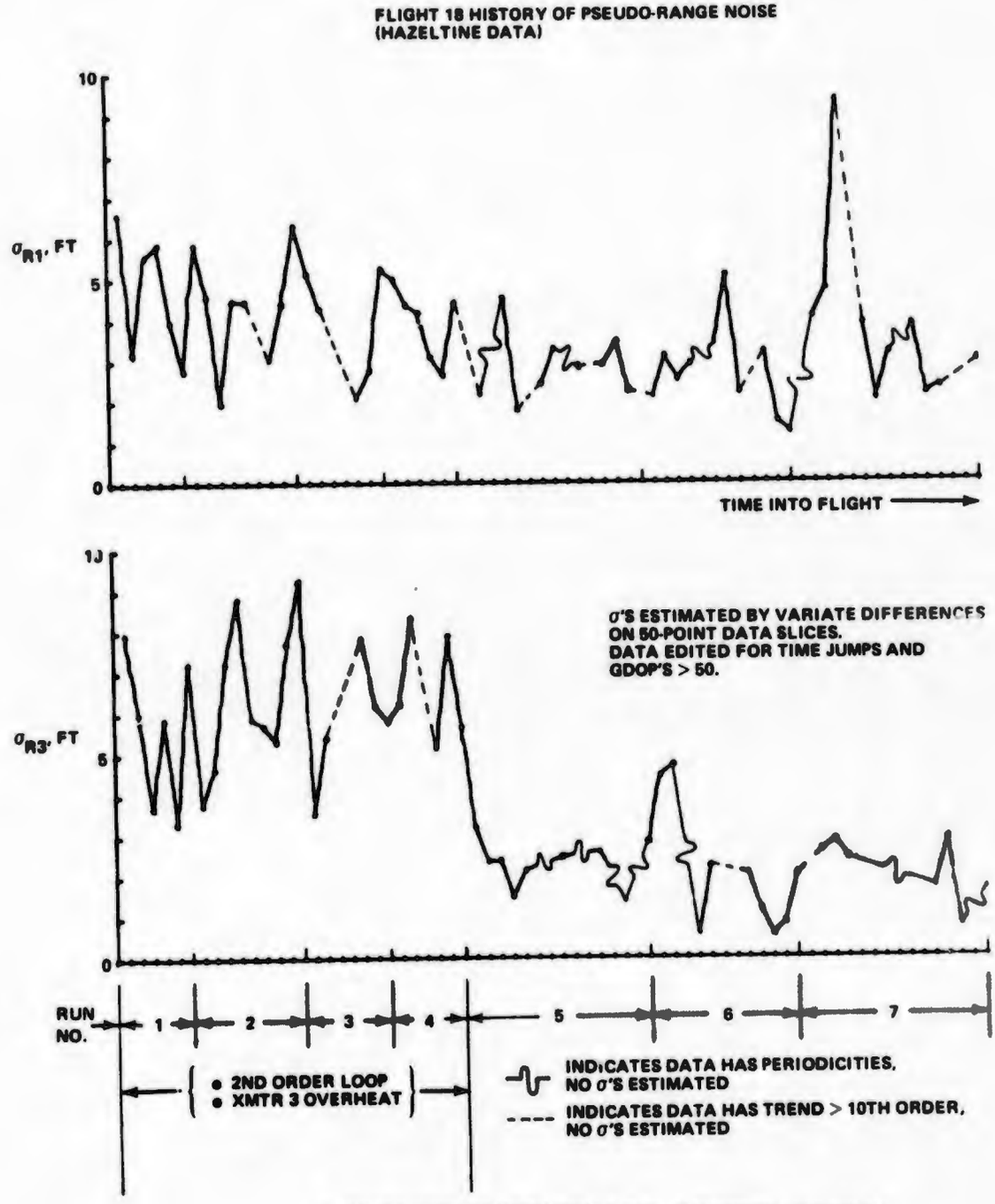

Figure 6-6 Position Residual and Pseudo Range Noise Effects Resulting from Transmitter 3 Overheat During Flight 18

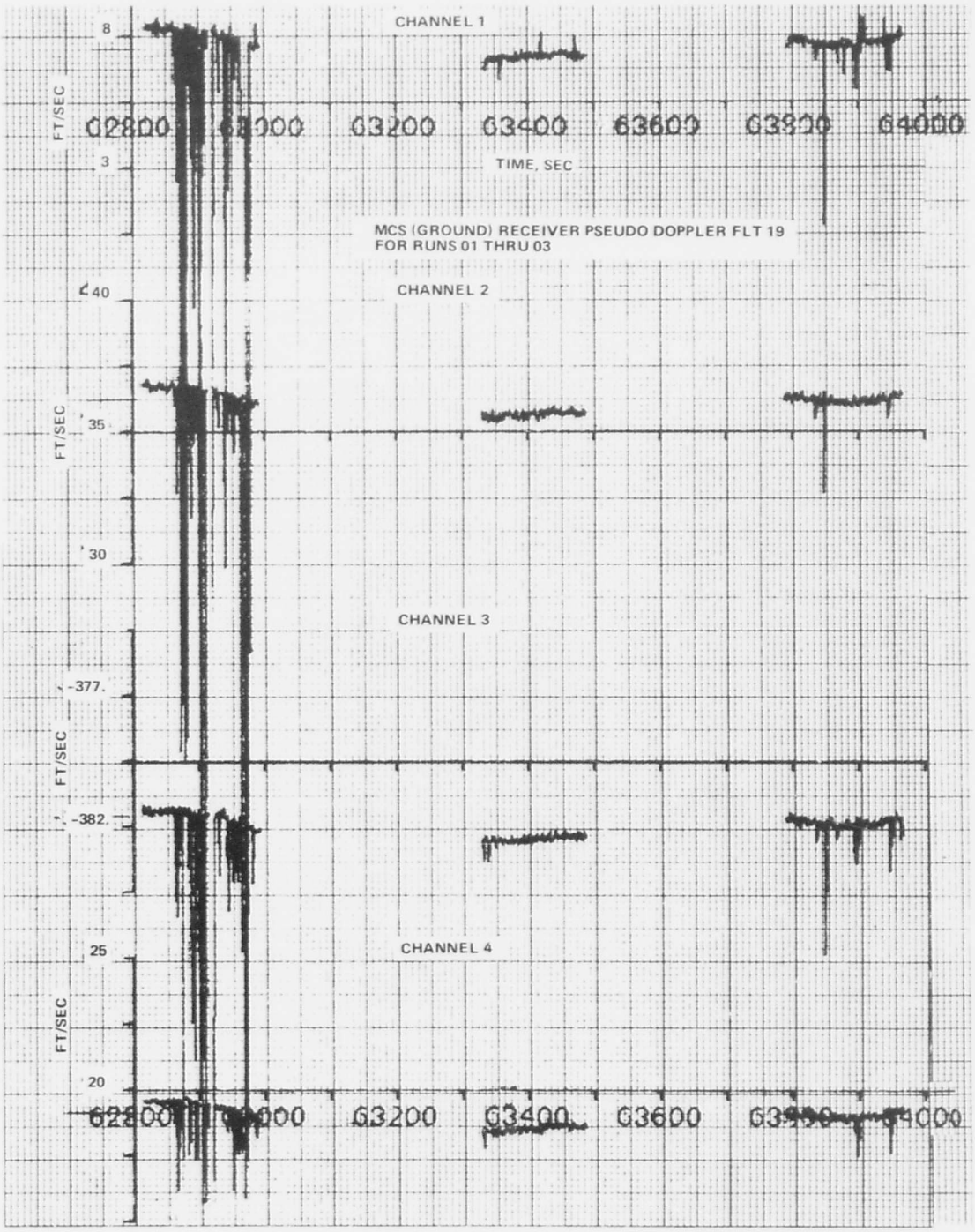

Figure 6-7 Frequency Offset of Transmitter Oscillator Relative to Ground Receiver Oscillator

error vector configurations from the two receivers. This indicates that some of the steady-state error components are located in the airborne receivers and not in the common ground system providing the basic data. One of these error sources, the HC receiver ranging error sensitivity to received signal level, was observed on the next flight.

6.1.4 Flight 20

The purpose of Flight 20 was to examine signal power level effects on the navigation accuracy by varying the signal level while holding other variables, especially flight geometry, as constant as possible. Twelve runs were accomplished producing good solution data for the HC receiver. The MRL receiver failed just before takeoff.

To show the effect of signal power level on the Hazeltine airborne receiver, two runs have been selected. Run 2 was conducted with a signal level of -123dbm at the airborne receiver, and run 10 had a level of -140dbm. The run 2 data are shown in Figures 6-8 through 6-12. The flight profile and general solution performance is shown in Figures 6-8 and 6-9 which depict the flight profile in the X-Y and X-Z planes along with the error vectors connecting the profile (WSMR data) to the test system navigation solution. The corresponding time history of the residual determined by subtracting the WSMR reference data from the system navigation solution is shown in Figures 6-10, 6-11 and 6-12. The residuals are computed at the system data output rate of 5 data frames per second while the error vectors of Figures 6-8 and 6-9 are computed once per second.

The X-coordinate position error is very small for the entire run as shown in Figure 6-8. Figure 6-10 shows the X-coordinate position residual to be less than 15 ft. Since on this run the aircraft flew from south to north, t=0 on the residual plot is equivalent to Y = -14,000 ft. At t-20, the aircraft is over Salt Site at Y=0, and at t=40 the aircraft is north of the transmitter grid at Y = 14,000 ft. Figure 6-9 shows the Y error to be about + 40 ft at the beginning of the run (Y = -17,000 ft) and to gradually become smaller throughout the run. The residual plot in Figure 6-11 confirms this indicating an almost linear slope with time lessening the error to about 18 ft by the end of the data run. Similarly the Z-coordinate solution data depicted below the WSMR reference in Figure 6-9 has a corresponding residual plot, Figure 6-12 quantifying the error at approximately -35 ft.

A similar presentation is given for run 10, -140dbm, in Figures 6-13 through 6-17. The most dramatic change is seen in the Z-coordinate errors. The error vector at Y = 20,000 ft has increased from about 40 ft for run 2 (Figure 6-9) to about 75 ft for run 10. Measurements made of the signal level sensitivity on the bench indicate that a channel with poor performance can give variations of 10-12 ft under the dynamic range considered here. Observing the variations in the Z-coordinate, we see that the geometric mapping of range into position is amplifying the error at the north end of the flight path by a factor of 3.

Another viewpoint is taken in later discussions of the power level effect when we delineate the various error components and their magnitude.

6.1.5 Flights 22 and 23

Flight 22 explored a different geometrical relationship from aircraft to transmitters. The purpose of this was to simulate a 30°Y satellite cluster as seen by a

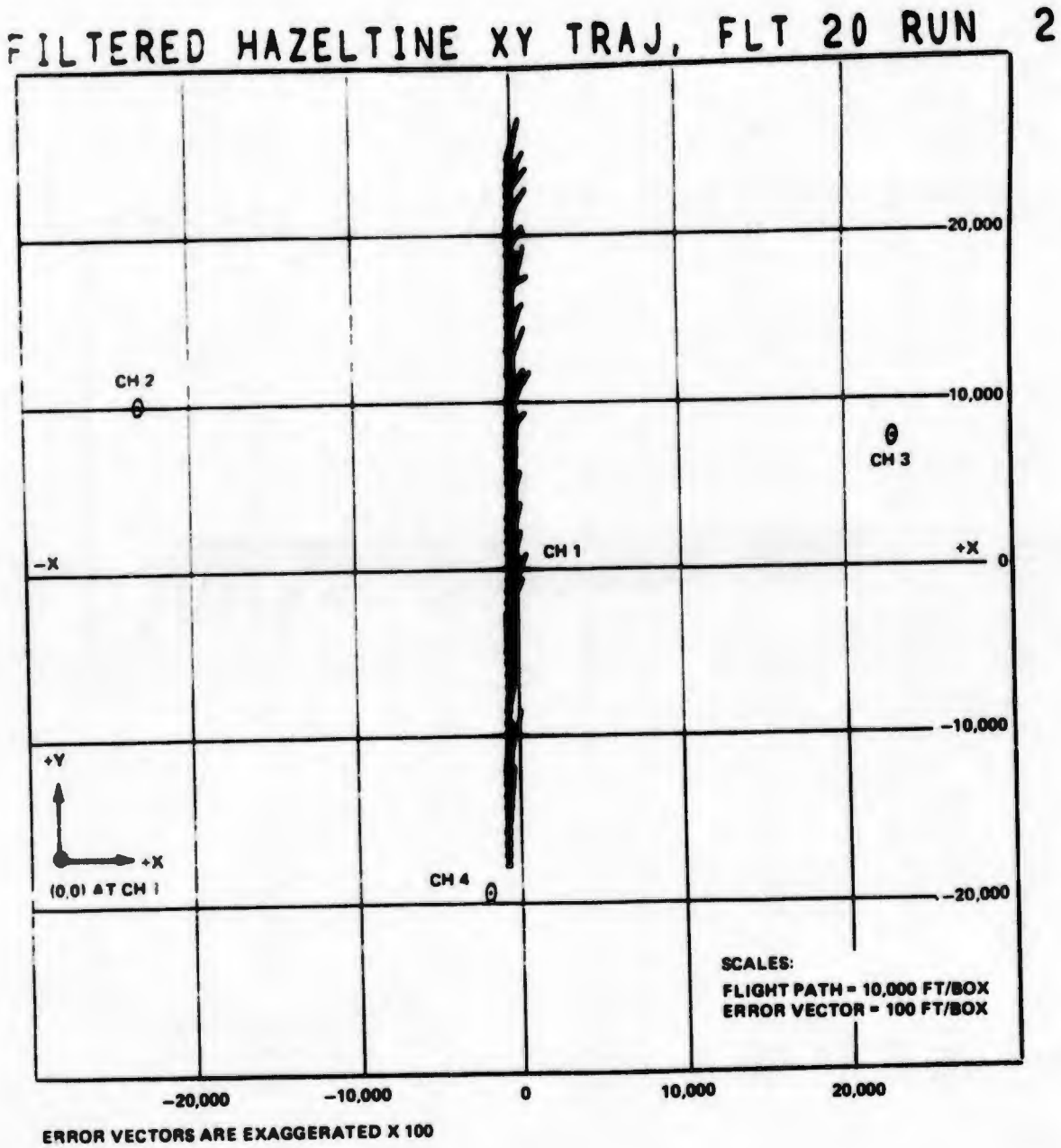

Figure 6-8 Area Navigation Summary Plot

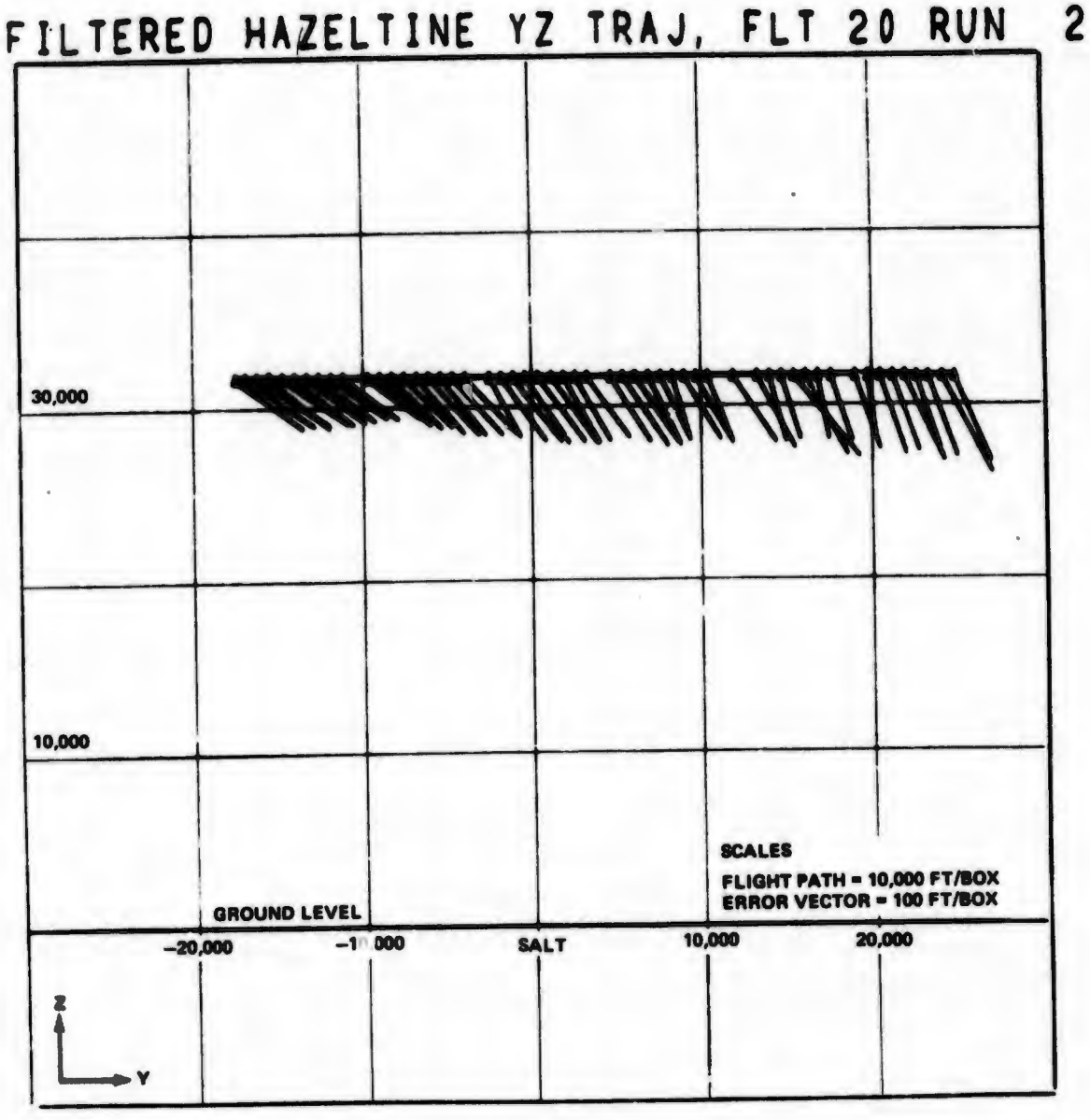

Figure 6-9 Area Navigation Summary Plot

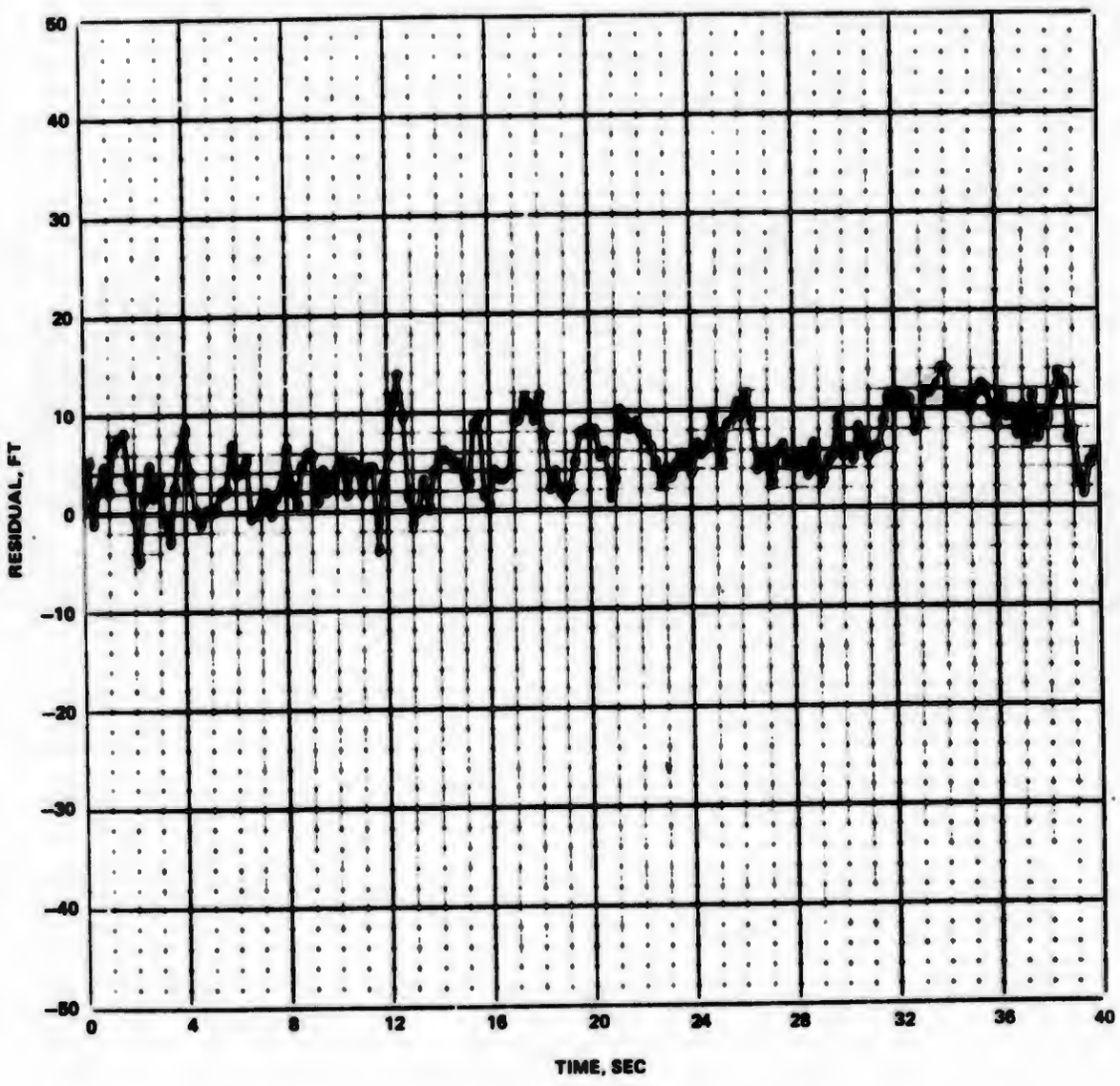

Figure 6-10 X Position Residual vs Time HAZ Flight 20 Run 02

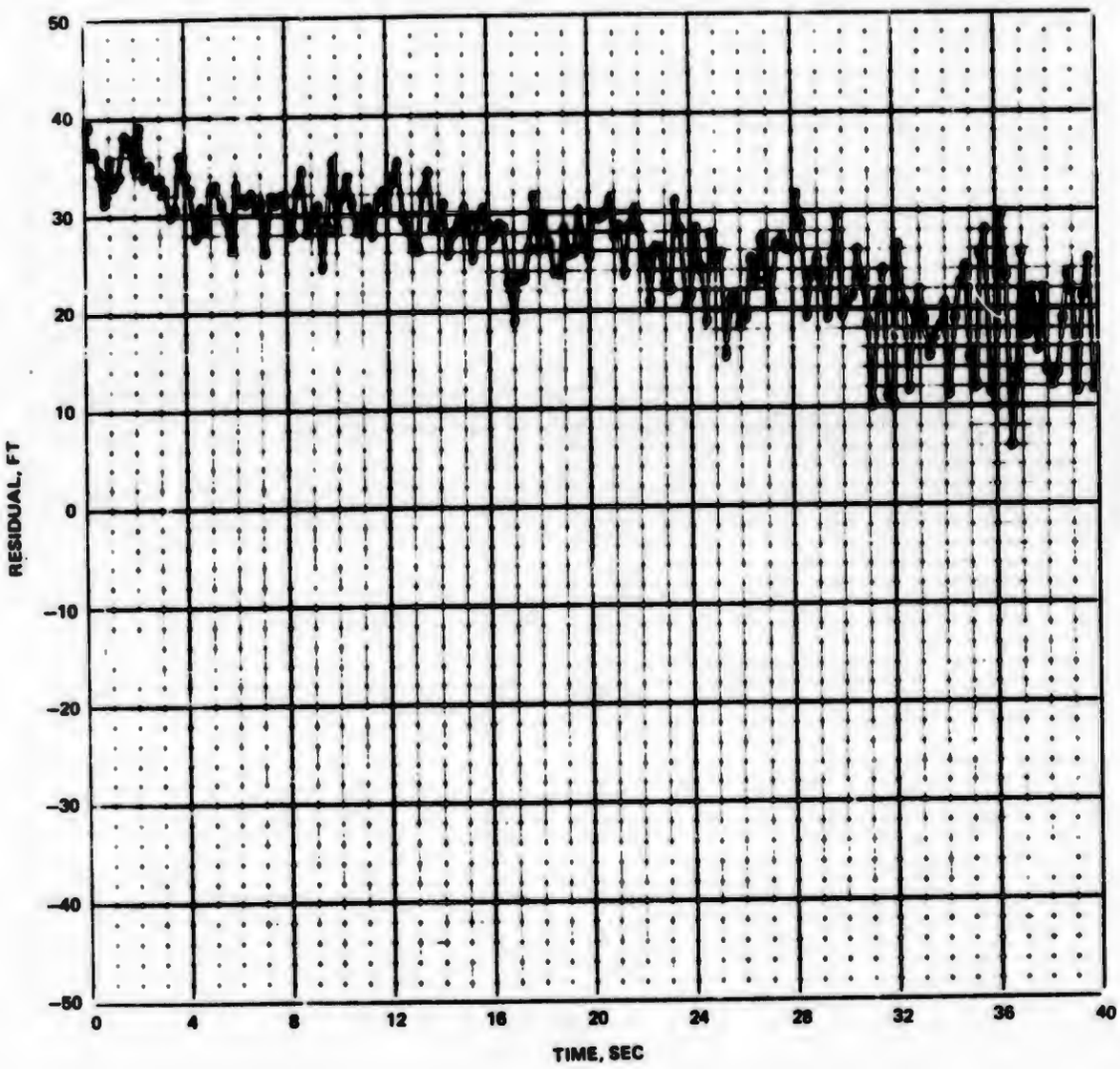

Figure 6-11 Y Position Residual vs Time HAZ Flight 20 Run 02

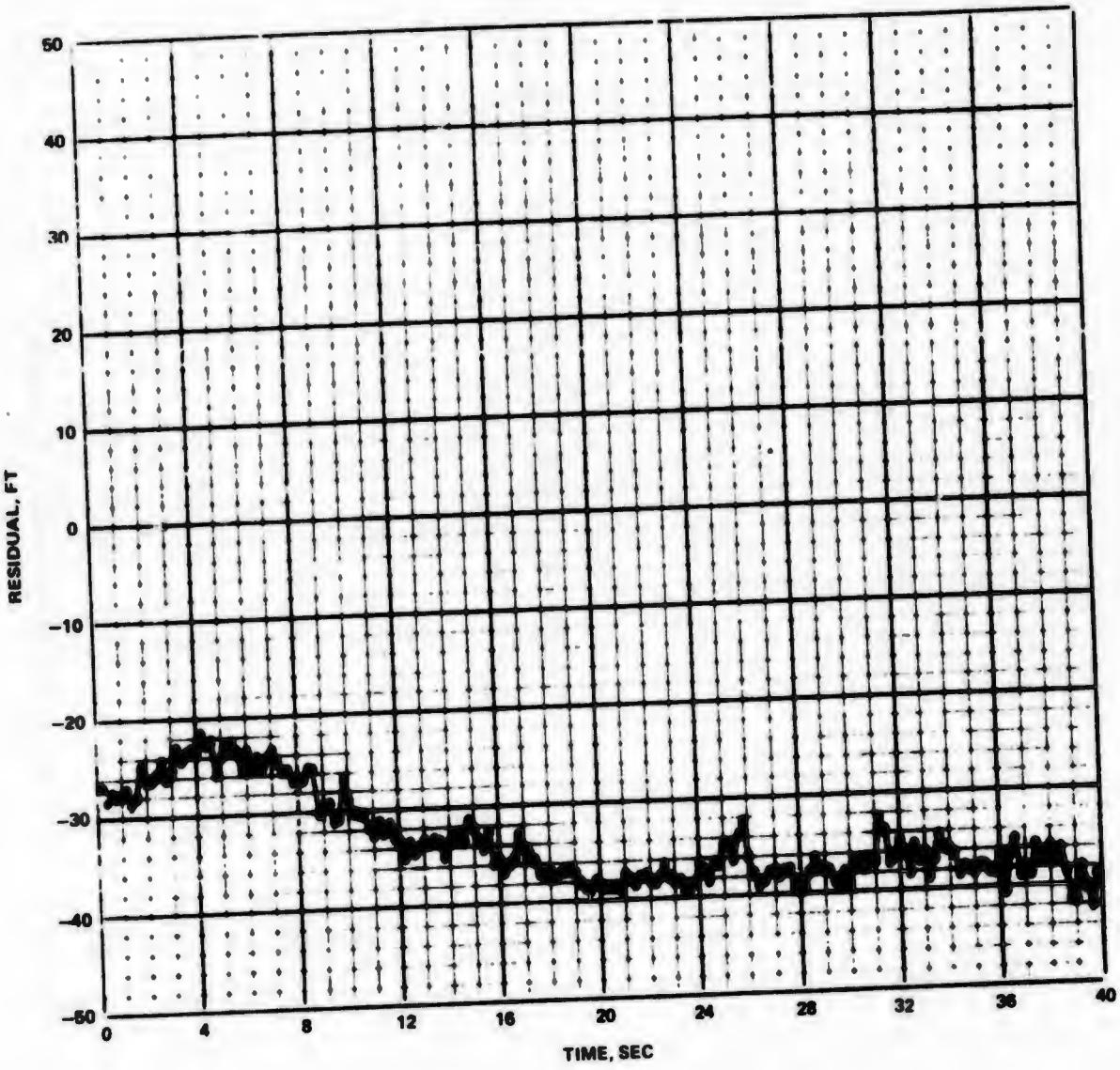

Figure 6-12 Z Position Residual vs Time HAZ Flight 20 Run 02

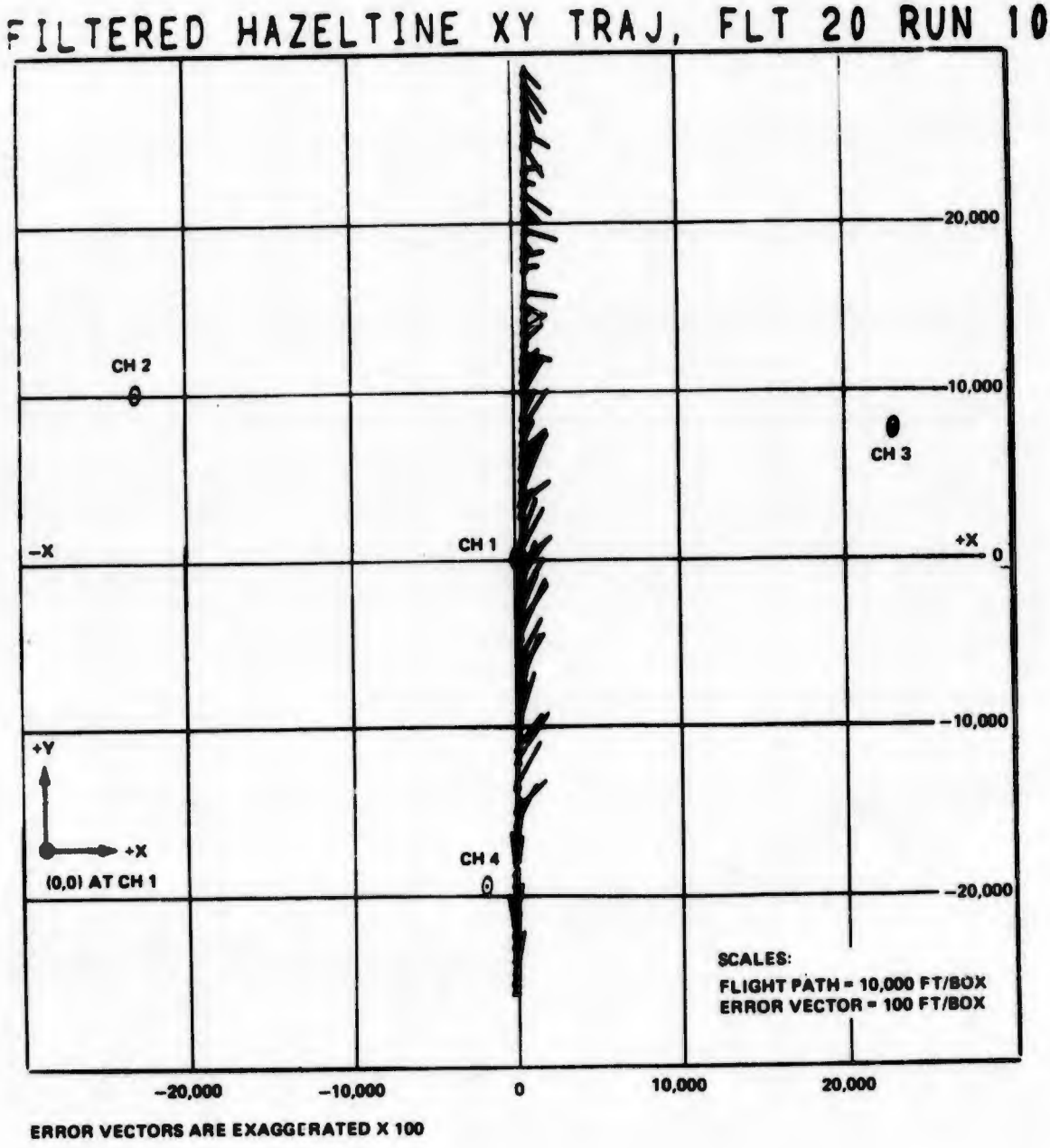

Figure 6-13 Area Navigation Summary Plot

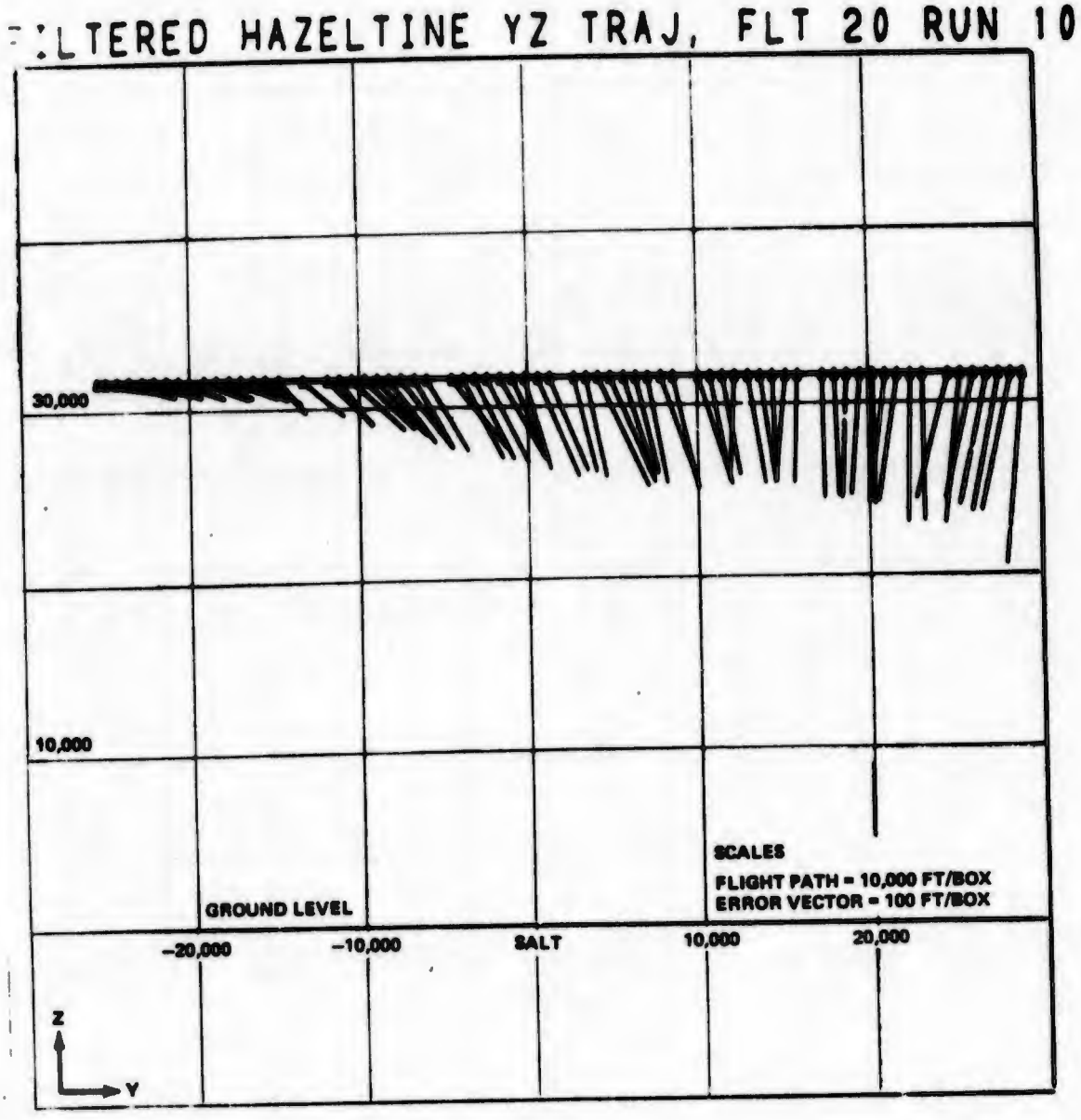

Figure 6-14 Area Navigation Summary Plot

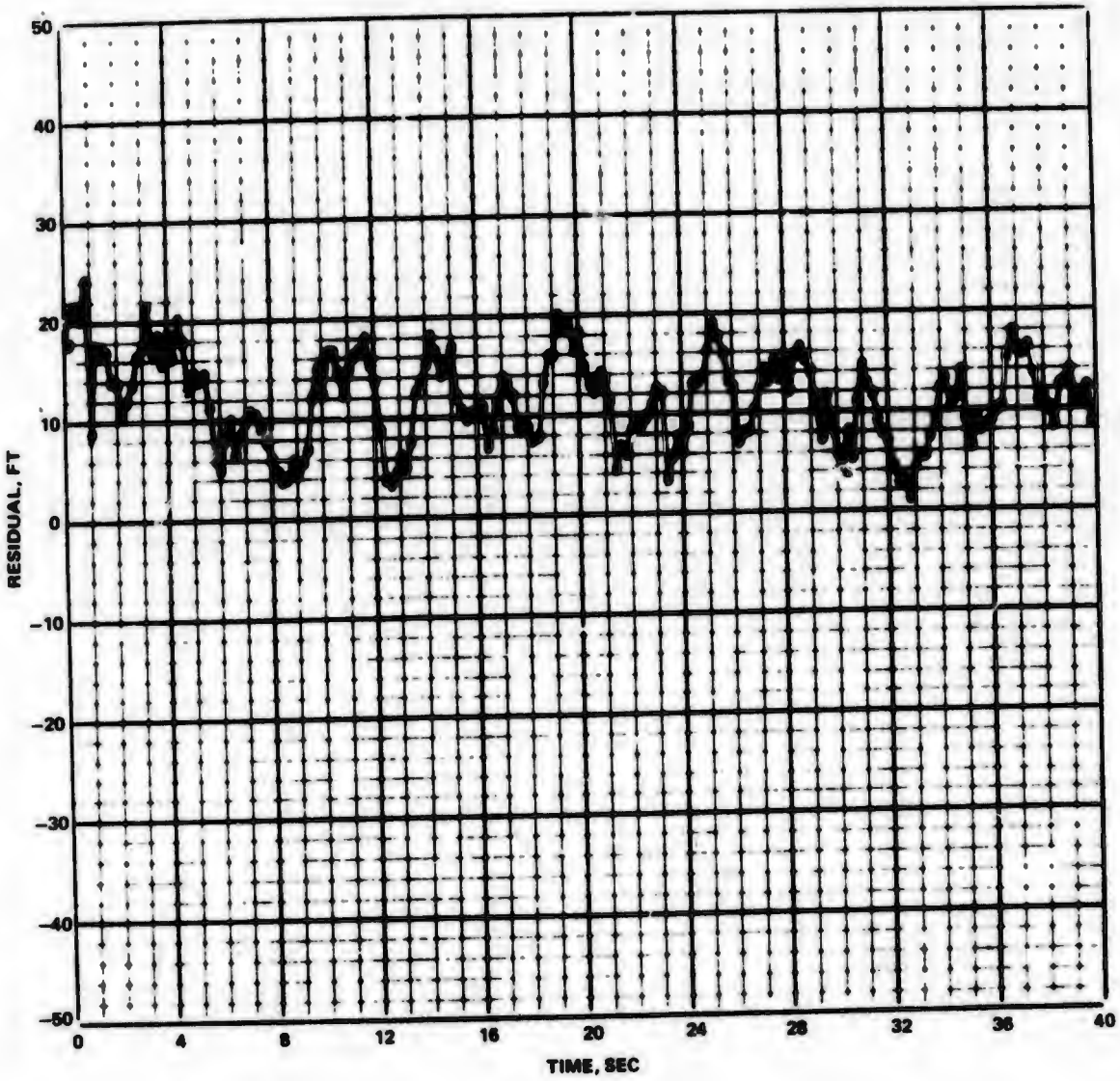

Figure 6-15 X Position Residual vs Time HAZ Flight 20 Run 10

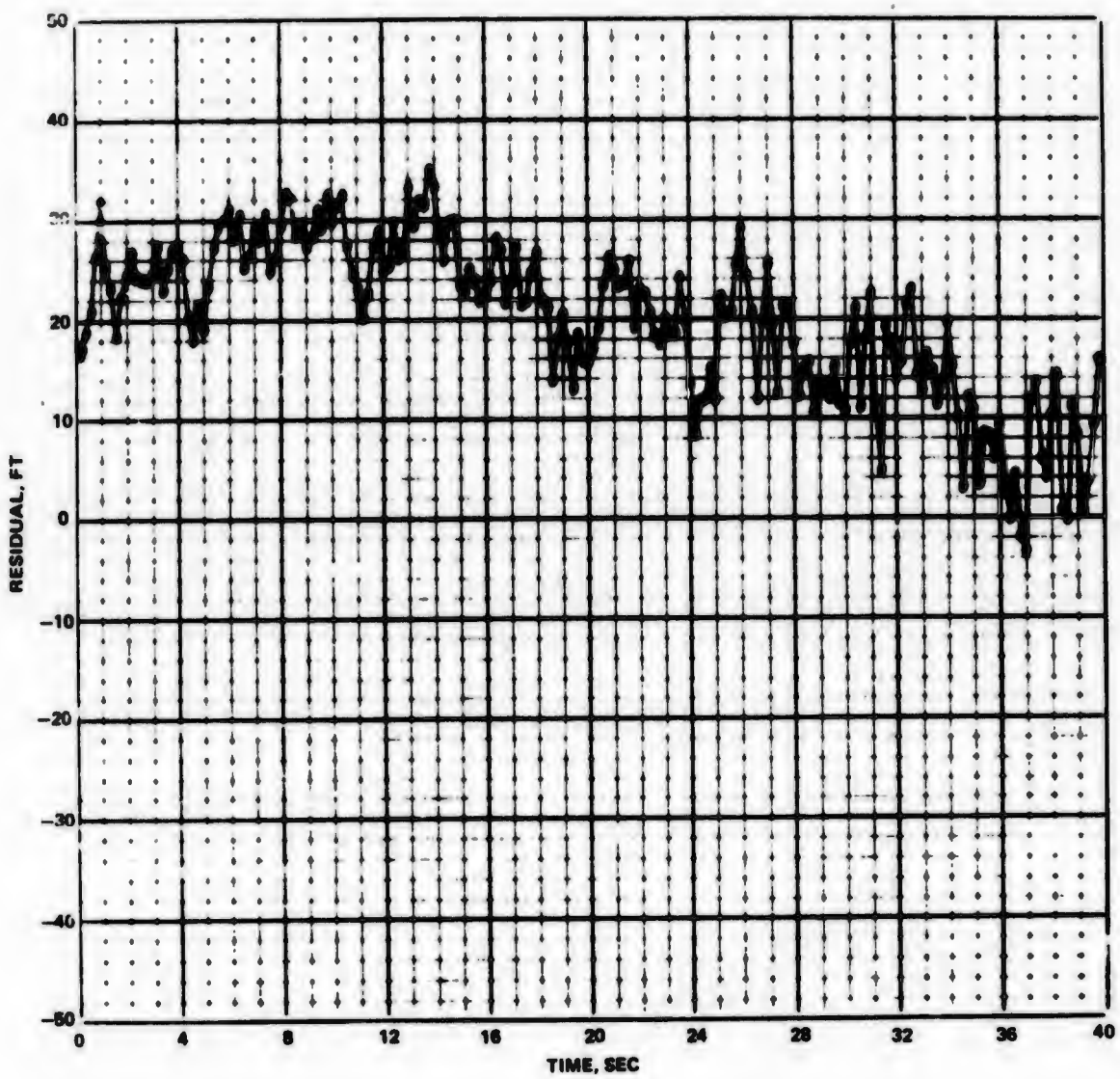

Figure 6-16 Y Position Residual vs Time HAZ Flight 20 Run 10

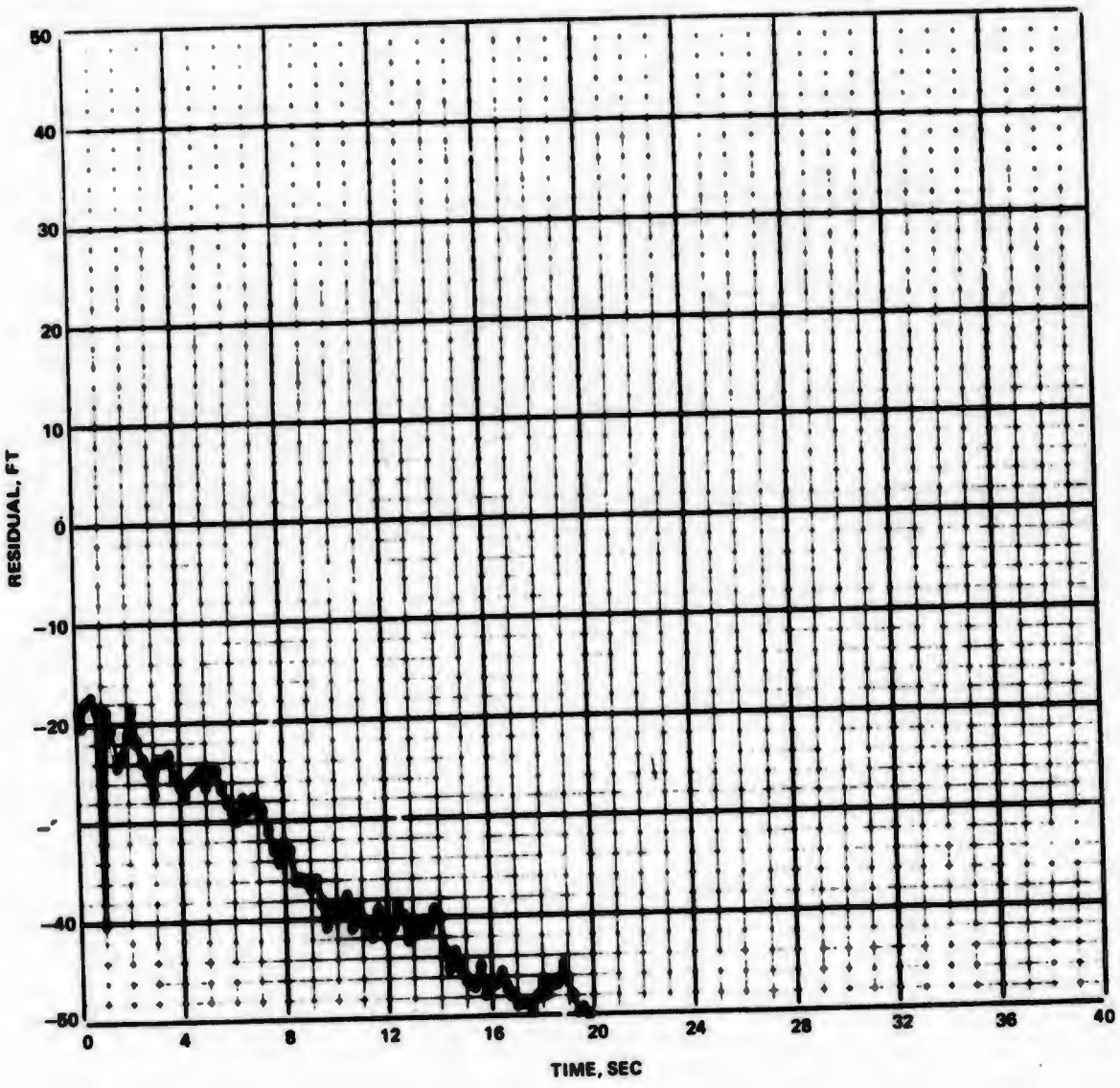

Figure 6-17 Z Position Residual vs Time HAZ Flight 20 Run 10

user over CONUS and to introduce another controlled variable in the test program to see if there were any unknown geometry dependencies in the system. Figures 6-18, -19 and 6-20, -21 show the HC and MRL receiver navigation solutions respectively. In general, the error magnitudes observed during this flight were considerably less than on any other flight in this data group. The navigation performance on flight 22 provided the key to a steady-state error source appearing on channel 4 on flights 17-20. This error source was localized to an erroneous ground link measurement resulting from rf cable impedance mismatches. By reviewing other ground link measurements, an improvement in the system performance was achieved by finding link measurements not contaminated by cable mismatches (see Section 4.2.1).

Flight 23 was conducted at low altitudes, approximately 3,000 ft above ground level, in order to introduce more range dynamics into the system than was possible at high altitude. The testing was much more difficult to conduct at these altitudes because the antenna pattern coverage from the transmitter sites was optimized for 30,000 ft runs. However, lock-up was achieved on most data runs for a long enough period to evaluate the system accuracy.

Data from run 5 is shown in Figures 6-22 through 6-25 for both HC and MRL receivers. As expected from our theoretical understanding of the system, no dynamics effects were observed in the pseudo range or pseudo range-rate measurements. The error contributions seen in these plots are from other sources similar to the rest of the flight 17 to 23 group. Once again there is a significant difference between HC and MRL solutions. These differences are only partly understood.

6.2 IDENTIFICATION OF ERROR COMPONENTS

In reviewing the navigation solution errors for flights 17-23, it is evident the solution steady-state errors changed from flight-to-flight. This was unexpected since the primary reason for reconfiguring the ground system prior to these flights was to eliminate delay variables. While this was largely accomplished, some delay variation remained in the system. The steady-state error trends for these flights are indicated by the average error in the interchannel residuals (μ_δR2-1, μ_δR3-1, μ_δR4-1) shown in Figure 6-26. We are discussing here the bias variation and not the gross differences in these three sets of measurements (μ_δR2-1 $\approx 4'$, μ_δR3-1 ≈ 0, μ_δR4-1 ≈ 15 ft), which is another topic.

An investigation of the data indicates that there are three predominant sources of this variation; apparent uplink antenna delay, signal level, and cable delay variation. Of these, only the signal level effect is specifically associated with the receiver hardware. The other two effects are peculiar to the test system set-up at WSMR. While the data are affected by all of these and the effects must be understood to provide information for improving future designs, the error source peculiar to the WSMR test set-up represent shortcomings in the overall simulation quality and should be considered in a different manner than the errors in the receiver equipment.

A review of the test profiles in flights 17-20 (Table 6-1) shows that these flights consisted of paths A and C only. There is a marked difference in the steady-state error effects from these two flight paths. Figure 6-27 and 6-28 show mean error variation resulting from the flight paths at 34,000 ft MSL (path A) and at 22,000 ft MSL (path C). The error shown in these figures is arrived at by differencing ranges i-1, i=2, 3, 4, in both the navigation system and the WSMR data, and then computing the residual between these quantities.

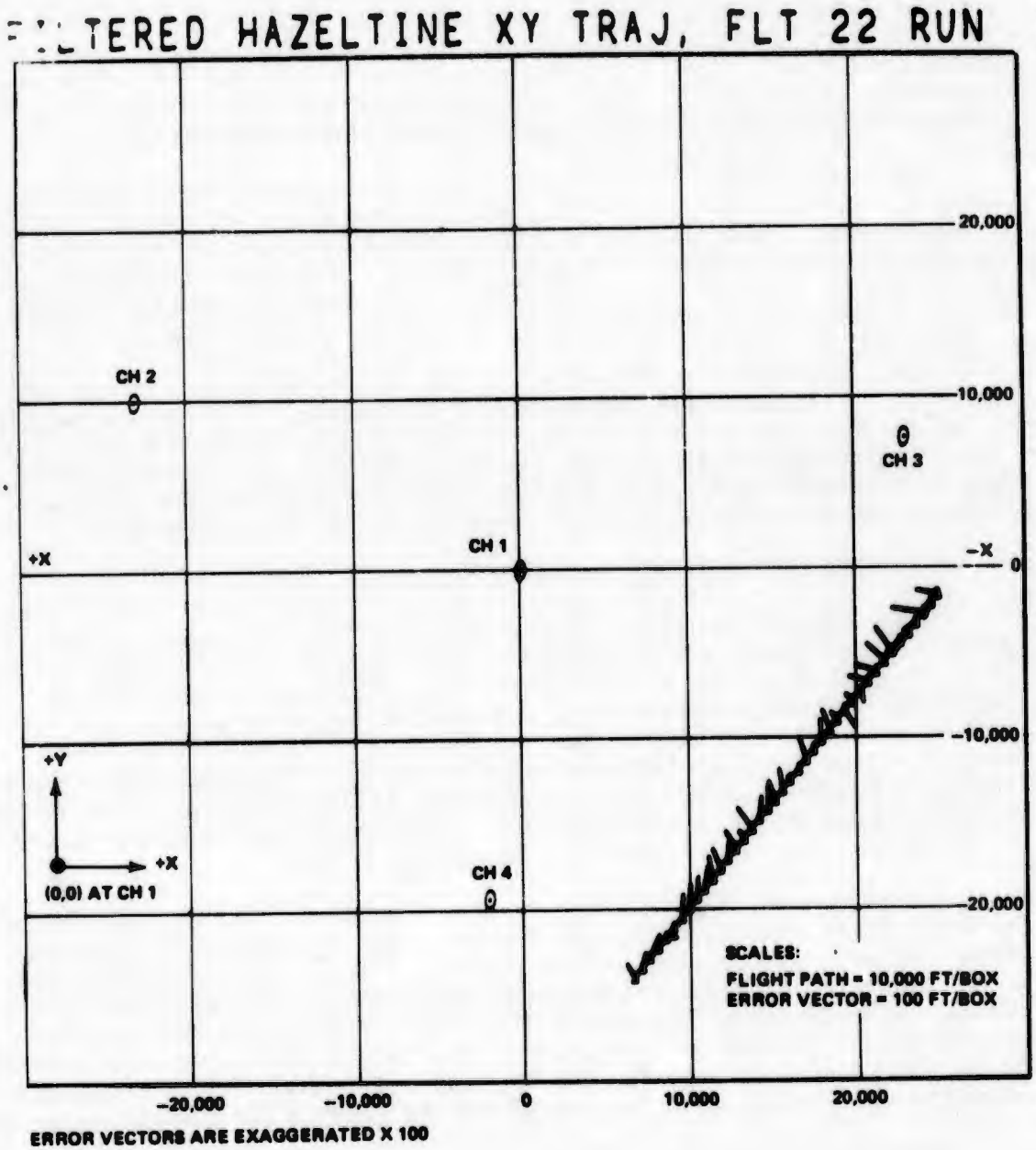

Figure 6-18 Area Navigation Summary Plot

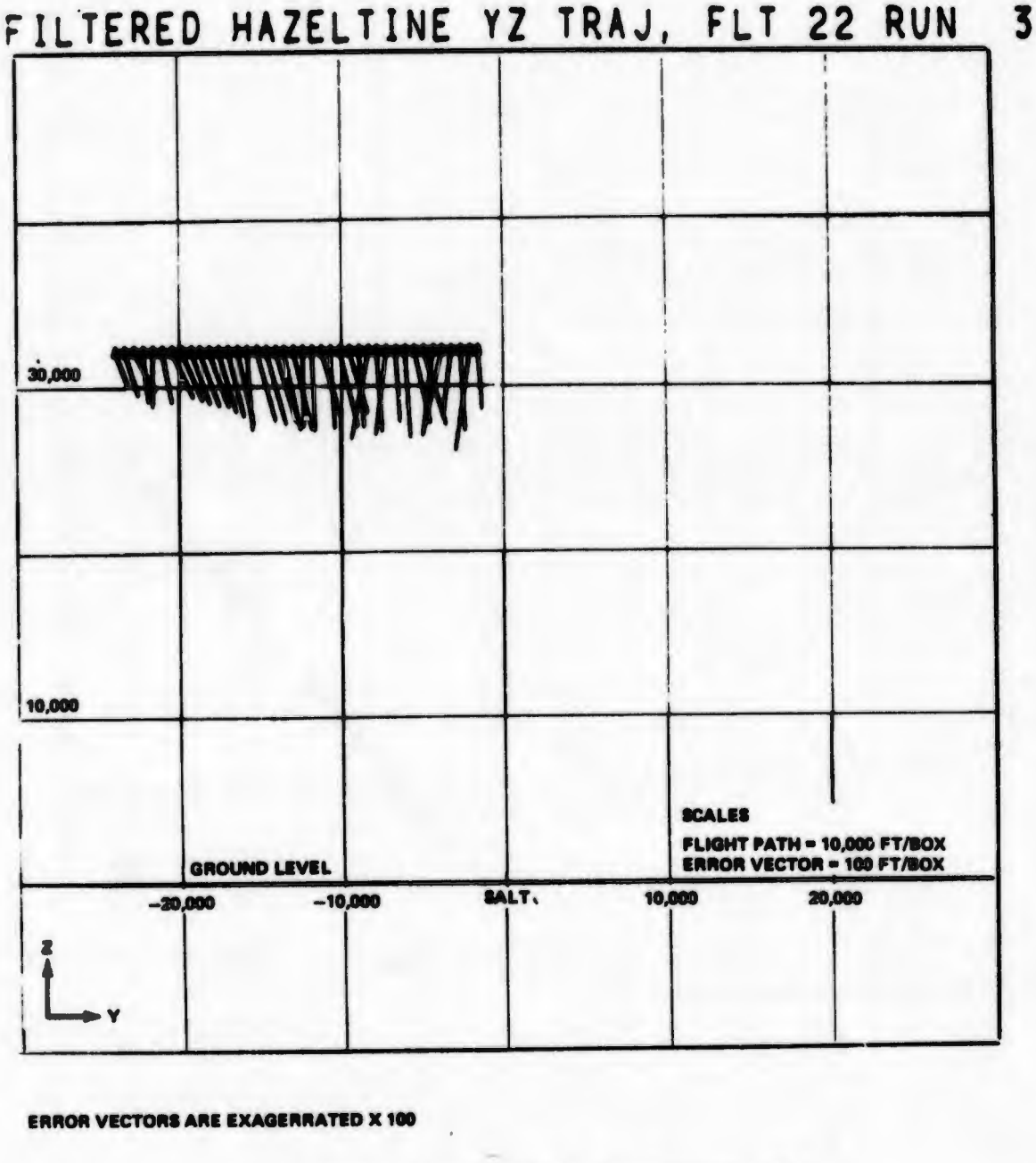

Figure 6-19 Area Navigation Summary Plot

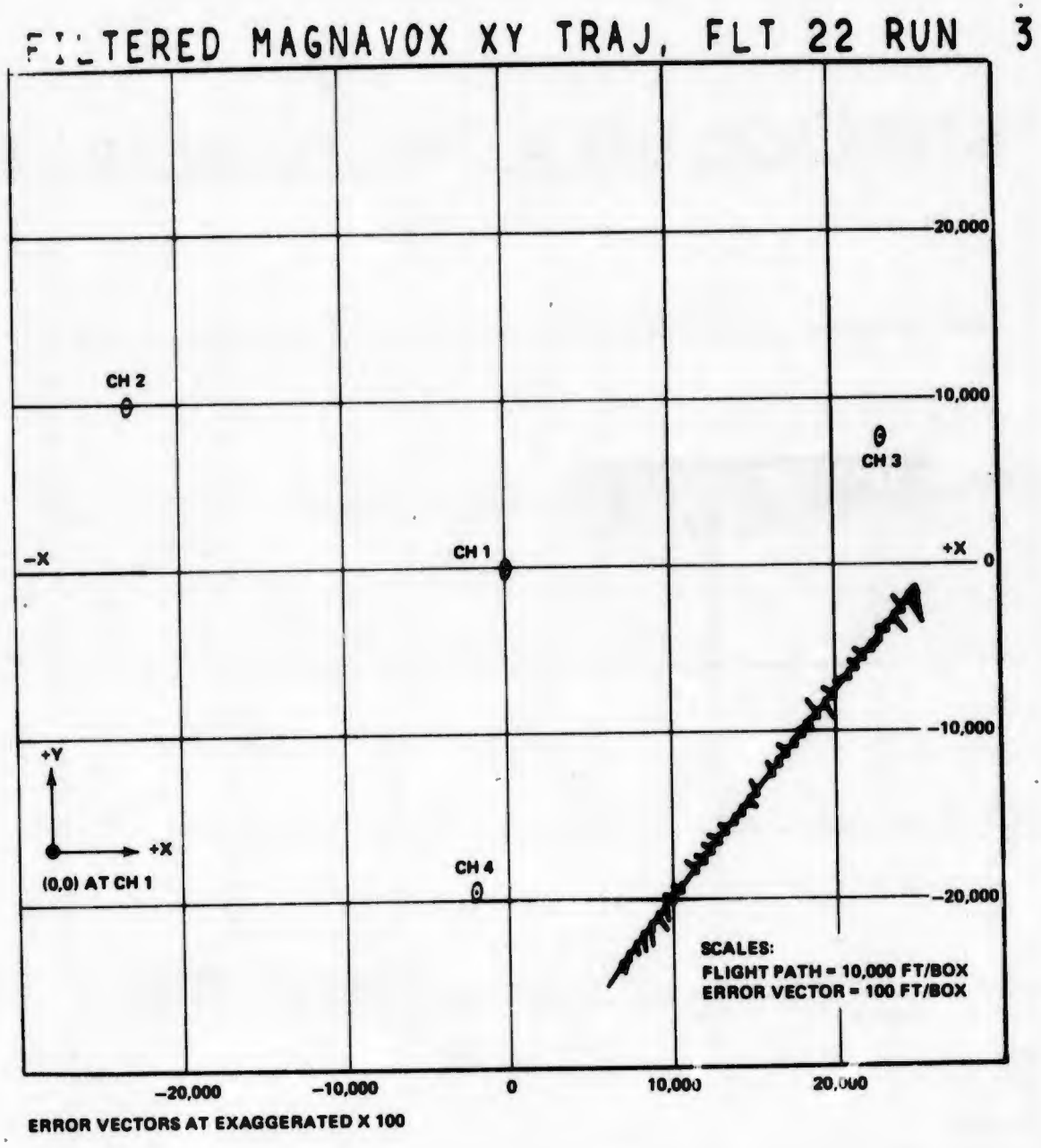

Figure 6-20 Area Navigation Summary Plot

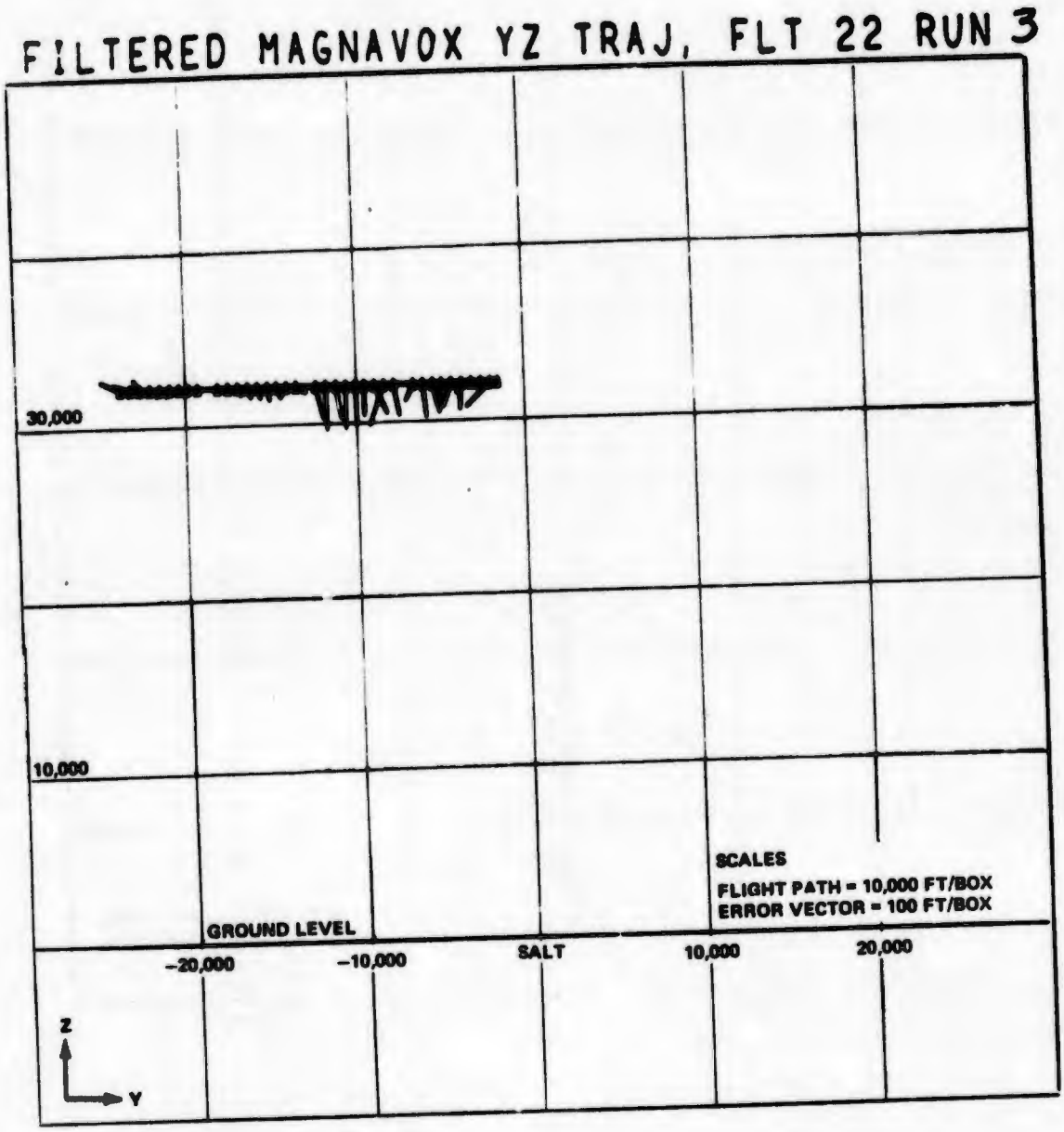

Figure 6-21 Area Navigation Summary Plot

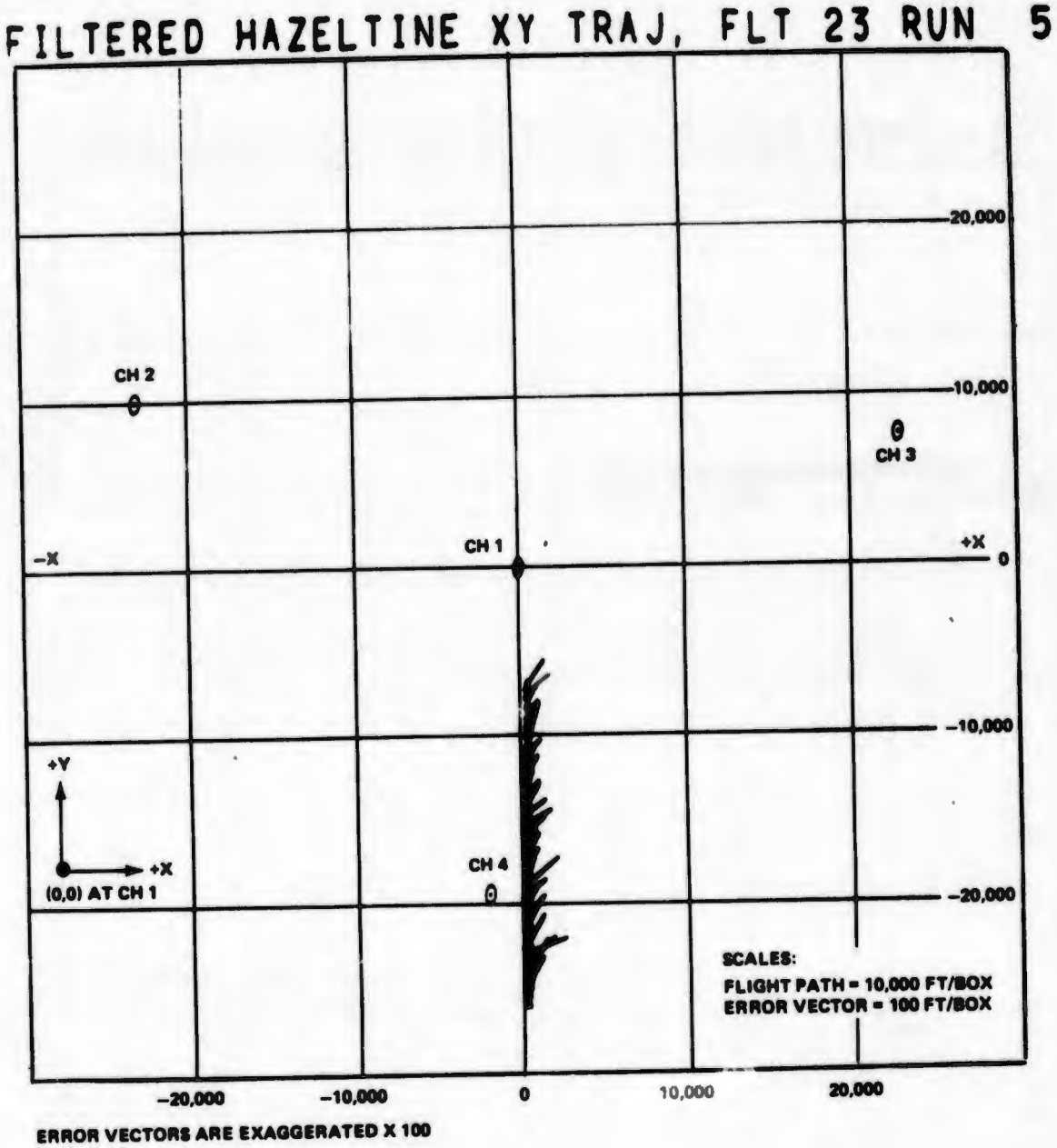

Figure 6-22 Area Navigation Summary Plot

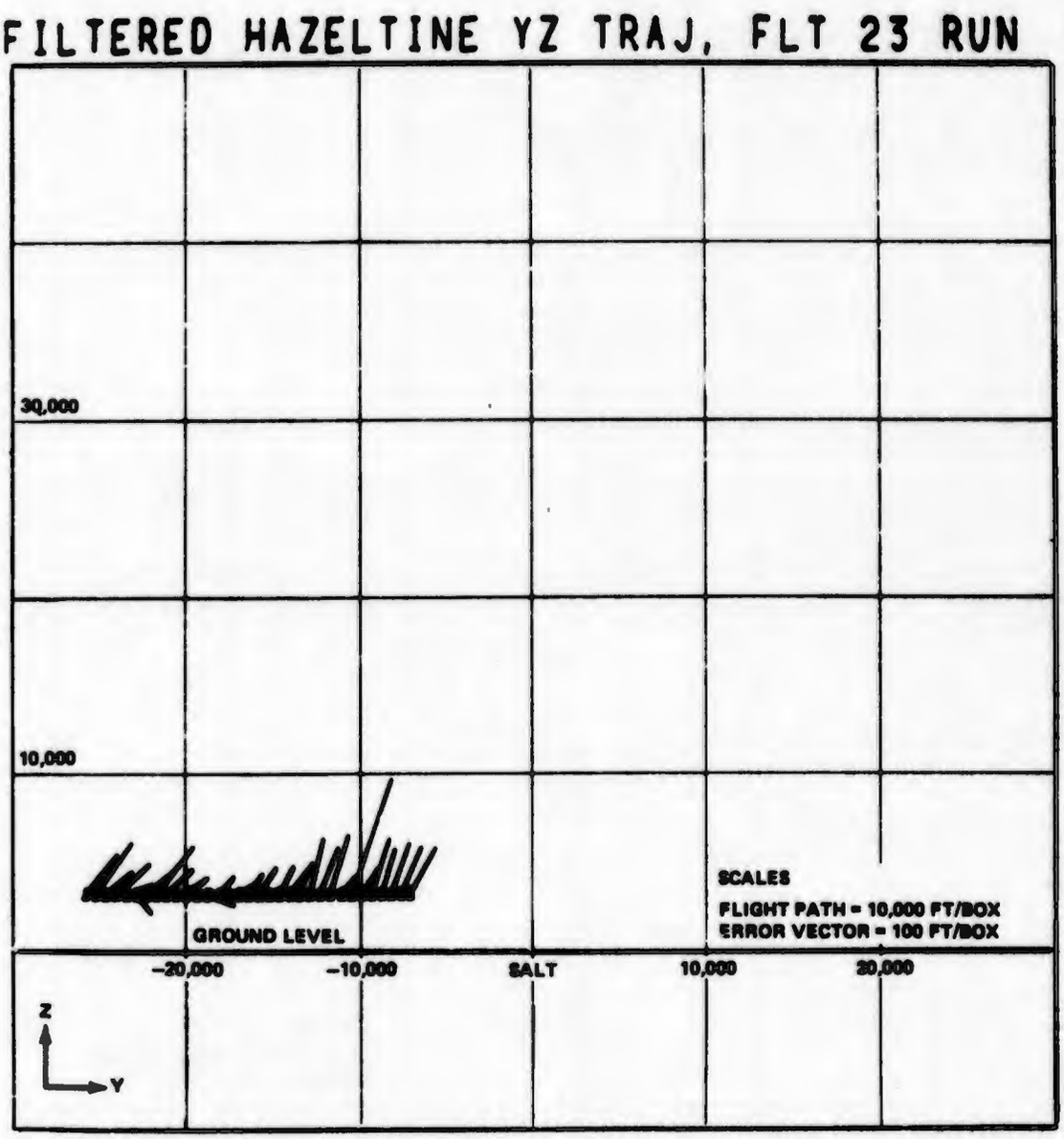

Figure 6-23 Area Navigation Summary Plot

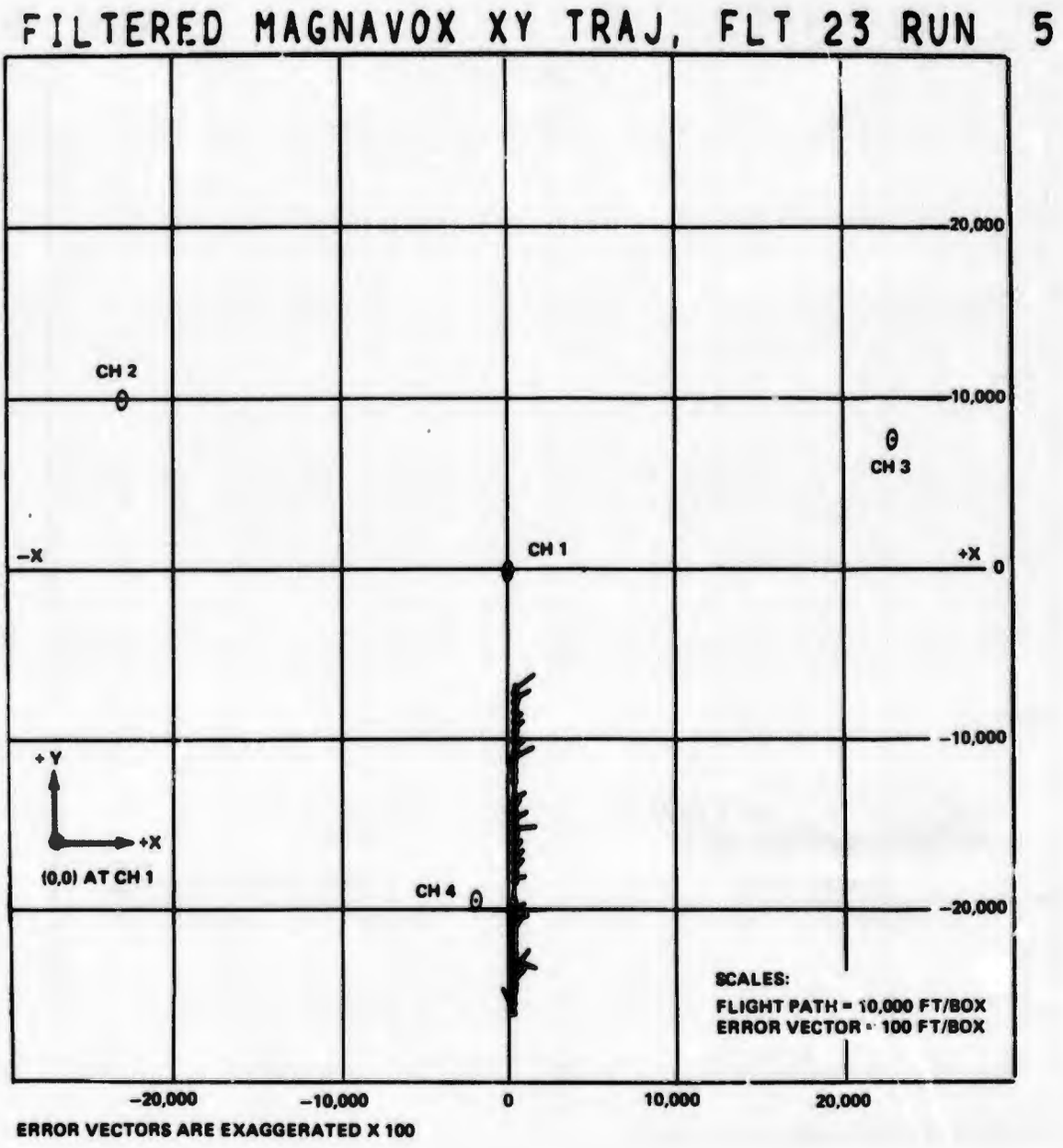

Figure 6-24 Area Navigation Summary Plot

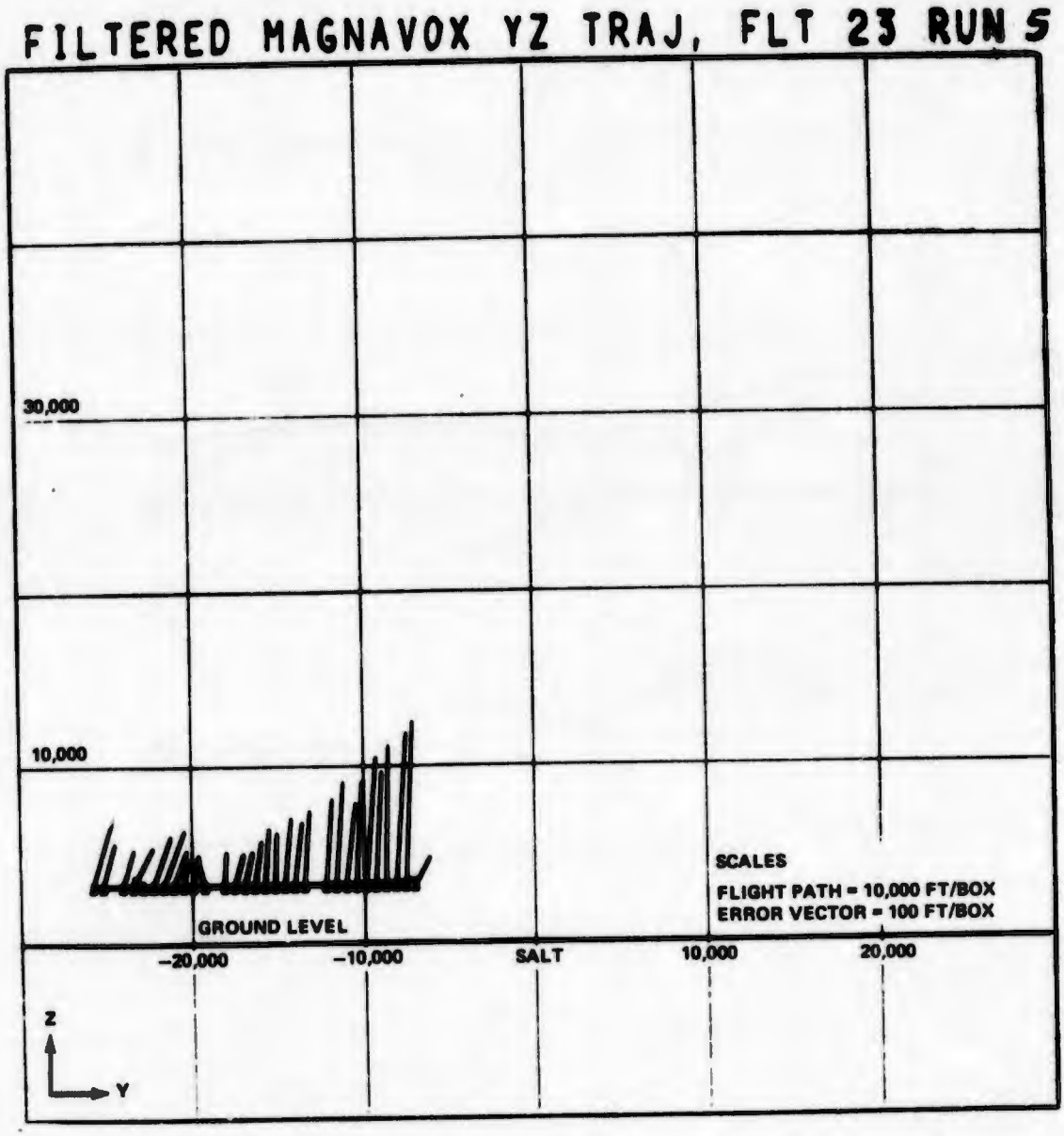

Figure 6-25 Area Navigation Summary Plot

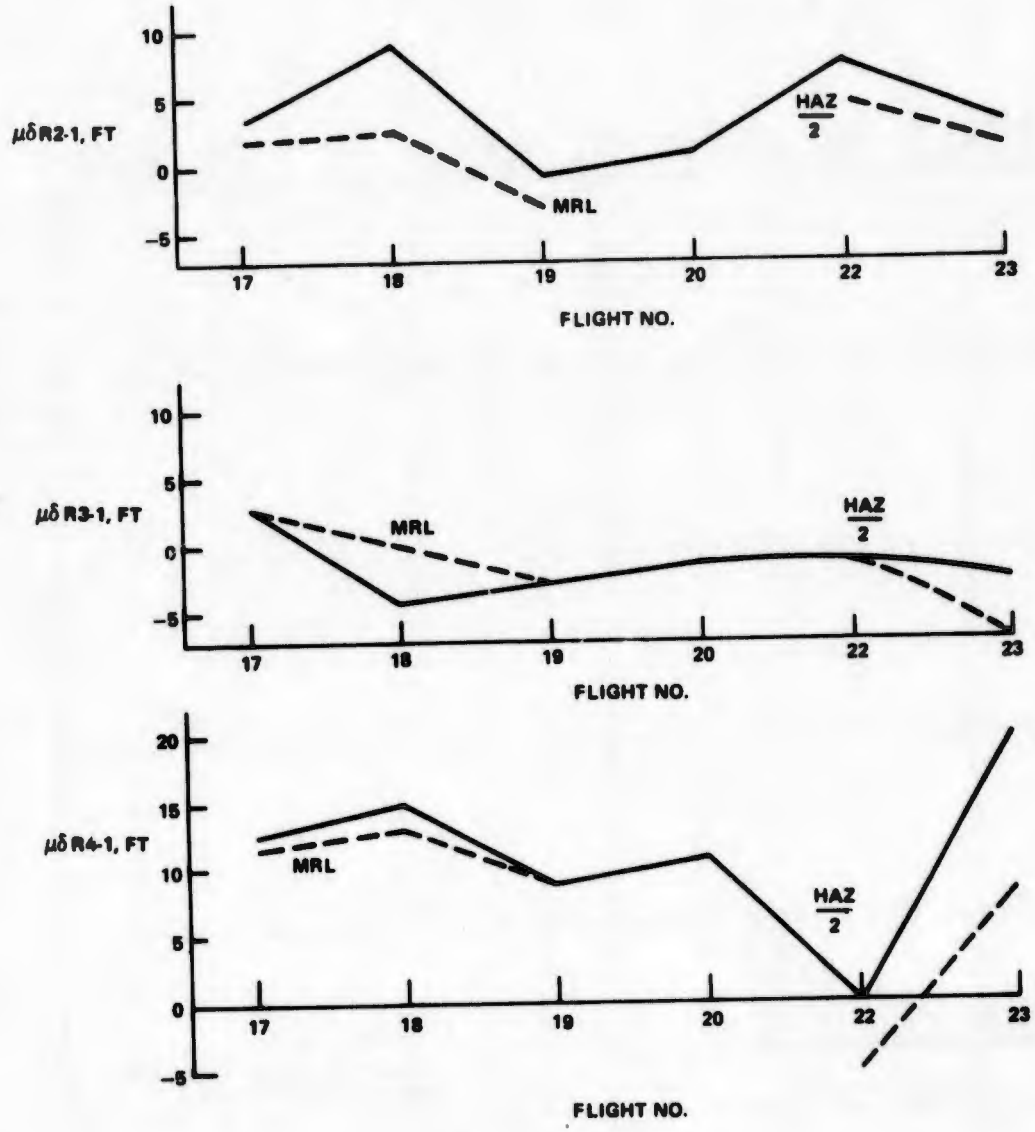

Figure 6-26 Steady State Error Trends Indicated by Interchannel Residuals for Flights 17-23

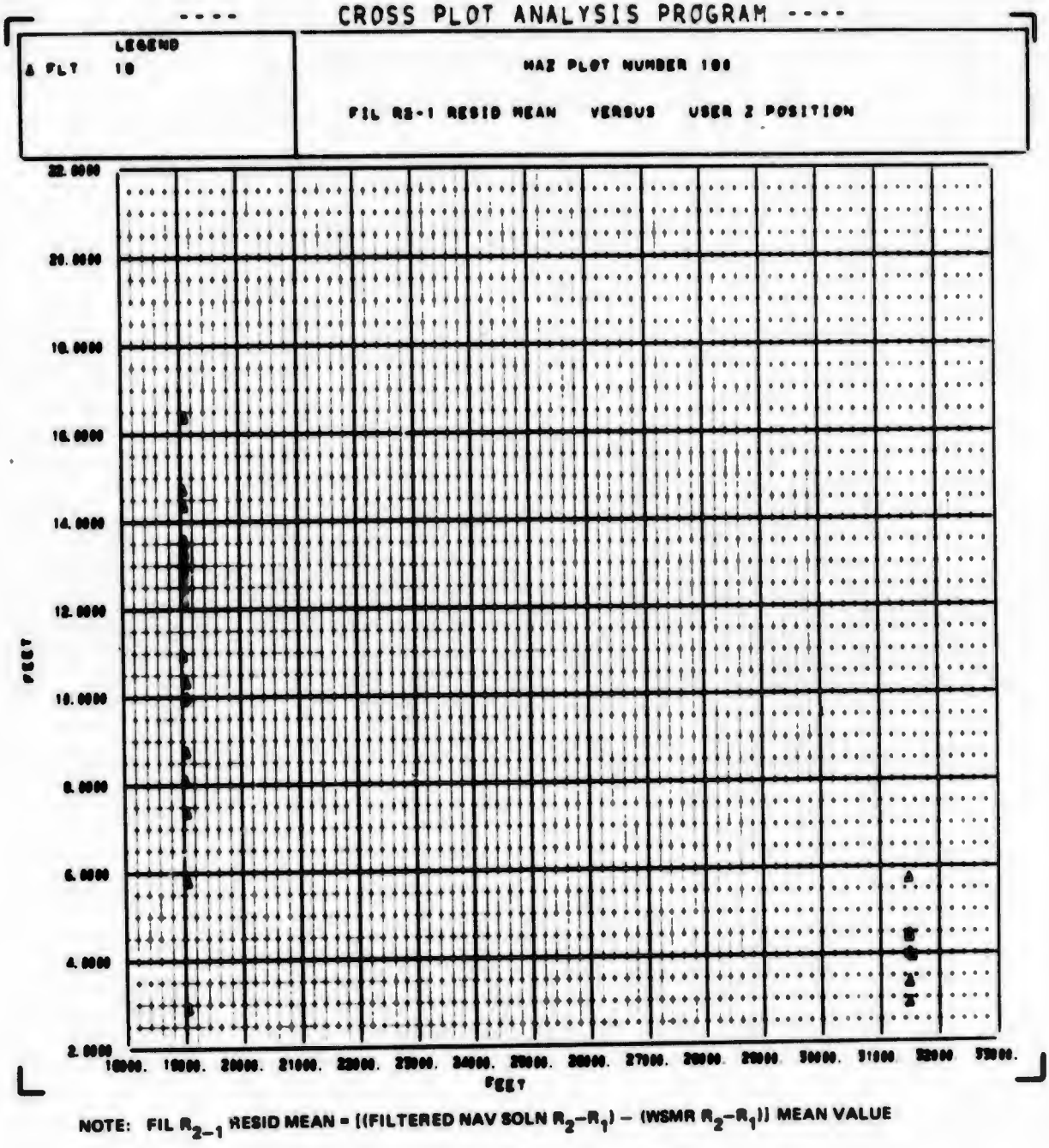

NOTE: FIL R_{2-1} RESID MEAN = [(FILTERED NAV SOLN R_2-R_1) – (WSMR R_2-R_1)] MEAN VALUE

Figure 6-27 Variation in Ranging Error Caused by Uplink Antenna Effect, Channel 2 HC

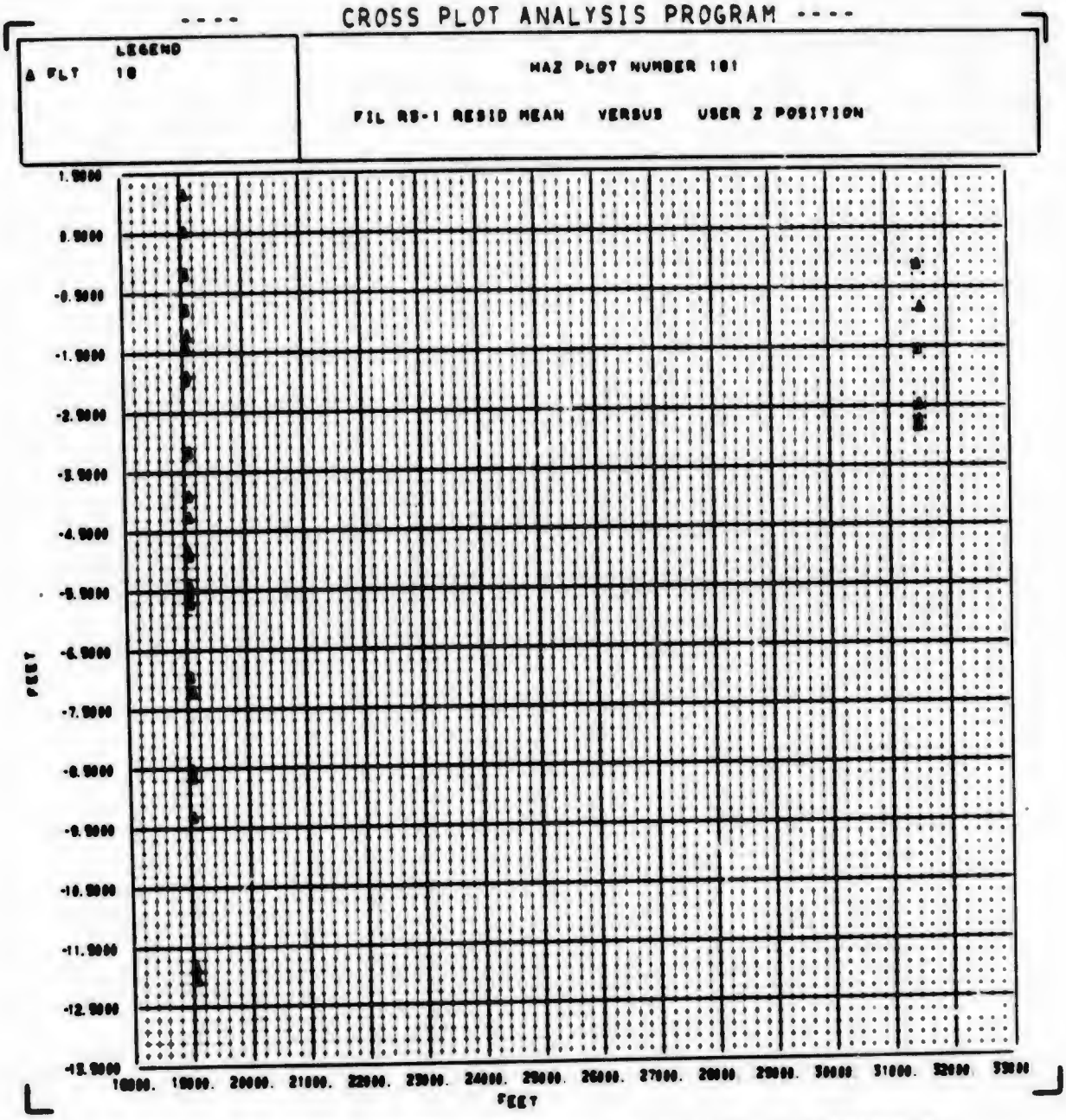

NOTE: FIL R_{3-1} RESID MEAN = [(FILTERED NAV SOLN R_3-R_1) – (WSMR BET R_3-R_1)] MEAN VALUE

Figure 6-28 Variation in Ranging Error Caused by Uplink Antenna Effect, Channel 3 HC

$$\mu \delta R_{i-1} = \frac{1}{K} \sum_{K=1}^{50} \left(R_{i-1_{raw}} - R_{i-1_{WSMR}} \right)_K \qquad i = 2,3,4$$

The data series is separated in 50 point slices to insure stationarity and average values are computed. The advantage of treating the ranging data in this fashion is that the clock bias term (B) is removed. Since there is no way to "measure" this term, we chose to remove it entirely rather than estimate it and thereby introduce another error.

The data in Figures 6-27, 6-28 and 6-29 has considerably more spread on the lower altitude flight path than at 32,000 ft. This effect is caused by the uplink antenna.

The error mechanism in the uplink antennas along with antenna range measurements is presented in detail in Section 4.2.1.3. For this discussion, it is sufficient to realize that the radiated signal has an apparent delay through the antenna which is a function of the angular direction of signal radiation. Since the aircraft passes through a larger antenna angular coverage at 22,000 ft than at 34,000 ft, the antenna effects on ranging errors are different for the two flight paths. (Figure 6-30).

The antennas at each site are not identical in this respect resulting in a different effect on each of the receiver channels. The effect on the HC receiver, Figures 6-27, 6-28, and 6-29 is essentially the same as for the MRL receiver, Figures 6-31, 6-32, and 6-33. When these effects are taken into account, the overall delay variation situation changes.

The antenna effect discussed above results in a flight path correction. The general result of the flight path correction is to reduce the amount of bias variation occurring from flight-to-flight (see Figure 6-34).

The second major error source causing bias variation is received signal level. This effect only shows up in the HC receiver, and only at levels in the range of -130 to -140dbm. For flight 17-20 these levels were reached during flight 20.

Figure 6-35 shows the data indicating significant signal level effects during flight 20. Other error data was investigated but showed no correlation with received signal level.

When these effects are factored into the overall delay variation picture, the variability from flight-to-flight decreases. Figure 6-36 indicates the composite steady-state errors (presented as an error band; previous plots only showed the mean value of the error band) with the flight path and signal level effects identified (this data only applies to the HC receiver). A considerable smoothing of the variation is obtained by accounting for these two effects. If we now look at the result of removing these errors for the moment in both HC and MRL data, the third major error, cable delay variability, can be observed. The mean value of the channel error for each of the flights for this case is shown in Figure 6-37. The data from both receivers and all channels referenced to channel 1 (2-1, 3-1, 4-1) show a slight downward trend of 2 to 5 ft. The conclusion is that there is a changing delay on the channel 1 ground

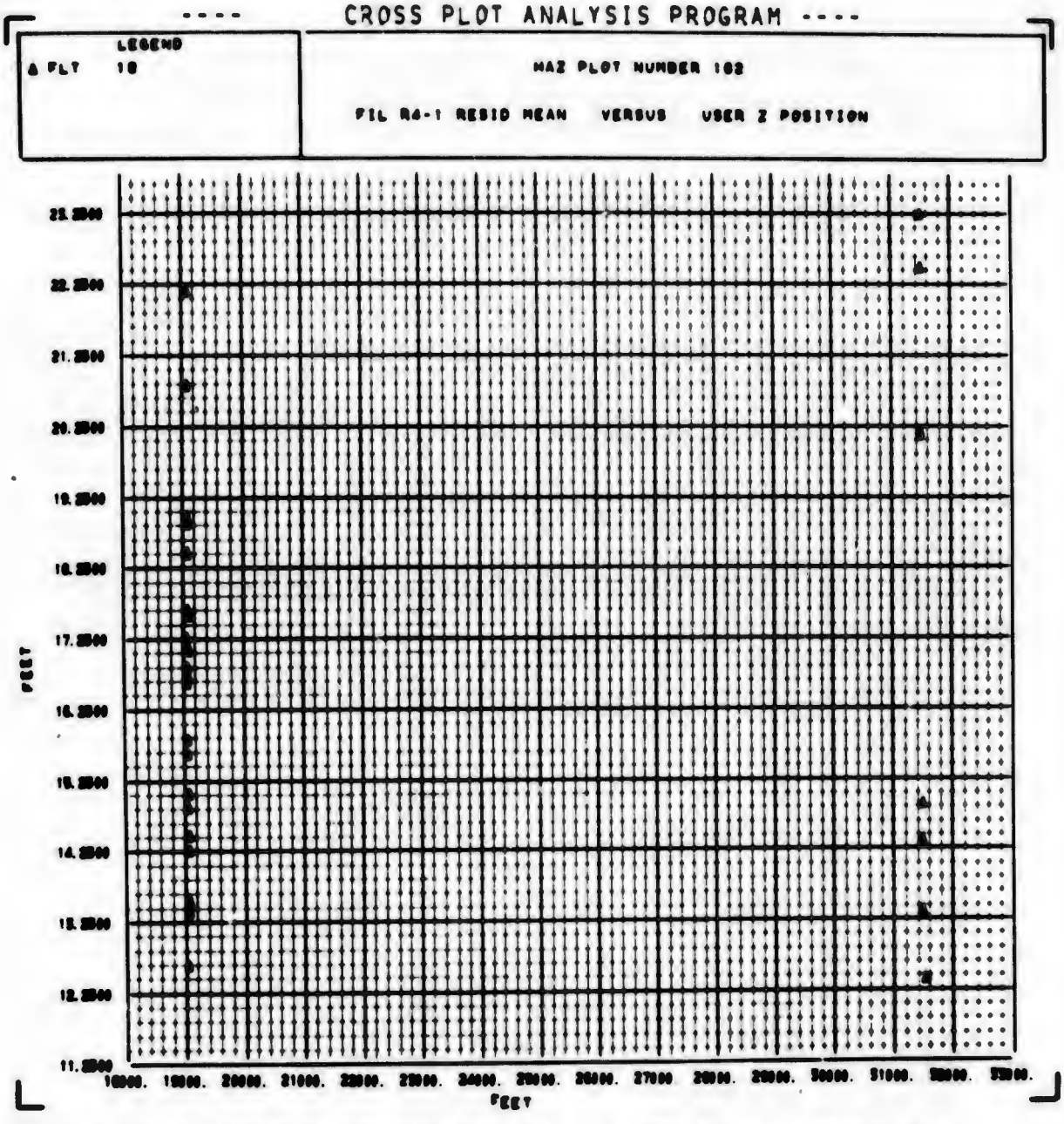

Figure 6-29 Variation in Ranging Error Caused by Uplink Antenna Effect, Channel 4 HC

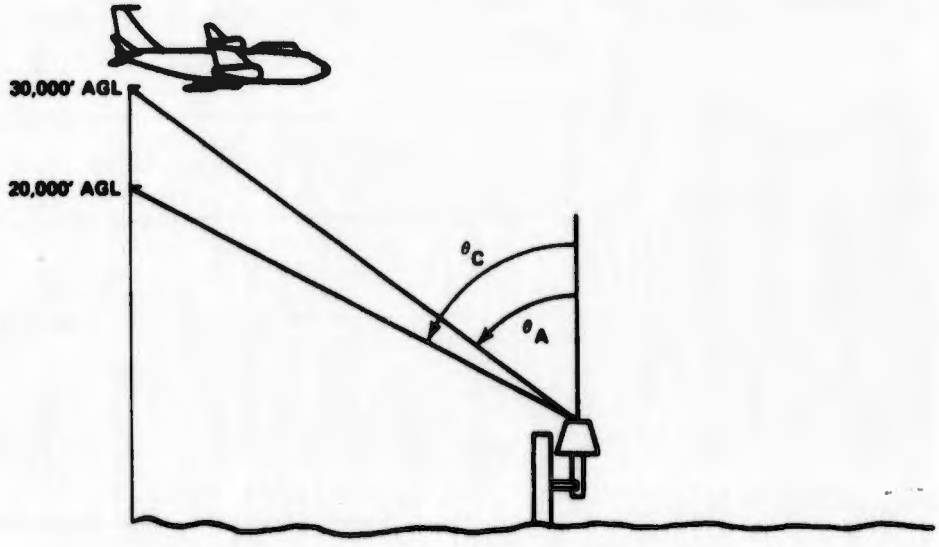

Fig. 4.1-8

Figure 6-30 Antenna Angular Coverage Differences for Area Navigation A, 30,000 Ft AGL and C, 20,000 Ft AGL Flight Paths

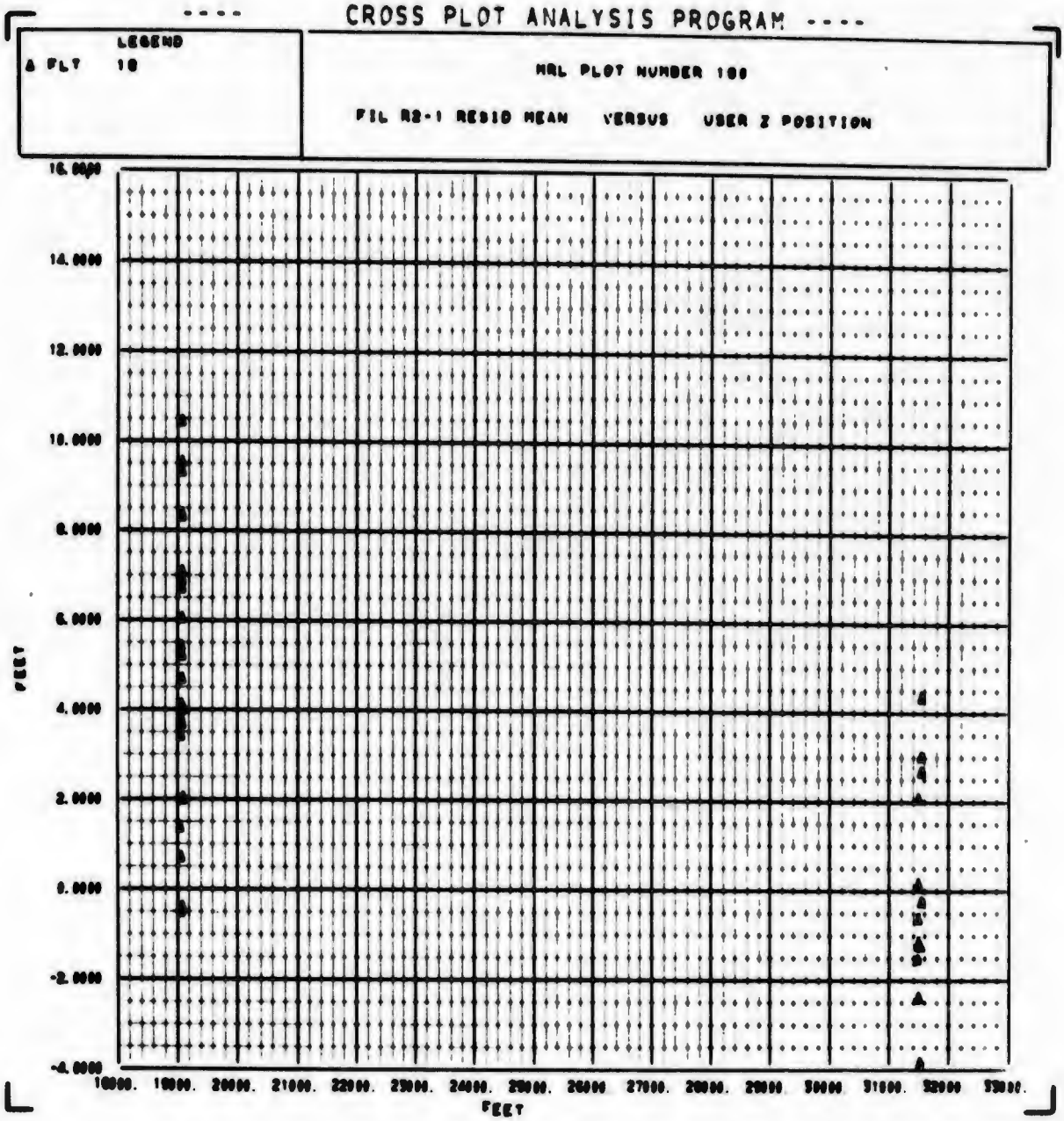

NOTE: FIL R_{2-1} RESID MEAN = [(FILTERED NAV SOLN R_2-R_1) – (WSMR BET R_2-R_1)] MEAN VALUE

Figure 6-31 Variation in Ranging Error Caused by Uplink Antenna Effect, Channel 2, MRL

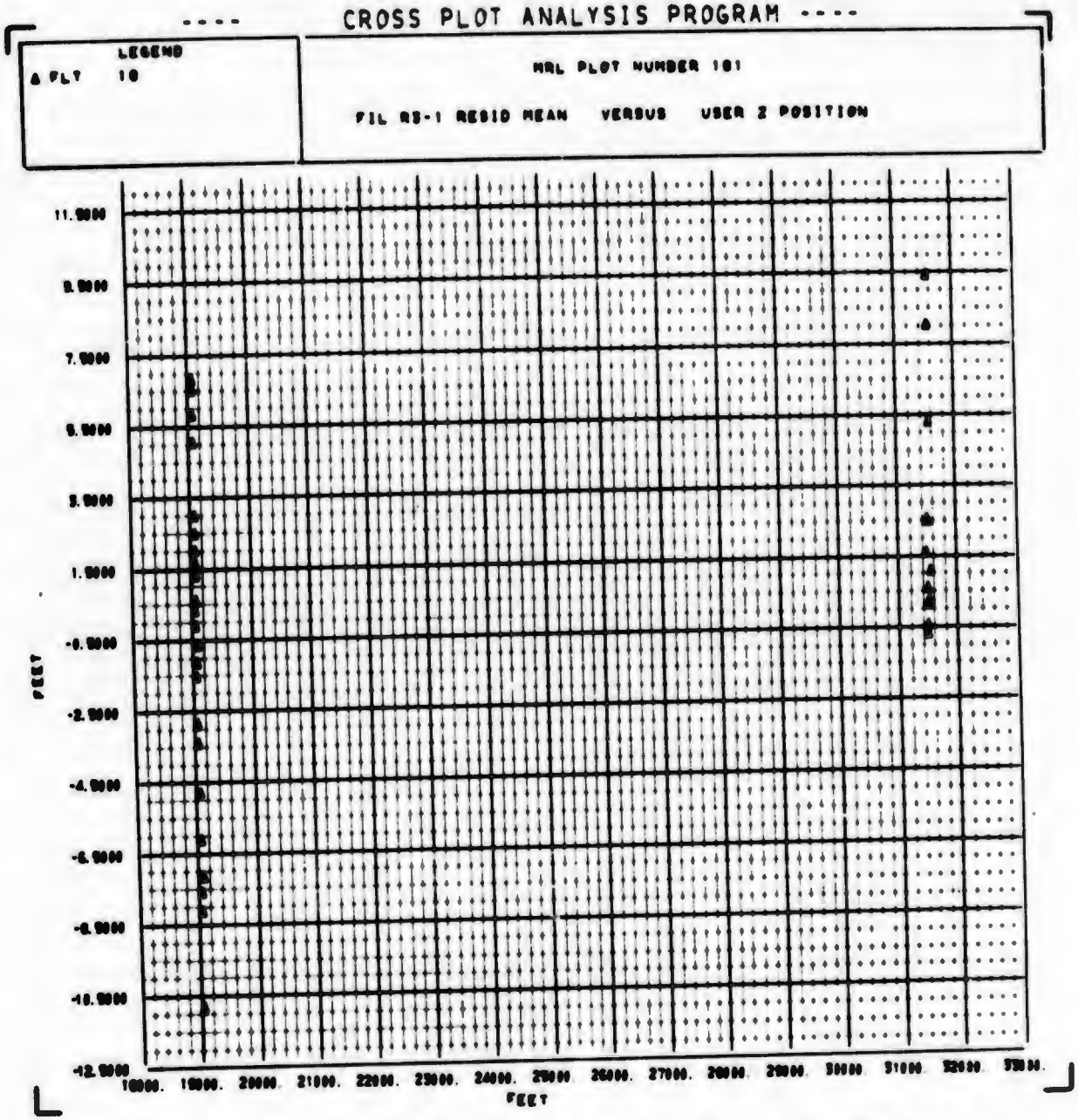

NOTE: FIL R_{3-1} RESID MEAN = [(FILTERED NAV SOLN R_3-R_1) – (WSMR BET R_3-R_1)] MEAN VALUE

Figure 6-32 Variation in Ranging Error Caused by Uplink Antenna Effect, Channel 3 MRL

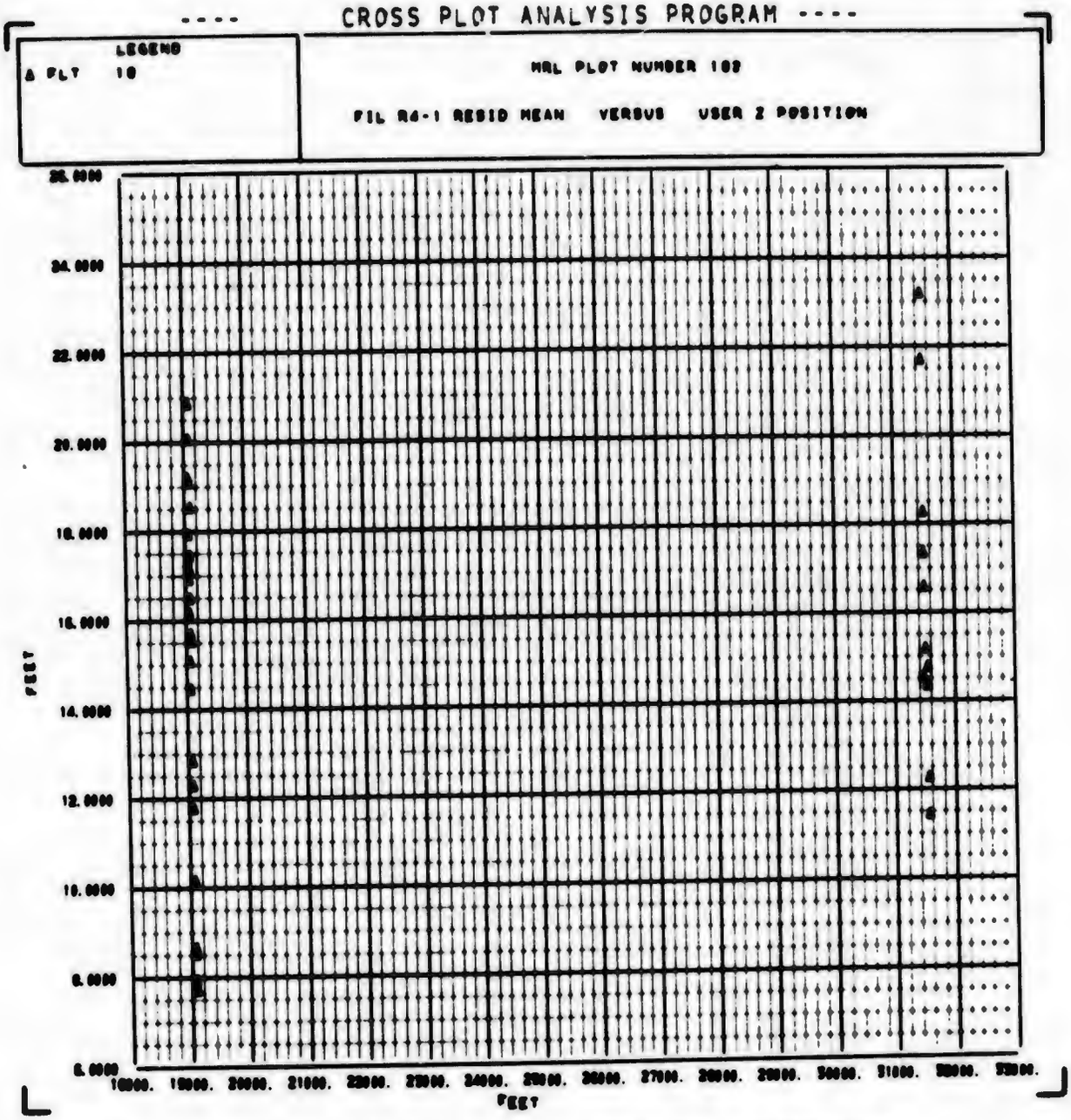

NOTE: FIL R_{4-1} MEAN = [(FILTERED NAV SOLN R_4-R_1) – (WSMR BET R_4-R_1)] MEAN VALUE

Figure 6-33 Variation in Ranging Error Caused by Uplink Antenna Effect, Channel 4 MRL

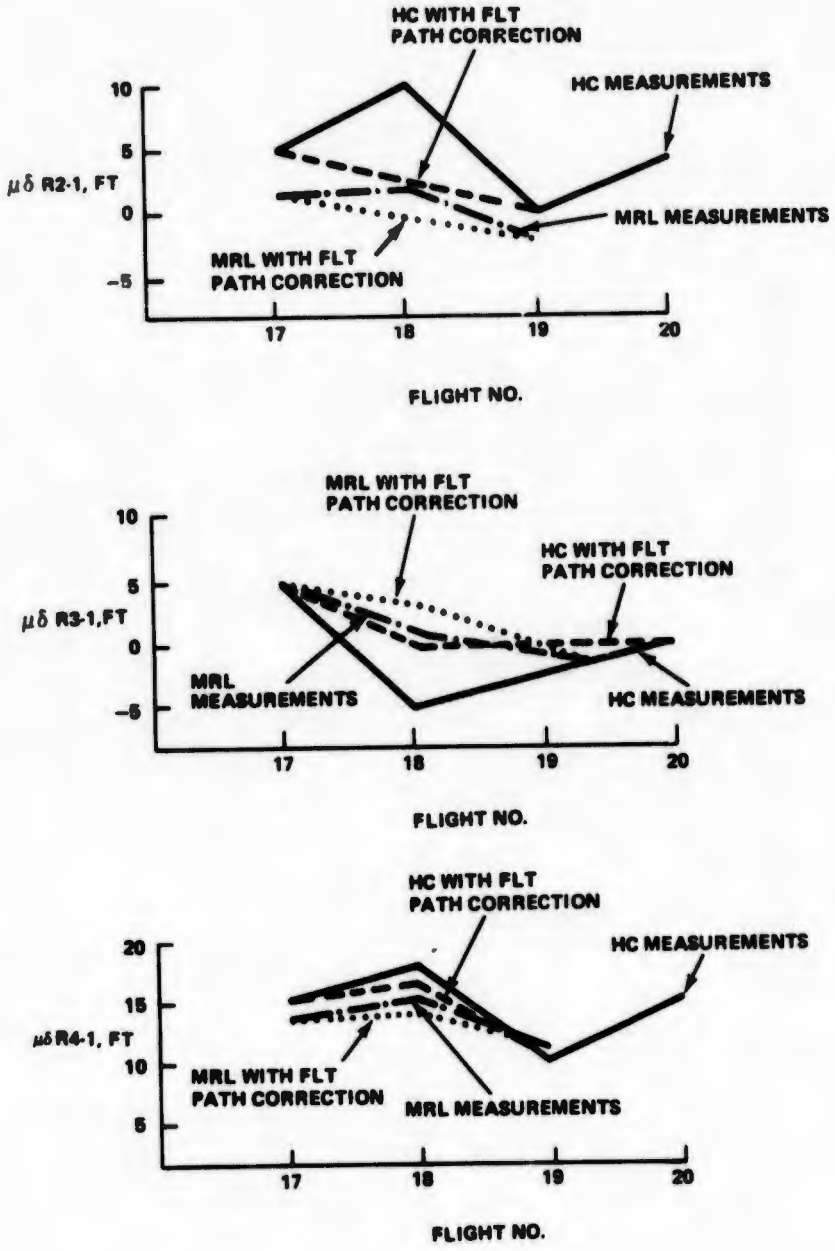

Figure 6-34 Reduced Bias Variation as a Result of Antenna Effect Correction, on Flights 17, 18, 19, 20

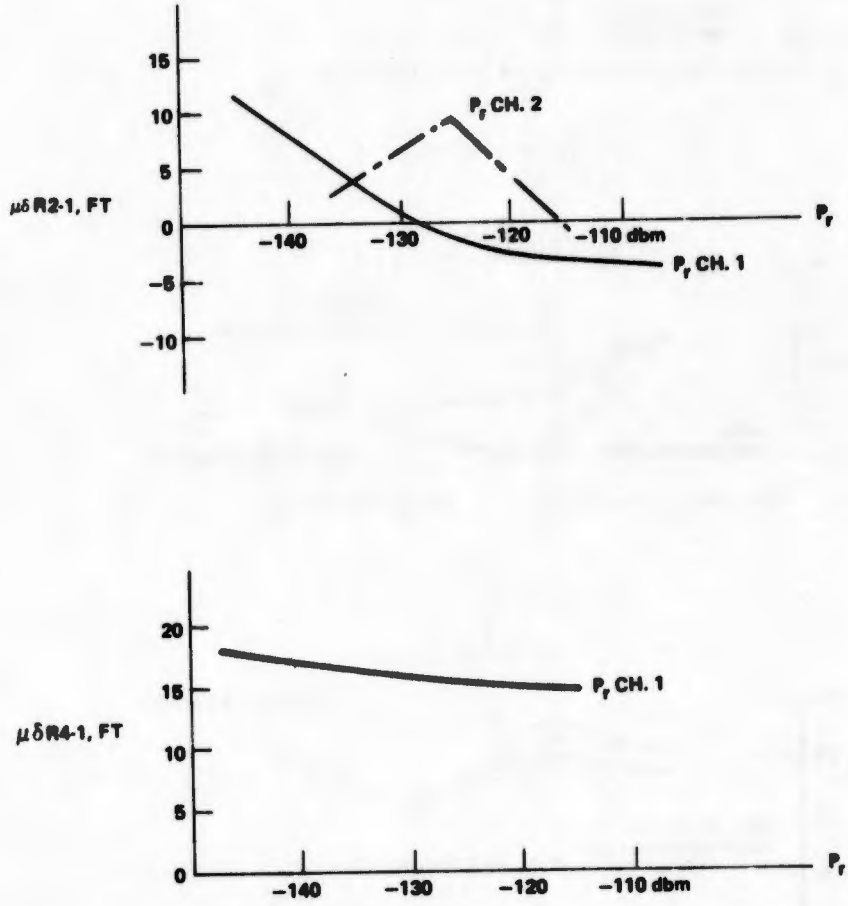

Figure 6-35 Signal Level Effects During Flight 20 on HC Receiver

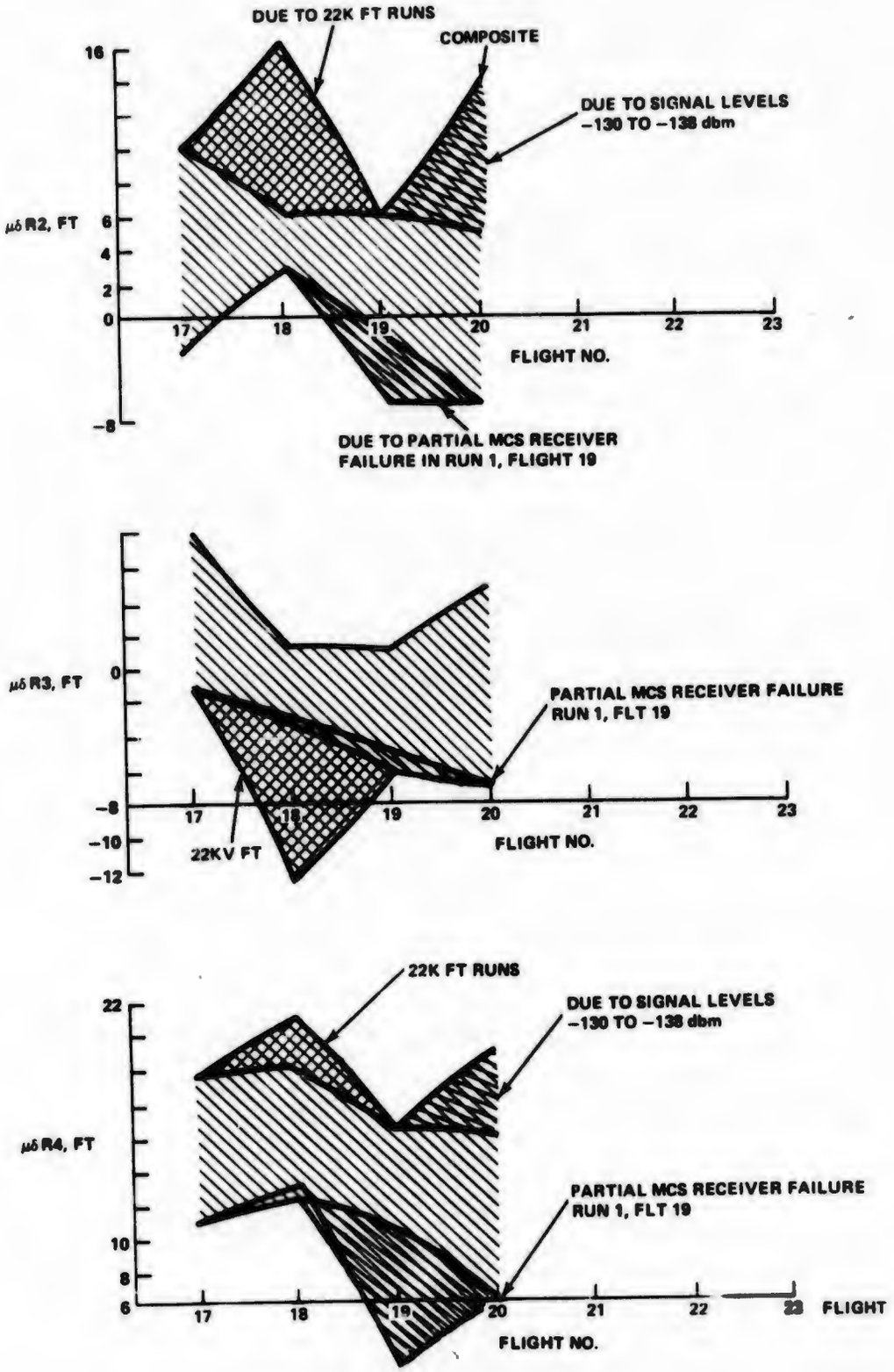

Figure 6-36 HAZ Channel Bias vs Flight

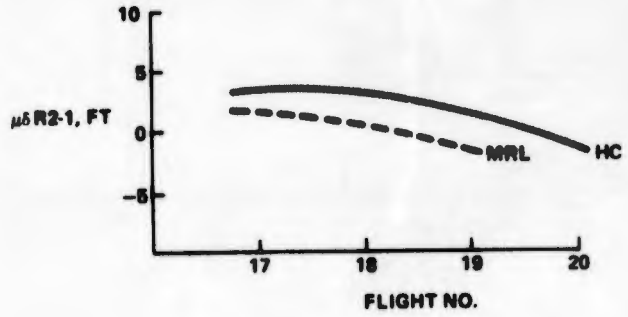

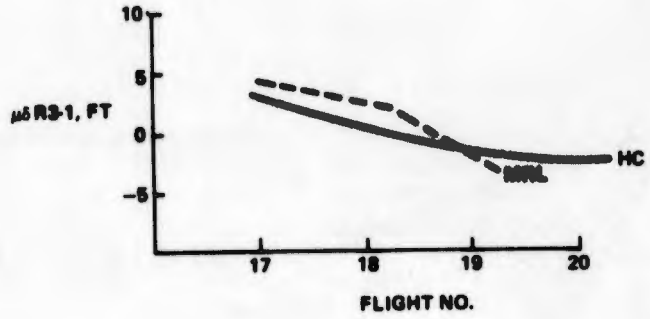

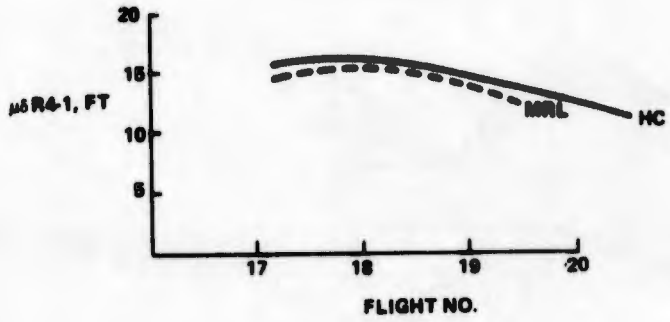

Figure 6-37 Bias Variation With Data Corrected for Flight Path, Power Level Effects, and Partial MCS Receiver Failure in Flight 19

link. Most probably, this is being caused by the Spiroline cable at the MCS site in the channel 1 link. This cable has a history of delay variation (see Section 4.2.1.2). The delay changes are often approximately the same as we see here in the flight data.

After removing this effect from the data, the remaining average delay variation is small (less than 2 ft). The cause of this variation is unclear but probably is affected by the 50 point sampling technique used for this analysis and the accuracy of the WSMR data used to derive the error residuals.

Two other pertinent observations can be made about the data behavior. There is a shift in the bias error between a northerly run and a southerly run on the same flight path, and there are multipath signals affecting the data in certain regions of the flight path.

On flight 20 we found there was a bias variation as a function of the direction of travel along the A path. Since only A paths are used in this flight, the variation due to the uplink antenna flight path error is not present and thus did not obscure the direction of travel effect. The largest effect shows up on Channel 2-1 bias errors where the mean error changes approximately 5 ft for opposite directions of travel along the A path. The variation on Channel 3-1 and 4-1 is on the order of 2 ft. Figures 6-38, 6-39 and 6-40 show the effect on flight 20. The cause of this effect is unclear at this time, but is most probably related to either an airframe multipath problem, or a WSMR reference data problem.

Multipath effects can be seen in the data primarily on channels 1 and 4. The multipath signals are using the ground as a reflecting surface and affecting the aircraft data at either low elevation angles when far away from the transmitting site, or at very high elevation angles encountered while passing over a transmitter. The unfiltered navigation solution is used in the analysis of multipath since filtering can mask certain of these effects. Figure 6-41 is an example of the overall technique. The interchannel residual between the navigation solution and the WSMR BET is formed as previously discussed without, however, averaging the data. Instead a spectrum analysis is conducted to determine if there are any significant frequency components. The spectral lines are calculated for each sample, hence, the units are cycles/sample. To convert to standard notation, b cycles/sample x 5 samples/second = 5b cycles/second. The significant spectral lines are determined from an amplitude test and are considered significant when the power spectral density is above 0.5.

Spectral lines exceeding the above criteria are then plotted versus User Y position as shown in the upper left hand corner of Figure 6-41.

Figures 6-42 through 6-44 depict the significant frequencies for the HC data from flight 20 as a function of user Y position. These plots show two regions of significant frequencies; a "lower" frequency region with nearly random distribution of spectral lines and an "upper region" of frequencies showing discernible trends.

In particular, Figure 6-44 giving the spectral lines of R4-1 data shows a gradual rolloff of frequencies from 1.25 Hz at 15,000 ft north of Salt to approximately 0.90 Hz at 25,000 ft north of Salt. A comparison with a simulated differential doppler (fade frequency) between station SC-50 and the aircraft (User) position shown on Figure 6-44 clearly identified the "upper region significant" frequencies as specular ground-

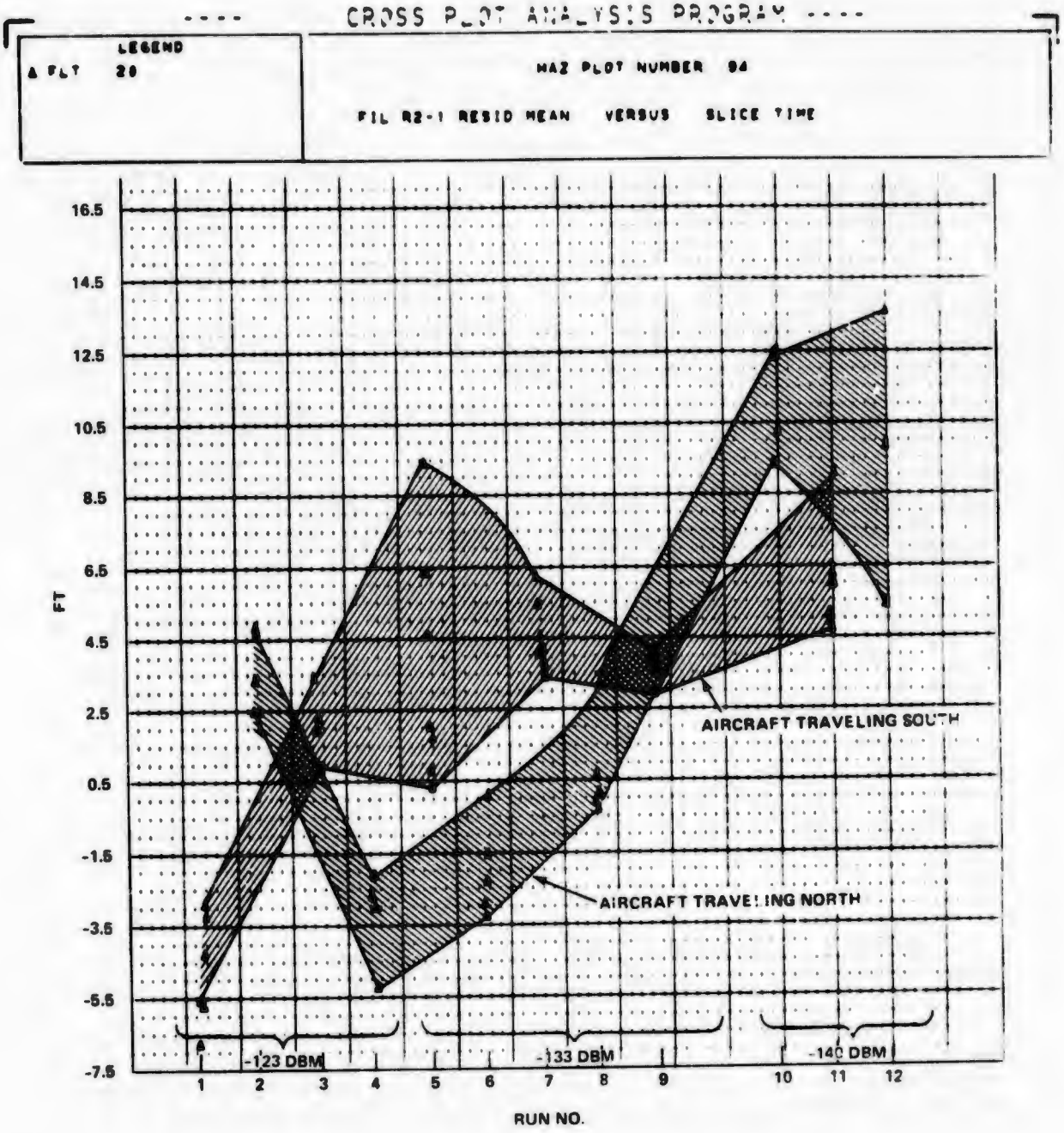

Figure 6-38 HC (R_{2-1}) Bias Variation as a Function of Direction of Travel Along Flight Path "A"

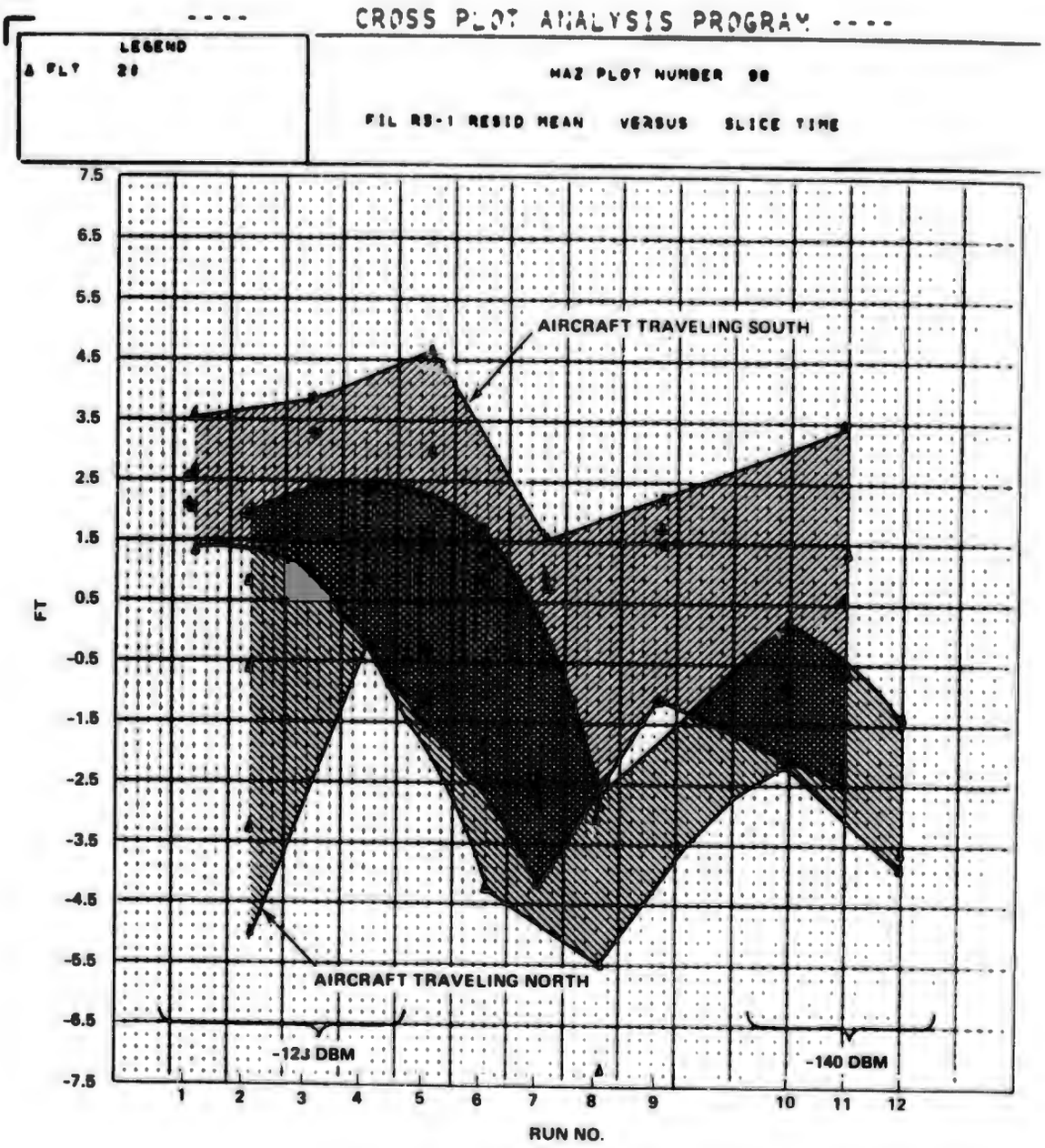

Figure 6-39 HC (R_{3-1}) Bias Variation as a Function of Travel Along Flight Path "A"

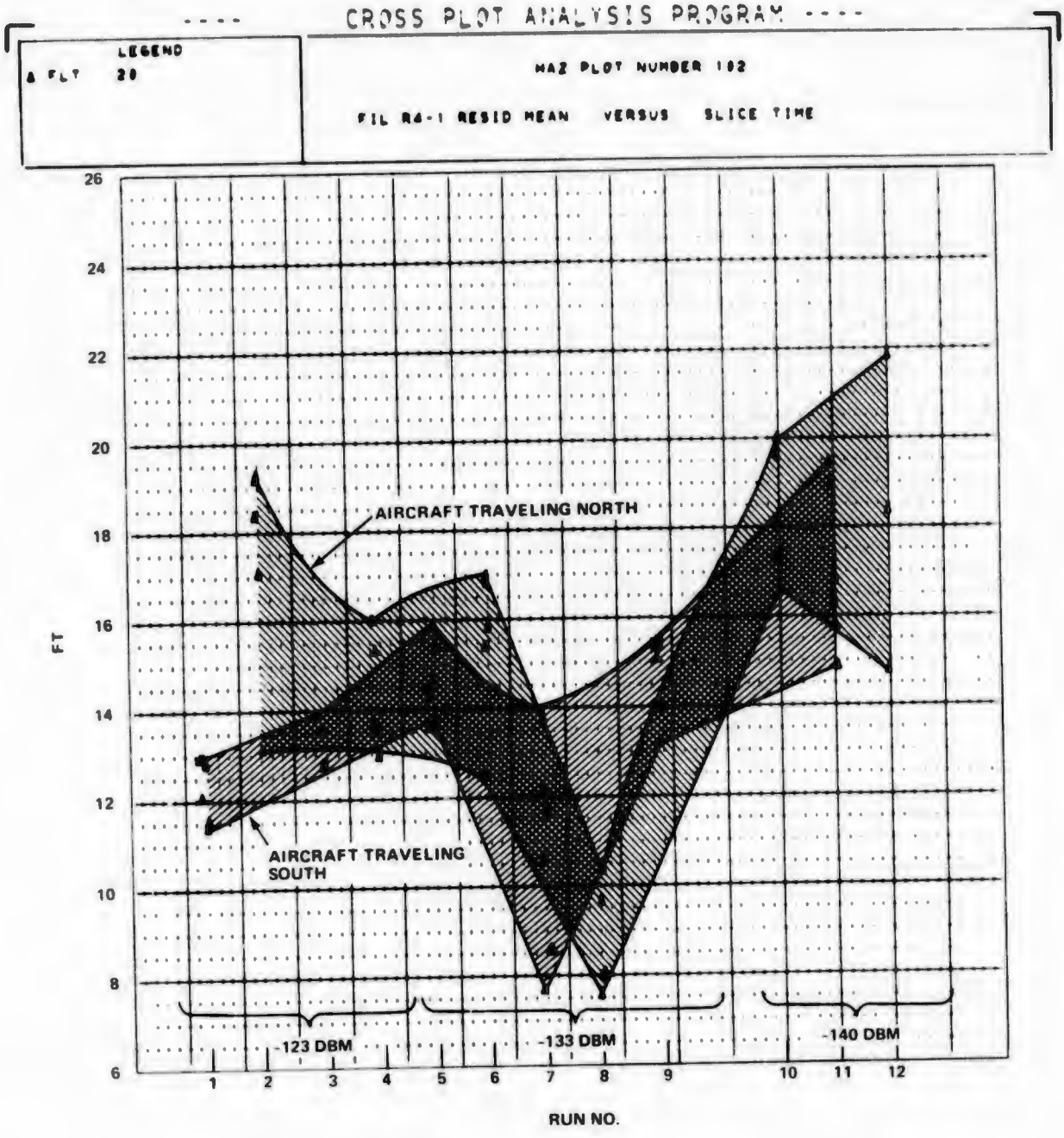

Figure 6-40 HC (R_{4-1}) Bias Variation as a Function of Travel Along Flight Path "A"

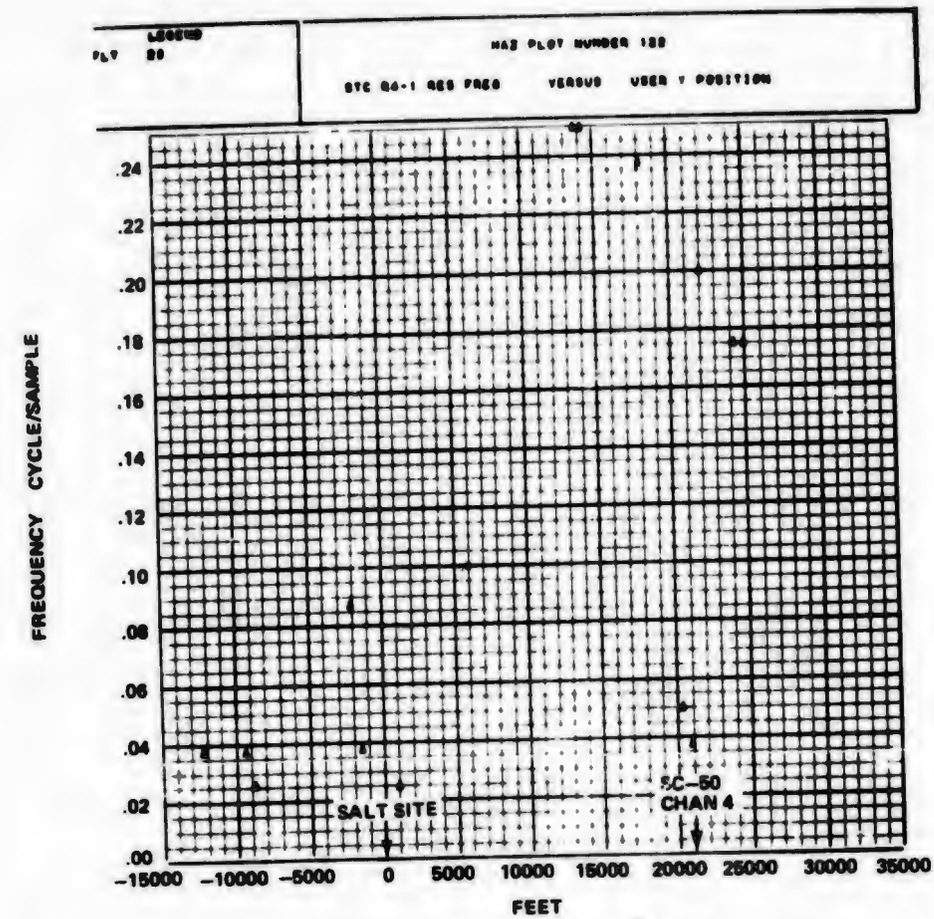

SIGNIFICANT SPECTRAL LINES (AMPLITUDE RATIO TEST) ARE PUT ONTO COMPOSITE PLOT AS SHOWN AT LEFT – COMPOSITE PLOT SHOWS SIGNIFICANT SPECTRAL LINES VS USER Y POSITION

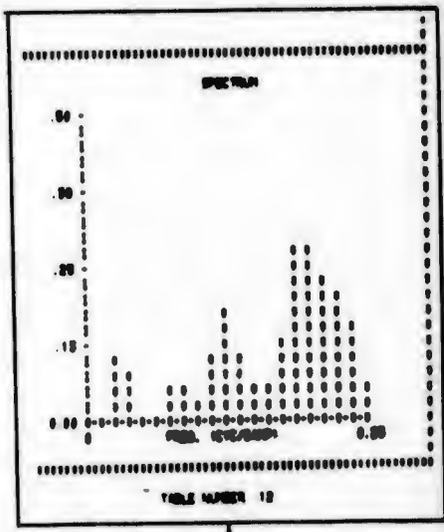

Y = 18,200'

Z = 30,000 AGL

"A" FLIGHT PLAN

Y = 11,500

Y = 17,500'

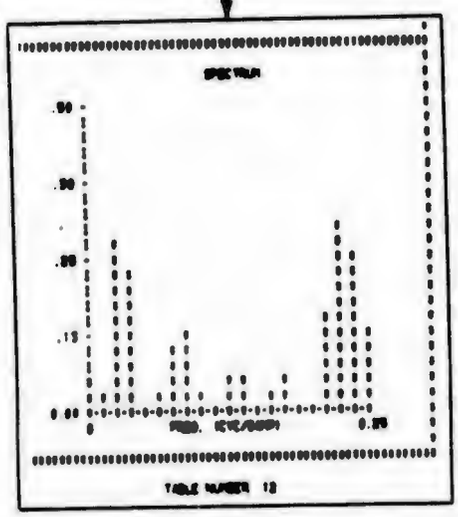

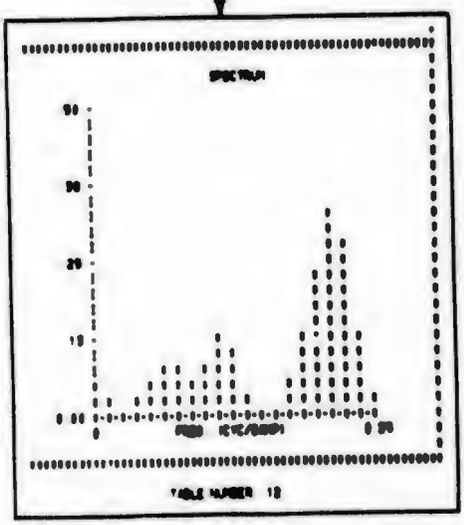

SALT SITE

SPECTRUM PLOTS SHOW AMPLITUDE SPECTRAL LINES OF CH. 4-1 RESIDUAL FROM THE UNFILTERED SYSTEM SOLUTION AND WSMR BET

NIFICANT SPECTRAL
IES (AMPLITUDE RATIO
ST) ARE PUT ONTO COMPOSITE
OT AS SHOWN AT LEFT –
MPOSITE PLOT SHOWS SIGNIFICANT
ECTRAL LINES VS USER
OSITION

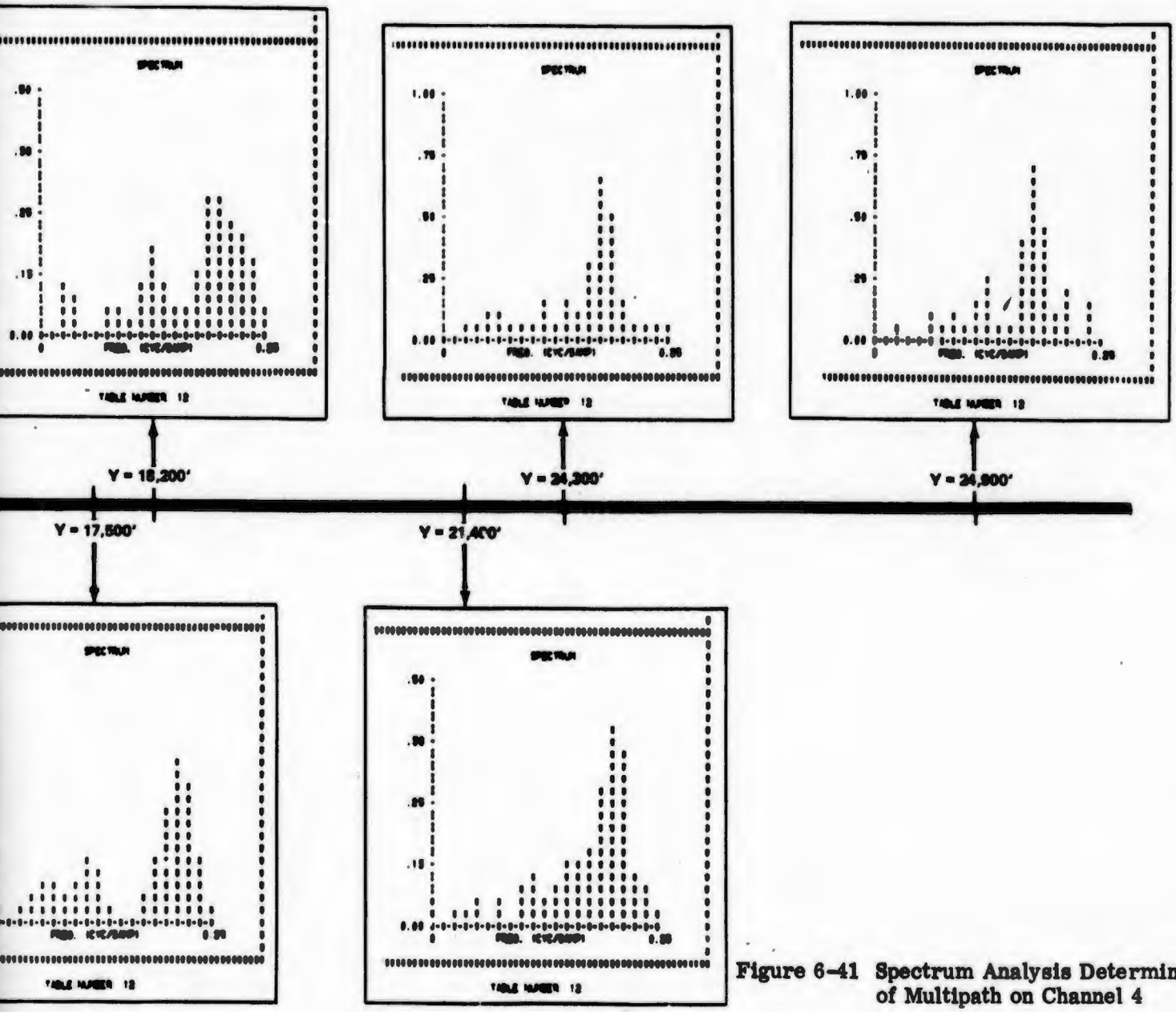

Figure 6-41 Spectrum Analysis Determination of Multipath on Channel 4

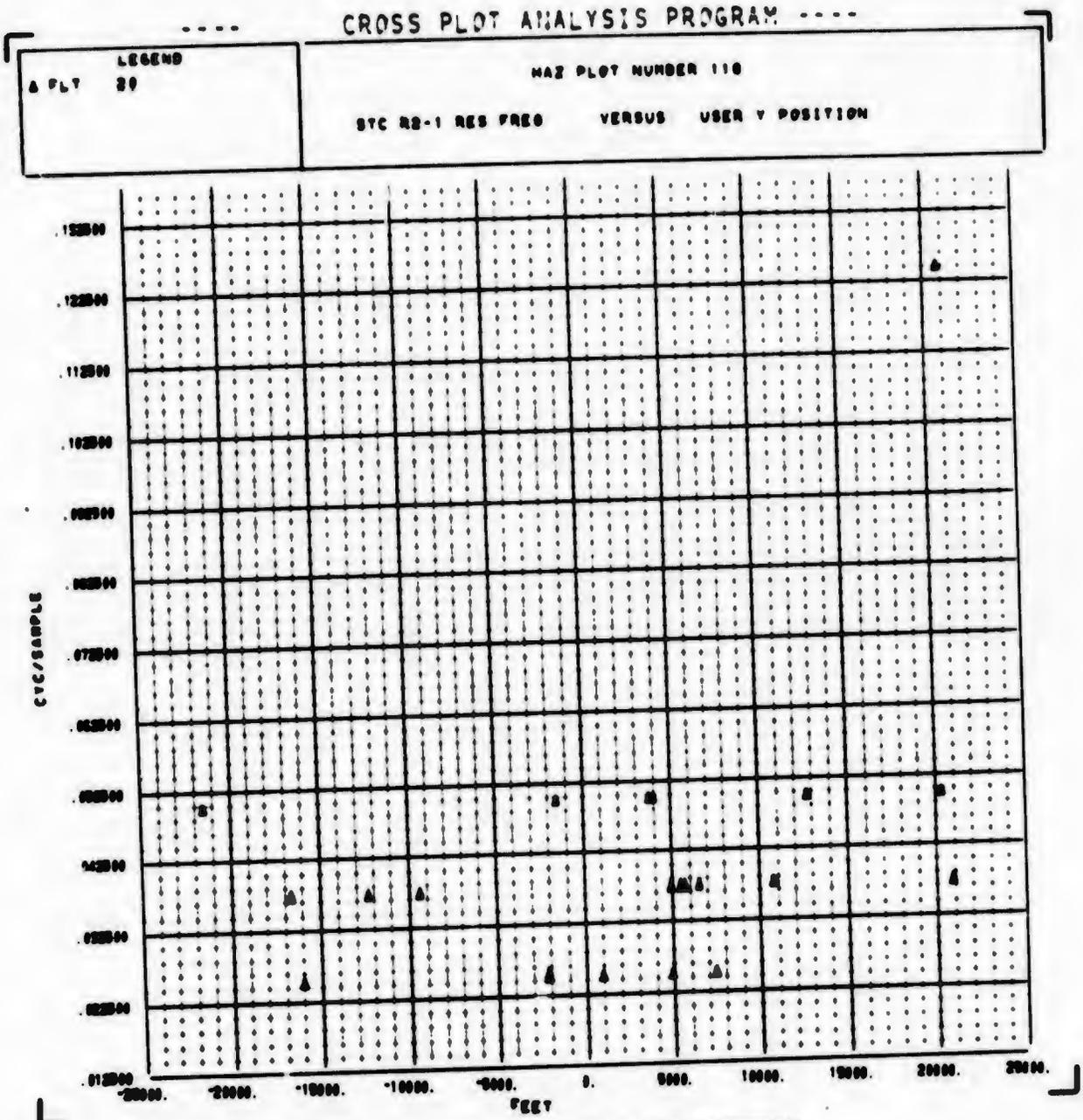

NOTE: STC R_{2-1} RES FREQ INDICATES THAT THE ORDINATE IS THE PROMINENT SPECTRAL LINES RESULTING FROM A FREQUENCY ANALYSIS OF THE RESIDUAL = [(STATIC NAV SOLN R_2-R_1) – (WSMR BET R_2-R_1)]

Figure 6-42 Channel 2-1 Residual Spectral Lines vs User Y Position

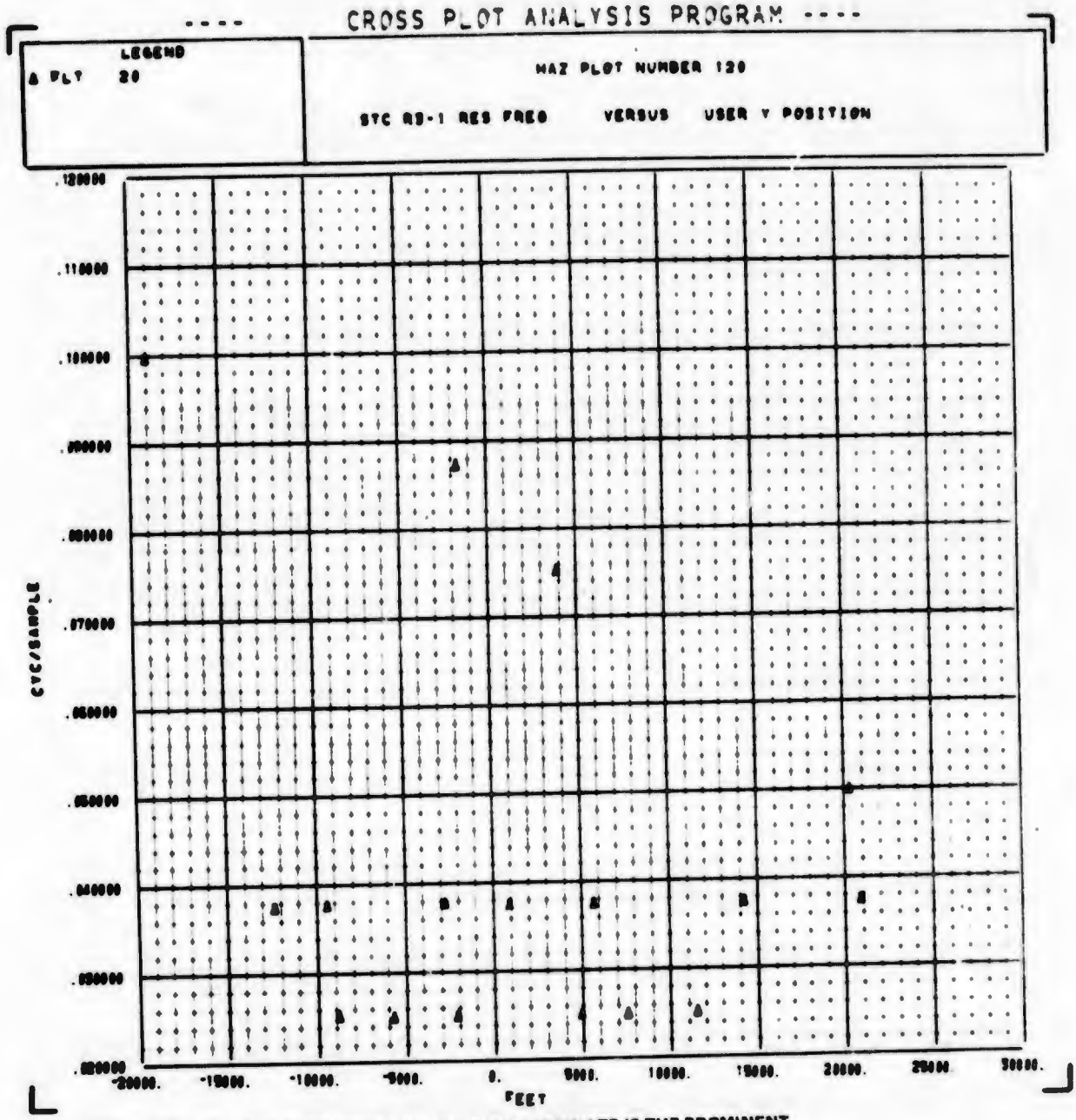

NOTE: STC R_{3-1} RES FREQ INDICATES THAT THE ORDINATE IS THE PROMINENT SPECTRAL LINES RESULTING FROM A FREQUENCY ANALYSIS OF THE RESIDUAL = [(STATIC NAV SOLN R_3-R_1) – (WSMR BET R_3-R_1)]

Figure 6-43 Channel 3-1 Residual Spectral Lines vs User Y Position

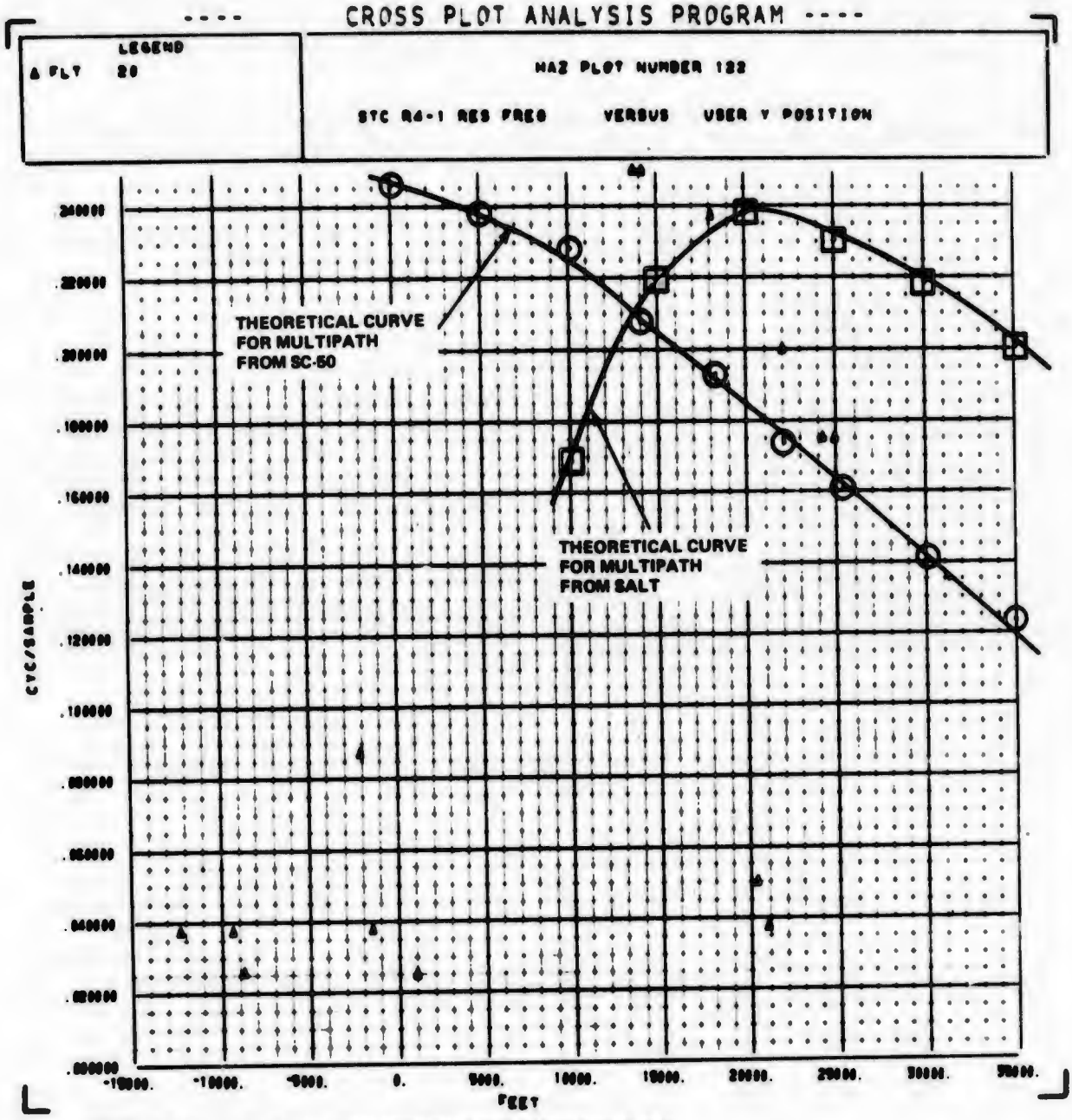

NOTE: STC R_{4-1} RES FREQ INDICATES THAT THE ORDINATE IS THE PROMINENT SPECTRAL LINES RESULTING FROM A FREQUENCY ANALYSIS OF THE RESIDUAL = [(STATIC NAV SOLN R_4-R_1) – (WSMR SET R_4-R_1)]

Figure 6-44 Channel 4-1 Residual Spectral Lines vs User Y Position

to-aircraft multipath from station SC-50, which is located approximately 20,000 ft south of Salt (35,000 to 45,000 ft from the user). Figure 6-45 shows the theoretical multipath fade frequency as a function of user distance from SC-50, channel 4.

At the same time the "lower" frequency region of Figures 6-42 through 6-44 show partly-specular-to-partly diffuse multipath fade frequencies caused by multipath from Salt (station 1). (See Section 4.3 for further discussion of these multipath errors.)

An examination of the plot of range 1 residual (navigation solution range 1 - WSMR range 1) vs range 4, (Figure 6-46) at approximately the same User Y location (since the plot against range 4 is almost the same as a plot against Y) shows a strong cyclic variation. The presence of specular multipath at distances of greater than 35,000 ft from SC-50 is expected since the aircraft antenna is essentially linearly polarized on the horizon and cannot reject the ground reflected signals.

6-3 THREE VIEWPOINTS OF THE SYSTEM PERFORMANCE

Having arrived at an understanding of the data behavior on flights 17-23, it is now possible to look at the user's navigation performance from different viewpoints. Since the overall objective of this test program was to verify through field experiments the theoretical understanding of the four channel correlation receiver behavior and to assess the potential performance which might be expected of this type of equipment, it is useful to examine the impact of the field test error mechanisms on the user navigation performance.

The field test error mechanisms may be divided into two broad categories. The experiment program is a simulation of the major features of the anticipated final system configuration. As such, it suffers the problems of all simulations, namely the inability to perfectly represent the actual system.

Error mechanisms such as the ground calibration link measurements, the uplink antenna delay, and multipath interference from ground reflections caused by the proximity of the transmitting antennas to the ground are unique to the WSMR tests. From an overall system evaluation viewpoint, these are shortcomings of the simulation.

Another category of error mechanisms are those indigenous to the receiver equipment. These include items influencing the psuedo range and pseudo range-rate measurement accuracies such as tracking loop implementation, basic oscillator characteristics and frequency management within the receiver, data output techniques, automatic calibration of receiver path delays, and basic path delay stability. An assessment of these types of error mechanisms is the primary purpose of the program since this equipment represents some of the current concepts for highly accurate correlation receivers.

These error sources have been discussed in this report and their individual impacts on the system measurement accuracy established. At this point, the question we want to answer is: How well can a user navigate with this system? A complete answer to this question, referring to some future operational system, is beyond the scope of this program. However, within the test program constraints, the user navigation performance can be examined.

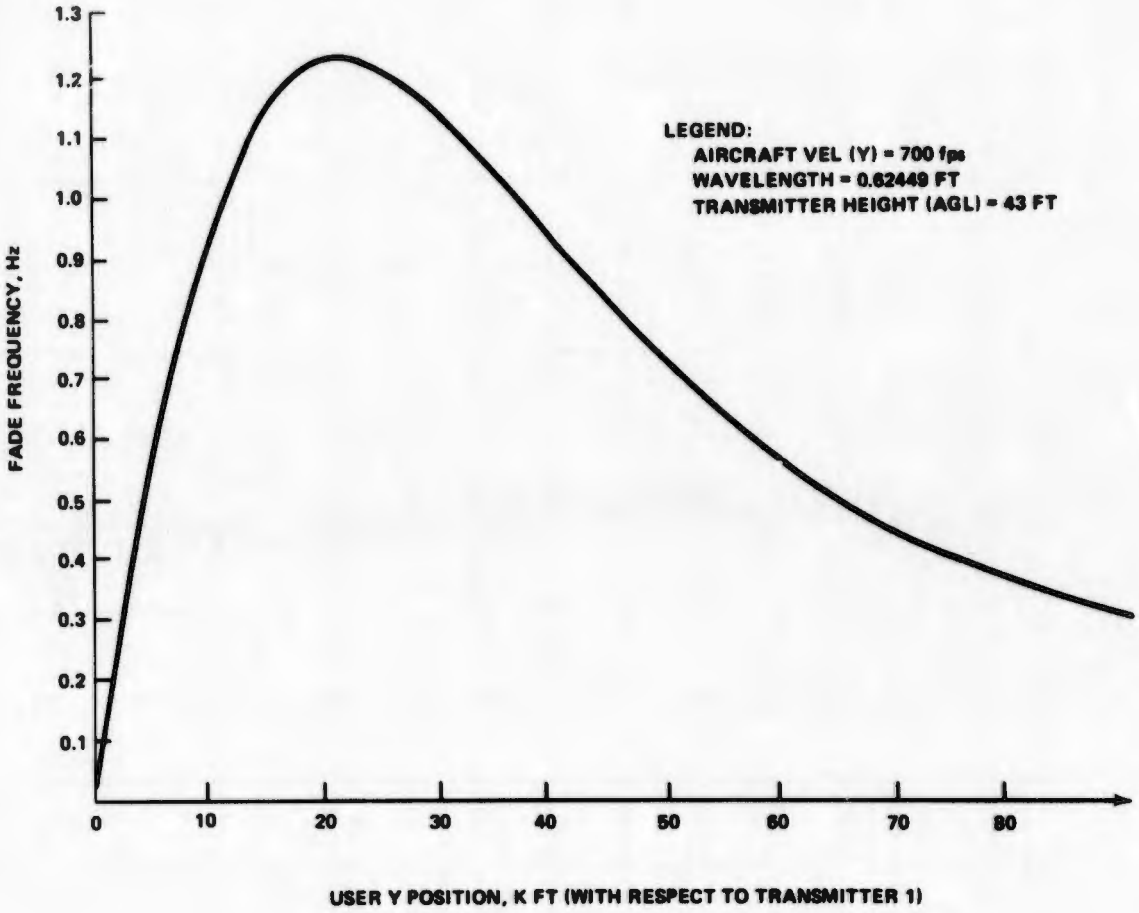

Figure 6-45 Differential Doppler Vs Ground Track Distance, K Ft

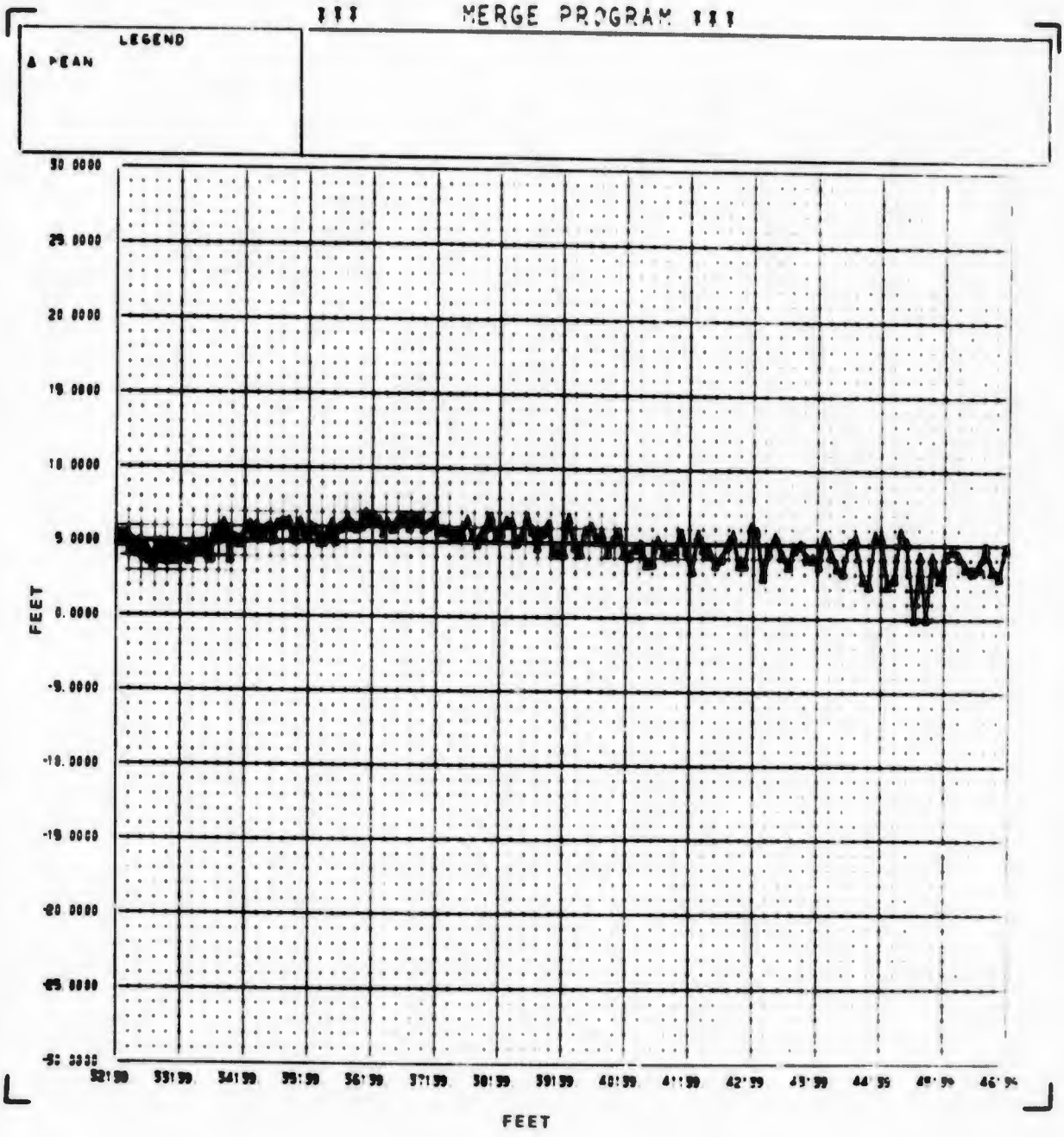

Figure 6-46 Range 1 Residual vs Range 4 HC Flight 20 Run 02

Three separate viewpoints (Cases) are taken in presenting the user navigation performances:

Case 1. After improving the ground system configuration prior to flight 17, the data recorded on flights 17-23 are presented as measured.

Case 2. As a result of analyzing the data results from flights 17-23, three remaining primary error sources were identified in the ground system: cesium measurements; uplink antenna delay, and some unstable rf cable delay. Of these, test measurement data are available to quantify and correct the cesium measurements and the uplink antenna delay. After correcting for two ground errors, thus removing as much of the test simulation shortcomings as possible, present the resulting data.

Case 3. After correcting for the two ground system errors (cesium measurements and uplink antenna delays) analyze the test results and determine the remaining steady-state errors. Arbitrarily correct the data for the remaining average steady-state error on the basis that regardless of the location of the error source(s), the error is essentially constant and can therefore be removed. (This procedure is typical of that used in current operational systems.)

The overall data results are presented in Figures 6-47 and 6-48. The user vector position error is shown in these figures as a cumulative percentage distribution for Cases 1, 2, and 3. These curves are derived by comparing the user position with the WSMR references position computing the total position error by vectorially adding the X, Y, and Z error components and determining the percentage of these total errors exceeding specified values (abscissa). For example, 50% of the HC data show a position error less than 37 ft for Case 1 navigation solutions; 90% of the MRL data show a position error less than 40 ft for Case 2 navigation solutions.

A similar presentation of the user vector velocity errors is given in Figure 6-49. Since the 3-case presentation is directed toward position errors, there is negligible effect on the velocity errors from the different viewpoints. Therefore only one set of curves is shown on this figure.

The navigation residual time series (nav solution - WSMR) corresponding to the three viewpoints were shown in Figures 2-1 through 2-6. The individual position and velocity component errors for both HC and MRL data shown in these figures indicate the impact of the correction terms used to generate Cases 2 and 3 on the fine structure of the data. Case 3 especially is significant since the correction terms are an average of the steady-state Case 2 errors from both HC and MRL data. The fact that one set of correction terms reduces the navigation errors of both receivers to almost the same small values strenghtens the rationale of the operational significance of Case 3.

The navigation system performance can be viewed another way to illustrate the extent of scattering of the errors. Figures 6-50 and 6-51 show the projection of the navigation position errors in the horizontal plane. Position errors are measured with respect to the WSMR reference data and computed at one second intervals along the flight path. The data in these figures are derived from the Case 3 navigation

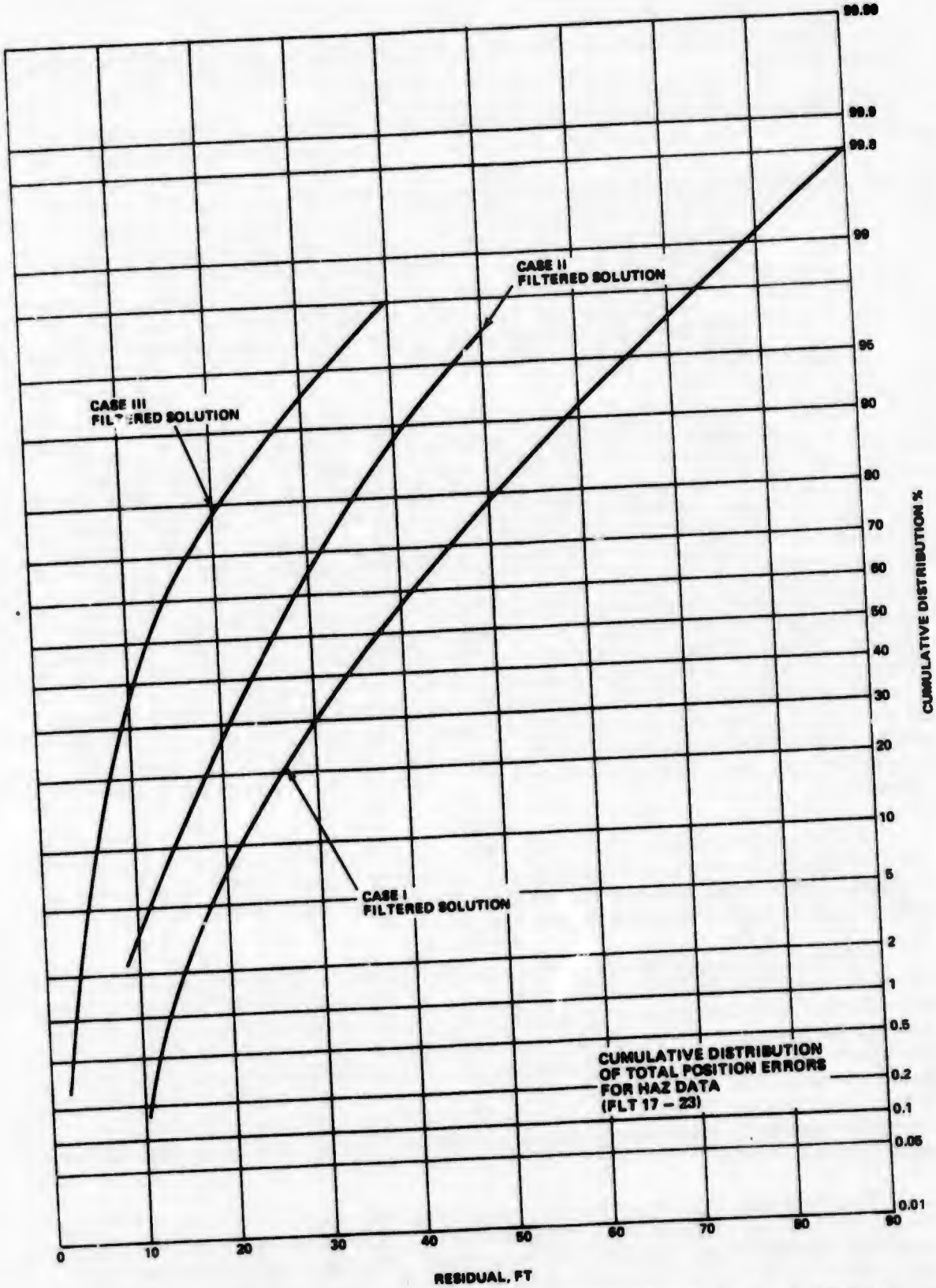

Figure 6-47 Cumulative Distribution of Total Position Error for HAZ Data (Flights 17-23)

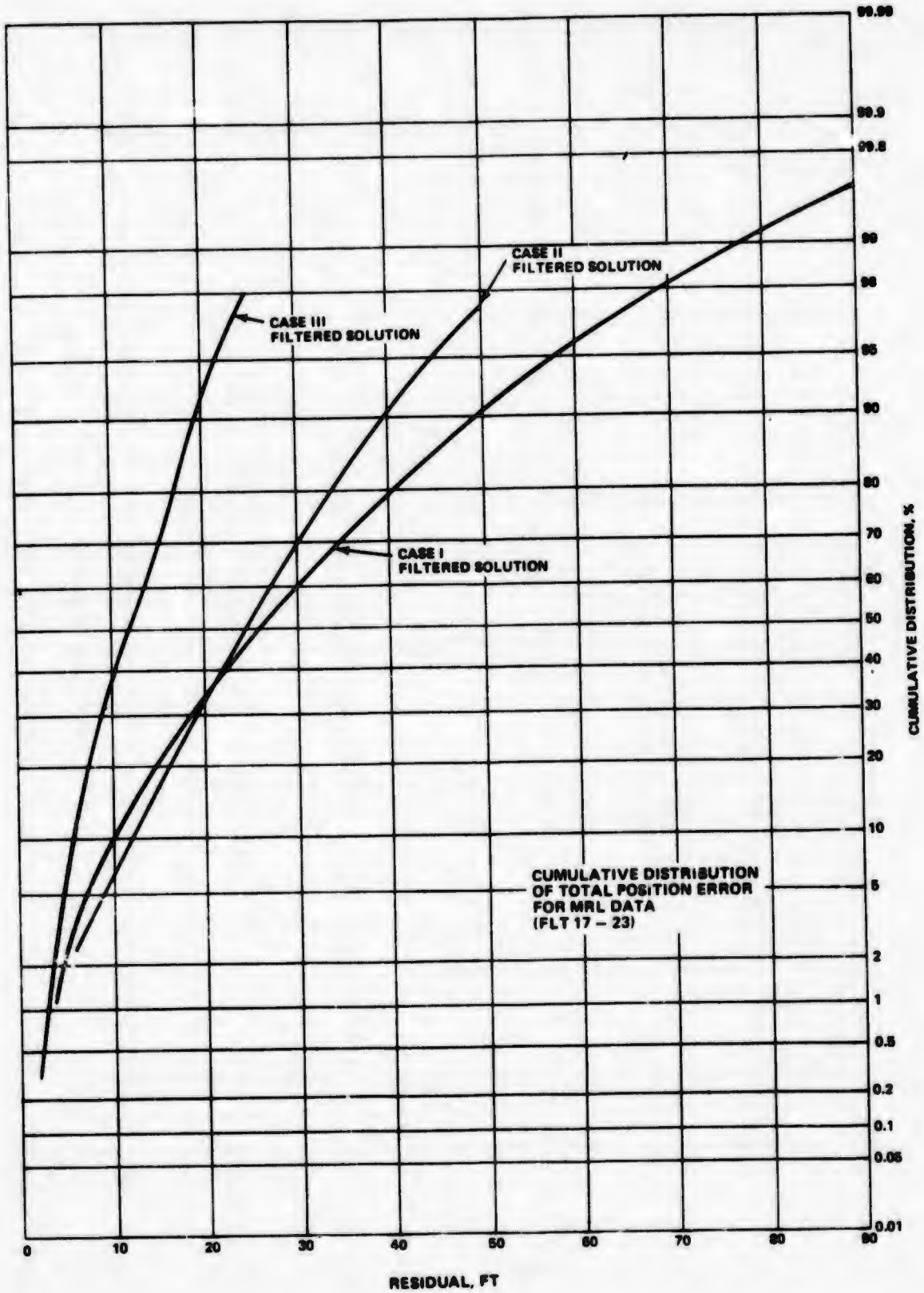

Figure 6-48 Cumulative Distribution of Total Position Errors for MRL Data (Flights 17-23)

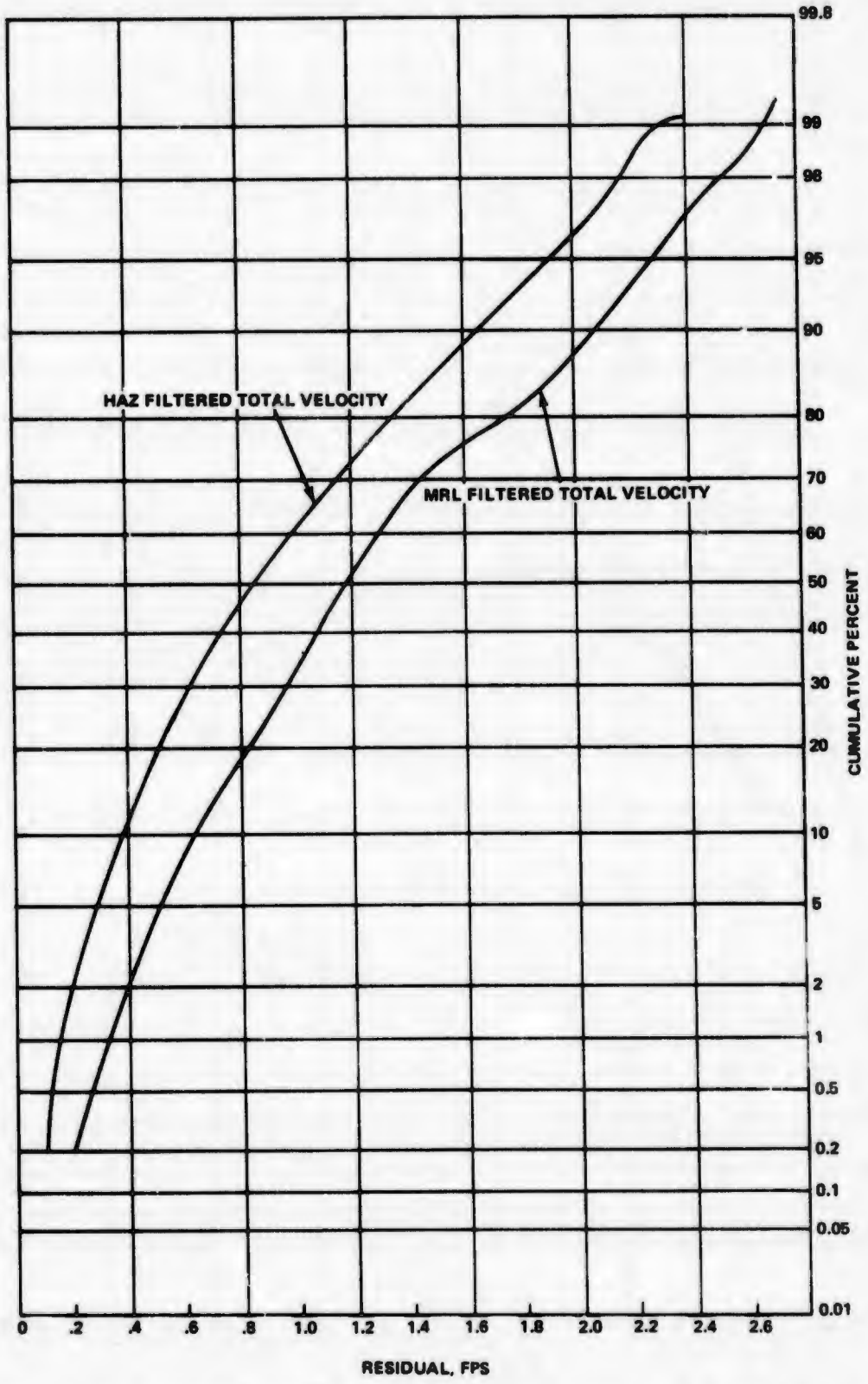

Figure 6-49 Cumulative Distribution of Velocity Errors for HAZ and MRL Data (Flights 17-23)

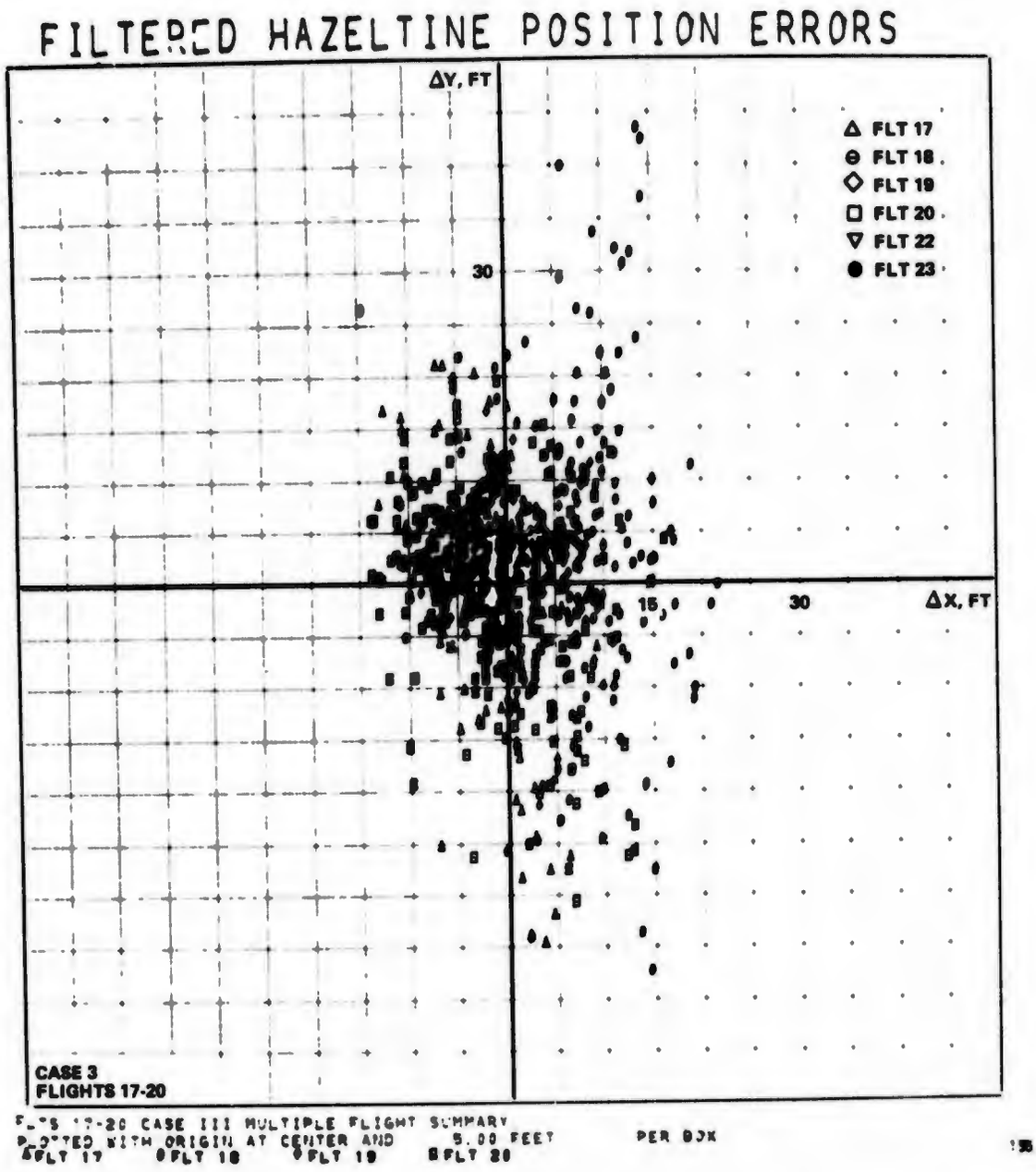

Figure 6-50 Horizontal Position Errors for HC Data, Area Navigation

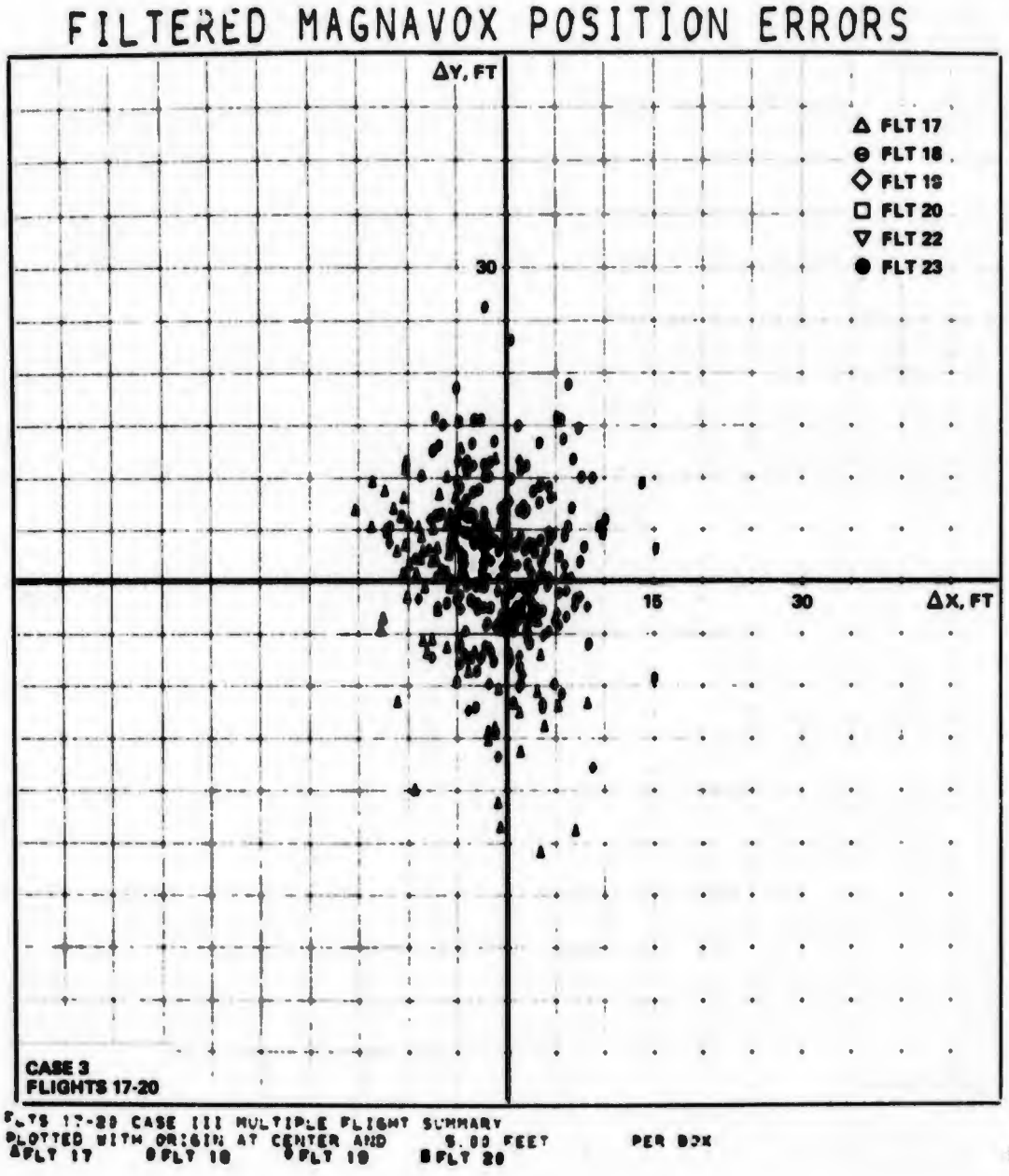

Figure 6-51 Horizontal Position Errors for MRL Data, Area Navigation

solution. For the HC data in Figure 6-50, a circle having a radius of 10 ft would enclose a majority of the horizontal position errors. Data scattering is seen to have occurred primarily on flights 18 and 20. On flight 18 second order loop performance was tested, resulting in noisy data, and on flight 20 low signal levels were used, causing both additional noise and a bias shift in the HC data.

The MRL horizontal position error data shown in Figure 6-51 indicates very similar results to the HC data. The MRL receiver was not functioning on flight 20 and was not tested in a second order loop configuration, thus eliminating much of the data scatter seen on the HC plot.

The horizontal velocity solution errors are shown in Figures 6-52 and 6-53 for the two receivers. A circle having a radius of 0.7 fps would enclose a majority of the data. Both receivers are seen to perform similarly. As discussed later in Section 10, the system velocity performance may in fact be superior to that indicated by these figures since the absolute accuracy of the WSMR velocity reference may be inferior to the test system's performance. None the less, the system velocity performance was extremely accurate and consistent.

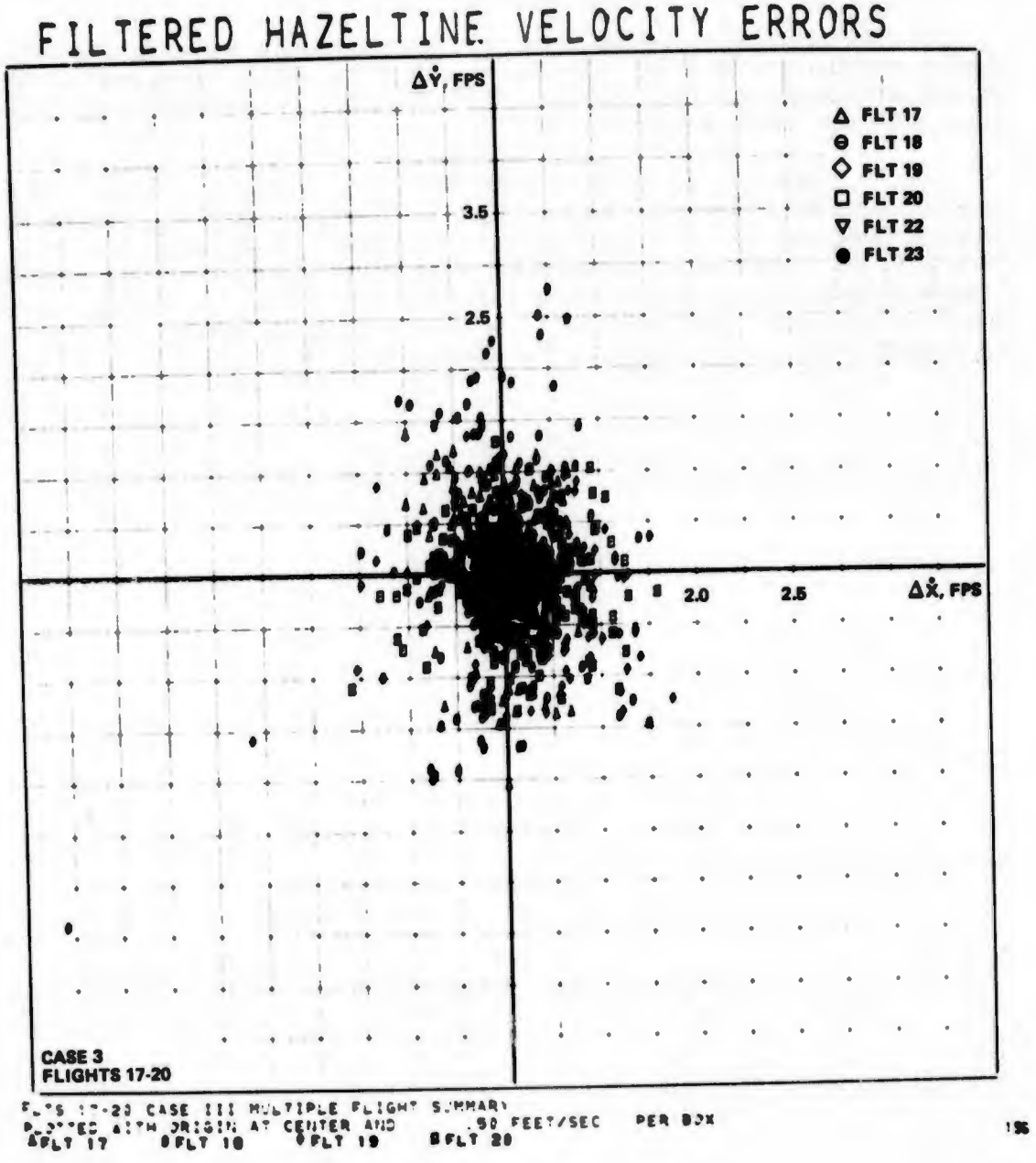

Figure 6-52 Horizontal Velocity Errors for HC Data, Area Navigation

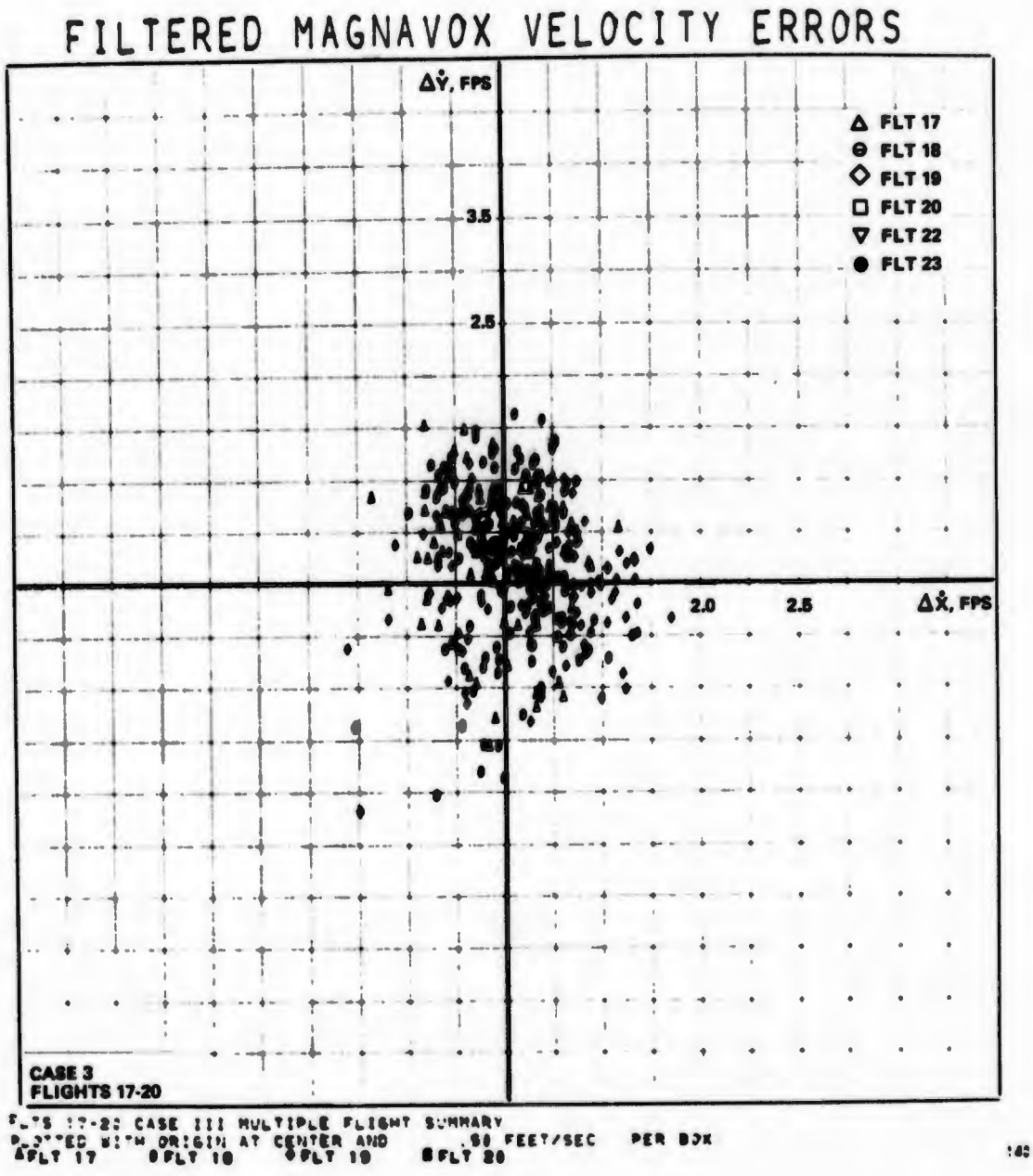

Figure 6-53 Horizontal Velocity Errors for MRL Data, Area Navigation

Security Classification

DOCUMENT CONTROL DATA - R & D

(Security classification of title, body of abstract and indexing annotation must be entered when the overall report is classified)

1. ORIGINATING ACTIVITY (Corporate author)	2a. REPORT SECURITY CLASSIFICATION
Grumman Aerospace Corporation Bethpage, New York, 11714	UNCLASSIFIED
	2b. GROUP

3. REPORT TITLE

FINAL REPORT, SYSTEM 621B USER EQUIPMENT DEFINITION AND EXPERIMENTS PROGRAM, PHASE II FIELD TESTS.

4. DESCRIPTIVE NOTES *(Type of report and inclusive dates)*

FINAL REPORT 11 Jan 1971 to 11 April 1973

5. AUTHOR(S) *(First name, middle initial, last name)*

John J. Courtney, Jr. — Paul Richards — Robert Regis (HC)
Ralph Laho — Michael Moore — Bert Glazer (MRL)
Ivan Kadar — Michael Neglia

6. REPORT DATE	7a. TOTAL NO. OF PAGES	7b. NO. OF REFS
11 April 1973		

8a. CONTRACT OR GRANT NO.	9a. ORIGINATOR'S REPORT NUMBER(S)
FO 4701-71-C0176	Vol. I. - None Vol. II. - None Vol. III. - None
b. PROJECT NO. SYSTEM 621B	
c.	9b. OTHER REPORT NO(S) *(Any other numbers that may be assigned this report)*
d.	SAMSO TR 73-65

10. DISTRIBUTION STATEMENT

Distribution limited to U. S. Government Agencies only; Test and Evaluation, February 1973. Other requests for this document must be referred to HQ SAMSO/XRN.

11. SUPPLEMENTARY NOTES	12. SPONSORING MILITARY ACTIVITY
The distribution of this report is limited because it contains technology requiring disclosure only within the Department of Defense.	Space and Missile System Organization (XRLO) P.O. Box 92960, Worldway Postal Center Los Angeles, California, 90009

13. ABSTRACT

System 621B is a concept for a global satellite - based precision navigation system designed to meet the requirements of land, sea and air military forces in an advantageous cost effective manner. One of the most important elements in this system is the user receiver. This report summarizes a series of flight and ground tests conducted at the White Sands Missile Range to evaluate the performance of a four-channel receiver in typical flight and field environments in order to solidify confidence in the predicted performance of System 621B receivers.

DD FORM 1 NOV 68 1473

Security Classification

14. KEY WORDS	LINK A		LINK B		LINK C	
	ROLE	WT	ROLE	WT	ROLE	WT
Receiver Test						
Flight Test of Navigation Receiver						
Ground Equipment for Receiver Test						
Flight Test Data Processing						
Airborne Installation						
Antenna Design and Installation						
Flight Test Data Analysis						
Multipath Testing						